A Framework for Automated Optimisation of Tension Leg Platforms for 15 MW Floating Offshore Wind Turbines

M.C. Boersma

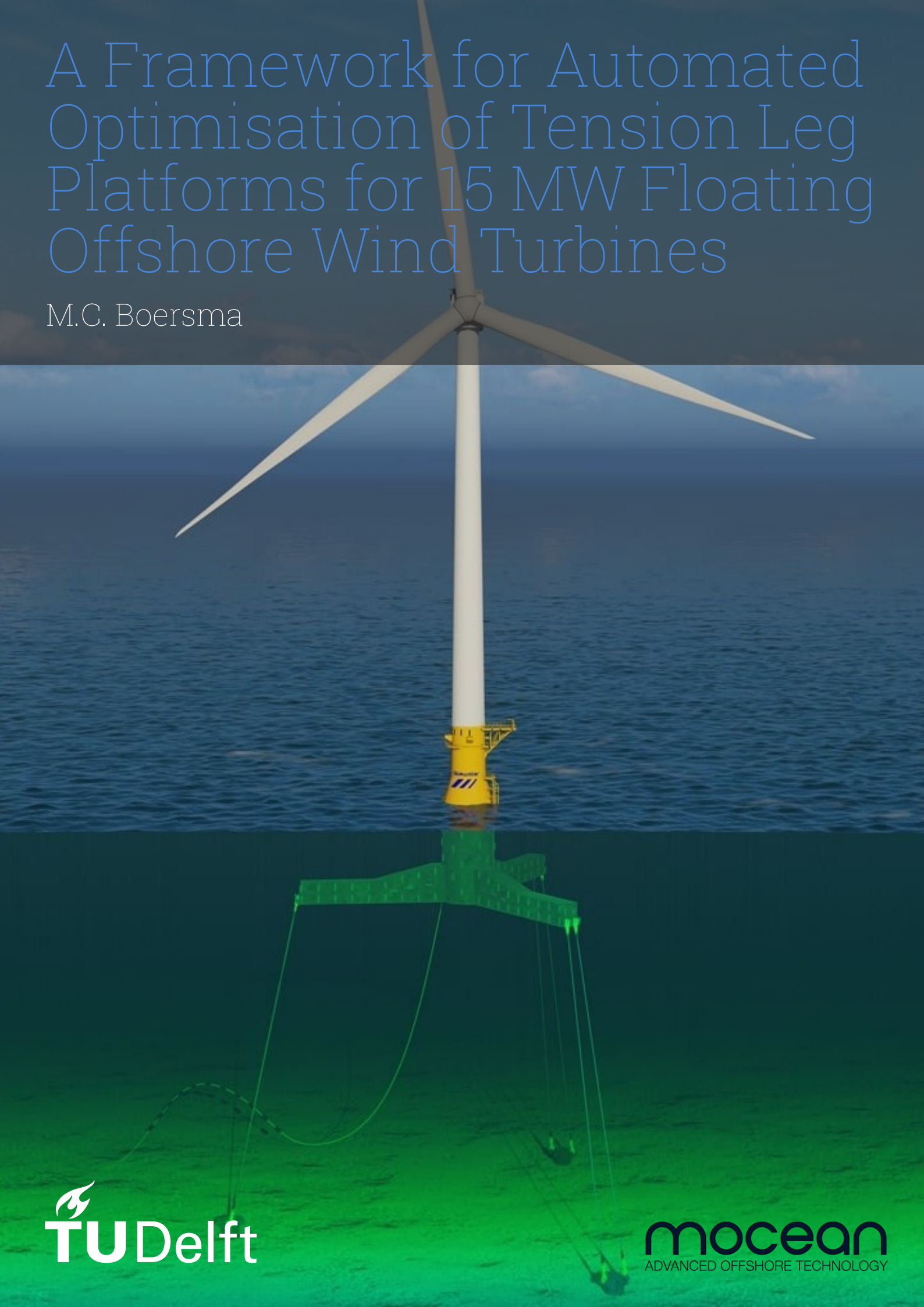

TU Delft

mocean
ADVANCED OFFSHORE TECHNOLOGY

A Framework for Automated Optimisation of Tension Leg Platforms for 15 MW Floating Offshore Wind Turbines

by

M.C. Boersma

to obtain the degree of Master of Science

at the Delft University of Technology

to be defended publicly on Tuesday July 29, 2025 at 15:45 PM.

Student number:	4861566	
Project duration:	December 2024 – July 2025	
Thesis committee:	Dr. ir. O. Colomés Gené	TU Delft, Chairman
	Prof. Dr. Ir. A.V. Metrikine	TU Delft, Examiner
	Dr. Ir. S. Schreier	TU Delft, Examiner
	Ir. F.C. Lange	TU Delft, Supervisor
	Ir. J. Ruesen	Mocean, Supervisor

Cover: METCentre & Bluewater TLP [10]

An electronic version of this thesis is available at http://repository.tudelft.nl/.

TU Delft

mocean
ADVANCED OFFSHORE TECHNOLOGY

Preface

What a journey! With this master's thesis, I reach the end of my study period here in Delft. What started off as an endeavour in aerospace engineering led me, after two gap years, to pursue a master's in the fascinating world of Offshore & Dredging Engineering. It wasn't only a learning experience through all the research and theory I picked up along the way, but also the critical attitude and the experience of the thesis process itself that brought me a lot of personal development and insight.

First and foremost, I'd like to thank the entire team at Mocean for welcoming me with open arms and immediately making me feel part of the team. I truly enjoyed working with each and every one of you and learning from your experiences, which sometimes involves falling in the water and getting back up again. A special thank you to Joël for constantly supporting me throughout the process, helping me out whenever I was stuck or needed a bit of extra encouragement. After this journey, I see you more as a friend than a supervisor.

Great thanks to my TU Delft supervisor, Frank, for guiding me through this project while maintaining constructive feedback and especially for his consideration and the human touch he brought to his supervision. I also want to thank Oriol for providing valuable feedback throughout the process and for guiding the committee.

A huge thank you to my family, and especially my parents, for supporting me throughout my entire time in Delft. I probably should have come home more often and not stayed away for so long. Thanks also to my friends and housemates for all their support and for the countless desserts we shared and tested during this thesis period.

Of course, I can't leave out the one person who, no matter what, always took care of me when I was exhausted, needed support or just needed someone to listen to me talk about the complexity of a tension leg platform. My wonderful girlfriend, thank you for your endless support. The past few months would have been much more intense without you by my side.

M.C. Boersma
Delft, July 2025

Abstract

The need for more sustainable and cost-effective energy generation has increased the interest in offshore wind development in deep-water regions. Floating wind turbines offer a promising solution at water depths where bottom-fixed structures are not feasible. Currently, the implementation of floating wind turbines remains limited due to high costs and complex system dynamics. There is a need for efficient, automated optimisation tools that can efficiently identify cost-effective design spaces early in the development process. While optimisation studies have been conducted for semi-submersible and spar-type platforms, limited optimisation related research exists on tension leg platforms (TLPs). This study addresses that gap by developing an optimisation framework for TLPs supporting 15MW wind turbines, allowing for efficient, accurate and cost-effective design iterations while considering platform specific dynamics,.

To achieve this, a frequency-domain model was developed by extending the open source RAFT software. The extensions incorporate features particularly relevant to TLP modelling, including tower flexibility, a sum-frequency force approximation and an analytical tension leg mooring module. The resulting frequency-domain model achieves an error margin within $\pm 16\%$ of non-linear time-domain simulations for TLPs with (near) vertical tendons, while reducing computational time by 98.5%. This makes the model suitable for dynamic analysis within optimisation studies, while enabling TLP-specific response characteristics to be captured at a fraction of the computational cost.

The developed model was integrated into a multi-step genetic algorithm-based optimisation framework to explore the design space, with the objective to reduce the levelised cost of energy (LCOE). The framework, built around a single-column TLP design with four pontoons with tendons at their ends, took into account six design variables to describe the essential system properties. The resulting six dimensional complex design space considers the main column diameter and draft, pontoon diameter and length, tendon angle and tendon pretension. To enable complete design performance evaluations and potentially provide early-stage insights that support certification preparation, each concept was assessed against an extensive set of load cases according to standards, covering both ultimate and fatigue loads in operational and extreme conditions.

The results of the optimisation study identified draft, tendon pretension, tendon angle and pontoon length as the most influential parameters for dynamic performance due to their strong influence on platform stability and mooring stiffness. The column and pontoon diameter had the most significant influence on platform mass and therefore platform cost, while pretension dominated mooring system cost. Despite the identification of these most influential variables, the highly coupled nature of TLPs requires to take all identified design variables into account.

A detailed cost model was implemented, enabling comparison of design concepts within the study, and comparison with floating wind platform designs in other research. To achieve this, the model combines variable platform and mooring costs with fixed lifecycle costs. Multiple optimisation runs revealed several distinct, cost-efficient design spaces, with convergence toward lower LCOE values with increasing iterations of the optimisation. The most cost-effective designs achieved LCOE values around 65 €/MWh, making them competitive with other floating wind concepts across different studies.

Altogether, this work provides an efficient optimisation framework for TLPs in the context of floating offshore wind. It enables accurate and cost-effective design iterations that account for TLP-specific dynamics while significantly reducing computational time. By considering a wide range of load cases and maintaining a balance between speed, adaptability and physical accuracy within a limited degree of uncertainty, the framework offers a holistic approach. This makes it well suited to support early-stage design decisions and concept selection for future deep-sea wind farms using TLPs.

Contents

List of Figures

List of Tables

1

Introduction

The necessity of affordable and sustainable energy sources is growing in this increasingly power demanding world. In regions like the North Sea, shallow waters enable the use of cost-effective bottom-fixed offshore wind turbine structures. However, in many parts of the world, water depths increase significantly when moving further offshore. For example, areas off the coast of Norway and around the Mediterranean Sea typically reach depths of 200 m or more, as illustrated in Figure 1.1. These deeper waters, which are not economically viable for bottom-fixed structures, hold potential for sustainable energy generation but remain unused due to technological and economic challenges. Floating offshore wind turbines (FOWTs), for example the one depicted in Figure 1.2, offer a promising solution to unlock this deep water offshore wind potential.

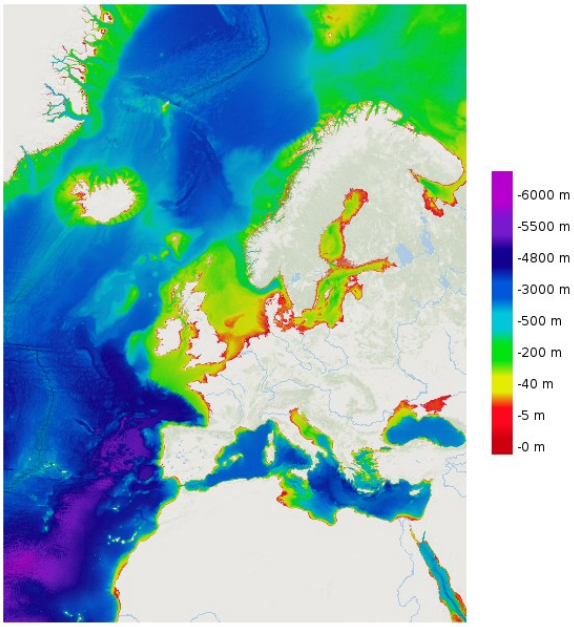

Figure 1.1: Bathymetry map of Europe [31]

Figure 1.2: PelaStar 15 MW concept [37].

Despite their potential, floating offshore wind turbines are not yet widely implemented in deep-water areas. The main barrier is the relatively high cost compared to other energy generation methods, making floating wind a less attractive investment. In addition, as a relatively new technology, FOWTs face various uncertainties and challenges across all stages of their lifecycle. To ensure that FOWTs become

a viable competitor in future electricity markets, both capital and operational costs must be reduced. One of the most significant cost drivers is the design of the substructure. An inefficient substructure increases material, manufacturing and installation costs. Additionally, poor substructure design negatively affects system dynamics, leading to higher operation and maintenance costs and reduced energy production. To address these challenges, preliminary design optimisation studies are conducted to efficiently identify promising designs before progressing to detailed analyses. Automating this early-stage optimisation process enables fast design iterations, reducing the time, effort and cost required for such a study.

Current optimisation studies for FOWTs have explored various floater concepts, but a comprehensive and automated optimisation framework specifically for tension leg platforms (TLPs) in offshore wind is noticeably absent. TLPs show potential for FOWTs due to their relatively small motions, typically lightweight design and small mooring footprint. However, TLP design is complex due to the unique highly coupled behaviour and the stiff system properties compared to other floating wind platforms. While TLPs have been studied more extensively in the oil and gas sector, those designs are not directly transferable to offshore wind applications, as they do not account for the large aerodynamic thrust forces and overturning moments imposed by wind turbines. An optimisation framework specifically for TLPWTs is therefore essential to enhance performance, reduce costs and improve the competitiveness of TLP-based FOWTs in the global energy market.

1.1. Research Question

In order to contribute to this development of making TLP-based wind turbines more competitive, the following research question was constructed to address the presented research gaps and relevance:

“ How can a frequency-domain-based optimisation framework be developed for 15 MW tension leg platform wind turbines to enable efficient, accurate and cost-effective design iterations, considering tension leg platform specific dynamics?”

1.2. Socio-Techno-Economic Relevance

This research aims to accomplish more than filling the research gap. It is driven by four key socio-techno-economic goals:

1. Cost Reduction and Design Improvement: Develop an optimisation framework to help offshore wind developers reduce costs and enhance TLP designs in the early design stages.
2. Industry-Wide Applicability: Form the foundation for an easily adjustable framework that can be adapted to various TLP designs, streamlining the technical design process.
3. Environmental Impact: Promote sustainable energy by reducing material usage in floating offshore wind designs and making FOWTs economically competitive with non-renewable energy sources, driving the adoption of green energy generation.
4. Social Impact: Contributing to the long-term vision of enabling renewable energy generation in deep water areas, providing fair access to sustainable and reliable energy worldwide.

In the following chapters, the context of this research is elaborated upon. Chapter 2 presents a literature review for all different aspects of FOWT optimisation, highlighting the current research gaps that lead to the main research question and the sub-questions. Next, a theoretical framework is presented in Chapter 3 to provide the theory used throughout this research. This is followed by Chapter 4, which explains how this theory is put into practice to get to the acquired results. Chapter 5 to Chapter 7 present the results obtained during this research for the constructed model and the optimisation framework. This thesis concludes with a discussion, conclusion and recommendations for further research in Chapter 8 and Chapter 9.

2

Literature Review

Optimisation studies follow a similar workflow. The process starts with the selection of the floater and wind turbine type, followed by formulating the optimisation problem with clear objectives and constraints. A suitable model is then developed or adapted from existing models to represent system behaviour while ensuring computational efficiency. An overview is shown in Figure 2.1.

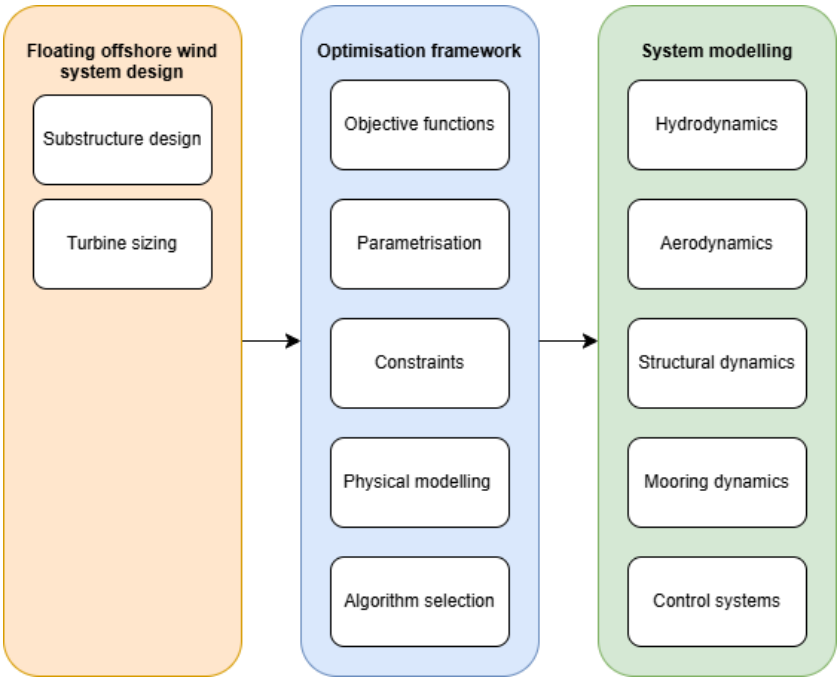

Figure 2.1: The different aspects of an optimisation study.

2.1. Floating Offshore Wind System Design

First of all, a substructure and turbine design are selected for which the optimisation will be performed. This section aims to elaborate on the current design trends in floating wind substructures and offshore wind turbines.

2.1.1. Substructure Design

Currently, three types of floating offshore wind substructures are considered the most promising. These substructure types are illustrated in Figure 2.2. While spar buoys and semi-submersibles can be moored

using either slack or taut mooring systems, tension leg platforms exclusively rely on tensioned moorings.

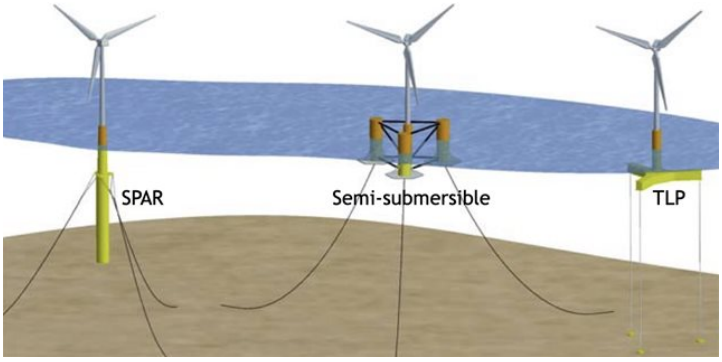

Figure 2.2: The three main types of floaters currently used for FOWT analysis [69].

In the context of optimisation, numerous studies have been conducted with different substructure concepts. These include both studies focusing on specific concepts and those comparing a variety of concepts and design spaces. Figure 2.3 illustrates the number of studies performed for each concept up to 2023.

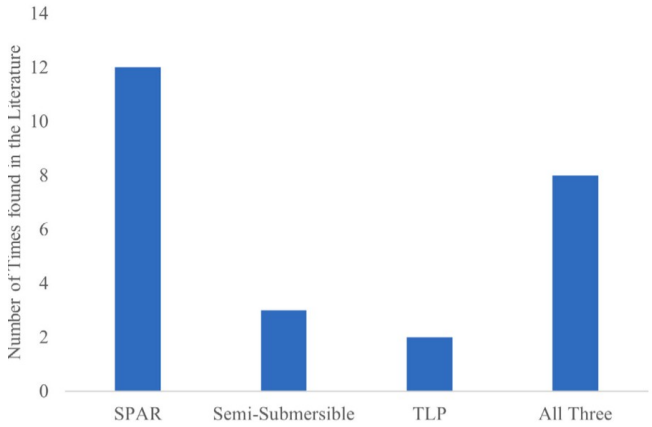

Figure 2.3: Frequency of references in the literature for different types of floating offshore wind platforms until 2023 [102].

As shown in the figure, spar buoys are the primary structures used in optimisation studies. The popularity of this design is likely due to the simplicity for optimisation, as it consists of a single cylindrical structure which simplifies the design space [62, 46, 87].

Semi-submersibles are increasingly studied over the years. They feature relatively simple transportation and installation procedures, making them flexible for various construction locations and harbours. In addition, they typically use cost-effective catenary mooring lines and are suitable for a wide range of water depths [66, 57, 56].

In the context of offshore wind, TLPs are less frequently used in design optimisation studies compared to other floater types. The primary reasons for this are the current challenges associated with their installation and the lack of full-scale tests and accompanying results. However, TLPs show great motion performance reducing the nacelle acceleration and pitch angles for example, which is a key risk in FOWT design [17, 57, 93]. While TLPs have been studied and deployed in the oil and gas sector, those applications do not experience the same magnitude of aerodynamic forces and overturning moments introduced by large offshore wind turbines, which significantly alters the platform design requirements [115]. This emphasizes the importance of a TLP-specific optimisation framework for future studies in order to make this concept more competitive in floating wind applications.

2.1.2. Turbine Sizing

Due to vast offshore space and advancing technologies, offshore wind enables the possibility of using increasingly larger wind turbines. Using fewer but larger turbines aims at reducing the cost of energy for offshore wind. Onshore wind turbines typically have an average capacity of around 3 MW, while the largest operational offshore turbines currently reach up to 12 MW [8]. Current optimisation studies utilise turbines of varying sizes which range from the well studied 5 MW reference turbine [104, 57, 62, 114, 59] to the 15 MW reference turbine [87, 56]. To put the turbine sizes used in research into context, Table 2.1 provides an overview of currently operating floating offshore wind farms, the turbine sizes they use and an example of a planned wind farm. This emphasizes the need for optimisation frameworks to be compatible for the next generation of 15MW+ offshore wind turbines.

Table 2.1: Overview of floating offshore wind projects, their operational status and turbine capacities [28, 29, 88, 95].

Project Name	Status	Type of Turbine
Hywind Scotland	In Operation	6 MW
Hywind Tampen	In Operation	8 MW
Kincardine Offshore Wind Farm	In Operation	9.5 MW
The Salamander Project	Planned for 2030	15-20 MW

2.2. Optimisation Framework

Typically, optimisation frameworks follow a series of standard steps for which a schematic overview is given in Figure 2.4.

- Identification of the objective(s) for the optimisation study.
- Identification of the most influential design variables with respect to the objective function and constraints.
- Setting up an efficient, accurate model to represent the systems response.
- Identification of the constraints of the optimisation study.
- Selection of the optimisation algorithm and stopping criteria.

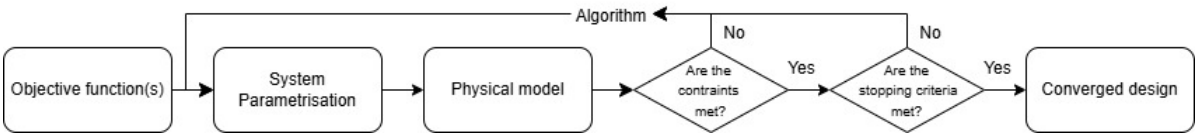

Figure 2.4: Schematic overview of an optimisation framework.

2.2.1. Optimisation Objectives

The most commonly used objectives in FOWT optimisation studies are cost and system motion response [102, 104, 57, 64, 62, 87, 36, 116, 46, 59, 56]. Currently, cost is the main objective due to the relatively high expenses associated with floating offshore wind compared to other energy sources. However, the way cost is incorporated varies widely, particularly in terms of which system components are included [57, 36]. To enable meaningful comparisons across studies, it is recommended to include all life-cycle cost components, ensuring the optimisation results reflect the full economic performance of the design.

System motion response in turn is of importance since reducing the experienced motions, such as surge and pitch, will prevent excessive loads on the structure and reduce fatigue of vulnerable parts of the system. With less excessive loads and fatigue, the system will have a longer life time and less O&M costs. Some studies consider only the rotor nacelle acceleration while others also consider translational

motion and minimising the static angle of inclination. The reason for taking into account the translational motion in the objective is the inclusion of limits on the power cable design [104, 57, 42, 62, 62].

It becomes clear that a significant trade-off exists between cost and response in floating offshore wind turbine optimisation studies. Balancing these two objectives is essential for developing economically viable and operationally efficient designs. There are two approaches to address this issue. The first is to use Pareto front modelling, which can evaluate trade-offs and identify optimal solutions that balance cost minimisation with system response reduction based on a weighting function relating the two objectives. The second approach is to address this issue by defining a set of realistic constraints ensuring cost-efficient results while remaining within known response constraints. Future research should focus on developing a method to compare system cost with system response, the biggest bottleneck for developing this method is the lack of sufficient data to formulate a relation between O&M cost and system response [26].

2.2.2. System Parametrisation

The number of variables used in optimisation should be as little as possible, as an increased number of free variables comes with an increased design space, which will result in large increases in computational time. Previous research into the design variables of TLPs showed that parameters which have a large effect on system mass and stiffness were the most influential factors for floater design considering cost and response [5]. Among these variables are the ballast mass, platform diameter and tendon pretension for example. This is reasonable as heavy, stiffer floaters will have smaller response but will be more costly as more material is used.

Following from this research a careful selection should be made in order to represent these most influential aspects. For this reason most research choose their free variables for system geometry and mass [4, 4, 52]. Several studies also include mooring line configuration to make the optimisation more complete as mooring lines also greatly determine system stiffness, especially for TLPs [57, 104, 46]. Furthermore, considering TLP design, the tendon angle may have a large influence on system response indicating to take this design variable into account in future TLP optimisation studies [112, 60].

2.2.3. Physical Modelling

After a parametrised structure is constructed it is key to accurately model the system in order to get realistic response outputs. There are two main types of models:

1. Frequency domain model (FD)
2. Time domain model (TD)

Frequency domain models are linearised models that are suited for efficiently and accurately modelling steady-state systems. Their primary strength lies in their ability to perform rapid calculations, making them particularly useful for early-stage design and optimisation. However, FD models have a significant limitation, they cannot account for non-linearities in the system. This restricts their applicability when dealing with phenomena such as large-amplitude motions resulting in highly non-linear forces.

In contrast, time domain models offer a much higher level of accuracy as they can capture all aspects of the system, including transient responses and non-linear forces. This makes them useful for detailed analysis and validation of complex systems. However, this accuracy comes at a cost as TD models are computationally intensive and require significant time and resources, particularly for large-scale systems or long simulation periods [54].

Frequency Domain Models in Optimisation

Numerous studies have used frequency-domain models for optimisation in floating offshore wind turbines. Most models are in-house frequency domain models which vary in complexity considering all aspects of the system modelling [57, 14]. More recent research demonstrates the optimisation of a semi-submersible platform using RAFT [56, 41]. However, one notable limitation of RAFT is the assumption that the system behaves as a fully rigid body, which may reduce accuracy. Another prominent tool is the OrcaFlex frequency-domain module by Orcina. This module is able to account for mean wave drift forces and first-order hydrodynamics only, disregarding second-order wave forces. Although all frequency-domain models benefit from high computational efficiency due to their linear formulation,

this same linearity limits their ability to capture non-linear phenomena. Different strategies have been proposed to approximate these effects. For example, RAFT includes a linearised drag damping formulation to mimic non-linear hydrodynamic damping. More recently, RAFT has introduced a module for estimating difference-frequency Quadratic Transfer Functions (QTFs) [13].

Time Domain Models in Optimisation
The most accurate models for floating offshore wind turbine analysis are time-domain models. Especially since they can include the non-linear effects of the system. Examples of time-domain models are OpenFAST and MoWiT [59, 62]. However, their high computational cost remains a significant drawback also limiting the amount of design variables that can be used while remaining within realistic computational time.

To address these challenges, a more computationally efficient model called SLOW was developed [63]. This model was specifically designed for efficient time-domain optimisation of FOWT substructures by using a lower-order time-domain approach with key simplifications. For example, SLOW reduced the degrees of freedom and used the Newman's approximation for second-order drift forces, avoiding the need to compute full quadratic transfer functions (QTFs). These simplifications allowed for more efficient computations while remaining accuracy for optimisation purposes.

2.2.4. Optimisation Constraints

Constraints typically fall into two categories. The first involves defining allowable ranges for design variables to maintain system evaluation within realistic boundaries. These ranges are often based on engineering judgement and practical considerations such as construction, transportation and operational requirements.

The second type of constraints are the system performance constraints. These constraints can be for static and/or dynamic analyses. Static constraints, such as limits on mean static pitch angle and mean surge offset, are widely used in research to provide a baseline for system stability and system requirements for mean offsets for example. However, static constraints alone underestimate the behaviour of the system. Including dynamic constraints, such as allowable motion amplitudes or accelerations, improves the accuracy of motion analysis and ensures the system operates safely under realistic conditions [46, 57, 104, 24, 57].

Studies also incorporate constraints specific to critical components. For example, mooring line tensions must remain within allowable limits to avoid dangerous, highly non-linear slack events or failure, while rotor nacelle assembly (RNA) accelerations are constrained to ensure turbine durability over the lifetime. These component-specific constraints are particularly important to ensure the structural and operational integrity of FOWTs [57] [104]. Typical values of constraints used in literature can be seen in Table 2.2.

Table 2.2: Constraint values used in FOWT optimisation studies.

Constraint	Unit	Limit	Optimisation Study
Max static pitch angle	deg	10	[57]
Max static + dynamic pitch angle	deg	10	[57]
	deg	10	[104]
Max RNA acceleration	m/s^2	2.0	[24]
	m/s^2	1.0	[57]
Max horizontal offset	% of depth	10	[46]
	% of depth	15	[24]
Min line tension (TLP)	kN	0	[104]
	kN	0	[57]

2.2.5. Optimisation Algorithm

Optimisation relies on the use of algorithms to systematically explore the design space. A wide variety of algorithms are available, with one primary distinction being gradient-based versus gradient-free algorithms.

Gradient-based algorithms use the gradients of objective functions to converge to an optimum. These algorithms are particularly useful for problems where gradients can be calculated analytically. However, one limitation of gradient-based optimisation is that they converge to local optima, especially in complex design spaces, which means the resulting design may not represent the global optimum.. This limitation can be mitigated by employing a multi-start sequence, which begins the optimisation process from different initial designs to ensure a more comprehensive exploration of the design space. Gradient-based algorithms are efficient and fast when the objective function is smooth and differentiable, but they tend to struggle with problems that involve discontinuities or highly non-linear behaviour [97]. Some optimisation studies have successfully applied gradient-based methods for floating wind design, enabling rapid convergence even with a large number of design variables [93]. This was achieved by ensuring that the entire model could be described using analytical gradients.

Since floating wind system design spaces are often highly non-linear and discontinuous, gradient based optimisation algorithms are often not suitable. On the other hand, gradient-free algorithms operate without relying on gradient information. They rely on sampling strategies to explore the design space and identify optimal solutions. These algorithms are advantageous for problems where gradients are difficult to compute, when the design space is discontinuous or there are multiple objectives. Gradient-free optimisation is typically more computationally expensive, as it evaluates a broader range of designs, but it has the benefit of being less prone to local optima and better suited for global optimisation. As a result, gradient-free algorithms are often the method of choice for problems requiring exploration of the non-linear design space or for multi-objective optimisation [97]. Previous optimisation studies, where such a gradient-free algorithm was used, showed that the algorithm could efficiently optimise for cost and response, forming a Pareto front to evaluate the trade-off between these two objectives [57].

2.3. System Modelling

Floating offshore wind turbine systems are complex coupled aero-hydro-servo-elastic systems that require advanced modelling solutions. Unlike bottom-fixed turbines, which rely on rigid substructures that restrict large translations and rotations, floating turbines experience increased loads due to the significant movements of their substructures. This section aims to identify the modelling techniques used in optimisation literature for hydrodynamics, aerodynamics, mooring dynamics, structural dynamics and control systems. A schematic overview of the complex coupling between these system inputs is presented in Figure 2.5.

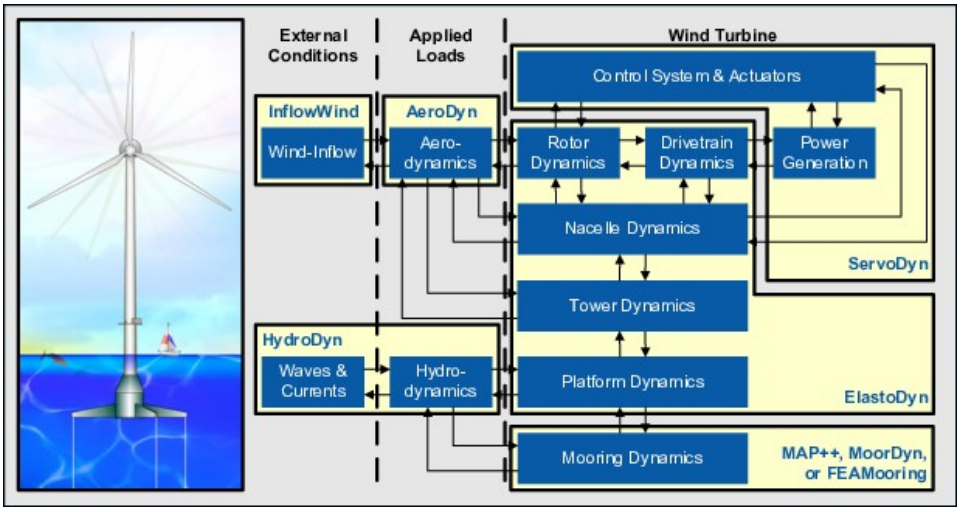

Figure 2.5: A schematic overview of all different couplings in a floating offshore wind turbine system [53].

2.3.1. Hydrodynamics

Accurate hydrodynamic modelling is crucial in floating offshore wind optimisation studies. One of the primary distinctions in hydrodynamic models in optimisation studies, is whether they account solely for linear hydrodynamics or also include non-linear hydrodynamics. As discussed in subsection 2.2.3, frequency-domain models are limited to linear analyses and therefore include linear forces with the possibility of adding linear approximations of non-linear effects. In contrast, non-linear hydrodynamics can often only be accurately captured through time-domain analyses. The two main approaches that are commonly used for hydrodynamic modelling in optimisation studies are potential flow theory and Morison theory. Higher fidelity modelling tools like CFD could be applied as well. However, these tools are too computationally expensive for optimisation purposes.

Potential flow

Wave–structure interaction in offshore systems is commonly modelled using potential flow theory, which is based on first-order and second-order wave potentials. This approach neglects viscous effects by assumption but remains widely used due to the accuracy for many offshore geometries. First-order wave forces arise from the linear wave potential, while second-order forces originate from the pressure over the variable submerged surface and the interaction between first-order wave components, resulting in sum- and difference-frequency effects due to combinations of different first order wave frequencies. In frequency-domain analyses, linear diffraction theory typically yields only the diagonal elements of the Quadratic Transfer Function (QTF), allowing for the calculation of first-order forces. While full diffraction analysis is more computationally expensive, it provides the complete QTF, enabling the accurate modelling of second-order forces.

Several studies have adopted variations of the potential theory approach. For example, WAMIT and Orcawave are commonly used to compute first-order hydrodynamics [57]. RAFT uses pyHAMS for linear diffraction and uses Newman's approximation [32] to estimate second-order difference-frequency forces [41]. However, Newman approximation does not accurately capture sum-frequency contributions.

A more comprehensive approach was taken by [4], where all second-order forces were modelled using full QTFs in a time-domain simulation. Industry-standard tools like OpenFAST [53] and OrcaFlex [82] also support full potential flow analysis by interfacing with solvers such as WAMIT and OrcaWave to compute complete QTFs.

Morison Equation

The dimensionless ratio λ/D, where λ is the wave length and D is the main column diameter, represents the hydrodynamic slenderness of a structure. For slender structures ($\lambda/D > 5$), diffraction effects are minimal and hydrodynamic forces are often estimated using the Morison equation, which is based on viscous drag and inertial forces. This method enables quick analytical, potentially strip-based, estimation of hydrodynamics.

RAFT applies Morison-based strip theory in the frequency domain by dividing the structure into segments and estimating local forces [41]. This method is computationally efficient but less accurate in mild sea states. Similarly, OpenFAST supports strip theory in the time domain [53] and OrcaFlex may use Morison elements, which apply the same principle per structural panel.

A recently included estimation of second-order forces in RAFT, uses Rainey's approximation (valid for $\lambda/D > 10$), which is an extended version of the morison equation, with kim and yue scattering effect compensation [13]. While currently limited to difference-frequency effects, this method can approximate full QTFs for slender bodies and yields results within minutes, compared to several days for full diffraction analysis.

Overview

From this comparison of methods, several conclusions can be drawn. Potential theory provides an accurate hydrodynamic analysis for most of the conditions. However, when dealing with slender structures and large wavelengths, it is more efficient to use a Morison-based model. Next to this, linear analyses give quick approximations of first- and/or second-order loads making them more suitable for optimisation purposes. An important current limitation of linear analyses is the inability to represent sum-frequency effects. Further research should focus on the significance of these sum-frequency forces and understanding the implications of excluding or approximating them using Rainey approximation.

2.3.2. Moorings

Mooring lines are typically modelled in one of the the three following ways:

- Static
- Quasi-static
- Dynamic

A static mooring line analysis is based on deriving the linear mooring stiffness from the zero offset equilibrium position. This stiffness is then used in the systems analysis for motions around this position based on the assumption of small motions.

The primary distinction between quasi-static and dynamic analyses lies in how the wave-frequency (WF) responses of the floater are handled [70]. In a dynamic analysis, the time-varying motions at the fairlead are calculated and used as inputs for the mooring line dynamic analysis. This approach also captures the time-dependent effects arising from mooring line added mass, drag forces, damping and acceleration relative to the water. By incorporating these factors, dynamic analysis provides a more accurate representation of the mooring line's behaviour under time-varying conditions.

A quasi-static analysis disregards the inertial and damping forces acting on the mooring line. Instead, the analysis assumes that the shape of the mooring line and the tension distribution along the length depend solely on the top and end positions. This simplification reduces computational complexity but does not account for time-dependent effects. Quasi-static analysis is based on a systems small motions around a certain mean offset position, extending the static analysis by accounting for mean wave drift forces and wind loads [70].

For the case of tension leg platforms usual practice is to use a static mooring analysis around the zero offset position where the tendons are assumed to be linear springs [32, 5, 115], one of the main assumptions for this type of analysis is small motions. In the case of TLP optimisation two important effects are often disregarded which may have a large impact. Due to the high stiffness of TLPs, tendons might experience so called springing and ringing forces. Springing forces are due to resonance of the tendons and can have great effect on system fatigue. Ringing is a third order transient phenomenon which only occurs for specific conditions, for example idling in extreme conditions. Ringing forces may significantly influence fatigue and maximum tendon tension loads [5].

2.3.3. Aerodynamics

The aerodynamic thrust forces on floating offshore wind turbines impose significant loads on the system, particularly as turbine sizes continue to increase. Current aerodynamic models are well-developed, however they are primarily designed for fixed-bottom turbines used in both onshore and offshore applications. Incorporating the dynamic effects of larger turbines and the movement of floating platforms requires extra care. Unsteady aerodynamic effects are particularly critical for tension leg platforms due to their higher natural frequencies, which may interfere with the 3P (blade passing) frequency, leading to complex unsteady aerodynamic interactions that need to be carefully analysed [84].

Blade element momentum theory (BEMT) is widely used in FOWT optimisation because of the computational efficiency and compatibility with linear analysis methods. This method combines blade elements theory (small elements of a blade with local forces) with momentum theory which calculates the thrust through a rotor plane based on the mass, momentum and energy laws of conservation. The eventual goal of this BEMT analysis is to determine the steady state thrust [105].

Several implementations of BEMT in simulation software exist, such as CCBlade used in RAFT and an in house BEM model in SLOW [64]. However, BEMT has limitations, as it assumes steady flow and neglects root and tip losses. To address these shortcomings, empirical corrections have been developed. Examples include models for hub and root losses [12], which account for turbulent wake effects caused by recirculation. Despite these corrections, they are not exact representations and may introduce inaccuracies in certain conditions, which can propagate through the optimisation process.

More detailed aerodynamic solvers, such as computational fluid dynamics (CFD) and free wake vortex analysis, are frequently used in advanced wind turbine analysis. However, their computational expense makes them impractical for optimisation studies.

2.3.4. Control Systems

The loads on a floating offshore wind turbine system are significantly influenced by the turbine controller. Wind turbines commonly employ the following types of control:

- Torque control
- Pitch control
- Yaw control

Torque control is usually used to maximise power output from the cut in wind speed to the rated wind speed. After reaching the rated wind speed the torque will remain constant and the pitch control will actively adjust the blade pitch in order to prevent the aerodynamic loads exceeding the systems capacity until the cut out wind speed is reached where the blades are completely feathered so no thrust is created any more. Torque and pitch control are usually taken into account in optimisation studies. Most studies disregard yaw control, operating under the assumption that the turbine remains perpendicular to the wind direction. Yaw control is particularly relevant in wind farm design for wake steering [43].

In early floating wind optimisation research, turbine controls were often excluded. However, due to their large impact on aerodynamic loading, they are increasingly incorporated into system models and even co-optimised. Recent studies have included control optimisers like ROSCO [2, 111, 56] to enhance system modelling and more accurately predict aerodynamic loads. Frequency-domain models, such as RAFT, typically linearise the control mechanisms, which can result in overestimation of aerodynamic loads by approximately 10% [101].

2.3.5. Structural Dynamics

Considering structural dynamics, the existing literature uses various approaches. Some studies use a full rigid body model, while others adopt multi-body dynamics to represent the different components of the system. Additionally, certain research focuses on evaluating stresses throughout the entire structure, whereas other studies rely on design standards to ensure the system remains within prescribed limits.

The simplest way to model a floating offshore wind turbine system is to treat the entire structure as a rigid body. This approach has been well used in previous studies [56]. However, this simplification results in system natural frequencies that deviate significantly from reality. Studies comparing rigid and flexible towers in FOWT systems demonstrated that tower flexibility has a significant impact on system response especially for TLPs [38]. More recent frequency-domain models incorporate tower flexibility, showing an improved resemblance to fully flexible models. Here the tower is modelled by Euler beam elements [14, 93, 87].

In optimisation studies, the structural design is typically not the primary focus. Often studies employ design standards to determine the thickness of the structure for example [56]. Other studies use a constant thickness value of approximately 0.05 meters [57, 114].

2.4. Discussion

This literature review reveals several research gaps that offer promising directions for future studies. This section presents a summary of the conclusions, the accompanying research gaps and the recommendations for further research.

Floating Offshore Wind System Design

Optimisation in the field of floating wind has gotten an increased interest in recent years, with most efforts focused on spar buoys and semi-submersibles. However, Tension Leg Platforms remain relatively under explored. Current research on TLPWTs optimisation either includes TLPWTs as part of broader studies or rely on simplified analyses. Future work should focus on dedicated optimisation studies for TLPWTs, considering their specific characteristics. Such studies could enhance performance, reduce costs and improve the competitiveness of TLP-based floating offshore wind turbines in the global energy market. Furthermore, future optimisation studies should remain easily adaptable for different mooring line materials. In order to remain relevant for current and future turbine design the future optimisation research should be based on 15 MW + wind turbines.

Optimisation Framework
Considering the optimisation framework itself, the main objective of existing studies is to reduce costs. The reason for this is that FOWTs remain expensive compared to competing energy sources. However, including the cost related to increased loads and motions of FOWTs remains complex. Especially since there is no data for this in practice. Future studies should aim to include these costs through either a detailed cost analysis or the use of well defined constraints on turbine motions. The latter aims at excluding significant cost increases compared to bottom fixed turbines allowing for more straightforward determination of the costs associated with operation and maintenance. Next to this, future studies should include all life-cycle costs in order to make sure design concepts become comparable across different studies.

In optimisation, the amount of free variables limits the computational efficiency as it increases the design space. For this reason it is key to determine the most influential free variables and keeping the quantity at a minimum. This means that future research should also incorporate a sensitivity analysis in order to check whether the set of free variables can be reduced by omitting the free variables that show to have little effect on the systems characteristics.

Modelling the system response of FOWT systems involves a lot of complexity. While time-domain models offer more detailed analysis, frequency-domain models offer efficient analyses. For optimisation studies, frequency domain models should be used as the goal of optimisation studies is to quickly converge to a small set of concepts which can be studied in a more detailed analysis. These frequency domain models however, do need to include the most important phenomena related to the specific system in use. Due to the inherent limitation of linear analyses in frequency-domain models, careful attention should be given to the validity of linearising FOWT systems.

Considering the constraints, future studies can benefit from a well thought out combination of static and dynamic constraints to keep motions within defined limits, allowing for better cost approximation. Next to this, future research should incorporate more constraints on system natural frequencies avoiding resonance, especially for stiff structures like TLPs where the high natural frequencies may induce resonance due to sum-frequency wave loads and the 3P blade frequency. The effects of these constraints may greatly influence the systems design space which should be further investigated.

In the context of optimisation algorithms, gradient-based and gradient-free algorithms were identified. Genetic algorithms, as a gradient-free method, are widely used for multi-objective optimisation due to their ability to explore complex design spaces. However, they become computationally expensive as the number of free variables increases. Gradient-based optimisation, on the other hand, allows for efficient problem solving and the inclusion of more design variables, but it is prone to local optima and problems with smooth gradients. This issue should be resolved in future studies by implementing a multi-start sequence. The choice of algorithm should be guided by the specific requirements of the study, balancing computational efficiency, design complexity, number of objectives and the need for global versus local solutions.

System Modelling
Considering the system modelling, several key improvements were identified through literature. A careful evaluation for different substructure types is essential, particularly considering the sensitivity to non-linear second-order wave forces. For tension leg platforms, the high stiffness of the platform may lead to significant sum-frequency wave loads. In cases where these loads excite, an assessment is necessary to determine the significance of these effects and to evaluate whether linearisation in the frequency domain remains valid. If not, suitable methods for approximating these second-order sum-frequency effects in linear analysis should be explored or methods to avoid the excitation regions should be developed by implementing constraints on the systems natural frequencies.

Another key improvement for the system modelling is including flexible structural members in the analysis. Some in house frequency domain codes account for this, but most studies model the entire system as a rigid structure. While this assumption may be more valid for spar buoys and semi submersibles which often already have longer natural periods, it is of significant importance for TLP design as structural flexibility shows large influence on the overall system natural frequencies and resulting response. Future studies need to incorporate this flexibility, especially for the turbine tower as the tower bending frequencies often are near to the sum-frequency excitation ranges.

Most optimisation studies use quasi-static mooring analysis for catenary moorings and linearised static mooring analysis for taut moorings. However, the latter approach leads to large discrepancies when compared to non-linear analyses. To address this, future research should incorporate quasi-static analysis to model taut mooring line stiffness more accurately. Quasi-static analyses have demonstrated good agreement with more detailed dynamic analyses. Nevertheless, further validation is needed by integrating the linear quasi-static mooring system into the fully coupled aero-hydro-servo-elastic framework to asses realistic and reliable results.

Summary of Recommendations
In summary the most important recommendations and improvements for future research are:

- The need for a TLPWT specific optimisation framework for 15MW+ wind turbines.
- Research into the most influential variables in order to reduce design space and increase computational efficiency.
- The need for an accurate and efficient frequency domain model for TLPWTs.
- Implementing flexible structures which greatly influences natural frequencies, overall system response and eventual design results.
- The implementation of quasi-static mooring analysis for TLPWTs.
- Evaluate the importance of non-linear TLPWT specific effects and identifying methods to take them into account or avoid them in TLPWT design optimisation.
- Defining a set of constraints to keep system motions within limits allowing for more a more straightforward determination motion induced costs.
- A full lifecycle cost model enabling cost comparison of FOWT concepts within an optimisation study and enabling comparison across different FOWT platform studies.
- Defining constraints to avoid resonance excitation ranges, especially for TLPWTs.

2.5. Research Gap & Questions

Based on the discussion and recommendations presented in Section 2.4. The scope of the research will be to construct a frequency domain based optimisation framework for 15 MW tension leg platforms wind turbines. This framework will specifically address the importance of TLP specific response considering structural modelling, mooring line modelling and taking into account approximations or corrections accounting for important non-linear effects. Furthermore, a well defined cost function will allow for concept comparison within the optimisation study and comparison across different studies. This led to the following research question and accompanied sub questions.

Research Question

“How can a frequency-domain-based optimisation framework be developed for 15 MW tension leg platform wind turbines to enable efficient, accurate and cost-effective design iterations, considering tension leg platform specific dynamics?”

Sub Questions

1. How can TLP-specific dynamic effects be represented in a frequency-domain based optimisation framework?
2. Which design variables most significantly affect TLPWT performance?
3. What is the validity of linearising TLPWT with respect to system response?
4. What key elements should a cost model include to account for the cost of a tension leg platform, enabling comparison with other design studies?
5. How can an optimisation problem be structured to allow for efficient exploration of the design space in the context of TLPWT optimisation?

3

Theoretical Framework

This theoretical framework provides the necessary background to address the constructed research questions. The theoretical study is divided in two parts. The first part consists of the theoretical background for the optimisation problem formulation, presented in Section 3.1. This is followed by an analysis of the theory behind the physical model, presented in Section 3.2.

3.1. Optimisation

Optimisation is a broad concept. In the context of design engineering, optimisation is to find a design that is as good as possible within the defined design space while minimising the objective. The formulation of such an optimisation problem is described in subsection 3.1.1. The different algorithms and how they are used to exploit the design space is described in subsection 3.1.2.

3.1.1. Optimisation Formulation

The mathematical formulation for an optimisation problem is based on a definition of the objective function, the variables to optimise for and the constraints. A base case can be seen in Equation 3.1 [97].

$$\begin{aligned} &\text{Minimise} && f(\mathbf{x}) \\ &\text{with respect to} && \mathbf{x} \\ &\text{subject to} && h_i(\mathbf{x}) = 0, \quad i = 1 \text{ to } p \\ & && g_j(\mathbf{x}) \leq 0, \quad j = 1 \text{ to } m \end{aligned} \tag{3.1}$$

Here $f(x)$ is the objective function, x is the variable to optimise for, $h(x)$ are the equality constraints and $g(x)$ are the inequality constraints which limit the design space.

3.1.2. Optimisation Algorithms

In optimisation there are two main types of algorithms namely gradient based algorithms and gradient free algorithms.

Gradient Based Algorithms

Gradient based algorithms, as it says in the name, determine the minimum of the objective function by following the gradient. This type of optimisation algorithm works only if the objective function has an analytical gradient which can be easily computed. Determining the gradient is often the most computational expensive step. By assessing the gradient after every iteration step it will quickly converge to an optimal solution.

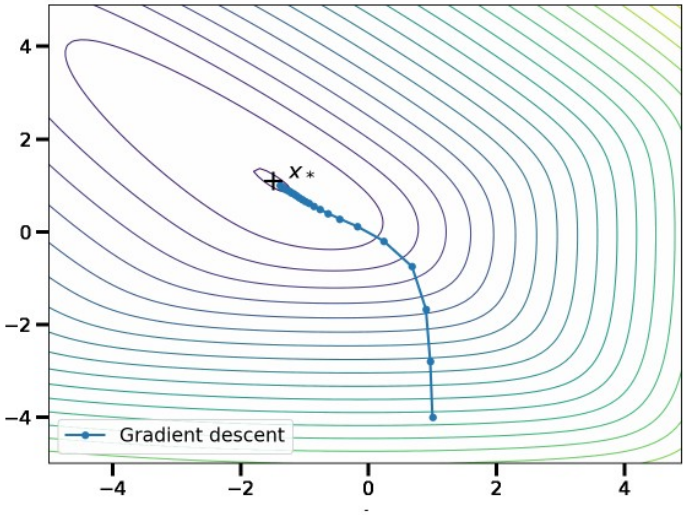

Figure 3.1: Example of the convergence path of a gradient based algorithm [9].

The main downside of gradient based optimisation is that it is highly dependent on the initial values when considering non-convex optimisation problems. Depending on the initial values it will minimise to a local minimum, potentially disregarding another minimum elsewhere within the design space. An example of such a local convergence while there is a more optimal solution can be seen in Figure 3.2. This issue can be resolved by multi-starting the optimisation problem with different initial values. This will give more confidence in determining whether the obtained minimum is the global minimum. For the optimisation study in this research however, with a large non-linear design space, a gradient based algorithm is not suitable.

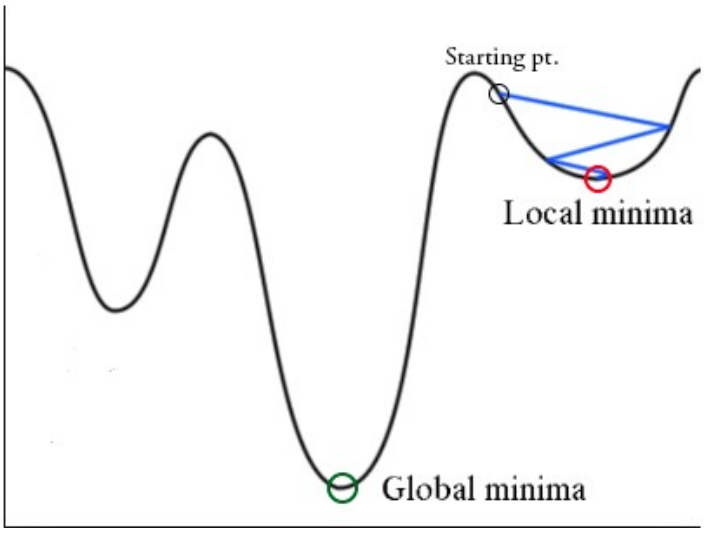

Figure 3.2: Local minima in gradient based algorithms [15].

Gradient Free Algorithms

Gradient free algorithms, in contrary to the gradient based algorithms, have a more holistic approach. Instead of determining the local gradient they exploit the entire design space with initial guesses. These are then used to evaluate the design space guiding the gradient free algorithm to the global optimum. An example of the convergence of a gradient free algorithm can be seen in Figure 3.3.

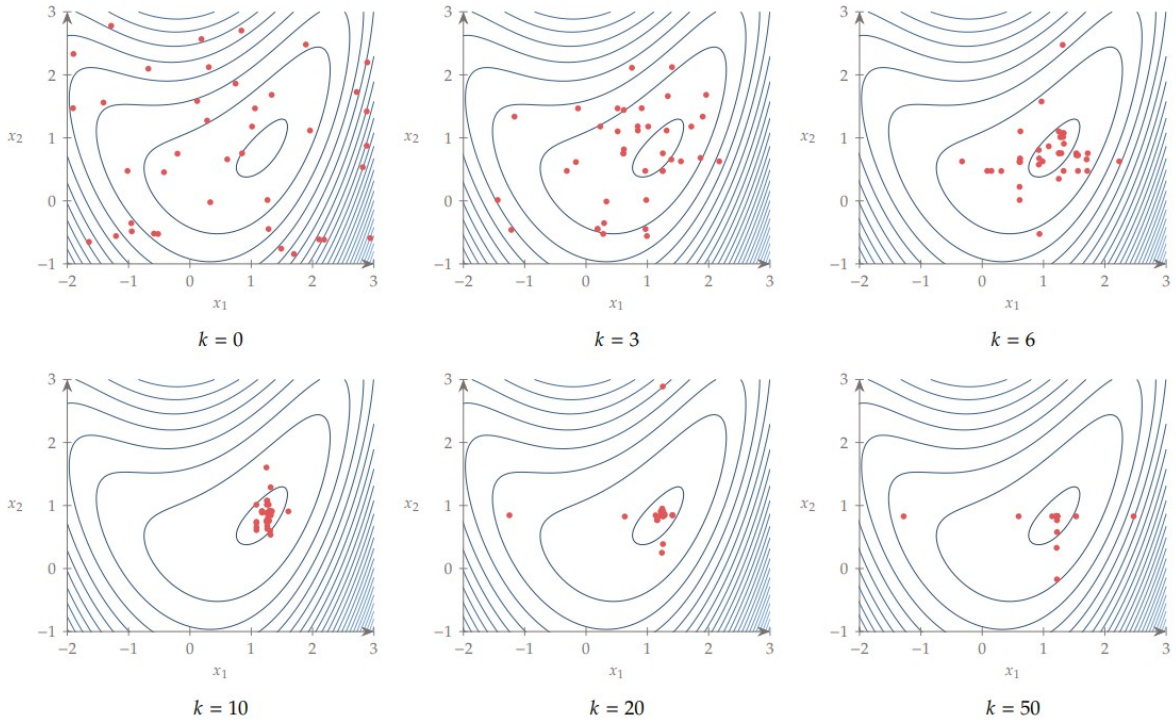

Figure 3.3: Example of the convergence path of a gradient free algorithm (genetic algorithm) for k iterations [74].

Advantages of this type of algorithm are that they are easy to use, can often handle multiple objectives and converge to a global minimum instead of getting caught in local minima like gradient-based algorithms. The biggest downside of this type of algorithms are their computational expensiveness as they need to asses a lot of initial design points [97]. In addition, an upper bound for the number of iteration steps is included in the stopping criterion. The gradient free algorithm terminates when either the stopping criterion or the maximum number of iteration steps is reached. Because this research has a non-linear discontinuous design space, it will make use of a gradient free algorithm.

3.2. System Modelling

To model a floating offshore wind system, the behaviour of all subcomponents and external forces acting on the structure needs to be adequately represented. This section presents the theoretical foundation used in this research to get to the obtained numerical results. The analysis is carried out in the frequency domain, due to the computational efficiency of such models. A key simplification of using a frequency-domain approach is the assumption of linearity and small amplitude motions. As a result, non-linear effects, such as large displacements and non-linear system couplings are not captured. In this framework, the external forces acting on the system are decomposed into a mean component and a dynamic component. The static offset of the system is determined by solving the following equilibrium.

$$\mathrm{C}\,\overline{x} = \overline{\mathrm{F}}_{\mathsf{aero}} + \overline{\mathrm{F}}_{\mathsf{hydro}} + \overline{\mathrm{F}}_{\mathsf{moor}}(\overline{x}) \tag{3.2}$$

Here, C denotes the system stiffness matrix. The vectors $\overline{\mathrm{F}}_{\mathsf{aero}}$ and $\overline{\mathrm{F}}_{\mathsf{hydro}}$ represent the steady aerodynamic and hydrodynamic forces, respectively, while $\overline{\mathrm{F}}_{\mathsf{moor}}(\overline{x})$ corresponds to the mooring reaction forces, which are non-linear functions of the static offset $\overline{x}$. Once the mean offset is obtained, the dynamic response about this equilibrium position is computed from the linearised frequency-domain equation of motion:

$$\left(-\omega^2\left[\mathrm{M}+\mathrm{A}\right]+i\omega\mathrm{B}+\mathrm{C}\right)\hat{\xi}(\omega) = \hat{\mathrm{F}}(\omega) \tag{3.3}$$

In this equation, M is the structural mass matrix, A is added mass matrix (consisting of the hydrodynamic and aerodynamic added mass) and B contains the structural, viscous and aerodynamic damping contributions. The stiffness matrix C includes hydrostatic, structural and mooring stiffness evaluated at the offset position. $\hat{\xi}(\omega)$ is the complex response amplitude and $\hat{\mathrm{f}}(\omega)$ represents the frequency-dependent excitation forces from wind and waves. A schematic representation of the excitation forces and the coordinate system used throughout this research is presented in Figure 3.4 and Figure 3.5.

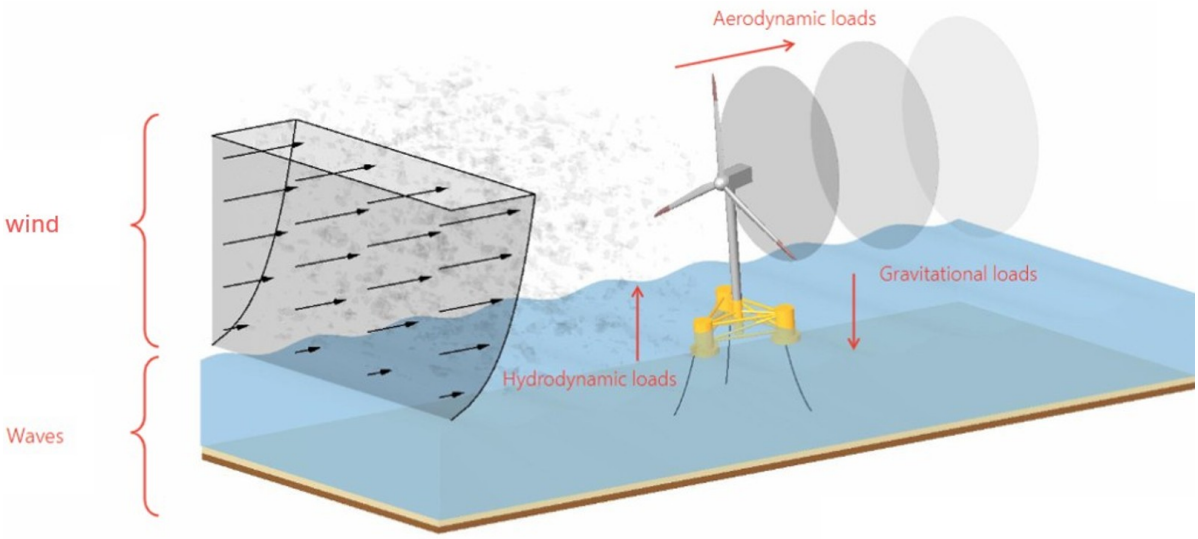

Figure 3.4: A description of the environmental loads [105].

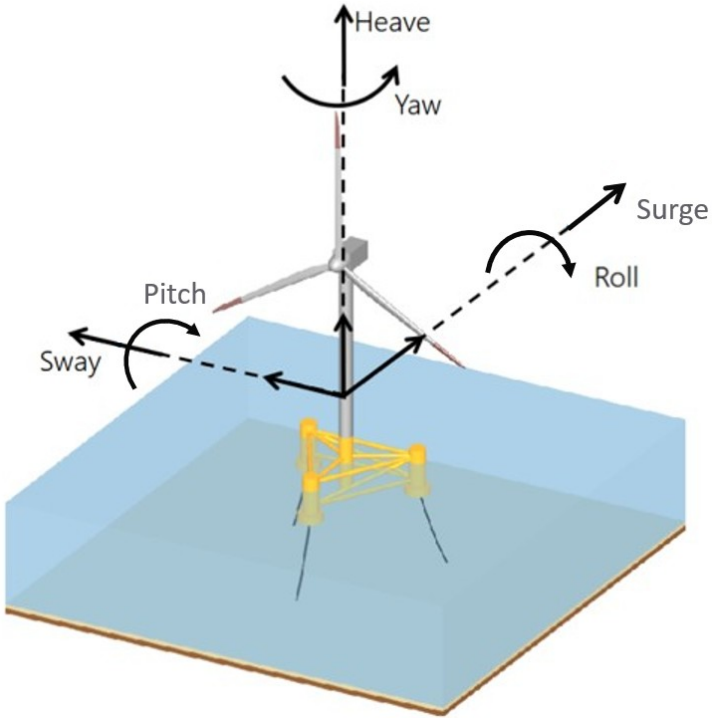

Figure 3.5: A description of the coordinate system [105].

3.2.1. Structural Modelling

The structure in this model consists of a rigid platform, flexible tower and rigid RNA. A simplified overview can be seen in Figure 3.6.

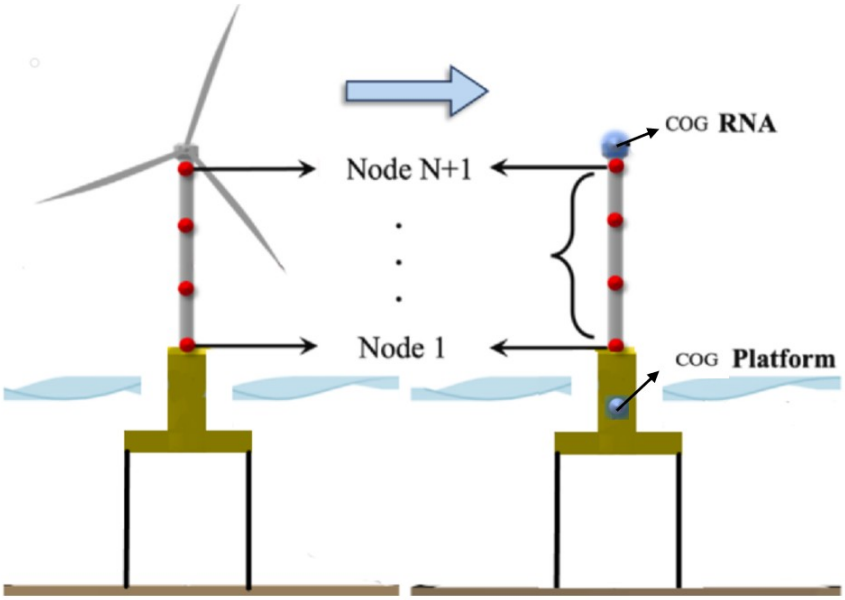

Figure 3.6: A schematic overview of the structural modelling

The rigid structures is initially modelled with six degrees of freedom, three translations and three rotations. The tower will be modelled with 2 node 3D combined Euler beam elements with a total of twelve degrees of freedom per element, three translations and rotations per node. The mass and stiffness matrix for every i^{th} element can be described by Equation 3.4 which will result in a 6x6 matrix.

$$M^i = \begin{bmatrix} M^{i-1}_{i-1,i-1} & M^i_{i-1,i} \\ M^i_{i,i-1} & M^i_{i,i} \end{bmatrix} \quad K^i = \begin{bmatrix} K^{i-1}_{i-1,i-1} & K^i_{i-1,i} \\ K^i_{i,i-1} & K^i_{i,i} \end{bmatrix} \tag{3.4}$$

These are the local mass and stiffness matrices per element. A more detailed overview with all matrix entries can be seen in Appendix B. Putting everything together the eventual mass and stiffness a matrices for N elements will be 6(N+1) x 6(N+1). Furthermore, the structural damping will be approximated by Raleigh damping described in Equation 3.5

$$B = c_1[M] + c_2[K] \tag{3.5}$$

Here, c_1 and c_2 are coefficients which are determined by solving the following set of equations for the two most critical modes where ζ_1 and ζ_2 are the critical damping ratios and ω_1 and ω_2 are the excitation frequencies of the modes. For this research the critical damping ratios are taken to be 0.02 based on previous studies [91].

$$\zeta_1 = \frac{1}{2}\left(c_1\omega_1 + \frac{c_2}{\omega_1}\right) \tag{3.6}$$

$$\zeta_2 = \frac{1}{2}\left(c_1\omega_2 + \frac{c_2}{\omega_2}\right) \tag{3.7}$$

The importance of including tower flexibility is stipulated in previous research conducted by NREL [38]. This research showed the effect of tower flexibility on second-order excitations for a TLP. The main

finding was that tower flexibility greatly influenced the pitch natural frequency, which in turn influenced the impact of the second-order wave loads. Figure 3.7 and Figure 3.8 show how adjusting the tower properties affects the pitch natural frequency. These figures show the frequency ranges where the first- and second-order forces are excited. the difference between the two towers is that Figure 3.7 shows the original flexible tower and Figure 3.8 shows a shortened tower which in turn is stiffer.

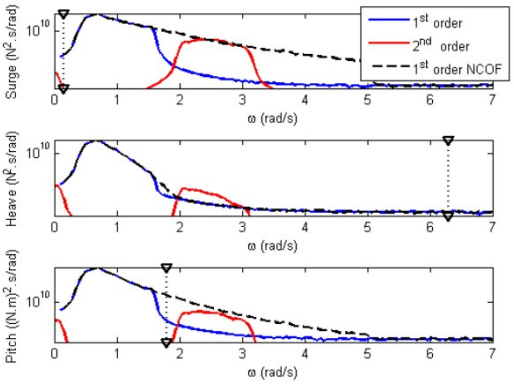

Figure 3.7: PSDs of all first- and second-order contributions to the wave loads for Flexible tower with original length. Vertical markers indicate the eigenfrequencies [38].

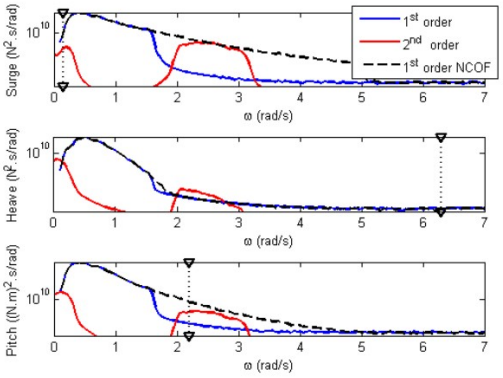

Figure 3.8: PSDs of all first- and second-order contributions to the wave loads for Flexible tower with shorter length. Vertical markers indicate the eigenfrequencies [38].

From these figures it becomes clear that both difference and sum-frequency forces differ for different tower properties. Where difference-frequency are relevant for surge in both tower scenarios, it can be seen that for the shorter tower the pitch natural frequency moves into the range where the second-order sum-frequency loads excite. This can also be seen in the system response. Figure 3.9 shows the pitch motions of the system. When comparing the 'flexible O' and 'flexible S' lines it can be seen that a considerable peak in the flexible S line can be seen at a frequency of approximately 2.1 [rad/s], which is mainly due to the second-order sum-frequency forces. This may cause issues in design as resonances occur, emphasizing the need to take tower flexibility into account.

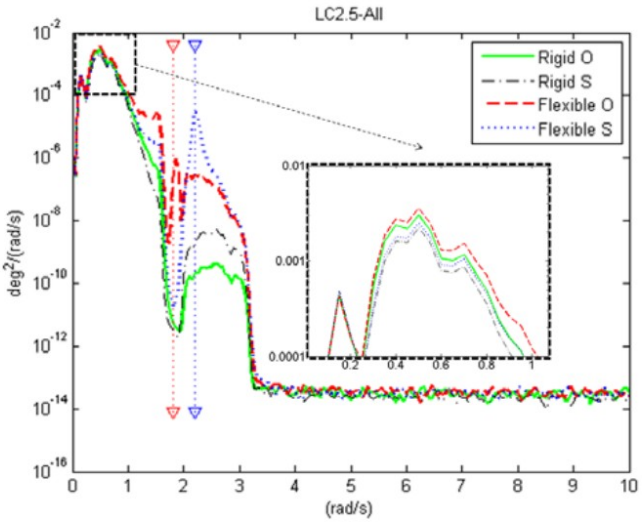

Fig. 22: Effects of tower's flexibility on pitch motions for LC2.5-All for both towers (O and S).

Figure 3.9: Effects of tower flexibility on pitch motions.

3.2.2. Hydromechanics

This research focuses on wave-induced loads acting on tension leg platforms. For this reason, the effects of currents and tidal variations are excluded from the analysis. Tidal variations and the current induced mean forces can have an effect on system stiffness, as the tendon length changes with tidal variations and the mooring stiffness changes with mean offsets. This is however out of the scope of the current research and therefore not included.

There are several hydromechanical approaches to simulate the system's response, depending on the system geometrical and site characteristics. Hydromechanic modelling starts with an assessment of the hydrostatic performance of the platform, followed by an evaluation of the hydrodynamic properties. First-order potential flow theory is commonly used for modelling wave excitation about a steady-state position. This approach is linear and captures the primary wave-structure interaction effects. For higher-fidelity analysis, second-order potential theory may be added to account for sum- and difference-frequency wave effects. However, this comes at a significantly increased computational cost. An alternative to potential flow for slender structures ($D/\lambda < 1/5$) is the use of Morison's equation in combination with strip theory. This method is more computationally efficient and allows for approximate inclusion of second-order effects using simplified formulations.

The choice of hydrodynamic model typically depends on both the wave environment in which the structure operates and the geometric characteristics of the floater. In this study, computational efficiency is also a key consideration. Figure 3.10 presents an overview of different wave regimes and the relative importance of hydrodynamic effects. For structures operating in diffraction-dominated regimes, potential flow theory provides the most accurate predictions. In contrast, for inertia- and drag-dominated regimes, Morison's theory is more suitable. The structure in this research will have a diameter ranging from 10-20 meters with wave lengths of 80-320 meters and wave heights from 1 up to 10.5 meters making the system operate on the line of the diffraction, all inertia and small drag region. For the sake of computational efficiency and given that the system operates most of the time in or near the inertia-dominated regime, this research uses the Morison equation in combination with a strip theory approach.

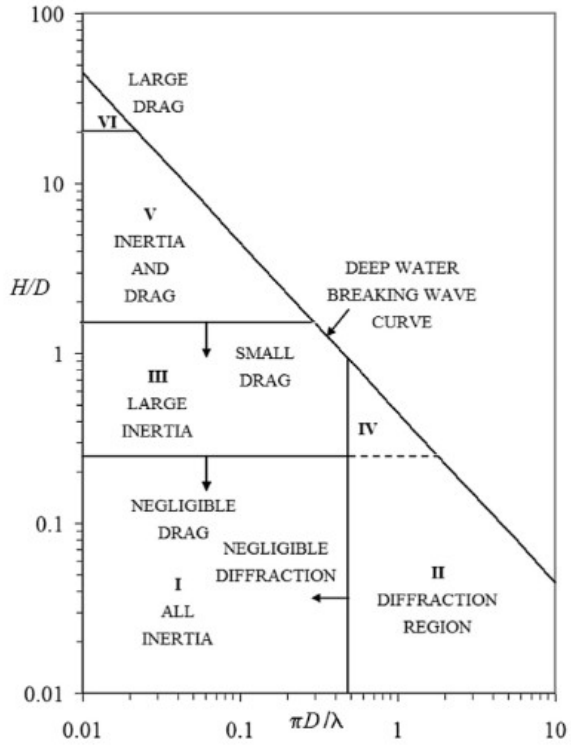

Figure 3.10: Different wave force regimes [78].

Hydrostatics
First, the hydrostatics need to be determined of the substructure. Hydrostatic calculations are based on the pressure distribution while standing still in water. The hydrostatic pressure determines the stability of a structure, when not moored as a TLP. Considering the platform as a rigid body, the hydrostatic stiffness is determined by the platform centre of buoyancy, water plane area and the systems centre of gravity. The hydrostatics of a TLP can be determined by the following equations [5].

$$C_{33} = \rho g A_{wp} \tag{3.8}$$

$$C_{35} = C_{53} = -\rho g \iint_{A_{wp}} x \, dx \, dy \tag{3.9}$$

$$C_{44} = \rho g \nabla z_B - M g z_G + \rho g \iint_{A_{wp}} y^2 \, dx \, dy \tag{3.10}$$

$$C_{55} = \rho g \nabla z_B - M g z_G + \rho g \iint_{A_{wp}} x^2 \, dx \, dy \tag{3.11}$$

Where:

- C_{33} : Hydrostatic restoring coefficient in the heave direction.
- C_{35}, C_{53} : Coupled hydrostatic restoring coefficients between heave and pitch.
- C_{44} : Hydrostatic restoring coefficient for roll motion.
- C_{55} : Hydrostatic restoring coefficient for pitch motion.
- ρ : The density of the fluid.
- g : The acceleration due to gravity.
- A_{wp} : The water plane area of the floating structure.
- x, y : The horizontal and vertical coordinates on the water plane area.
- ∇ : Displaced volume.
- z_B : The vertical position of the centre of buoyancy.
- M : The mass of the entire system.
- z_G : The vertical position of the centre of gravity.

Since this study makes use of a single circular column TLP, Equation 3.8 - Equation 3.11 can be simplified. As there is no offset in water plane area, C_{53} and C_{35} become zero. The last term of Equation 3.10 and Equation 3.11 which refers to the water plane moment of inertia is the same about all axes. This results in a single description of this term as $\pi D^4/64$. The resulting set of equations describing the hydrostatics becomes the following.

$$C_{35} = C_{53} = 0 \tag{3.12}$$

$$A_{wp} = \frac{\pi D^2}{4} \tag{3.13}$$

$$I_{wp} = \iint_{A_{wp}} y^2 \, dx \, dy = \iint_{A_{wp}} x^2 \, dx \, dy = \frac{\pi D^4}{64} \tag{3.14}$$

$$C_{44} = C_{55} = \rho g I_{wp} + \rho g \nabla z_B - M g z_G \tag{3.15}$$

Resulting in the following formulation of the hydrostatic stiffness matrix.

$$\mathrm{C}_{hydro} = \begin{bmatrix} 0 & 0 & 0 & 0 & 0 & 0 \\ 0 & 0 & 0 & 0 & 0 & 0 \\ 0 & 0 & \rho g A_{wp} & 0 & 0 & 0 \\ 0 & 0 & 0 & \rho g I_{wp} + \rho g \nabla z_B - M g z_G & 0 & 0 \\ 0 & 0 & 0 & 0 & \rho g I_{wp} + \rho g \nabla z_B - M g z_G & 0 \\ 0 & 0 & 0 & 0 & 0 & 0 \end{bmatrix}. \tag{3.16}$$

Morison Equation

As mentioned before, this research will use the Morison equation in combination with a strip theory approach. The strip theory approach is based on applying the Morison equation to a strip of the geometry. For cylindrical structures this is described in Equation 3.17 [41].

$$\Delta f = [\underbrace{\rho\left(1 + C_a\right)\frac{\pi}{4}D^2\dot{u}}_{\text{inertia}} - \underbrace{\rho C_a \frac{\pi}{4}D^2\dot{v}}_{\text{added mass}} + \underbrace{\frac{1}{2}\rho C_d D(u-v)|u-v|}_{\text{drag}}]\Delta l \tag{3.17}$$

Here, Δf represents the hydrodynamic force, D is the cylinder diameter and Δl is the strip length. The coefficients C_a and C_d represent the added mass and drag coefficients, respectively. The variables u and v denote the wave particle velocity and the floater velocity. For each strip, the local added mass is computed using the following expression.

$$\mathrm{A}_L = \rho \Delta V \left(C_{a,p1}\mathrm{p}_1\mathrm{p}_1^T + C_{a,p2}\mathrm{p}_2\mathrm{p}_2^T\right), \tag{3.18}$$

Here, p_1 and p_2 are the orthogonal transverse unit vectors and $Ca, p1$ and $Ca, p2$ are the corresponding added mass coefficients, which are identical for cylinders. The local added masses are then transformed to a reference point where they are summed to get the resulting added mass of the structure. Next to this, the local inertial forces for every strip are determined including the local fluid acceleration as a function of wave frequency, as described in Equation 3.19.

$$\hat{f}_{I,L}(\omega) = \rho \Delta V \left[(1 + C_{a,p1})\mathrm{p}_1\mathrm{p}_1^T + (1 + C_{a,p2})\mathrm{p}_2\mathrm{p}_2^T\right] i\omega\hat{u}_L(\omega) \tag{3.19}$$

This equation is also used to determine axial terms. The only difference there is that the effective volume is based on a hemisphere, sized according to the strip theories axial exposed area. When looking at the drag term, it depends on the quadratic wave particle velocity, which is not suitable for linear analysis. For this reason the drag term needs to be linearised. This is done by approximating it as a viscous damping term. The local damping term of every strip can be determined with the following equation.

$$\mathrm{B}_L = \frac{1}{2}\rho\sqrt{\frac{8}{\pi}}\left(\sigma_{u,q}A_q C_{d,q}\mathrm{q}\mathrm{q}^T + \sigma_{u,p1}A_{p1}C_{d,p1}\mathrm{p}_1\mathrm{p}_1^T + \sigma_{u,p2}A_{p2}C_{d,p2}\mathrm{p}_2\mathrm{p}_2^T\right), \tag{3.20}$$

Here, A_q is the effective axial drag area of the strip, $C_{d,q}$ is the axial drag coefficient and q is the axial unit vector. The drag contribution to excitation forces can then be calculated by multiplying the local water velocity amplitudes with the linearised viscous damping as described in Equation 3.21.

$$\hat{\mathrm{f}}_{d,L}(\omega) = \mathrm{B}_L\hat{\mathbf{u}}_L(\omega), \tag{3.21}$$

The Importance of Second-Order Wave Effects

For the optimisation framework used in this thesis, a frequency domain analysis is used which makes it crucial to asses the effects of linearising the system and approximating the non-linear second-order wave effects. Including the difference-frequency effects in frequency domain is well researched by including them with the Newman approximation which allows for inclusion of difference-frequency effects in linear analysis with reasonable accuracy [107]. The sum-frequency force inclusion however, is complex to approximate as mentioned before. For most FOWT these effects do not pose a threat as their

natural frequencies are typically low. However, in TLP design these forces may be important since TLP systems are considered stiff and therefore resonance in the sum-frequency range might occur. Several papers did a study for the influence of second-order sum-frequency effects [6]. This research found that in uncoupled aero-hydrodynamic analysis, the effect of sum-frequency effects becomes significant, especially for pitch acceleration and tendon tension which can be seen in Figure 3.11 and Figure 3.12.

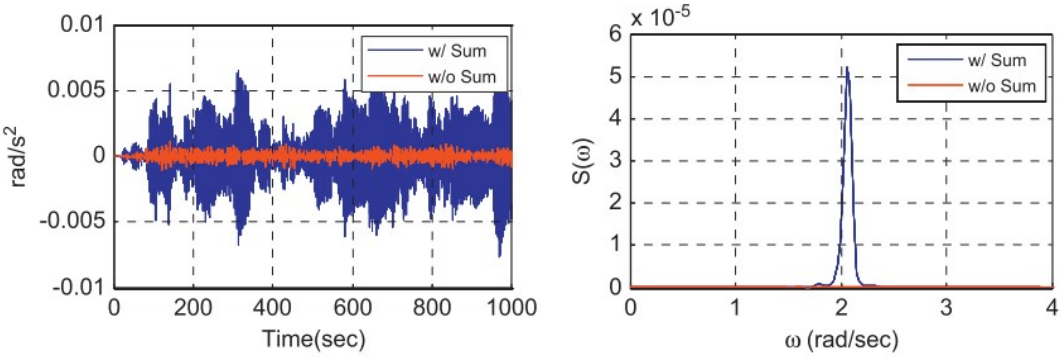

Figure 3.11: Time history and spectrum of the pitch acceleration (uncoupled) [6].

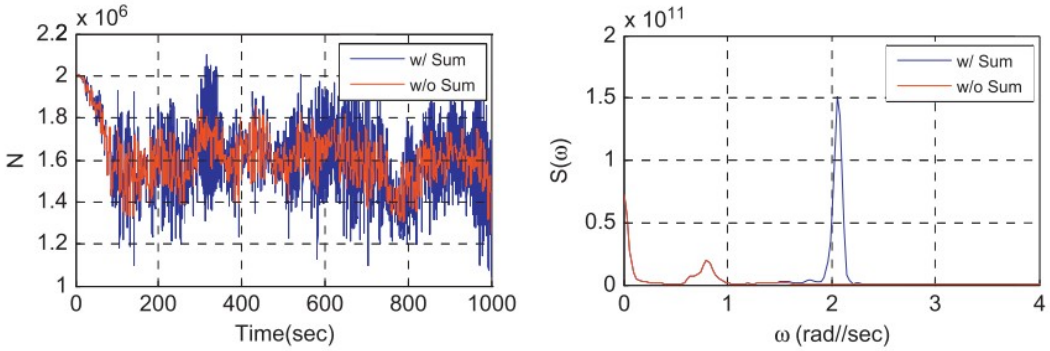

Figure 3.12: Top-tension time history and spectrum of a downwind tendon (uncoupled) [6].

However, in coupled aero-hydrodynamic analysis it was found that the aerodynamic force and associated damping almost completely damp out the sum-frequency effects as can be seen in Figure 3.13 and Figure 3.14.

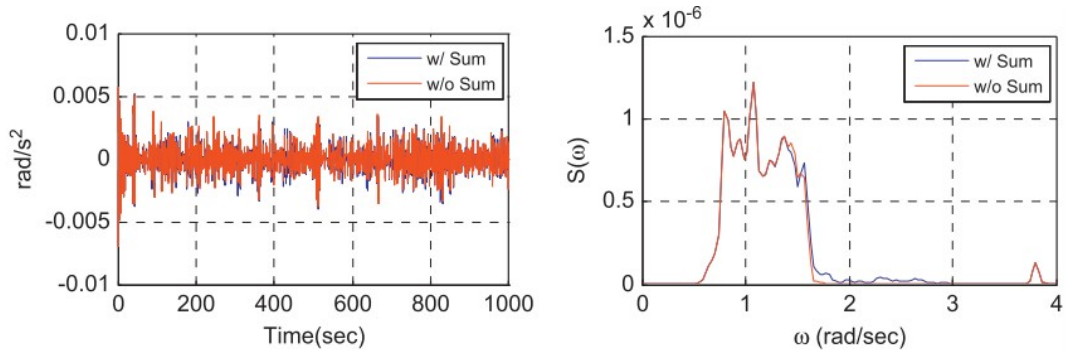

Figure 3.13: Time history and spectrum of the pitch acceleration (coupled) [6].

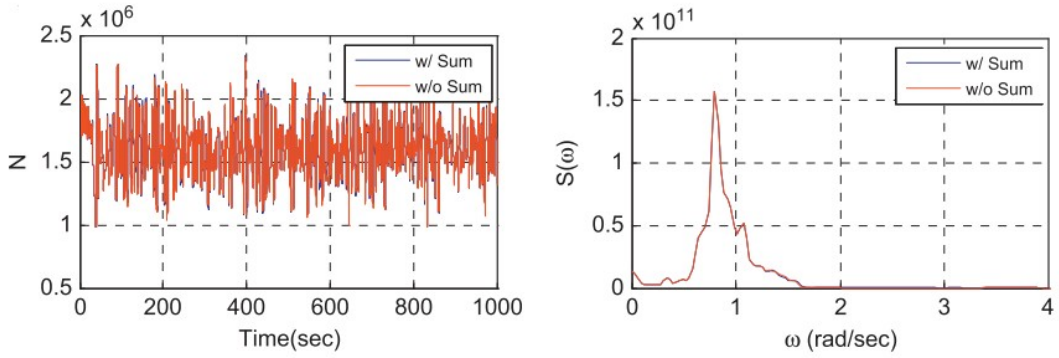

Figure 3.14: Top-tension time history and spectrum of downwind tendon (coupled) [6].

Other research on the sum-frequency effects also found a minimal influence the system response in operational conditions. During storm conditions, the influence of the sum-frequency loads was more significant. The sum-frequency loads also do not affect the mean values of the response but do influence the standard deviation. This means that sum-frequency forces mostly affects the stress cycles and therefore fatigue of the FOWT systems [5]. It should be noted, however, that the conditions associated with this increase in stress cycles due to the absence of aerodynamic damping do not occur frequently. Therefore, the eventual contribution to fatigue life may be less significant than expected. Nevertheless, because of the sum-frequency induced effects, care should be taken in TLP design compared to other floaters as serious resonance due to sum-frequency forces may occur. Here system flexibility plays a large role as it greatly influences the pitch and tower fore-aft bending natural frequencies which are near to the sum-frequency excitation zone in TLP design.

Rainey's Approximation for Second-Order Wave Loads

A previous study on the approximation of second-order wave loads for frequency domain analysis presented a method to calculate the difference-frequency loads for slender structures [13]. This research used Rainey's approximation which is limited to slender bodies ($\lambda/D > 10$). To make it more widely applicable this research included a correction for the wave scattering effects. Rainey's approximation extends Morison's equation to second-order effects. The transverse force per unit length $df_{p1}(t)$ acting on a cylinder segment of length dl is given by:

$$\begin{aligned}\frac{\mathrm{d}f_{p_1}(t)}{\rho A\ \mathrm{d}l} &= (1+C_{a,p_1})\left(\frac{\partial u}{\partial t}+u\frac{\partial u}{\partial p_1}+v\frac{\partial u}{\partial p_2}+w\frac{\partial u}{\partial q}\right)\\ &\quad - C_{a,p_1}\left[\ddot{x}_S-(u-\dot{x}_S)\frac{\partial w}{\partial q}+2\omega_{p_2}(w-z_S)\right]\\ &\quad - \mathrm{g}\cdot\hat{\mathrm{p}}_1+\frac{\mathrm{d}f_{NC,p_1}(t)}{\rho A\ \mathrm{d}l}\end{aligned} \tag{3.22}$$

Where:

- ρ is the fluid density
- A is the cross-sectional area of the cylinder ($A=\pi R^2$ for circular cylinders)
- $C_{a,p1}$ is the added mass coefficient in the $\hat{\mathrm{p}}_1$ direction
- $\mathrm{u}=u\hat{\mathrm{p}}_1+v\hat{\mathrm{p}}_2+w\hat{\mathrm{q}}$ is the undisturbed fluid velocity at point S
- $\dot{\mathrm{x}}_S$ is the velocity of point S on the cylinder
- $df_{NC,p1}(t)$ is the non circular force component for non circular cylinders

The axial and transverse loads acting on the ends of the cylinder are given by Equation 3.23 and Equation 3.24 where $\mathcal{V}_{end}$ is a reference volume, A_{end} is the area of the end face and z_{end} is the vertical coordinate of the end point.

$$\begin{aligned}\mathrm{f}_{\text{end, axial}}(t) = &\left(-\frac{\partial \varphi}{\partial t} + \rho g z_{\text{end}} - \frac{1}{2}\rho\left(\mathrm{u}-\hat{\mathrm{x}}_S\right)_T \cdot \left(\mathrm{u}-\hat{\mathrm{x}}_S\right)_T\right) A_{\text{end}}\,\hat{\mathrm{q}} \\ &+ \rho \mathcal{V}_{\text{end}}\, C_{a,\text{ end}}\left[\left(\frac{\mathrm{Du}}{\mathrm{D}t} - \mathrm{x}_S\right)\cdot\hat{\mathrm{q}}\right]\hat{\mathrm{q}}\end{aligned} \tag{3.23}$$

$$\mathrm{f}_{end,transv}(t) = C_a \rho A_{end}\left[\left(\mathrm{u}-\dot{\mathrm{x}}_S\right)\cdot\hat{\mathrm{q}}\right]\left(\mathrm{u}-\dot{\mathrm{x}}_S\right)^T \tag{3.24}$$

To adapt the slender-body approximation to the frequency domain, the formulation by Pinkster is applied. The second-order force components are given in Equation 3.25, where (0), (1) and (2) represent the zeroth-, first- and second-order contributions, respectively, and u^- represents the difference-frequency velocity.

$$\begin{aligned}
f^{(2)}_{\phi^-,x}(t) &= \rho\pi R^2\left(1+C_a\right)\int_{L_0}\frac{\partial u^-}{\partial t}\,\mathrm{d}l \\
f^{(2)}_{\mathrm{conv},x}(t) &= \rho\pi R^2\left(1+C_a\right)\int_{L_0}\mathrm{u}^{(1)}\cdot\nabla u^{(1)}\mathrm{d}l \\
f^{(2)}_{\mathrm{axdv},x}(t) &= \rho\pi R^2 C_a\int_{L_0}\left(u^{(1)}-\dot{x}^{(1)}_S\right)\frac{\partial w^{(1)}}{\partial z^{(0)}}\mathrm{d}l \\
f^{(2)}_{\mathrm{rslb},x}(t) &= -\rho\pi R^2 C_a\int_{L_0}2\omega^{(1)}_y\left(w^{(1)}-\dot{z}^{(1)}_S\right)\mathrm{d}l \\
f^{(2)}_{\mathrm{x\cdot\,V},x}(t) &= \rho\pi R^2\left(1+C_a\right)\int_{L_0}\mathrm{x}^{(1)}_{\mathrm{S}}\cdot\nabla\frac{\partial u^{(1)}}{\partial t}\,\mathrm{d}l \\
\mathrm{f}^{(2)}_{\mathrm{rotN}}(t) &= m\xi^{(1)}_R\times\dot{\xi}^{(1)}_T \\
f^{(2)}_{\eta-x}(t) &= \rho\pi R^2\eta^{(1)}_r\left[\left(1+C_a\right)\frac{\partial u^{(1)}}{\partial t}\bigg|_I - C_a x^{(1)}_{\mathrm{wL}} - \mathrm{g}\cdot\hat{\mathrm{p}}^{(1)}_1\right]
\end{aligned} \tag{3.25}$$

Wave scattering effects are taken into account by a correction based on the analytical solution of the second-order wave diffraction problem described in Equation 3.26.

$$\begin{aligned}\mathrm{F}^{K\&Y}_{V^2,jl} =& \frac{2i\rho g R}{\pi}\sqrt{\frac{\bar{h}}{\bar{k}_j\tanh\left(\bar{k}_j\bar{h}\right)}}\sqrt{\frac{\bar{h}}{\bar{k}_l\tanh\left(\bar{k}_l\bar{h}\right)}} \\ &\times\sum_{n=0}^{\infty}\frac{\Omega^-_{n,jl}\left[I^-_{jl}+I^+_{jl}n(n+1)/\left(\bar{k}_j\bar{k}_l\right)\right]}{\cosh\left(\bar{k}_j\bar{h}\right)\cosh\left(\bar{k}_l\bar{h}\right)}\left[\left(\hat{\mathrm{k}}\cdot\hat{\mathrm{p}}_1\right)\hat{\mathrm{p}}_1+\left(\hat{\mathrm{k}}\cdot\hat{\mathrm{p}}_2\right)\hat{\mathrm{p}}_2\right]\end{aligned} \tag{3.26}$$

$\bar{h} = H/R$ is the non-dimensional water depth, $\bar{k}_j = k_j R$ is the non-dimensional wave number, and I^-_{jl} and I^+_{jl} are integrals defined in terms of the cylinder geometry. This theory and implementation in RAFT can be extended for sum-frequency QTF approximations [13]. This is done by including the following terms.

$$f^{(2)}_{\phi^+,x}(t) = \rho\pi R^2\left(1+C_a\right)\int_{L_0}\frac{\partial u^+}{\partial t}\,\mathrm{d}l \tag{3.27}$$

$$\begin{aligned}\mathrm{F}^{K\&Y}_{V^2,jl} =& \frac{2i\rho g R}{\pi}\sqrt{\frac{\bar{h}}{\bar{k}_j\tanh\left(\bar{k}_j\bar{h}\right)}}\sqrt{\frac{\bar{h}}{\bar{k}_l\tanh\left(\bar{k}_l\bar{h}\right)}} \\ &\times\sum_{n=0}^{\infty}\frac{\Omega^+_{n,jl}\left[I^-_{jl}+I^+_{jl}n(n+1)/\left(\bar{k}_j\bar{k}_l\right)\right]}{\cosh\left(\bar{k}_j\bar{h}\right)\cosh\left(\bar{k}_l\bar{h}\right)}\left[\left(\hat{\mathrm{k}}\cdot\hat{\mathrm{p}}_1\right)\hat{\mathrm{p}}_1+\left(\hat{\mathrm{k}}\cdot\hat{\mathrm{p}}_2\right)\hat{\mathrm{p}}_2\right]\end{aligned} \tag{3.28}$$

3.2.3. Moorings

For the mooring system analysis in this research a quasi-static mooring model will be used. This model will have analytical Jacobians and is based on the Moorpy module [40]. First of all, the mean offset of the system is determined, a schematic overview of a 2D tension leg system at a mean offset can be seen in Figure 3.15. The mean offset is determined by iteratively solving the following equations for X_F and Z_F which denote the location of the fairlead with respect to the anchor. In a 3D system every local tendon reaction force in x and z is determined, after which it is translated to the global reference frame.

$$F_{mean-hydro} + F_{mean-aero} = \sum F_{moor} \tag{3.29}$$

$$F_{moor-x} = T_0 \left(\frac{X_F}{L_0 + \Delta L} \right) + EA \left(\frac{\Delta L}{L_0} \right) \left(\frac{X_F}{L_0 + \Delta L} \right) \tag{3.30}$$

$$F_{moor-z} = T_0 \left(\frac{Z_F}{L_0 + \Delta L} \right) + EA \left(\frac{\Delta L}{L_0} \right) \left(\frac{Z_F}{L_0 + \Delta L} \right) \tag{3.31}$$

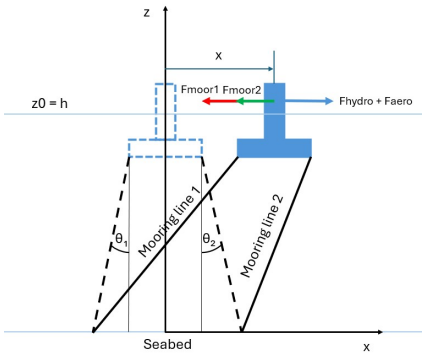

Figure 3.15: A sketch of the mooring system mean offset.

After the determination of the mean offset the tendons will be modelled as linear springs for displacements around the mean offset. A schematic can be seen in Figure 3.16

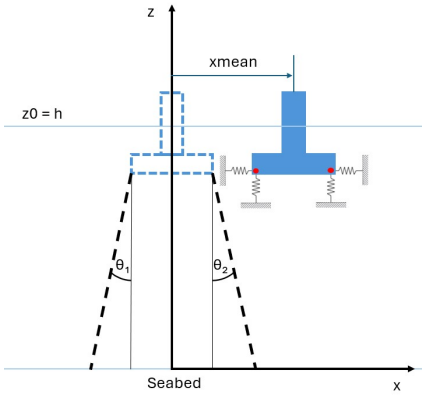

Figure 3.16: A sketch of the mooring system modelled as linear springs at the mean offset position.

The final stiffness for N tendons modelled as linear springs is described in Equation 3.32 and Equation 3.33 [3]. T is the pretension of the tendon in offset position, L is the tendon length, α is the tendon angle with the sea bed, D is the vertical distance between the fairlead and the reference frame, R is the distance between the fairlead and the centre line of the main column and KI is the tendon axial stiffness (EA/L). A schematic can be seen in Figure 3.17 [3].

$$\mathrm{K} = \sum_{m=1}^{N} \begin{bmatrix} K_{11} & 0 & 0 & 0 & K_{15} & 0 \\ 0 & K_{22} & 0 & K_{24} & 0 & 0 \\ 0 & 0 & K_{33} & 0 & 0 & 0 \\ 0 & K_{42} & 0 & K_{44} & 0 & 0 \\ K_{51} & 0 & 0 & 0 & K_{55} & 0 \\ 0 & 0 & 0 & 0 & 0 & K_{66} \end{bmatrix} \tag{3.32}$$

$$\begin{aligned}
K_{11} &= \frac{1}{2} \cdot \frac{T}{L}(1 + \sin^2 \alpha) + K_I \cos^2 \alpha \\
K_{15} &= -\frac{T}{2L}\left(D + D \sin^2 \alpha + a \sin \alpha \cos \alpha\right) + K_I \left(\frac{1}{2} D \cos^2 \alpha - a \sin \alpha \cos \alpha\right) \\
K_{22} &= K_{11} \\
K_{24} &= -K_{15} \\
K_{33} &= \frac{T}{L} \cos^2 \alpha + K_I \sin^2 \alpha \\
K_{42} &= K_{24} \\
K_{44} &= \frac{TD \sin \alpha}{L} + \frac{1}{2} a \cos \alpha + \frac{1}{2} \cdot \frac{T}{L}(a \cos \alpha + D \sin \alpha)^2 + D^2 + \frac{1}{2} K_I (D \cos \alpha - a \sin \alpha)^2 \\
K_{51} &= K_{15} \\
K_{55} &= K_{44} \\
K_{66} &= \frac{Ta}{L}(a + L \cos \alpha)
\end{aligned} \tag{3.33}$$

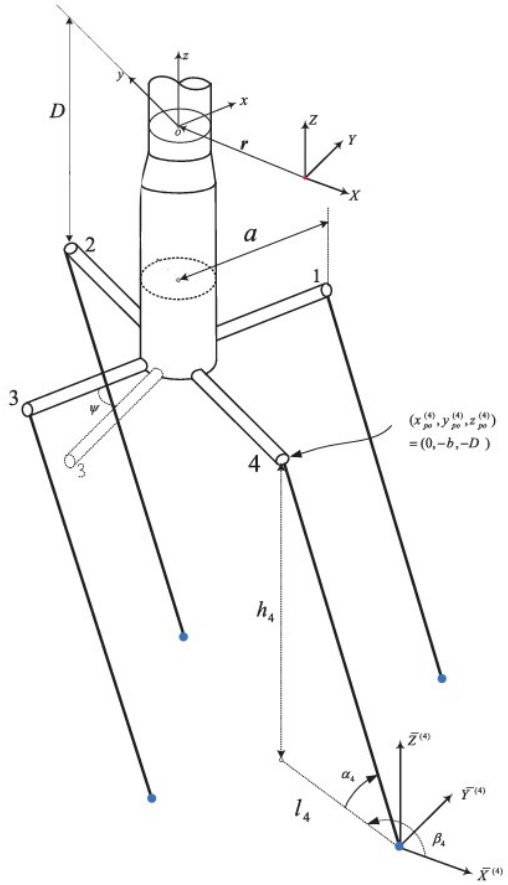

Figure 3.17: A sketch of the mooring system variables used for the linearised mooring stiffness matrix [3].

Springing & Ringing
Due to the stiff characteristics of tension leg platforms, the tendons may experience so called springing, a steady state resonant response due to sum-frequency forces and ringing, a transient resonant response in severe seas [39]. Previous research on the effects of springing found that springing effects had very little effects on the mean tendon tension. However, the tendon tension variation increased by 2-9 % during storm conditions. This indicates that springing might have a large effect on the fatigue performance as also emphasized before indicating the relevance of springing excited due to sum-frequency forces. Ringing loads are mainly induced on structures with the following hydrodynamic criteria [33]:

- Presence of surface piercing columns.
- Small Keulegan-Carpenter number (KC < 5).
- Small diameter-wavelength ratio (D/λ < 2).
- Comparable wave height and cross-sectional structure dimensions (D $\approx$ H).

Singular column TLPWT in particular, may meet these criteria. Ringing forces on tendon tension increases the maximum tendon tension ranges 5 - 30% for different TLPWT designs and environmental conditions, as can be seen in Figure 3.18 [5]. This figure shows the maximum tendon tension, divided by the pretension where the substructure is subjected to first-order potential flow and viscous drag (P1+V), first- & second-order potential flow and viscous drag (P2+V) and first- & second-order potential flow with viscous drag and ringing forces (P2+V+R). This research also found that viscous damping had negligible impact on the ringing resonance effects. Structural damping is not incorporated in this research but may have an effect.

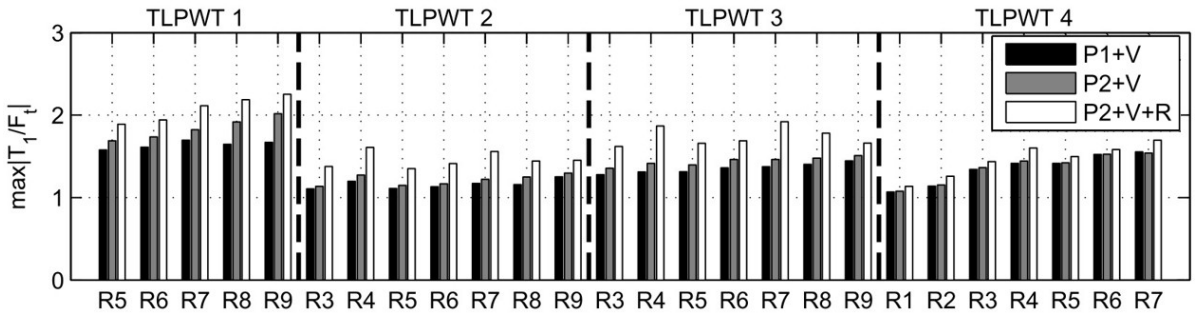

Figure 3.18: 1-hour expected maximum tension in the downwind tendon divided by pretension at the tendon top [5].

This research also showed that tendons with less axial stiffness show larger responses, indicating that using synthetic tendon materials, such as HMPE, UHMWPE and LCP, will increase the maximum tendon tension due to increases in response compared to steel wires. This is also supported by other studies that assess tendon performance for different material types, showing that for synthetic fibres the tendon tension and fatigue increase compared to steel wires [83].

Springing and ringing loads are inherently non-linear so are hard or can not not be taken into account in a frequency domain based analysis of TLPWTs. Springing effects may be accounted for with the inclusion of sum-frequency forces using Rainey approximation. Ringing forces however only occur during transient situations making them not possible to take into account in this research. Future research should asses the impact of such a decision in this framework and the eventual design results.

3.2.4. Aerodynamics & Control
For aerodynamic analysis, a blade element momentum theory (BEMT) analysis will be performed. This method for aerodynamic analysis is widely used and combines blade elements theory (small elements of a blade with local forces) with momentum theory which calculates the thrust through a rotor plane based on the mass, momentum and energy laws of conservation. The eventual goal of this BEMT analysis is to determine the steady state thrust.

The classical BEMT is based on a few steps [25]. The first step is to divide the rotor blades into small elements. The aerodynamic force acting on every element is then described by Equation 3.34. For all

the blade elements the local aerodynamic forces can be calculated based on the angle of attack (α) and lift (C_L) and drag (C_D) coefficients. With the wind velocity (U), induction factor (a) and inflow angle (ϕ) due to the rotational velocity, the local forces on each element (dF_n) can be calculated. The induction factor expresses the reduction in axial flow velocity through the disk. Visual representation of the blade elements and variables is presented in Figure 3.19.

$$dF_n = 1/2\rho V_{res}^2 c(c_l cos(\phi) \ + \ c_d sing(\phi))dr \tag{3.34}$$

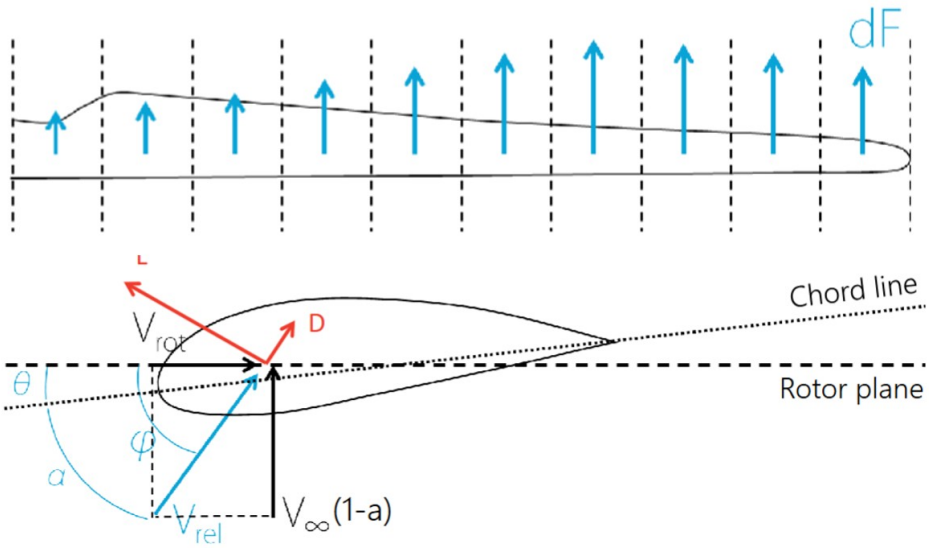

Figure 3.19: Visual representation of blade elements and variables [105].

During the second step, the rotor disk is assumed to be an actuator line disk as depicted in Figure 3.20. The change in momentum and pressure across the disk determines the thrust force. Following the local force calculation, the induction factor is used to determine the induction in axial flow velocity. Equation 3.35 calculates the thrust force of the actuator disk dT.

$$dT = 4\pi r \, dr \, \rho U^2 (1 - a)a \tag{3.35}$$

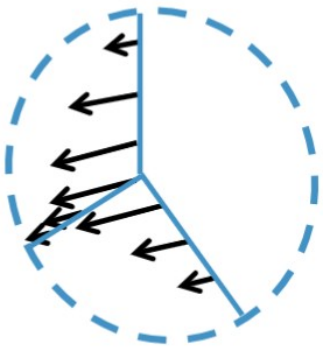

Figure 3.20: Visual representation of the actuator line disk [105].

As the last step, the force on each blade element from the first step is compared to the thrust force. The force on each blade element is multiplied by the number of blades (B). This results in Equation 3.36

The induction factor can be determined iteratively resulting in an equal value of the blade element force and thrust force.

$$B \cdot dF_n = dT \tag{3.36}$$

As BEMT is based on 2D analysis certain 3D effects are not taken into account. These can be included however with corrections:

- Hub and tip losses. In 3D, vortices will be created at the hub and at the blade tips which influence the induced velocity. The simple Prandtl correction was developed in order to account for this effect [79].
- Large induction factors: When the axial induction factor becomes very large (a>0.5) or negative, typically in high-load conditions or when a turbine is stalled, the wake behind the rotor becomes turbulent and the standard momentum theory predicts unrealistic results, like wake velocity reversal. Empirical corrections, such as the Buhl correction, are applied to ensure smooth transitions and physically realistic results [79].

Although these corrections are effective, there will always remain some error relative to higher fidelity models like CFD. However the computational efficiency of BEMT is well suited for the optimisation in this research.

Turbine Control Systems
This study makes use of torque and pitch control to control the aerodynamics. Torque control is used to maximise power output from the cut in wind speed to the rated wind speed. After reaching the rated wind speed the torque will remain constant and the pitch control will actively adjust the blade pitch in order to prevent the aerodynamic loads exceeding the systems capacity until the cut out wind speed where the blades are completely feathered so no thrust is created any more. Yaw control is disregarded in this study as unidirectional load cases are considered and the turbine is assumed to be perpendicular to the wind.

A visual representation of the different operating regions of the torque and pitch control can be seen in Figure 3.21. In this figure it can be seen that the torque increases throughout region two, whereas the blade pitch remains constant at $0°$. Throughout region three, the torque remains constant and the blade pitch is adjusted.

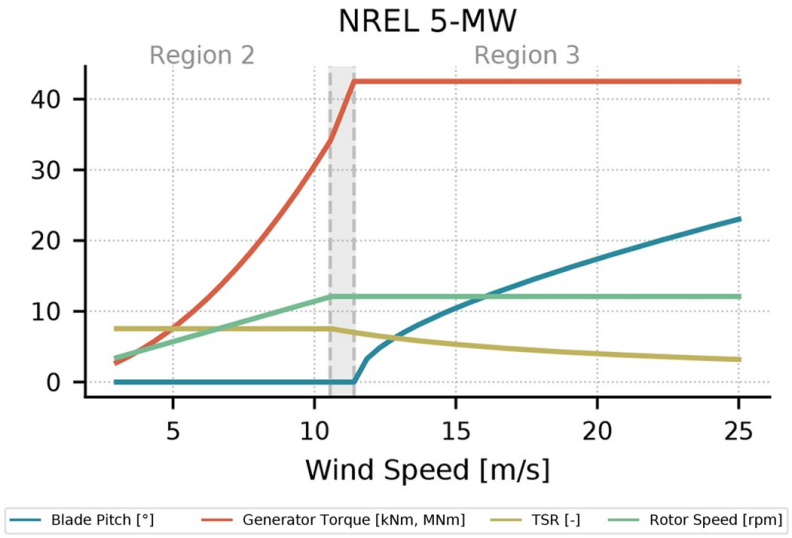

Figure 3.21: Control regions of a wind turbine [2].

When including pitch and torque control, the rotor thrust, determined with the BEM analysis, can be linearised to Equation 3.37 for FD domain calculations according to previous research [101].

$$T = \bar{T} + T_U \Delta(U - \dot{x}) + T_\Omega \Delta\Omega + T_\beta \Delta\beta \tag{3.37}$$

U represents the mean wind speed and $\dot{x}$ is the fore-aft nacelle velocity. The subscripts of T indicate the partial derivatives of thrust with respect to wind speed and rotor speed. A similar linearisation approach can be applied to the generator torque.

$$I_r \dot{\Omega} = Q_U \Delta(U - \dot{x}) + Q_\Omega \Delta\Omega + Q_\beta \Delta\beta - N_g \Delta\tau_g, \tag{3.38}$$

I_r represents the rotor mass moment of inertia, N_g is the gearbox ratio and τ_g is the generator torque. The blade-pitch control input $\Delta\beta$ includes proportional and integral gains ($k_{P\beta}$ and $k_{I\beta}$), as well as a nacelle-velocity-feedback gain, k_{Px}, which provides additional damping to reduce platform motion [2].

$$\Delta\beta = k_{P\beta}\Delta\Omega + k_{I\beta} \int \Delta\Omega \, \mathrm{d}t + k_{Px}\dot{x} \tag{3.39}$$

The generator torque control term $\Delta\tau_g$ also includes proportional and integral gains as described in Equation 3.40.

$$\Delta\tau_g = k_{P\tau}\Delta\Omega + k_{I\tau} \int \Delta\Omega \, \mathrm{d}t \tag{3.40}$$

The above equations are combined to give Equation 3.41, where $H_{QT}(\omega)$ is the transfer function to convert rotor torque to thrust described in Equation 3.42.

$$T(\omega) = T_U U(\omega) - (T_U - k_{Px}T_\beta) i\omega x(\omega) - H_{QT}(\omega)[Q_U U(\omega) - (Q_U - k_{Px}Q_\beta) i\omega x(\omega)], \tag{3.41}$$

$$H_{QT}(\omega) = \frac{(\Omega_\beta + k_{P\beta}T_\beta) i\omega + k_{I\beta}T_\beta}{\omega^2 I_r + i\omega(Q_\Omega + k_{P\beta}Q_\beta - N_g k_{P\tau}) + k_{I\beta}Q_\beta - N_g k_{I\tau}}. \tag{3.42}$$

From this, the fore-aft terms for aerodynamic added mass, damping and turbulent wind excitation can be determined by the following expressions formulated in previous research [41].

$$a_{\text{aero}}(\omega) = \Re\left\{ \frac{1}{i\omega} \left[T_U - k_{Px}T_\beta - H_{QT}(\omega)(Q_U - k_{Px}Q_\beta) \right] \right\}, \tag{3.43}$$

$$b_{\text{aero}}(\omega) = \Im\left[T_U - k_{Px}T_\beta - H_{QT}(\omega)(Q_U - k_{Px}Q_\beta) \right], \tag{3.44}$$

$$f_{\text{aero}}(\omega) = (T_U - H_{QT}(\omega)Q_U)U(\omega) = H_U(\omega)U(\omega). \tag{3.45}$$

These quantities are then transformed to a reference point, accounting for their coupled effects on surge and pitch motion. By doing this, the final aerodynamic added mass matrix, $A_{\text{aero}}(\omega)$, damping matrix, $B_{\text{aero}}(\omega)$ and excitation vector, $f_{\text{aero}}(\omega)$, are obtained.

4

Methodology

This methodology presents how the theory is put into practice to get to the obtained results and address the research question. This consist of the following steps.

- **Definition of Base Case Design and Design Conditions:** The analysis begins by establishing a reference configuration, including the definition of environmental conditions.
- **Optimisation Formulation:** An optimisation formulation is developed to identify cost-effective TLP configurations. This formulation consists of a clearly defined objective function, a set of physical and operational constraints and an optimisation algorithm. The algorithm explores the design space for the design with best performance in terms of levelised cost of energy while remaining within structural and operational limitations.
- **RAFT Model Adaptation:** The frequency-domain RAFT model, originally developed for six degree of freedom semi-submersible and spar platforms, is adapted to represent a tension leg platform. This involves modifying the hydrodynamic calculations, mooring system characteristics and system structural dynamics to reflect TLP specific dynamics.
- **Validation Model Construction:** In order to validate the constructed RAFT TLP frequency domain model for further use, a simple Orcaflex model is constructed which is used to compare to the RAFT results.

4.1. Base Case Design and Design Load Cases

This section elaborates on the base case design that serves as the foundation for the modelling, simulation and optimisation in this research. The base case includes the geometric properties of the floating substructure, mooring layout and turbine characteristics. Additionally, the relevant environmental conditions, such as wind speed, wave height and wave peak period are determined. These conditions reflect representative design load cases and are selected to ensure that the system's performance and structural integrity are assessed under realistic scenario's.

4.1.1. Base Case System Design

As base case design, this research used the MIT/NREL open source TLP design. [5] This platform was originally designed for a 5MW turbine, but for this research was scaled to a 15MW turbine. A more detailed description of the simplified scaling method can be seen in Appendix A. This design consists of a single cylindrical column with four pontoons at the bottom where tendons are attached to the pontoon ends. This base case, as well as all future designs will have a 15 meter freeboard from the water level to the turbine tower base according to standards. Furthermore, the drag coefficient is assumed of a smooth cylinder and the added mass coefficient is iteratively found by comparing the first-order loading between RAFT and Orcawave, but in theory should be equal to one [54]. A schematic overview can be seen in Figure 4.1. The basic properties of this floater for a 15MW turbine can be seen in Table 4.1.

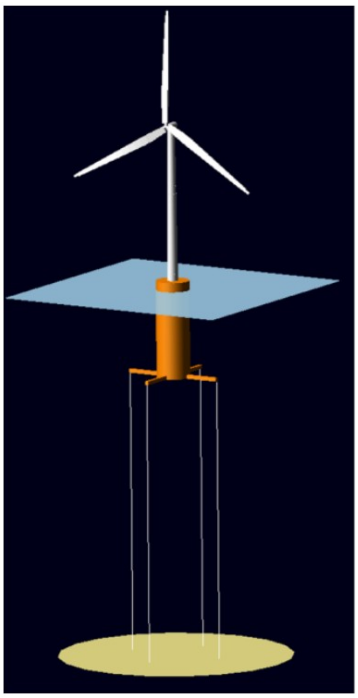

Figure 4.1: A schematic of the MIT/NREL TLP [75].

Table 4.1: Basic Properties of MIT/NREL TLP [75].

Static Properties	Value	Unit
Platform diameter	18	m
Platform draft	45	m
Total displacement	11,866	m^3
Platform mass	2,007,724	kg
Distance between fairleads	54	m
Concrete (ballast) mass	2,014,542	kg
Ca	0.97	-
Cd	0.6	-

The reference platform in this case is a steel shell structure with a Magna dense ballast. The material properties can be seen in Table 4.2. The thickness of the shell structures are determined by Equation 4.1 according to standards [47], where D is the shell structure diameter and t the accompanied thickness.

$$\frac{D}{t} = 60 \tag{4.1}$$

Table 4.2: Platform material properties [68] [113].

Material	Value	Unit
MagnaDense density	5100	kg/m^3
MagnaDense cost	150	€/ton
Young's modulus, steel	210	GPa
Steel Density	7850	kg/m^3
Steel Cost	800	€/ton

Tendon Design

In this framework the mooring properties are taken into account in the model through an equivalent stiffness (EA). This gives flexibility to the framework for the use of different types of tendon materials and diameters. However, as a base case, this research uses steel wire tendons. This research also assumes that a combination of multiple tendons per pontoon is possible, for these cases the equivalent stiffness per pontoon is assumed to be the sum of those tendons. Assuming that the pretension is approximately 30% of the MBL [80], the EA for a system can then be determined by Equation 4.2. For this base case the mooring properties and additional parameters can be seen in Table 4.3

$$EA = \frac{T_{pretension}/0.3}{MBL_{single-line}}\,\pi(0.08)^2 \tag{4.2}$$

Table 4.3: Tendon properties [110] [105].

Property	Unit	Value
Tendon Length	m	75
Pretension per tendon	kN	14000
EA	9273	MN/fairlead
MBL	mT/line	2166
Diameter	mm/line	160
Cost	€/m	1487.4

The reason for using steel wires and not synthetic material tendon types is because steel tendons are more cost-effective and perform better than synthetic moorings in tension leg mooring systems [83]. Future developments may enhance the competitiveness of synthetic moorings for tension leg applications, for this reason the framework is kept adaptable by using an equivalent stiffness and adjustable amount of tendons.

Reference Turbines

To ensure that the framework and the results remain relevant to current industry trends, which can be seen in Figure 4.2, this research uses a 15 MW wind turbine in the optimisation process. To be more specific, the IEA-15MW reference turbine is used as the baseline system [35].

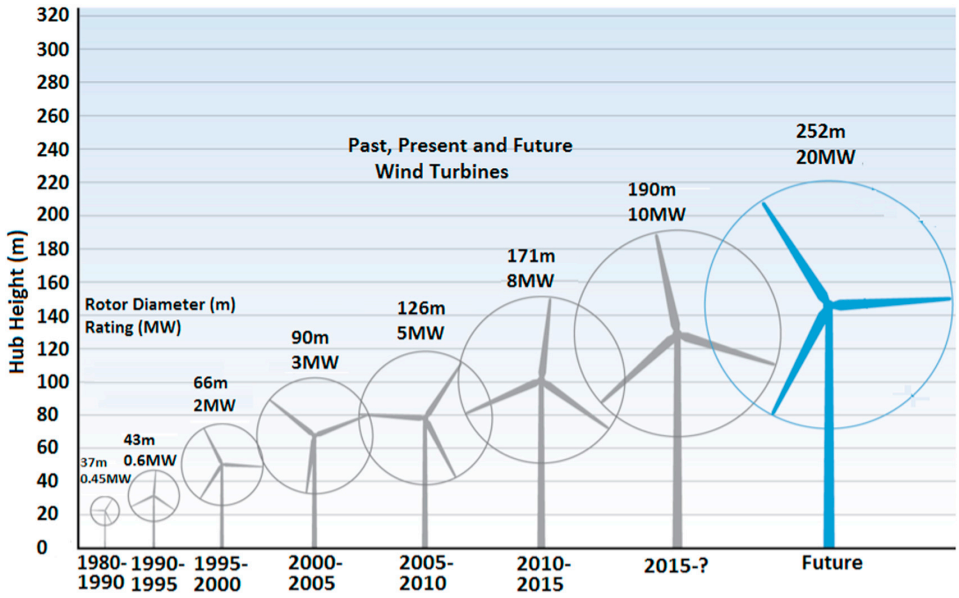

Figure 4.2: The advancements in turbine size over the past 40 years [50].

4.1.2. Site Characteristics & Design Load Cases

As reference site for this research, the Hywind Scotland site will be used with a water depth of 120 meters [49]. Considering optimisation it is favourable to asses as little design load cases (DLCs) as possible. For this reason, only assessing the design driving load cases for TLPWTs is essential. Previous studies showed that there is not one single design driving load case for TLPs making an elaborate set of DLCs necessary [75]. The IEC61400-I provides a complete overview of design load cases [51]. This research will focus on ultimate and fatigue limit states in aligned wind and wave conditions. Furthermore, occurrences of faults (DLC2.x, DLC7.x), start-up (DLC3.x), shut down (DLC4.x), emergency shutdown (DLC5.x) and transport, assembly, maintenance and repair (DLC8.x) are not included in this research. The DLCs that will be assessed are:

- DLC 1.1: The normal operation of the structure will be assessed to identify the ultimate loads due to possible resonances over the operating region.

- DLC1.2: This load case is almost the same as DLC1.1. However, the load factor changes as the goal of this load case is to assess the fatigue. This fatigue is based on the normal operation load case as the turbine will operate most of the life time in these conditions.
- DLC1.6a: This load case is based on operating during a severe sea state to asses the ultimate loads. For this load case the 50-year storm wave height will be combined with a rated wind speed which generates maximum thrust.
- DLC6.1a: This load case is based on an idling wind turbine in extreme wind and wave conditions assessing the ultimate loads in the absence of aerodynamic damping.

An overview of the DLCs that will be taken into account is given in Table 4.4. Including such an extensive set of load cases in accordance with relevant standards not only aids in concept performance evaluation, but may also contribute to a preliminary general performance assessment during the front-end engineering design phase. This enables the current framework to potentially provide early-stage insights that may support certification preparation while reducing the required engineering time.

Table 4.4: Design Load Cases taken into account this research.

DLC	Winds		Waves			Events	Type	Load Factor
Model	Model	Speed	Model	Height	Direction			
1) Power Production								
1.1	NTM	$V_{in} < V_{hub} < V_{out}$	NSS	$H_s = E[H_s\|V_{hub}]$	$\beta = 0°$	Normal operation	U	1.25
1.2	NTM	$V_{in} < V_{hub} < V_{out}$	NSS	$H_s = E[H_s\|V_{hub}]$	$\beta = 0°$	Normal operation	F	1.00
1.6a	NTM	$V_{in} < V_{hub} < V_{out}$	ESS	$H_s = 1.09 \times H_{s50}$	$\beta = 0°$	Normal operation	U	1.25
6) Parked (Idling)								
6.1a	EWM	$V_{hub} = 0.95 \times V_{50}$	ESS	$H_s = 1.09 \times H_{s50}$	$\beta = 0°$	Idling	U	1.35

Wind

The range of wind speeds that will be used in this research is from the cut-in wind speed to the cut-out wind speed and one 50 year storm wind speed. The operational wind speeds that will be taken into account are shown in Table 4.5 with an interval of 2 m/s for operational conditions according to IEC standards. V_{rated} is the rated wind speed that differs per turbine and V_{50} was determined from the Buchan met-ocean data.

Table 4.5: Mean wind speeds for turbine analysis at hub height for normal operation and at 10 m above sea level for the extreme event

Type	Normal operation												Rated speed	Extreme event
Mean speed [m/s]	3	5	7	9	10.59	13	15	17	19	21	23	25	10.59	41.76

These wind speeds are measured at hub height for normal operation and 10 meters above sea level for extreme conditions. The wind speeds at every height can be determined by Equation 4.3 for operational conditions and Equation 4.4 for extreme events.

$$V_{operational}(z) = V_{hub}\left(\frac{z}{z_{hub}}\right)^{0.14} \tag{4.3}$$

$$V_{extreme}(z) = V_{extreme,10m}\left(\frac{z}{z_{10m}}\right)^{0.11} \tag{4.4}$$

Next to the mean wind speed there is a frequency varying turbulence component. The Kaimal spectrum provides an empirical representation of the power spectral density of atmospheric turbulence [55]. The Kaimal spectrum describes the one-sided velocity component spectrum by Equation 4.5.

$$S_k(f) = \frac{4\sigma_k^2 L_k / V_{hub}}{(1 + 6fL_k/V_{\text{hub}})^{5/3}} \tag{4.5}$$

Where:

- f is the frequency [Hz],
- k is the velocity component index:
  - $k = 1$ represents the longitudinal component,
  - $k = 2$ represents the lateral component,
  - $k = 3$ represents the upward component,
- $S_k(f)$ is the single-sided velocity component spectrum,
- σ_k is the standard deviation of the velocity component,
- L_k is the integral length scale for each velocity component,
- V_{hub} is the mean wind speed at hub height.

Since this framework is built for the present and future large scale wind turbines, a Rotor Averaged Kaimal Spectrum (RAKS) is used to consider the spatial averaging effects of the rotor [23]. The RAKS provides a more representative turbulence model by accounting for these effects, leading to improved load predictions. The rotor does not respond to point turbulence, but rather to the spatial average of wind fluctuations across the swept area. High-frequency fluctuations tend to cancel out over the rotor disk, resulting in a spectral filtering effect. This filtering is captured by a power spectral density scaling factor $G(f, R)$, where R is the rotor radius:

$$G(f,R) = \frac{2}{(R\kappa)^3}\left[\mathcal{L}_1(2R\kappa) - I_1(2R\kappa) - \frac{2}{\pi} + R\kappa\left(-2\mathcal{L}_{-2}(2R\kappa) + 2I_2(2R\kappa) + 1\right)\right], \tag{4.6}$$

Where κ is defined by Equation 4.7 and $\mathcal{L}_\nu(\cdot)$ and $I_\nu(\cdot)$ are the modified Struve and modified Bessel functions of the first kind.

$$\kappa = 12\sqrt{\left(\frac{f}{V_{\text{ref}}}\right)^2 + \left(\frac{0.12}{L_u}\right)^2}, \tag{4.7}$$

The rotor-averaged Kaimal spectrum is then computed by applying the filtering function $G(f, R)$ to the standard Kaimal spectrum.

$$S_u^{\text{rotor}}(f) = \frac{1}{2\pi} \cdot G(f,R) \cdot S_u(f). \tag{4.8}$$

The turbulence spectral parameters used in Equation 4.5, define the relationship between different velocity components. Table 4.6 provides the standard deviation and integral scale values for different turbulence components.

Table 4.6: Turbulence spectral parameters for different velocity components.

Velocity Component Index (k)	Standard Deviation (σ_k)	Integral Scale (L_k)
1 (Longitudinal)	σ_1	$8.1\Lambda_1$
2 (Lateral)	$0.8\sigma_1$	$2.7\Lambda_1$
3 (Upward)	$0.5\sigma_1$	$0.66\Lambda_1$

Here σ_1 and Λ_1 represent the standard deviation and length scale of turbulence, respectively, as specified in IEC 61400-1 standards. This research will use two different turbulences for the different DLCs

taken into account. The first one is a normal turbulence model which will be used with the normal wind profile during operation described by Equation 4.10 where I_{ref} is described by Table 4.7 for different wind turbine classes (IEA15MW is class I). Next to this, Equation 4.11 describes the turbulence during extreme wind speeds.

$$\Lambda_1 = \begin{cases} 0,7z & z \leq 60m \\ 42m & z \geq 60m \end{cases} \tag{4.9}$$

$$\sigma_1 = I_{\text{ref}} \left(0,75V_{\text{hub}} + b\right); \quad b = 5,6 \text{ m/s}; \quad (\text{NTM}) \tag{4.10}$$

$$\sigma_1 = 0.11V_{hub}; \quad (EWM) \tag{4.11}$$

Table 4.7: Basic parameters for wind turbine classes

Wind turbine class		**I**	**II**	**III**	**S**
V_{ref}	[m/s]	50	42.5	37.5	Values
A	I_{ref} (-)	0.16			specified
B	I_{ref} (-)	0.14			by the
C	I_{ref} (-)	0.12			designer

Waves

The range of significant wave heights during operational conditions corresponding to the wind speeds defined in Table 4.5 can be determined using Equation 4.12. This relation is based on the Buchan joint wind-wave scatter diagram. To calculate the associated significant wave heights, the wind speeds at hub height from Table 4.5 were first converted to the wind speed at 100 meters above sea level using Equation 4.3.

$$H_s = 0.719e^{0.0832V_{wind,100m}} \tag{4.12}$$

The associated spectral peak period could be determined by linear interpolation of the mean wave heights and periods measured at the Buchan site. The linear interpolation was done according to the following data points giving the relation described in Equation 4.13.

Table 4.8: Spectral peak period T_p as a function of significant wave height H_s at Buchan Deep; mean values.

H_s [m]	1	2	3	4	5	6	7	8	9	10	11
T_p [s]	6.8	7.9	8.8	9.6	10.4	11.2	11.9	12.6	13.3	14	14.6

$$T_p = 0.7673H_s + 6.4055 \tag{4.13}$$

For the extreme sea states of DLC1.6a and DLC 6.1a the 50 year significant wave height and peak period were measured to be 10.5 meters and 14.3 seconds, respectively. Eventually, for the frequency domain model the sea states will be represented by a JONSWAP spectrum. The spectral density of the surface elevation for the JONSWAP spectrum is given by Equation 4.14

$$S_{JS}(f) = C(\gamma) \cdot S_{PM}(f) \cdot \gamma^{\alpha(f)} \tag{4.14}$$

Where:

- $S_{JS}(f)$ is the JONSWAP spectral density function (m^2/s),
- $S_{PM}(f)$ is the Pierson Moskowitz (PM) spectral density function,
- $C(\gamma)$ is the normalizing factor,
- γ is the peak-shape parameter,
- $\alpha(f)$ is the peak enhancement function.

The normalizing factor ensures that the JONSWAP spectrum has the same total wave energy as the PM spectrum:

$$C(\gamma) = \frac{\int_0^\infty S_{PM}(f)df}{\int_0^\infty S_{PM}(f)\gamma^{\alpha(f)}df} \tag{4.15}$$

The JONSWAP spectrum recovers the PM spectrum when $\gamma = 1$. To account for the sharper peak observed in storm sea states, a peak enhancement function is introduced:

$$\alpha(f) = \exp\left(-\frac{(f-f_p)^2}{2\sigma^2 f_p^2}\right) \tag{4.16}$$

Where:

- f is the wave frequency (Hz),
- f_p is the peak frequency (Hz),
- σ is the spectral width parameter.

The parameter σ takes different values depending on the frequency,

$$\sigma = \begin{cases} 0.07, & f \leq f_p \\ 0.09, & f > f_p \end{cases}$$

The peak-shape parameter γ varies based on the ratio $T_p/\sqrt{H_s}$.

$$\gamma = \begin{cases} 5, & \frac{T_p}{\sqrt{H_s}} \leq 3.6 \\ \exp\left(5.75 - 1.15\frac{T_p}{\sqrt{H_s}}\right), & 3.6 < \frac{T_p}{\sqrt{H_s}} \leq 5 \\ 1, & \frac{T_p}{\sqrt{H_s}} > 5 \end{cases} \tag{4.17}$$

The complete formulation of the JONSWAP spectrum becomes:

$$S_{JS}(f) = 0.3125 \cdot H_s^2 \cdot T_p^{-4} \cdot f^{-5} \cdot \exp\left(-1.25\left(\frac{f}{f_p}\right)^{-4}\right) \cdot (1 - 0.287\ln\gamma) \cdot \gamma^{\alpha(f)} \tag{4.18}$$

Final Design Load Cases

Taking the above considerations, the final DLCs that will be taken into account are presented in Table 4.9. These loads will be modelled by a rotor averaged Kaimal spectrum and a JONSWAP spectrum for the dynamic analysis.

Table 4.9: Wind and wave conditions for the IEA 15 MW turbine

IEA 15 MW					
$z_{hub} = 144.39$ m					
V_{hub} [m/s]	V_{100m} [m/s]	H_s [m]	T_p [s]	λ [m]	$Occurence$ [%]
Operational DLC 1.1 & 1.2					
3	2.83	0.91	7.10	78.79	7.63
5	4.72	1.07	7.22	81.45	10.97
7	6.61	1.25	7.36	84.62	13.79
9	8.50	1.46	7.52	88.41	15.05
11	10.39	1.71	7.72	92.94	14.72
13	12.28	2.00	7.94	98.39	12.70
15	14.17	2.34	8.20	104.97	9.43
17	16.06	2.74	8.50	112.93	5.96
19	17.95	3.20	8.86	122.62	3.73
21	19.84	3.75	9.28	134.47	1.93
23	21.73	4.38	9.77	149.03	0.86
25	23.62	5.13	10.34	167.01	0.32
Operational Wind with Extreme Wave at Rated Wind Speed DLC 1.6a					
11.17	-	10.50	14.3	319.27	0.00
Extreme Wind and Wave when Idling DLC 6.1a					
41.76	-	10.50	14.3	319.27	0.00

4.2. Optimisation Problem Formulation

Considering the optimisation, four different main pillars are defined. These are selection of the design variables, definition of the objective function, definition of the constraints and the selection of optimisation algorithm.

4.2.1. Design Variables

As elaborated upon in Chapter 3, a selection needs to be done to keep the design variables at a minimum. This will enhance computational time of the optimisation framework while converging to the most cost-efficient designs. As the TLP is a highly coupled system which greatly depends on the mass, buoyancy and tendon properties, it is deemed best to incorporate all design variables which may have a significant effect on these parameters. For this reason the following design variables are taken into account which together describe the rest of the system.

- Main column diameter
- Main column draft
- Tendon pretension
- Tendon angle
- Pontoon length
- Pontoon diameter

4.2.2. Objective Function

The goal of the optimisation framework is to identify the most cost-efficient design that satisfies all the constraints while allowing comparability of the results within the study and across other studies. To achieve this, the model combines variable platform and mooring costs with fixed lifecycle costs, based on cost models in literature [26] [5]. Eventually, minimising the levelised cost of energy is the objective of this study. The *LCOE* represents the net present value of all system costs per MWh of energy produced

over the system's operational lifetime. It effectively reflects the minimum selling price per MWh required to recover all capital, operational and decommissioning costs. The *LCOE* is defined in Equation 4.19. Cost models in literature often depend on wind farm capacity and the number of turbines installed. To scale these models to a single floating wind unit, it is assumed that a typical floating wind farm will consist of 88 units [26]. Throughout this section, a conversion factor of 0.88 may be applied to convert costs from US dollars to euro's.

$$LCOE = \frac{1.1 \cdot CAPEX + OPEX + DECEX}{LEP} \quad [€/\text{MWh}] \tag{4.19}$$

CAPEX represents the capital expenditures, such as costs related to the construction and installation of the turbine units. A factor of 1.1 is applied to account for contingencies throughout the process. *OPEX* denotes the operational expenditures over the system's lifetime, while *DECEX* refers to the costs associated with decommissioning. *LEP* is the lifetime energy production of the system.

CAPEX

The first component of the objective function is the *CAPEX*, which is defined in Equation 4.20.

$$CAPEX = C_{\text{Turbine \& tower}} + C_{\text{Electrical systems}} + C_{\text{Construction}} + C_{\text{Installation}} \quad [€] \tag{4.20}$$

The turbine and tower cost and the cost of electrical systems are described by Equation 4.21 and Equation 4.22.

$$C_{\text{Turbine \& tower}} = 1081 \cdot (TC[kW])^{0.991} \quad [€] \tag{4.21}$$

$$C_{\text{Electrical systems}} = C_{\text{MVAC}} + C_{\text{HVAC}} + C_{\text{Sub-offshore}} = 299600 \cdot D_{sub} + 651250 \cdot DCF + 245318 \cdot DCF \quad [€] \tag{4.22}$$

Here, TC is the turbine capacity, C_{MVAC} is the cost for inter turbine cables, C_{HVAC} is the cost of a windfarm to shore transmission cable, $C_{\text{Sub-offshore}}$ is the cost of an offshore substation, D_{sub} is the distance of a floating wind unit to floating wind unit (which is on average 7 rotor diameters [27]) and DCF is the distance to coastal facilities.

The construction cost includes all expenses related to the materials used in the platform, the cost of anchors capable of withstanding the required vertical loads and the costs of the tendons itself. This is evaluated using Equation 4.23, based on the input parameters listed in Table 4.10 and the MBL of the tendon which is determined by Equation 4.24.

$$C_{\text{Construction}} = M_{\text{steel}} C_{\text{steel}} + M_{\text{Ballast}} C_{\text{Ballast}} + 4\left(T_{\text{pretension}} C_{\text{anchor}} + \text{MBL} \cdot L_{\text{moor}} C_{\text{moor}}\right) \quad [€] \tag{4.23}$$

$$MBL = \frac{T_{pre}}{0.3} \tag{4.24}$$

Table 4.10: Pricing index of different aspects of the platfrom [61] [4] [105] [26].

Variable	Value	Unit
C_{steel}	800	€/tonne
$C_{Ballast}$	150	€/tonne
C_{anchor}	100	€/kN
C_{moor}	70	€/m/MN

For tension leg platforms, installation constitutes a significant portion of the total cost, often exceeding that of conventional floating platforms. This is primarily due to two factors. First, TLPs are generally not self-stable, making direct tow-out to the installation site infeasible. Second, the use of tensioned moorings typically requires additional external ballast during installation to facilitate the connection of pre-tensioned tendons, introducing further complexity and cost. The cost associated with TLP installation is estimated using the following expressions where WD is the water-depth.

$$C_{\text{Installation}} = C_{\text{Structure-inst}} + C_{\text{Turbine-inst}} + C_{\text{Port\&Staging-inst}} + C_{\text{Electrical systems}} \quad [€] \tag{4.25}$$

$$\begin{aligned} C_{\text{Structure-inst}} &= \left(\frac{99{,}746{,}000 + 21{,}625 \cdot WD + 75{,}650 \cdot DCF}{600{,}000}\right) \cdot TC \cdot 0.88 \quad [€] \\ C_{\text{Turbine-inst}} &= \left(\frac{230{,}000{,}000 + 452{,}861 \cdot DCF}{600{,}000}\right) \cdot TC \cdot 0.88 \quad [€] \\ C_{\text{Port\&Staging-inst}} &= \left(\frac{34{,}151{,}022 + 55{,}231 \cdot DCF}{600{,}000}\right) \cdot TC \cdot 0.88 \quad [€] \\ C_{\text{Electrical systems}} &= (128400 \cdot D_{sub} + 513375 \cdot DCF + 32850 \cdot TC) \cdot 0.88 \quad [€] \end{aligned} \tag{4.26}$$

OPEX

The operational expenditures (*OPEX*) associated with the floating unit are defined in Equation 4.27.

$$\textit{OPEX} = C_{\text{maintenance}} + C_{\text{operation}} + C_{\text{port}} \quad [€] \tag{4.27}$$

The maintenance cost accounts for annual activities such as tendon inspections. The operational cost includes expenses related to personnel, vessels and logistics required for maintenance operations. The port cost represents annual fees for the use of port facilities. The total annual *OPEX* is calculated by Equation 4.28

$$\textit{OPEX} = (50{,}129.6 + 28.6 + 23.1) \cdot TC \cdot 0.88 \quad [€/yr] \tag{4.28}$$

DECEX

After an operational lifetime of 25 years, the decommissioning cost of the floating offshore wind turbine system is estimated by Equation 4.29.

$$\textit{DECEX} = 137{,}500 \cdot TC \cdot 0.88 \quad [€] \tag{4.29}$$

LEP

The lifetime energy production (*LEP*) is based on an operational period of 25 years. Using the occurrence statistics of every environmental condition (EC) provided in Table 4.9 and the average power output under each environmental condition, the total energy produced over the system's lifetime can be estimated. To account for turbine downtime and maintenance, a capacity factor of 0.55 is applied [108]. This leads to the following expression for the lifetime energy production:

$$\textit{LEP} = 0.55 \sum_{\text{EC}} \text{occurrence}_{\text{EC}} \cdot \text{lifetime} \cdot P_{\text{avg,EC}} \quad [\text{MWh}] \tag{4.30}$$

4.2.3. Constraints

When considering the constraints for this study, three categories are defined.

- Constraints on the design variable ranges
- Hard constraints on system performance
- Soft constraints on system performance

Constraints on the Design Variables

The optimisation process may explore a wide range of design options in search of the optimum. However, allowing an unrestricted design space can significantly increase computational time while leading to unrealistic or impractical solutions. To maintain efficiency and ensure feasible results, appropriate bounds are imposed on the design variables.

- **Main column diameter:**
  As the IEA 15MW tower base diameter is 10 meters, this value is the minimum diameter of the platform main column. The maximum diameter is governed by manufacturability. Current industry limits allow for steel columns up to 15.5 meters. Assuming future advancements, a maximum diameter of 20 meters is adopted [72].

$$10\,[\mathrm{m}] \leq D_{\text{main column}} \leq 20\,[\mathrm{m}]$$

- **Main column draft:**
  The maximum draft is typically limited by the site water depth and installation requirements. As the water depth at the reference site is 120 meters, a maximum draft of 110 meters is assumed, allowing for seabed clearance. The minimum draft of 15 meters ensures platform stability and keeps tendons fully submerged.

$$15\,[\mathrm{m}] \leq \text{Draft}_{\text{main column}} \leq 110\,[\mathrm{m}]$$

- **Tendon pretension:**
  Pretension provides the primary stability for TLPs. A minimum value of 500 [kN] allows for design flexibility, while the maximum of 24 [MN] is based on maximum four tendons per pontoon with an MBL of $\pm$ 20 [MN] each, assuming the maximum pretension is 30% of the MBL [80].

$$500\,[\mathrm{kN}] \leq T_{\text{pretension}} \leq 24{,}000\,[\mathrm{kN}]$$

- **Tendon angle:**
  To ensure feasible configurations that enhance system stability and dynamic response, the tendon angle is constrained to a range known to provide beneficial performance. Below this range, platform behavior deteriorates due to unfavourable load orientations and reduced restoring capability [60].

$$70^\circ \leq \alpha_{\text{tendon}} \leq 90^\circ$$

- **Pontoon length:**
  The pontoon length must be at least the main column radius to enable proper attachment. An upper bound of 60 meters is used to explore the design space, though practical constraints (e.g., yard space, transport) may refine this in future work.

$$R_{\text{main column}}\,[m] \leq L_{\text{pontoon}} \leq 60\,[\mathrm{m}]$$

- **Pontoon diameter:**
  The pontoon diameter is constrained between a minimum of 1 meter and a maximum based on geometric compatibility with the main column, ensuring all pontoons may be welded onto the structure. A schematic reasoning can be seen in Figure 4.3

$$1\,[\mathrm{m}] \leq D_{\text{pontoon}} \leq \sqrt{2}\,R_{\text{main column}}\,[\mathrm{m}]$$

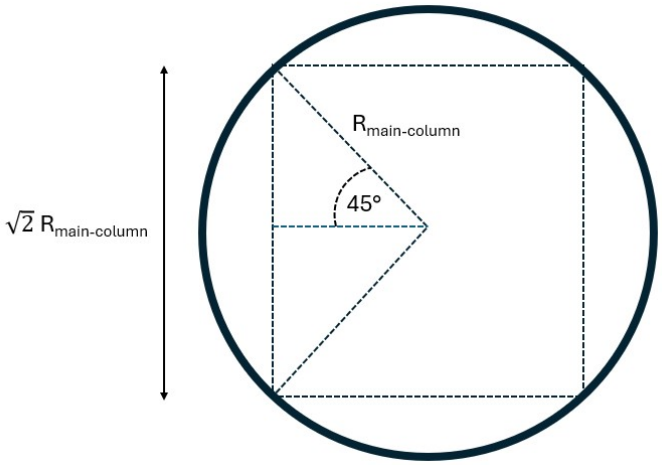

Figure 4.3: Schematic overview of the upper limit of the pontoon diameter.

Hard Constraints on System Properties
To efficiently eliminate unfeasible or physically invalid designs early in the optimisation process, several hard constraints are identified.

- **Static equilibrium:**
  The system's weight, buoyancy and tendon pretension must be in equilibrium and each component must be positive.

$$W_{\text{system}} + T_{\text{pretension}} - F_{\text{buoyancy}} = 0$$

with

$$W_{\text{system}} > 0 \qquad T_{\text{pretension}} \geq 0 \qquad F_{\text{buoyancy}} > 0$$

- **Natural frequency exclusion zones:**
  The system's natural frequencies may not coincide with the 1P and 3P excitation frequencies of the wind turbine to avoid resonance-related instability.

$$f_{\text{n,i}} < 0.083\,\text{Hz} \quad \text{or} \quad 0.126\,\text{Hz} < f_{\text{n,i}} < 0.249\,\text{Hz} \quad \text{or} \quad f_{\text{n,i}} > 0.378\,\text{Hz}$$

Soft Constraints on System Performance
Instead of strictly excluding certain designs through hard constraints, soft constraints are used to penalise violations in a more flexible way. This approach allows the optimisation algorithm to better explore the design space and identify solutions that may slightly exceed certain limits but could become feasible with minor design modifications.

- **Maximum surge offset:**
  To limit riser deflection, the maximum surge offset is restricted to 10% of the water depth [46].

$$\text{x}_{\text{surge}} \leq 12\,[\text{m}]$$

- **Minimum tendon tension:**
  To avoid slack events that can cause highly non-linear snap loads, tendons must remain under tension at all times.

$$\text{T}_{\text{moor,min}} > 0\,[\text{kN}]$$

- **Maximum tendon tension:**
  To avoid tendon failure, the maximum tendon tension is limited to the minimum breaking load (MBL). An upper bound of 80 [MN] is assumed, accounting for the possibility of multiple tendons per pontoon.

$$\text{T}_{\text{moor,max}} < 80{,}000\,[\text{kN}]$$

- **Fatigue damage:**
  The lifetime fatigue damage must remain below 1.0 to ensure the structural integrity of components throughout the operational lifetime.

$$D_{\text{fatigue}} < 1.0$$

- **RNA acceleration:**
  To protect the main bearings within the nacelle, the nacelle acceleration is limited to 2.8 [m/s^2], following guidelines used in prior work [85].

$$a_{\text{nacelle}} \leq 2.8\,[\text{m/s}^2]$$

- **Maximum pitch angle:**
  To prevent excessive dynamic loading and motion on the rotor-nacelle assembly (RNA), the nacelle pitch angle (static + dynamic) is constrained to 10° [85].

$$\theta_{\text{pitch,nacelle}} \leq 10^\circ$$

Optimisation Formulation Summary
Combining the objective function and all the constraints the following optimisation formulation could be constructed.

Objective function	$f(\mathbf{x}) = \mathit{LCOE} = \dfrac{1.1 \cdot \mathit{CAPEX} + \mathit{OPEX} + \mathit{DECEX}}{\mathit{LEP}}$ [€/MWh]
Design variables	$\mathbf{x} = \{D_{\text{main column}},\ \text{Draft}_{\text{main column}},\ T_{\text{pre}},\ \alpha_{\text{tendon}},\ L_{\text{pontoon}},\ D_{\text{pontoon}}\}$
Design variable ranges	$13\,\text{m} \leq D_{\text{main column}} \leq 20\,\text{m}$ $15\,\text{m} \leq \text{Draft}_{\text{main column}} \leq 110\,\text{m}$ $500\,\text{kN} \leq T_{\text{pre}} \leq 24{,}000\,\text{kN}$ $70^\circ \leq \alpha_{\text{tendon}} \leq 90^\circ$ $R_{\text{main column}}\,[\text{m}] \leq L_{\text{pontoon}} \leq 60\,[\text{m}]$ $1\,\text{m} \leq D_{\text{pontoon}} \leq \sqrt{2}\,R_{\text{main column}}\,[\text{m}]$
Hard constraints	$W_{\text{system}} + T_{\text{pre}} - F_{\text{buoyancy}} = 0$ $W_{\text{system}} > 0, \quad T_{\text{pre}} \geq 0, \quad F_{\text{buoyancy}} > 0$ $f_{n,i} < 0.083\,\text{Hz}$ or $0.126 < f_{n,i} < 0.249\,\text{Hz}$ or $f_{n,i} > 0.378\,\text{Hz}$
Soft constraints	$x_{\text{surge}} \leq 12\,\text{m}$ $T_{\text{moor,min}} > 0\,\text{kN}$ $T_{\text{moor,max}} < 80{,}000\,\text{kN}$ $D_{\text{fatigue}} < 1$ $acc_{\text{nacelle}} \leq 2.8\,\text{m/s}^2$ $\theta_{\text{pitch,nacelle}} \leq 10^\circ$

(4.31)

4.2.4. Optimisation Algorithm

To identify the optimal design parameters for the TLP platform concept, a Genetic Algorithm (GA) was implemented in Python using the DEAP (Distributed Evolutionary Algorithms in Python) library. Genetic Algorithms are population-based stochastic search techniques inspired by natural selection. A GA starts with an initial population of candidate solutions (individuals), evaluates their fitness based on an objective function and iteratively generates new populations through biologically inspired operations which are selection, crossover and mutation.

In each generation, individuals are selected based on their fitness. Selected individuals undergo crossover to exchange parameter values and mutation to introduce variability. The process repeats over multiple generations, ideally converging towards optimal or near-optimal solutions. The settings of the different algorithm parameters and their reasoning can be seen in Table 4.11.

Table 4.11: Genetic algorithm settings and reasoning.

Parameter	Value	Reasoning
Population size	500	A relatively large population improves genetic diversity and therefore exploration of the design space. This aligns with guidelines for optimisation with more than 5 design variables [103].
Generations	5	Relatively small but based on literature which found that that genetic algorithms in combination with a large and highly non-linear design space tend to converge more reliably with larger populations. For this reason less generations are used to remain within computational time limits [106].
Initialization	Latin Hypercube Sampling (LHS)	LHS ensures a complete of indivduals, aiming to prevent premature convergence. This type of sampling is recommended in previous research for Genetic algorithms with a highly complex design space [65].
Selection	Tournament (size 3)	Efficient method to control the convergence compared to other selection methods. It balances convergence and diversity [76].
Crossover method	Simulated Binary Crossover (SBX)	This type of cross over generates children around the parent solutions, with a tunable distribution controlling the spread. This allows both local exploitation and occasional global exploration. [20].
Crossover probability (p_c)	0.8	A common value which promotes exploration by keeping the design space diverse [103].
Mutation method	Polynomial Bounded Mutation	Commonly used as it remains within the defined bounds and produces fine changes but also occasionally implements large changes to promote diversity [19].
Mutation probability (p_m)	0.17	Often set to $1/n$ where n is the number of design variables, ensuring diversity but also remaining within the discovered design space [81].
Constraint handling	Penalty-based + feasibility checks	Penalty functions are straightforward and effective. Penalty based constraint handling may also allow for design concepts which just overshoot the constraints to be 'accepted'. These concepts may be more cost effective in terms of LCOE with only minimal adjustments to stay within the constraints.

To enhance computational efficiency, the GA is implemented using a three-stage evaluation process:

1. **Hard Constraint Check:**
   Individuals that violate hard physical constraints (as defined in subsection 4.2.3) are immediately penalised with a large penalty value. This avoids unnecessary computation by excluding physically infeasible solutions early in the process. The extremely large penalty prevents this individual to be selected for the next generation.
2. **Quasi-static Feasibility Check:**
   Individuals that violate soft constraints under quasi-static conditions (e.g., surge offset or tendon pretension limits) are also rejected by giving them an extremely large penalty. Since such configurations are expected to remain infeasible under dynamic conditions, this step prevents unnecessary dynamic simulations and reduces computational cost.
3. **Dynamic Evaluation:**
   Individuals that pass the previous checks proceed to full dynamic simulation. After evaluation, constraint violations are quantified and a relative penalty is applied to the fitness function to guide the optimisation process. This penalty is computed as a sum of squared normalized deviations from the constraint limits, where each term has the form $\left(\frac{Variable-Limit}{Limit}\right)^2$. This ensures smooth penalisation, where small deviations have a small penalty and large deviations have a quadratic increasing penalty, and comparability across constraints.

Since each individual design requires independent simulations. A multiprocessing strategy with 20 processors was used to evaluate individuals in parallel, reducing the computational time of the optimisation. A visual representation of the optimisation workflow is shown in Figure 4.4. This figure illustrates how the genetic algorithm progresses from the initial population, evaluates each design concept based on the objective function and constraints, and then generates a new population for the next generation. This process is repeated until the specified number of generations is completed and a most cost-efficient design is returned.

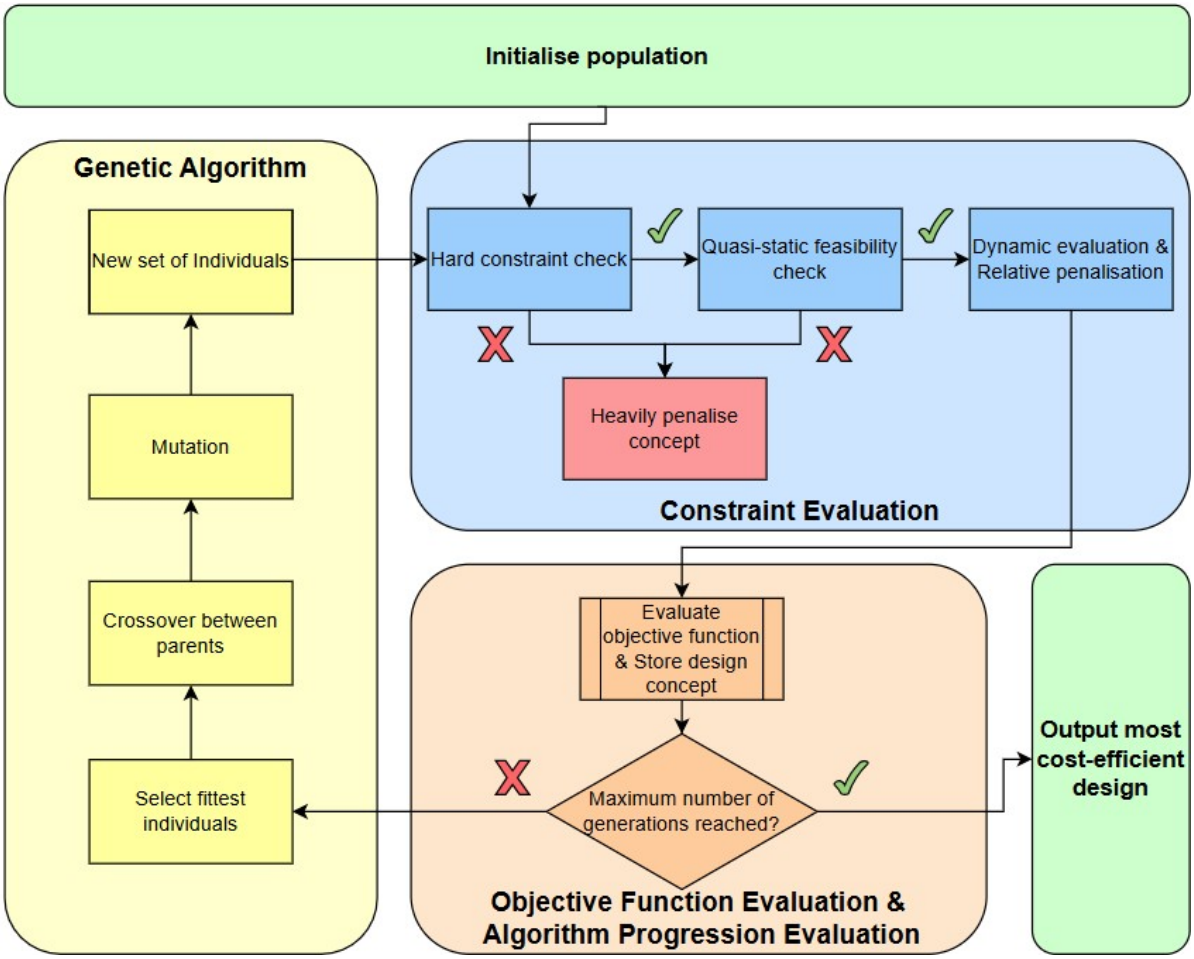

Figure 4.4: A schematic workflow of the optimisation problem.

4.3. RAFT Model Construction

As mentioned previously, this research makes use of the RAFT software, developed and published by the National Renewable Energy Laboratory in 2022 [41]. RAFT is a python based, 6-degree-of-freedom frequency domain modelling software originally developed for semi-submersible and spar buoy platform floating offshore wind turbines. RAFT consists of two main computational modules. The first is the quasi-static solver, `solve-statics`, whose workflow is illustrated in Figure 4.5. Upon completion of the static equilibrium solution, the solver proceeds to the linear dynamic module, `solve-dynamics`, as shown in Figure 4.6.

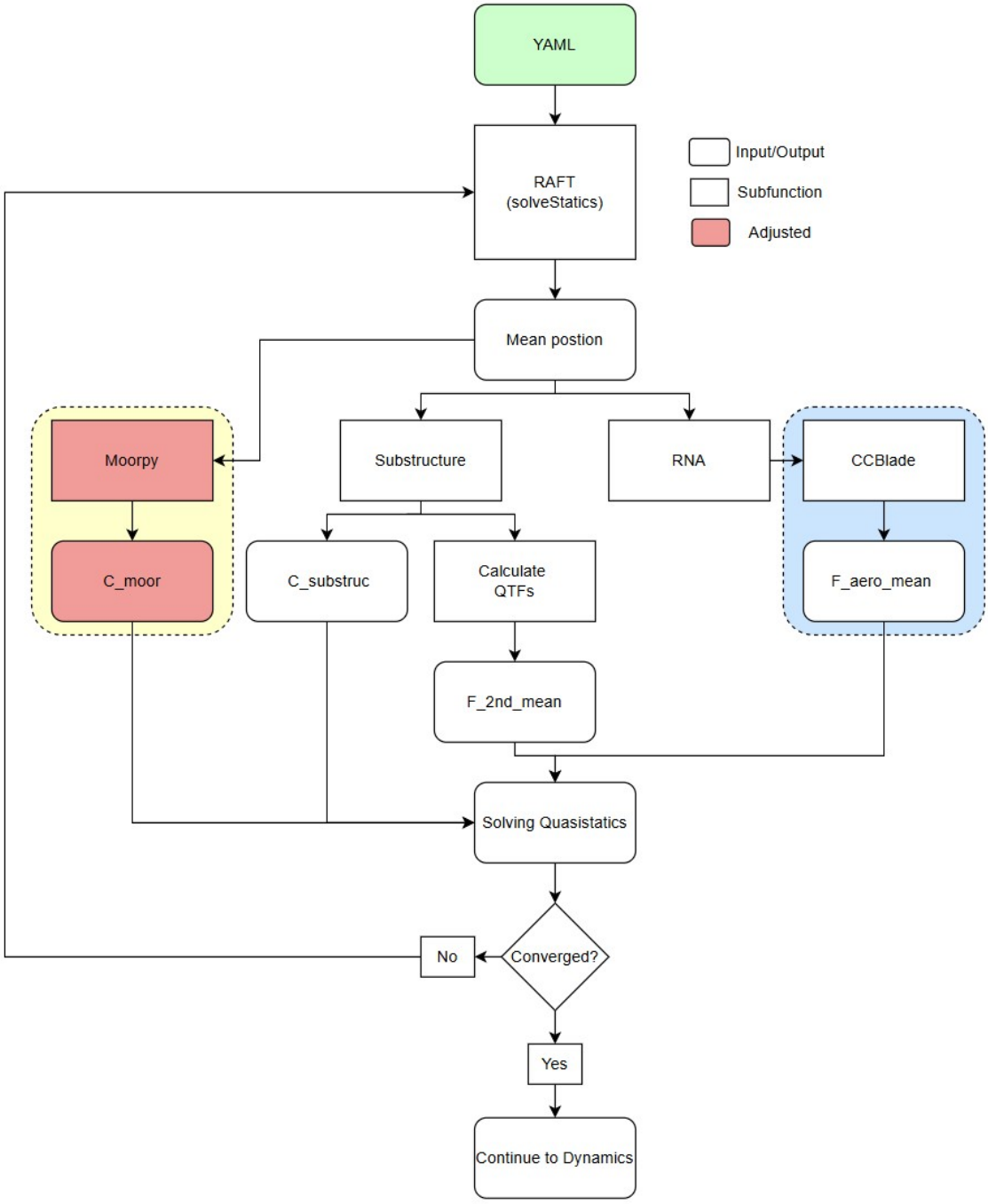

Figure 4.5: A schematic of the solve statics workflow in RAFT

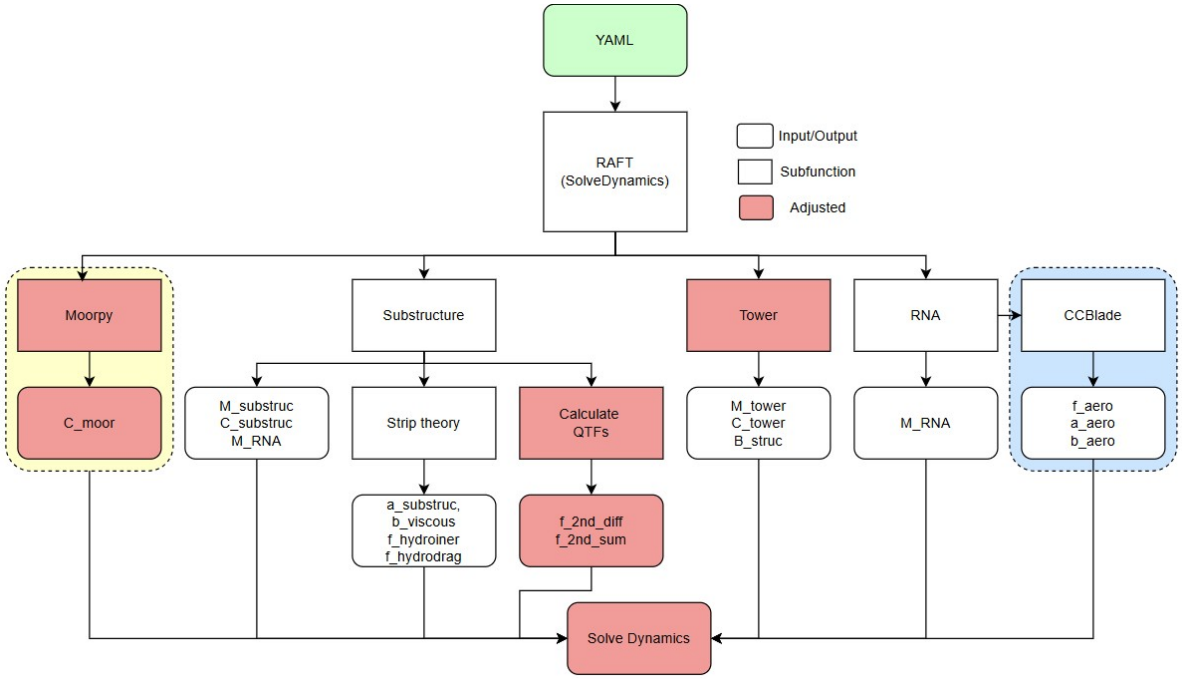

Figure 4.6: A schematic of the solve dynamics workflow in RAFT

After executing the described modules, RAFT provides both the mean value and the power spectral density (PSD) for the systems response. The standard deviation of the response is obtained as the square root of the zeroth spectral moment of the one-sided PSD. This is calculated by Equation 4.32, where ξ is the complex response amplitude. Based on this standard deviation, the corresponding maximum and minimum values of the response can be estimated using Equation 4.33.

$$\sigma = \sqrt{0.5\,|\xi|^2} \tag{4.32}$$

$$\text{Variable}_{max/min} = mean \pm 3\sigma \tag{4.33}$$

To adapt the software for the specific requirements of this research, several key modifications were implemented. These modifications are highlighted in red in the flowcharts presented in Figure 4.5 and Figure 4.6 and are summarised below.

- Inclusion of tower flexibility in the model.
- Implementation of tension leg mooring system dynamics.
- Integration of second-order sum-frequency load calculations.
- Incorporation of a fatigue damage estimation.

In addition to these extensions, computational efficiency was improved by reducing the number of active degrees of freedom where possible. Since pitch and fore-aft bending typically dominate the structural response of floating wind turbines, particularly under unidirectional wind and wave loading, the dynamic analysis was restricted to three primary degrees of freedom. These degrees of freedom are surge, heave and pitch. All other DOFs were constrained in order to reduce the computational cost during the optimisation process while retaining the essential dynamic behaviour of the system. However, the implementations give a basis for modelling in global 6 DOF, which could be further developed in future research.

4.3.1. Tower Flexibility

By modelling the tower using Euler-Bernoulli beam elements RAFT was extended from a rigid-body 6-DOF model to a coupled system that includes both rigid-body motions and flexible tower dynamics. This was achieved by implementing a finite element (FEM) model, discretising the tower into a series of beam segments as described in Section 3.1. A detailed overview of the properties per beam element can be seen in Section B.2. The floater properties are transformed and added to the base tower node through a rigid connection. Allowing for simple and straightforward integration of the tower and floater.

To account for structural damping, Rayleigh damping was applied with a damping ratio of 2% of critical damping. The damping coefficients were selected such that both the global surge mode and the first pitch-bending mode are damped.

4.3.2. Tension Leg Mooring

RAFT originally relies on the external `MoorPy` software package to compute catenary mooring properties. To enable compatibility with tension leg mooring systems, a custom tension leg mooring module was implemented within MoorPy. This extension allows the software to compute the quasi-static equilibrium of the TLP mooring system and return the corresponding analytically determined linearised mooring stiffness matrix at an offset position. This capability is essential for system-level linearisation and is based on the mooring stiffness formulation described in Chapter 3.

In the original RAFT implementation, the power spectral density (PSD) of the tendon tension was estimated using a tension Jacobian derived via a forward finite difference scheme. While this method is appropriate for catenary moorings, it is not suitable for tension leg systems due to their highly coupled, non-linear and stiff response characteristics. To address this limitation, a new approach was introduced wherein tendon tension variations are directly computed in the frequency domain from the platform motion. Given the frequency-dependent displacement and rotation of the platform, the resulting translations and rotations of each fairlead are determined. With the fairlead positions known, the elongation of each tendon is calculated. The corresponding tension variation is then computed using the following linear relationship.

$$T_{\text{moor},i}(\omega) = \frac{EA \cdot \Delta L_i(\omega)}{L_0} \tag{4.34}$$

where EA is the axial stiffness of the tendon, $\Delta L_i(\omega)$ is the dynamic elongation of the i-th tendon at frequency ω, and L_0 is the unstretched length.

4.3.3. Sum-Frequency Force Approximation

As described in Chapter 3, sum-frequency wave forces can have significant contributions to the structural response of tension leg platforms and should therefore be accounted for. Using the slender-body approximation developed by Rainey [92], the second-order wave loads due to sum-frequency interactions can be approximated. These forces originate from the quadratic interactions of linear wave components. Given a wave energy spectrum $S(\omega)$, the amplitude of the second-order sum-frequency excitation force in degree of freedom i_{DOF} at frequency $\omega_k = \omega_i + \omega_j$ is calculated by Equation 4.35.

$$f^{(+)}_{i_{\text{DOF}}}(\omega_k) = 4\sqrt{\sum_{i=0}^{N}\sum_{j=i}^{N} S(\omega_i)S(\omega_j)\left|Q^{(+)}_{i_{\text{DOF}}}(\omega_i,\omega_j,\beta)\right|^2} \cdot \Delta\omega \tag{4.35}$$

Key in this equation is to calculate the sum-frequency QTF, $Q^{(+)}_{i_{\text{DOF}}}(\omega_i,\omega_j,\beta)$. The underlying physics is governed by the second-order sum-frequency potential $\phi^{(2)}_{+}$, which satisfies the following equation.

$$\vec{F}_{\text{pot2}} = -\rho\nabla\phi^{(2)}_{+} \tag{4.36}$$

This potential arises from the non-linear interaction between two linear wave components with frequencies ω_1 and ω_2 and associated wave numbers k_1, k_2. The combined wave vector that results from this interaction is described by Equation 4.37.

$$\vec{k}_+ = \vec{k}_1 + \vec{k}_2 = \begin{bmatrix} k_1 \cos\beta_1 + k_2 \cos\beta_2 \\ k_1 \sin\beta_1 + k_2 \sin\beta_2 \\ 0 \end{bmatrix}, \quad \|\vec{k}_+\| = k_+ \tag{4.37}$$

Here, β_1 and β_2 are the wave headings of the incident components. The sum-frequency potential coefficient is approximated using Rainey's formulation which is expressed by the following equation.

$$\gamma_{12}^{(+)} = \frac{-ig}{2\omega_1} \cdot \frac{k_1^2\left(1-\tanh^2(k_1h)\right) + 2k_1k_2\left(1+\tanh(k_1h)\tanh(k_2h)\right)}{\frac{(\omega_1+\omega_2)^2}{g} + k_+\tanh(k_+h)} \tag{4.38}$$

$$\gamma_{21}^{(+)} = \frac{-ig}{2\omega_2} \cdot \frac{k_2^2\left(1-\tanh^2(k_2h)\right) + 2k_2k_1\left(1+\tanh(k_2h)\tanh(k_1h)\right)}{\frac{(\omega_1+\omega_2)^2}{g} + k_+\tanh(k_+h)} \tag{4.39}$$

$$\gamma^{(+)} = \frac{1}{2}\left(\gamma_{12}^{(+)} + \gamma_{21}^{(+)}\right) \tag{4.40}$$

Here, z is the vertical coordinate (positive upwards, with $z = 0$ at the mean free surface). The vertical distribution of the second-order potential is expressed by Equation 4.41.

$$A_{\mathsf{xy}}^{(+)}(z) = \frac{\cosh(k_+(z+h))}{\cosh(k_+h)}, \quad A_z^{(+)}(z) = \frac{\sinh(k_+(z+h))}{\cosh(k_+h)} \tag{4.41}$$

The resulting Eulerian acceleration field due to the second-order potential is described by the following equation.

$$\vec{a}^{(+)}(\vec{r}) = \begin{bmatrix} \gamma^{(+)}A_{\mathsf{xy}}^{(+)}(k_1\cos\beta_1 + k_2\cos\beta_2) \\ \gamma^{(+)}A_{\mathsf{xy}}^{(+)}(k_1\sin\beta_1 + k_2\sin\beta_2) \\ i\gamma^{(+)}A_z^{(+)}k_+ \end{bmatrix} (\omega_1+\omega_2)\cdot\exp\left(-i\vec{k}_+\cdot\vec{r}\right) \tag{4.42}$$

The second-order dynamic pressure field is given by Equation 4.43.

$$p^{(+)}(\vec{r}) = -i\rho(\omega_1+\omega_2)\gamma^{(+)}A_{\mathsf{xy}}^{(+)}\exp\left(-i\vec{k}_+\cdot\vec{r}\right) \tag{4.43}$$

To compute the wave loads on the structure, the local particle acceleration and pressure are evaluated along each member of the structure. These quantities are used in the strip-theory framework to compute the distributed hydrodynamic forces by the following equation.

$$\vec{f}_{\mathsf{inertial}} = \rho\, v_i\left[(1+C_{a1})\mathbf{P}_1 + (1+C_{a2})\mathbf{P}_2\right]\vec{a}^{(+)} \tag{4.44}$$

Here, v_i is the submerged volume per unit length, C_{a1}, C_{a2} are the added mass coefficients in two principal directions, and $\mathbf{P}_1$, $\mathbf{P}_2$ are the associated projection matrices. In addition to the inertial force, the pressure-induced force is evaluated by Equation 4.45.

$$\vec{f}_{\mathsf{pressure}} = A\cdot p^{(+)}\cdot\vec{n} \tag{4.45}$$

Here, A is the cross-sectional area and $\vec{n}$ is the unit normal vector. An axial correction term is also included for axial surfaces to the waves, such as the pontoon surface.

$$\vec{f}_{\mathsf{axial}} = \rho\, v_i\, C_{a,\mathsf{end}}\cdot\mathbf{Q}\vec{a}^{(+)} \tag{4.46}$$

Here, $C_{a,\text{end}}$ is an end correction factor and $\mathbf{Q}$ is the projection matrix along the axial direction. The total second-order sum-frequency force per unit length is given by the following equation.

$$\vec{f}_{\text{2nd}}^{(+)} = \vec{f}_{\text{inertial}} + \vec{f}_{\text{pressure}} + \vec{f}_{\text{axial}} \tag{4.47}$$

Each local force vector is converted to a generalized force in 6 degrees of freedom with Equation 4.48.

$$\vec{F}_{\text{6DOF}} = \begin{bmatrix} \vec{f} \\ \vec{r} \times \vec{f} \end{bmatrix} \tag{4.48}$$

This contribution is integrated over the length of each member and added to the QTF matrix by Equation 4.49.

$$Q_{i_{DOF}}^{(+)}(\omega_i, \omega_j, \beta_h) \mathrel{+}= F_{i_{DOF}} \cdot \Delta z \tag{4.49}$$

To reduce computational cost, only the upper triangle of the QTF is computed. The lower triangle is filled by using the symmetry of the sum QTF and mirroring the upper triangle to the lower triangle. The complete QTF matrix is then used in Equation 4.35 to evaluate the total second-order sum-frequency wave excitation forces acting on the structure for an arbitrary wave spectrum and direction.

4.3.4. Dirlik Fatigue Estimation

This research focuses on the optimisation of the substructure of the floating wind turbine system. Accordingly, fatigue life constraints are imposed on the structural components. It is assumed that the most fatigue critical region of the substructure is the connection between the pontoon and the main column because this connection experiences large bending moments from the tendon tension variation.

Fatigue analysis is typically performed using cycle counting methods applied to time-domain stress signals. However, as this study does not utilise time-domain simulations, an alternative frequency-domain approach is adopted. Specifically, the Dirlik method is employed to estimate fatigue damage. This method is well-established in literature and has demonstrated both accuracy and robustness across a wide range of loading conditions and spectral shapes [7]. It is based on the spectral moments of dynamic stress fluctuations rather than explicit cycle counting. Additionally, mean stresses are taken into account with Goodman correction [18]. To estimate the mean stress and the stress variation spectrum at the critical connection point, the structural system is idealised as shown in Figure 4.7. The resulting balance of forces and moments at the pontoon-to-column interface is described by the following equations.

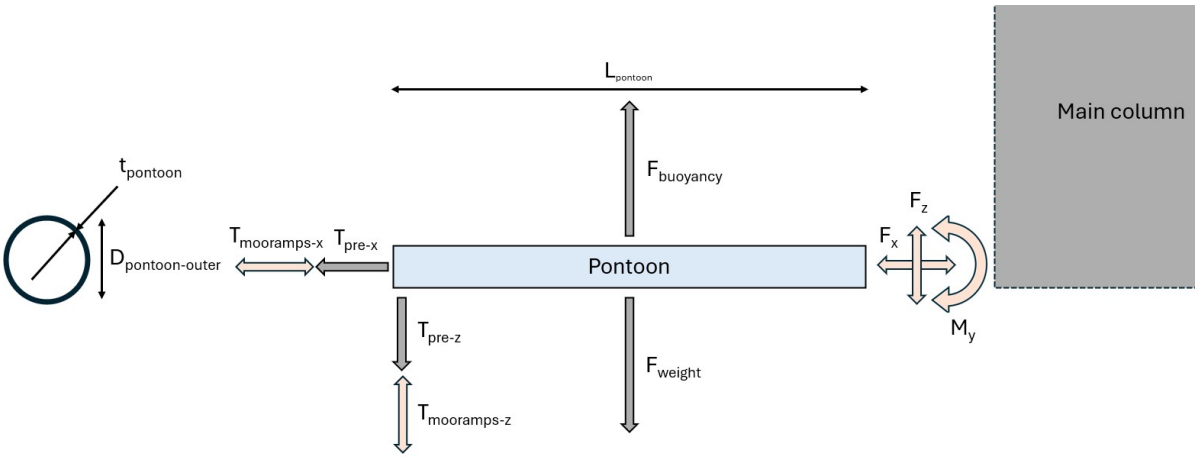

Figure 4.7: Schematic representation of varying loads on the pontoon-column connection.

$$\begin{aligned} F_{x_{mean}} &= T_{\text{pre}_x} & F_{x_{variable}} &= T'_{\text{moor,amp-}x} \\ F_{z_{mean}} &= T_{\text{pre}_z} + F_{\text{weight}} - F_{\text{Buoyancy}} & F_{z_{variable}} z' &= T'_{\text{moor,amp-}z} \\ M_{y_{mean}} &= T_{\text{pre}_z} \cdot L_{\text{pontoon}} + (F_{\text{weight}} - F_{\text{Buoyancy}}) \cdot \frac{L_{\text{pontoon}}}{2} & M_{y_{variable}} &= T'_{\text{moor,amp-}z} \cdot L'_{\text{pontoon}} \end{aligned} \tag{4.50}$$

Using the force and moment balance above, the corresponding stress components at the connection point are calculated as follows.

$$\begin{aligned} \sigma_{yy} = \frac{0.5 D_o M_y}{I}, \quad \sigma_{\text{axial}} = \frac{F_x}{A}, \quad \tau_z = \frac{F_z}{A}, \\ I = \frac{\pi}{64}(D_o^4 - D_i^4), \quad A = \frac{\pi}{4}(D_o^2 - D_i^2), \end{aligned} \tag{4.51}$$

The total stress range is computed using the von Mises criterion, with appropriate stress concentration factors (SCFs) applied to account for geometric discontinuities at the welded joint. These SCFs are detailed in Appendix B. The von mises stress is determined for both the dynamic and the mean stress, where the dynamic stress depends on frequency and the mean stress is constant.

$$\sigma_{\text{vm}}(\omega) = \sqrt{(\sigma_{yy}(\omega) \cdot SCF_{\text{bending}})^2 + (\sigma_{\text{axial}}(\omega) \cdot SCF_{\text{axial}})^2 + 3\tau_z(\omega)^2} \tag{4.52}$$

Using the dynamic stress at the critical location, the probability density function (pdf) of stress ranges is derived via the Dirlik method, which utilises the first four spectral moments of the stress power spectral density. The resulting pdf is given by Equation 4.53 where the different variables are defined in Equation 4.54.

$$\text{pdf}(Z) = \frac{1}{2\sqrt{m_0}} \left[\frac{D_1}{Q} e^{-\frac{Z}{Q}} + \frac{D_2 Z}{R^2} e^{-\frac{Z^2}{2R^2}} + D_3 Z e^{-\frac{Z^2}{2}} \right] \tag{4.53}$$

$$\begin{aligned} x_m = \frac{m_1}{m_0}\sqrt{\frac{m_2}{m_4}}, \quad \alpha_1 = \frac{m_1}{\sqrt{m_0 m_2}}, \quad \alpha_2 = \frac{m_2}{\sqrt{m_0 m_4}}, \\ D_1 = \frac{2(x_m - \alpha_2^2)}{1 + \alpha_2^2}, \quad D_2 = \frac{1 - \alpha_2 - D_1 + D_1^2}{1 - R}, \quad D_3 = 1 - D_1 - D_2, \\ R = \frac{\alpha_2 - x_m - D_1^2}{1 - \alpha_2 - D_1 + D_1^2}, \quad Q = 1.25 \cdot \frac{\alpha_2 - D_3 - D_2 R}{D_1}, \quad Z = \frac{S}{2\sqrt{m_0}} \end{aligned} \tag{4.54}$$

With this probability density function, the expected number of cycles at each stress range Z can be calculated by Equation 4.55 where T is the exposure time and f_p is the peak crossing frequency, defined by Equation 4.56.

$$n_{\text{cycles}}(Z) = f_p \cdot T \cdot \text{pdf}(Z) \tag{4.55}$$

$$f_p = \sqrt{\frac{m_4}{m_2}} \tag{4.56}$$

To compute the number of cycles to failure for each stress range, the SN-curve given in DNV-RP-C302 for welded joints under water is used which is expressed in Equation 4.57.

$$N(S) = \begin{cases} 10^{15.091 - 5\log_{10}(S)}, & \text{if } S < 65.816\,\text{MPa} \\ 10^{11.455 - 3\log_{10}(S)}, & \text{if } S \geq 65.816\,\text{MPa} \end{cases} \tag{4.57}$$

Here S is the stress range which is corrected for due to the mean stress component by the goodman correction described in Equation 4.58.

$$S_{corrected} = \frac{S}{1 - \frac{\sigma_{vm-mean}}{\sigma_y}} \tag{4.58}$$

Finally, the total fatigue damage over all stress ranges is obtained using Miner's rule.

$$D_{\text{tot}} = \sum \frac{n_{\text{cycles}}(Z)}{N(Z)} \tag{4.59}$$

If $D_{\text{tot}} < 1$, the connection is considered to have sufficient fatigue life over the design lifetime. The use of the Dirlik method in this context allows for efficient frequency-domain fatigue estimation and identifying designs which perform well in terms of fatigue while maintaining acceptable accuracy in the absence of time-domain simulations.

4.4. OrcaFlex Validation Model

To assess whether the RAFT model produces physically meaningful results and to determine the suitability for the optimisation study, a validation model is constructed using OrcaFlex. OrcaFlex is an industry-standard software tool widely used in offshore engineering. It is considered validated, making it a suitable software for model comparison. The OrcaFlex validation model is constructed in two main steps.

- Performing an OrcaWave analysis.
- Building and simulating the OrcaFlex simulation model.

4.4.1. OrcaWave Analysis

To validate the slender body approximation and the implementation of sum-frequency forces in RAFT, an OrcaWave diffraction analysis is performed. The structure was first reconstructed and meshed in Fusion 360, as shown in Figure 4.8. The resulting mesh was then imported into OrcaWave for hydrodynamic analysis using the wave frequency and heading conditions listed in Table 4.12.

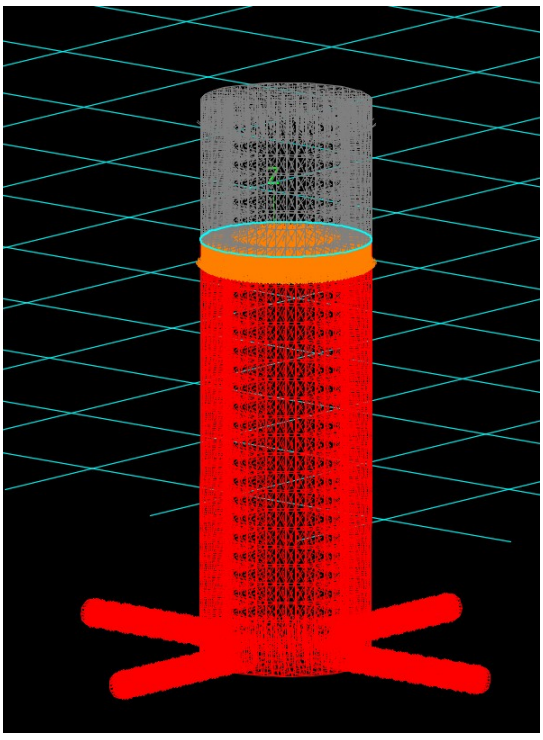

Figure 4.8: Wave mesh used in OrcaWave analysis.

Table 4.12: Frequency and heading values used in the OrcaWave analysis.

Frequency [rad/s]	Heading [deg]
0.25	0
0.50	45
0.75	90
1.00	135
1.25	180
1.50	225
1.75	260
2.00	305
2.25	360
2.50	
2.75	
3.00	
3.25	
3.50	

4.4.2. OrcaFlex Simulation Model

The Orcaflex simulation model is constructed by first implementing the rigid platform geometry. The platform is moored to the seabed using `Link` elements, which are massless, have no bending stiffness and possess only linear axial stiffness which is consistent with the RAFT implementation. The tower is modelled using a `Line` object with the same discretisation and physical properties as the tower in RAFT. On top of the tower, the IEA 15 MW reference turbine is placed using the built-in `Turbine` object, including a controller and Blade Element Momentum (BEM) aerodynamic modelling. A visual representation of the full simulation setup is shown in Figure 4.9.

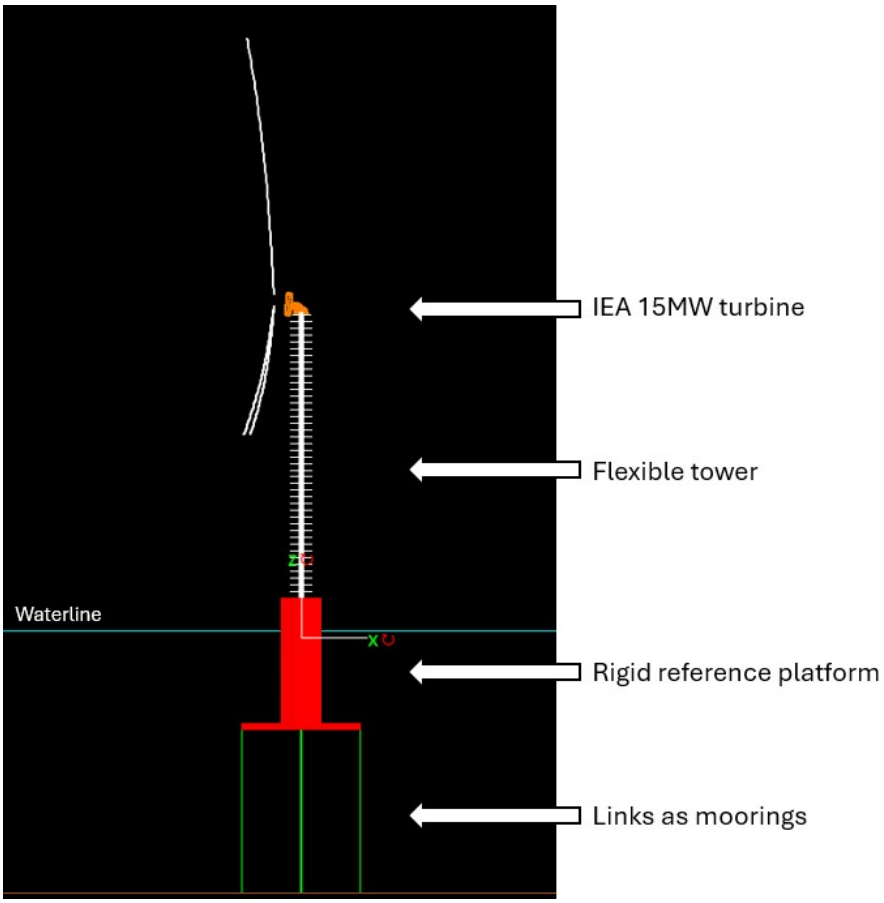

Figure 4.9: Representation of the `OrcaFlex` simulation model.

This simulation model is used to run one-hour time-domain simulations with the same spectral inputs of irregular waves and turbulent wind to ensure that the amount of spectral energy put into the system is the same for both models. The resulting time series are processed via Fast Fourier Transform (FFT) to obtain power spectral densities and statistical response data, which can then be directly compared with RAFT outputs for validation purposes.

5

RAFT Model Validation

To validate the newly implemented features and the simulation results produced by RAFT, a systematic validation study was conducted. This study involved comparisons with a reference model developed in OrcaFlex. In order to give a complete overview the following comparison steps were performed.

- **Modal analysis comparison:** Comparison of the newly implemented modal analysis extension in RAFT against the modal analysis results obtained from OrcaFlex.
- **Quasi-static response comparison:** Assessment of the platform's static equilibrium response under varying nacelle thrust loads, comparing RAFT and OrcaFlex outputs.
- **Wave loading comparison:** Evaluation of the dynamic platform response under wave excitation in two scenarios where the first one only includes first-order wave forces and the second one includes both first- and second-order wave forces. In addition, a comparison study is performed to asses the implementation of sum-frequency forces in RAFT.
- **Wind–wave loading comparison:** Analysis of the system response under combined wind and wave excitation, also conducted in two stages where the first one includes wind and first-order waves and the second one includes wind, first-order and second-order waves.
- **Added mass and damping comparison:** Comparison of the results with RAFT's linearised hydrodynamic coefficients against frequency dependent hydrodynamic coefficients from Orcwave.
- **Tendon angle influence:** The influence of tendon angle on response is assessed, where a comparison is made using the base case with tendons inclined at $80°$.
- **Modelling Effects, Consequences & Limitations:** Evaluation of the consequences of linearising TLPWTs in the current RAFT setup and limitations for the overall fidelity and applicability of RAFT in the optimisation framework.

5.1. Modal Analysis Comparison

Table 5.1 presents a comparison between the dominant modes identified in RAFT and OrcaFlex, which are visualised with magnified excursions in Figure 5.1 and Figure 5.2. These two modes were specifically selected because they dominate the degrees of freedom assessed in this research and are located near the excitation force frequency ranges. Since the TLP is a relatively stiff structure, the higher-order modes occur at significantly higher frequencies and are thus less likely to be excited under operational conditions. This will also become evident in the remainder of this comparison study.

Overall, RAFT and OrcaFlex exhibit comparable modal characteristics. A slight discrepancy is observed in the first pitch-bending frequency, suggesting that the RAFT model has a slightly stiffer structure in pitch-bending compared to Orcaflex. Nonetheless, the differences remain small and are not expected to significantly affect the dynamic response predictions in the frequency ranges of interest. This comparison shows that the implementation of a flexible turbine tower in RAFT is in line with the Orcaflex results.

Table 5.1: Comparison of dominant modes between RAFT and OrcaFlex.

Mode	RAFT [s]	OrcaFlex [s]	Δ [%]
Surge	31.02	31.02	-0.02
1st Pitch-Bending	3.67	3.85	4.72

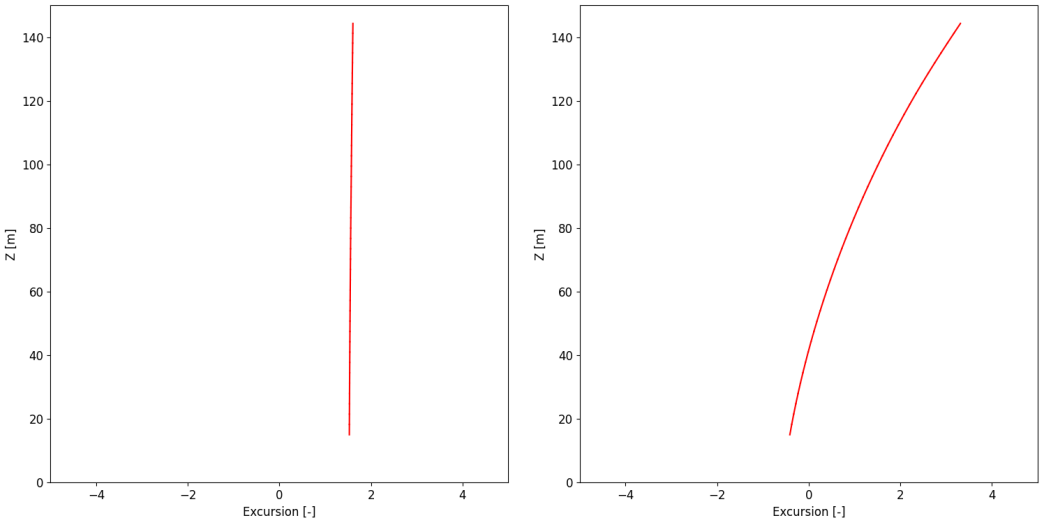

Figure 5.1: A visual representation of the governing mode shapes in RAFT.

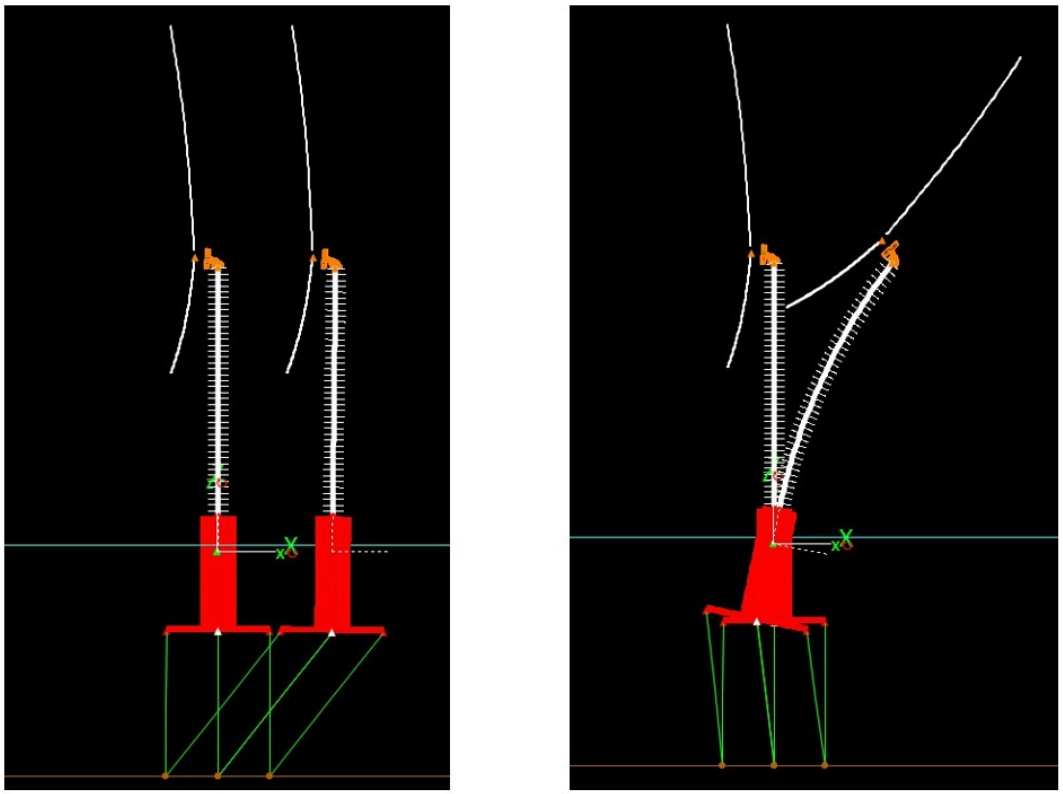

Figure 5.2: A visual representation of the governing mode shapes in Orcaflex.

5.2. Quasi-static Comparison

Following the modal analysis comparison, a quasi-static comparison was performed to assess the accuracy of the tension leg specific quasi-static solver for the mooring system, which was added in this research implemented in both MoorPy and RAFT. To carry out this validation, a range of mean thrust loads is applied at the nacelle from which the resulting platform responses in surge, heave, pitch and fore-aft tendon tensions are compared between RAFT and OrcaFlex. The applied loading spans from the thrust at cut-in wind speed up to 1.5 times the thrust at rated wind speed. Although thrust levels beyond approximately 2.75 MN are not expected to occur in real operational conditions, they are included in the analysis to evaluate the robustness of the quasi-static solver under extreme scenarios. The results of this comparison are shown in Figure 5.3.

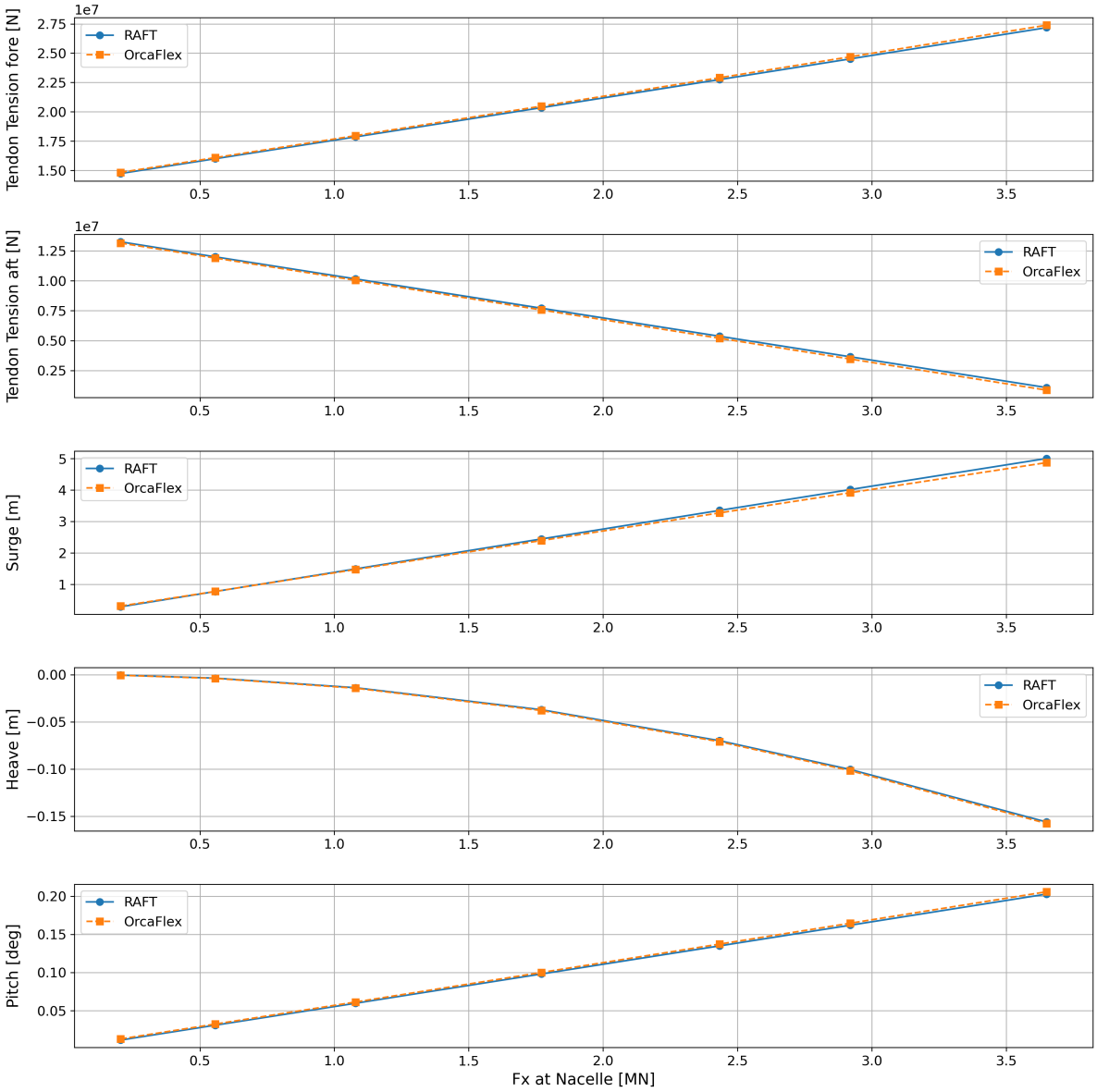

Figure 5.3: Comparison of quasi-static analysis between RAFT and OrcaFlex.

The results demonstrate a strong agreement between RAFT and OrcaFlex, confirming the accuracy of the newly implemented quasi-static formulation in RAFT/MoorPy. Additionally, the non-linear trend in heave displacement with increasing load is noteworthy and aligns with similar observations reported in literature [98].

5.3. Wave Case Comparison

After the quasi-static comparison, RAFT's performance under wave loading was assessed. This dynamic comparisons study was done for both a mild and an extreme sea state, under the assumption that these cases sufficiently span the range of operational conditions and thus serve to validate the RAFT model's dynamic accuracy. Before continuing with this dynamic analysis, several important remarks should be made. The dynamic validation is based on a statistical comparison between OrcaFlex and RAFT. The following variables, related to the dynamic constraints in the optimisation framework, are selected for comparison.

- Surge and pitch motions at both the floater and the hub, as these are the dominant degrees of freedom under the unidirectional load cases considered in this study.
- Fore and aft tendon tensions, which are critical for assessing the risk of exceeding the maximum allowable tendon tension and identifying potential slack events. In the system under investigation, the fore tendon typically experiences the highest tensions, while the aft tendon is subjected to the lowest tensions.
- Nacelle acceleration in surge direction, as it is a key parameter in turbine generator design which relates to turbine performance and fatigue.

The statistics of these response variables are compared using tables such as Table 5.2. These tables present the mean values, standard deviations and the corresponding maxima and minima. Additionally, the relative differences between RAFT and Orcaflex are shown for the standard deviations, providing insight into differences in the dynamic response, and the maxima and minima, providing insight into the overall differences. The relative differences are computed using Equation 5.1, where a negative value indicates that RAFT overestimates the response relative to OrcaFlex, while a positive value indicates that RAFT underestimates OrcaFlex.

$$\Delta_{\text{rel}}[\%] = \frac{\text{OrcaFlex} - \text{RAFT}}{\text{OrcaFlex}} \tag{5.1}$$

Discrepancies between the statistical results of OrcaFlex and RAFT are further analysed using the corresponding power spectral densities (PSDs). A selection of relevant PSDs is shown, but additional PSDs for load cases used in this validation study are provided in Appendix C. Next to this, several assumptions and boundary conditions are important to note.

- RAFT and the Orcaflex model have identical input spectral energy distributions for the wind and wave spectra.
- In the two models, the same constant added mass is applied and viscous damping values are approximately equal.
- The Orcaflex PSDs are constructed from one-hour OrcaFlex time-domain simulations.

5.3.1. Comparison with First-order Waves

Table 5.2 shows the statistical comparison between RAFT and OrcaFlex subjected to first-order wave loading. The results show relatively good agreement. However, it can be observed that with increasing wave height, RAFT increasingly overestimates the pitch response, as highlighted in Table 5.2.

Since pitch motion and tendon tensions are closely related, this also leads RAFT to overestimate the maximum tendon tension and underestimate the minimum tendon tension. This trend is further illustrated in Figure 5.4, which shows that RAFT overestimates the pitch response, mainly caused by the coupling between surge and pitch motions. To further elaborate on this, Figure 5.5 shows how the surge stiffness increases non-linearly with platform excursion. Because RAFT assumes linear stiffness, it underestimates the effective surge stiffness at larger displacements. This leads to an overestimation of the surge response, which in turn causes an overestimation of the pitch response due to surge–pitch coupling. This highlights a consequence and therefore also a limitation of RAFT's linearised approach.

In this comparison, the main difference between the RAFT and OrcaFlex models is this non-linearity of the mooring system, which is fully captured in OrcaFlex time domain simulations. Therefore, this analysis not only compares the RAFT response to Orcaflex response under first order waves, but also

provides insight into the effects of linearising mooring stiffness. This shows that linearising the mooring system can cause discrepancies up to $\pm$ 10% compared to non-linear time domain simulations for the current base case configuration.

Table 5.2: Statistical comparison of RAFT and OrcaFlex simulations under first-order wave loading with $H_s = 2$ [m], $T_p = 7.94$ [s] and $H_s = 5$ [m], $T_p = 10.34$ [s] with $V_w = 0$ [m/s].

Hs	Vw	Quantity	Unit	Mean_RAFT	Mean_OrcaFlex	Std_RAFT	Std_OrcaFlex	Δ Std [%]	Max_RAFT	Max_OrcaFlex	Min_RAFT	Min_OrcaFlex	Δ Max [%]	Δ Min [%]
2	0	Surge (platform)	m	0.00	0.00	0.19	0.18	-5.07	0.56	0.53	-0.56	-0.53	-5.08	5.05
2	0	Pitch (platform)	deg	0.00	0.00	0.00	0.00	0.77	0.01	0.01	-0.01	-0.01	0.79	-0.75
2	0	Surge (hub)	m	0.00	0.00	0.22	0.22	-2.71	0.66	0.65	-0.66	-0.65	-2.71	2.70
2	0	Pitch (hub)	deg	0.00	0.00	0.03	0.03	5.50	0.08	0.09	-0.08	-0.09	5.53	-5.48
2	0	Downwind tendon	kN	14000.00	13995.21	306.64	312.43	1.85	14919.93	14932.51	13080.07	13057.91	0.08	-0.17
2	0	Upwind tendon	kN	14000.00	13995.58	306.63	307.09	0.15	14919.90	14916.84	13080.10	13074.32	-0.02	-0.04
2	0	RNA accel. (X)	m/s^2	0.00	0.00	0.14	0.14	-0.29	0.42	0.42	-0.42	-0.42	-0.32	0.26
5	0	Surge (platform)	m	0.00	0.00	0.78	0.76	-3.50	2.35	2.26	-2.35	-2.27	-3.64	3.36
5	0	Pitch (platform)	deg	0.00	0.00	0.02	0.02	-9.44	0.05	0.05	-0.05	-0.05	-9.47	9.40
5	0	Surge (hub)	m	0.00	0.00	0.88	0.87	-1.74	2.65	2.60	-2.65	-2.61	-1.86	1.62
5	0	Pitch (hub)	deg	0.00	0.00	0.08	0.08	2.32	0.23	0.23	-0.23	-0.23	2.33	-2.31
5	0	Downwind tendon	kN	14000.00	13999.19	1097.98	1020.12	-7.63	17293.93	17059.56	10706.07	10938.82	-1.37	2.13
5	0	Upwind tendon	kN	14000.00	13997.22	1097.96	998.35	-9.98	17293.87	16992.26	10706.13	11002.18	-1.77	2.69
5	0	RNA accel. (X)	m/s^2	0.00	0.00	0.37	0.37	-2.04	1.12	1.10	-1.12	-1.10	-2.07	2.01

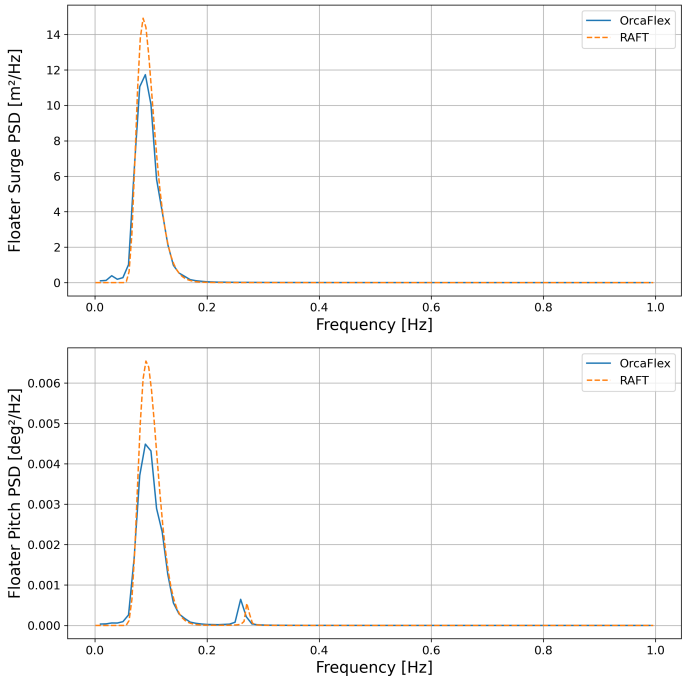

(a) Floater surge and pitch PSD.

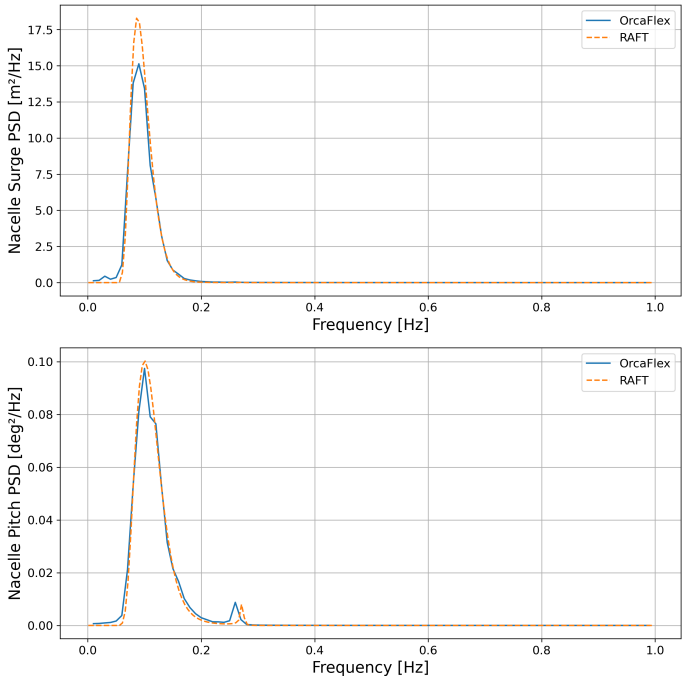

(b) Nacelle surge and pitch PSD.

Figure 5.4: Power spectral density comparisons at $H_s = 5$ [m], $T_p = 10.34$ [s], $V_w = 0$ [m/s] subjected to first-order waves (continued on next page).

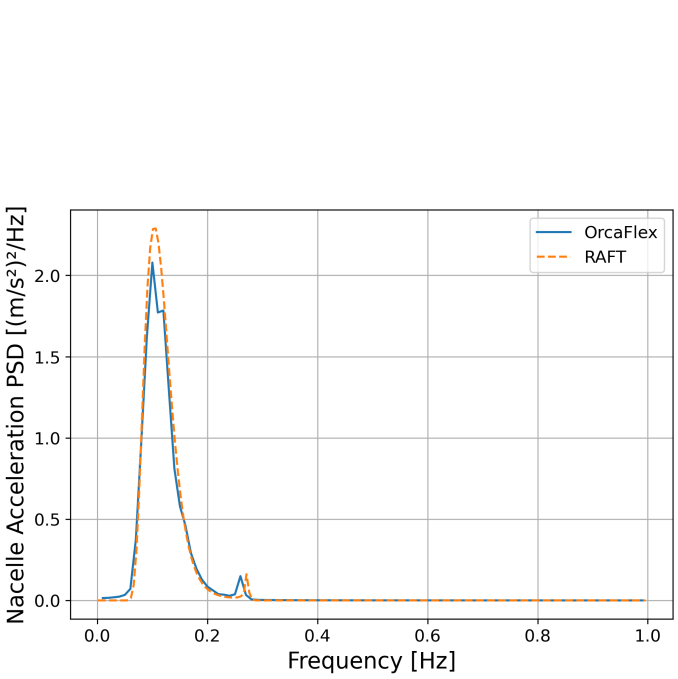

(c) Nacelle acceleration PSD.

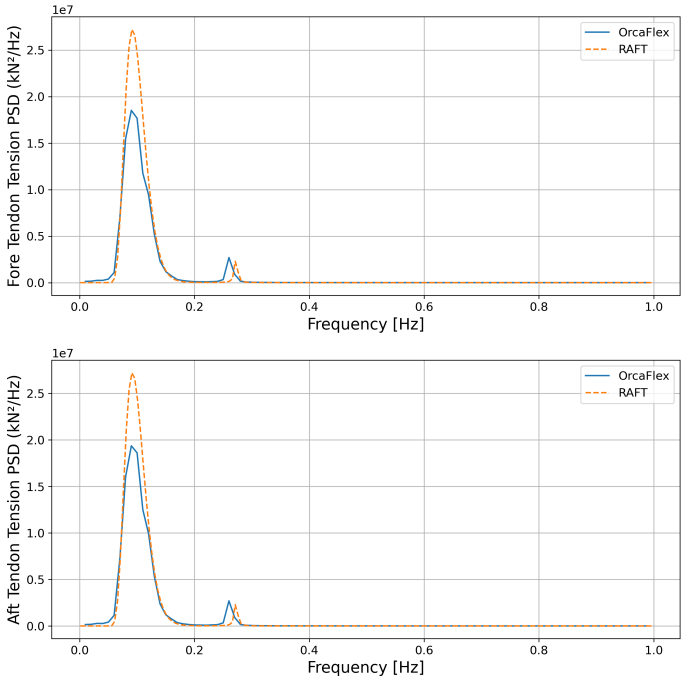

(d) Fore and aft tendon tension PSD.

Figure 5.4: (continued) Power spectral density comparisons at $H_s = 5$ [m], $T_p = 10.34$ [s], $V_w = 0$ [m/s] subjected to first-order waves.

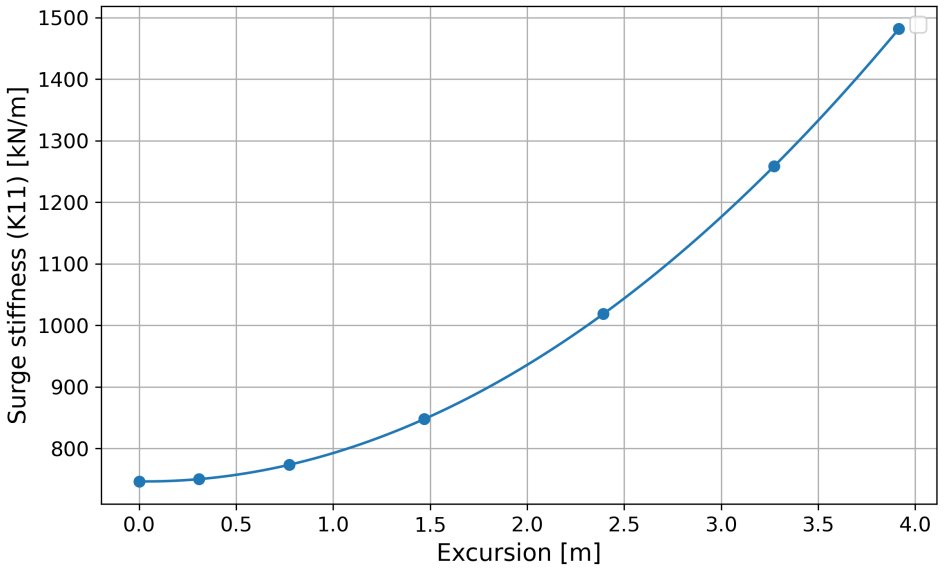

Figure 5.5: The surge stiffness (K_{11}) with increasing excursion.

5.3.2. Comparison with First- & Second-order Waves

When introducing second-order wave loading, the primary difference compared to the first-order case is that RAFT underestimates the surge response by approximately 8%, as highlighted in Table 5.3. As shown in Figure 5.6, this underestimation originates from the fact that RAFT produces a narrower response peak at the second-order difference-frequency excitation frequency.

This observation may indicate two contributing factors. First, RAFT may have slightly lower damping than OrcaFlex, resulting in a sharper but taller response peak at the difference-frequency. Determining and applying the same damping for both models remains a challenge experienced also in other studies [13]. Second, the discrepancy could originate from RAFT overestimating the second-order difference-frequency excitation forces compared to OrcaFlex. This is consistent with previous studies that employed a similar approximation method for modelling second-order loads [13].

Table 5.3: Statistical comparison of RAFT and OrcaFlex simulations under first-order wave loading with $H_s = 2$ [m], $T_p = 7.94$ [s] and $H_s = 5$ [m], $T_p = 10.34$ [s] with $V_w = 0$ [m/s].

Hs	Vw	Quantity	Unit	Mean_RAFT	Mean_OrcaFlex	Std_RAFT	Std_OrcaFlex	Δ Std [%]	Max_RAFT	Max_OrcaFlex	Min_RAFT	Min_OrcaFlex	Δ Max [%]	Δ Min [%]
2	0	Surge (platform)	m	0.00	0.00	0.19	0.18	-5.07	0.56	0.53	-0.56	-0.53	-5.08	5.05
2	0	Pitch (platform)	deg	0.00	0.00	0.00	0.00	0.77	0.01	0.01	-0.01	-0.01	0.79	-0.75
2	0	Surge (hub)	m	0.00	0.00	0.22	0.22	-2.71	0.66	0.65	-0.66	-0.65	-2.71	2.70
2	0	Pitch (hub)	deg	0.00	0.00	0.03	0.03	5.50	0.08	0.09	-0.08	-0.09	5.53	-5.48
2	0	Downwind tendon	kN	14000.00	13995.21	306.64	312.43	1.85	14919.93	14932.51	13080.07	13057.91	0.08	-0.17
2	0	Upwind tendon	kN	14000.00	13995.58	306.63	307.09	0.15	14919.90	14916.84	13080.10	13074.32	-0.02	-0.04
2	0	RNA accel. (X)	m/s^2	0.00	0.00	0.14	0.14	-0.29	0.42	0.42	-0.42	-0.42	-0.32	0.26
5	0	Surge (platform)	m	0.00	0.00	0.78	0.76	-3.50	2.35	2.26	-2.35	-2.27	-3.64	3.36
5	0	Pitch (platform)	deg	0.00	0.00	0.02	0.02	-9.44	0.05	0.05	-0.05	-0.05	-9.47	9.40
5	0	Surge (hub)	m	0.00	0.00	0.88	0.87	-1.74	2.65	2.60	-2.65	-2.61	-1.86	1.62
5	0	Pitch (hub)	deg	0.00	0.00	0.08	0.08	2.32	0.23	0.23	-0.23	-0.23	2.33	-2.31
5	0	Downwind tendon	kN	14000.00	13999.19	1097.98	1020.12	-7.63	17293.93	17059.56	10706.07	10938.82	-1.37	2.13
5	0	Upwind tendon	kN	14000.00	13997.22	1097.96	998.35	-9.98	17293.87	16992.26	10706.13	11002.18	-1.77	2.69
5	0	RNA accel. (X)	m/s^2	0.00	0.00	0.37	0.37	-2.04	1.12	1.10	-1.12	-1.10	-2.07	2.01

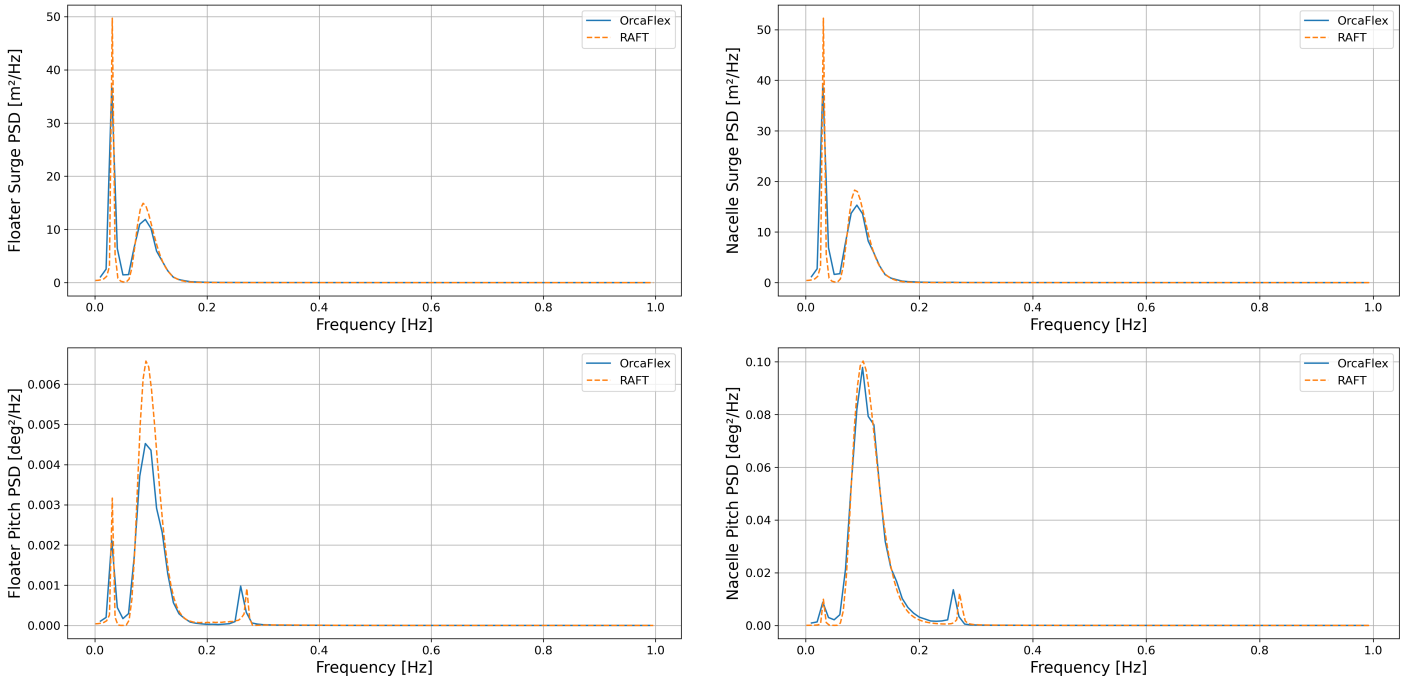

(a) Floater surge and pitch PSD.

(b) Nacelle surge and pitch PSD.

Figure 5.6: Power spectral density comparisons at $H_s = 5$ [m], $T_p = 10.34$ [s], $V_w = 0$ [m/s] subjected to first- and second-order waves (continued on next page).

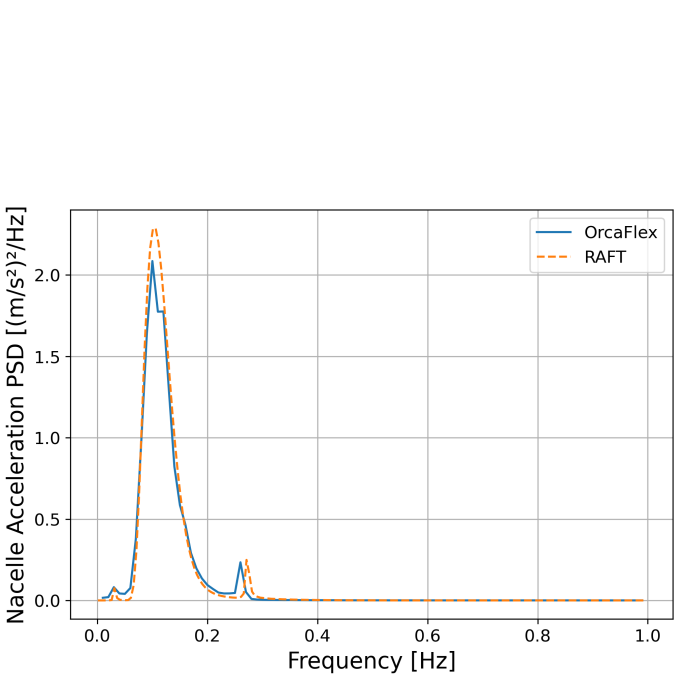

(c) Nacelle acceleration PSD.

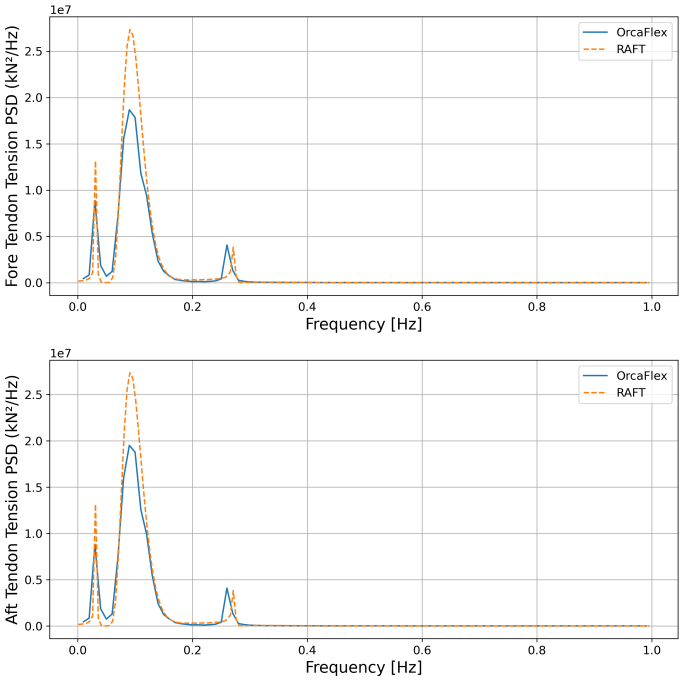

(d) Fore and aft tendon tension PSD.

Figure 5.6: (continued) Power spectral density comparisons at $H_s = 5$ [m], $T_p = 10.34$ [s], $V_w = 0$ [m/s] subjected to first- and second-order waves.

Sum-Frequency Force Contribution

The sum-frequency force contribution is present but of negligible impact for this particular floater design as can be seen when comparing Figure 5.4 with Figure 5.6. It can be seen that the pitch response at approximately 0.27 [Hz] increases with about 30% from 0.0007 to 0.001 [deg^2/Hz]. However, compared to the first-order wave peak this remains negligible. For other designs, the contribution of sum-frequency forces may become significant and therefore, the implementation of sum-frequency forcing in RAFT is further researched in this section. In Figure 5.7, it can be seen that the accuracy of the sum-frequency force approximation is relatively accurate compared to the sum frequency force calculation by full diffraction and on-linear time domain analysis. However, the contribution remains small compared to the first-order forcing which can seen in in the lower and zoomed in graph in Figure 5.7.

The discrepancy in the sum-frequency force calculation originates from the limitations of the Rainey approximation, which is primarily accurate for low ka values, where k is the wave number and a is the cylinder radius. This highlights a known limitation of the sum-frequency force model in RAFT for this specific floater geometry. Figure 5.8 compares the surge sum-frequency force calculated using the Rainey approximation with results from other semi-analytical methods and a CFD-based approach. The figure illustrates that as ka increases, the Rainey approximation significantly overestimates the sum-frequency force. For reference, the ka value is 0.338 for the current base case design with the load case corresponding to Figure 5.7. This value explains the observed overestimation in RAFT and aligns with findings in previous literature [94].

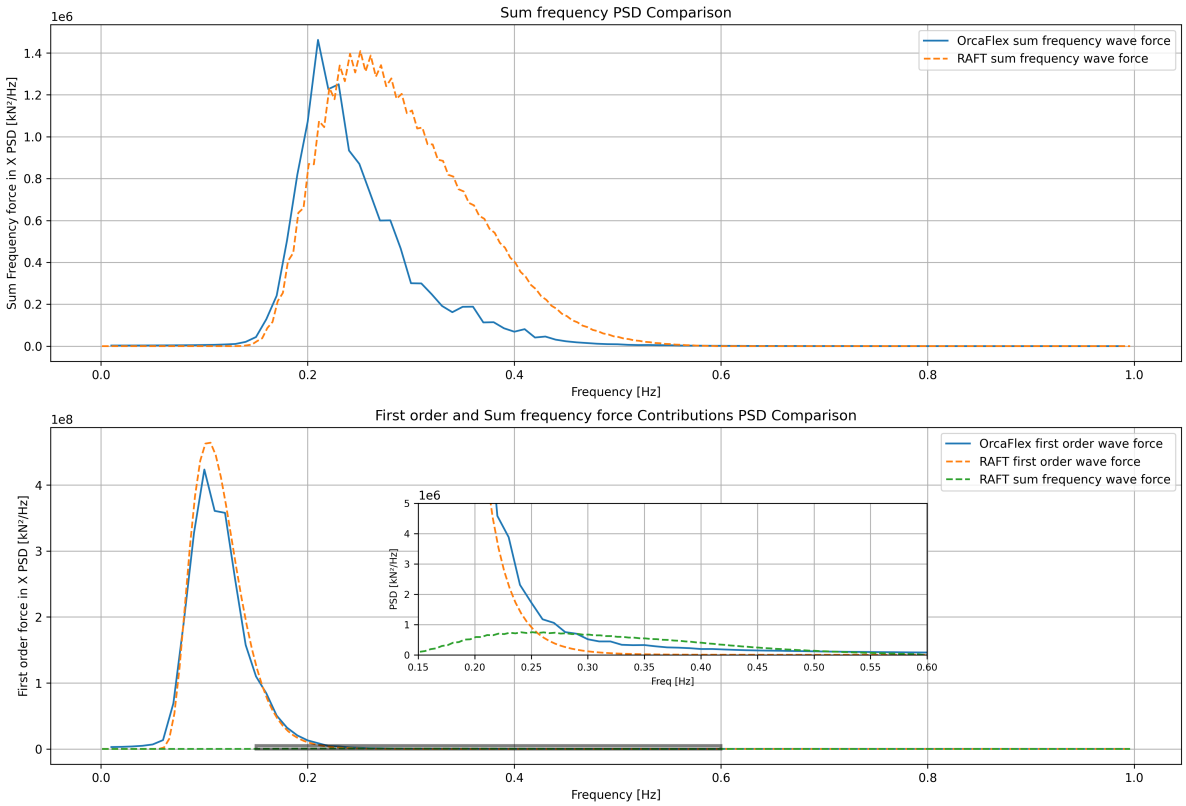

Figure 5.7: A sum-frequency force comparison between RAFT and Orcaflex for $H_s = 5$ [m], $T_p = 10.34$ [s], $V_W = 0$ [m/s].

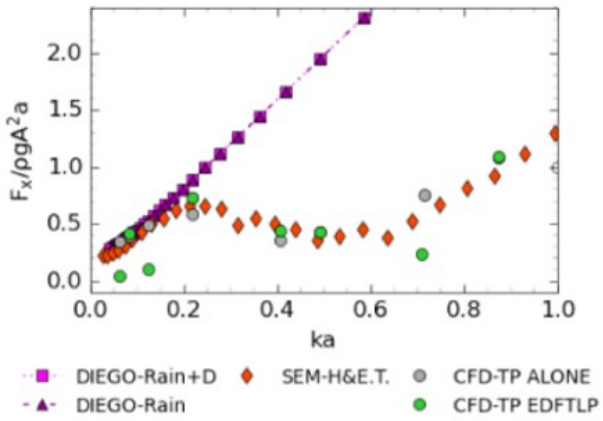

Figure 5.8: The sum-frequency force in surge (x) for different calculation methods [94].

Since the sum-frequency forces are several orders of magnitude smaller than the first-order wave forces and the differences with the OrcaFlex calculations remain within an acceptable margin, the current sum-frequency approximation is considered sufficient for the purpose of this study to take into account the influence of sum-frequency forces for TLP design. Next to this, RAFT tends to overestimate the contribution of sum-frequency forces, which results in more conservative design results instead of design results which, with more accurate analysis, would not meet the constraints.

5.4. Wind/Wave Case Comparison

After comparing the wave-only load cases between RAFT and OrcaFlex, where all discrepancies remain within a 10% error margin, wind loading is introduced to further evaluate the RAFT model. The addition of aerodynamic forcing leads to larger platform offsets and more complex coupled dynamics. First, the effect of wind loads in combination with first-order wave loading is assessed. After this, the full combination of first- and second-order wave loading together with wind loading is analysed to evaluate RAFT's performance under realistic and operational conditions.

5.4.1. Comparison with First-order Waves & Wind

Table 5.4 presents the statistical comparison between RAFT and OrcaFlex for two wind load cases. One load case has a moderate wind speed and one near the rated wind speed. It becomes clear that the dynamic discrepancies between RAFT and OrcaFlex increase significantly compared to the results without wind loading.

At lower wind speeds, RAFT underestimates both surge and pitch motions by approximately 20%, which also leads to an underestimation of tendon tensions. As the wind speed increases, RAFT continues to underestimate the dynamic surge response up to 30%, but starts to overestimate the pitch response. This shift indicates an increasing difference of RAFT's aerodynamic load modelling and coupled response prediction.

Table 5.4: Statistical comparison of RAFT and OrcaFlex simulations under first-order wave and wind loading with $H_s = 1$ [m], $T_p = 7.22$ [s], $V_w = 5$ [m/s] and $H_s = 2$ [m], $T_p = 7.94$ [s], $V_w = 13$ [m/s].

Hs	Vw	Variable	Unit	Mean_RAFT	Mean_OrcaFlex	Std_RAFT	Std_OrcaFlex	STD [%]	Max_RAFT	Max_OrcaFlex	Min_RAFT	Min_OrcaFlex	△Max [%]	△Min [%]
1	5	Surge (platform)	m	0.81	0.81	0.24	0.30	20.44	1.52	1.70	0.11	-0.07	10.76	-241.37
1	5	Pitch (platform)	deg	0.03	0.03	0.01	0.01	20.09	0.06	0.07	0.01	0.00	10.15	-729.38
1	5	Surge (hub)	m	1.05	1.02	0.28	0.36	22.12	1.89	2.11	0.20	-0.06	10.14	-416.78
1	5	Pitch (hub)	deg	0.12	0.12	0.03	0.04	18.39	0.22	0.24	0.01	-0.01	10.01	-292.66
1	5	Downwind tendon	kN	11921.36	11815.66	570.02	712.35	19.98	13631.44	13952.69	10211.29	9678.62	2.30	-5.50
1	5	Upwind tendon	kN	16085.77	16182.30	569.96	715.96	20.39	17795.64	18330.17	14375.90	14034.43	2.92	-2.43
1	5	RNA accel. (X)	m/s^2	0.02	0.00	0.07	0.07	-3.11	0.23	0.20	-0.19	-0.20	-12.88	-6.66
2	13	Surge (platform)	m	2.09	2.01	0.52	0.76	30.78	3.66	4.27	0.52	-0.26	14.39	-296.73
2	13	Pitch (platform)	deg	0.08	0.07	0.02	0.02	-10.99	0.14	0.12	0.03	0.03	-13.06	-20.54
2	13	Surge (hub)	m	2.70	2.52	0.60	0.83	26.93	4.51	5.00	0.89	0.05	9.80	-1771.45
2	13	Pitch (hub)	deg	0.30	0.26	0.07	0.06	-10.81	0.49	0.44	0.10	0.09	-11.80	-15.87
2	13	Downwind tendon	kN	8623.20	8616.26	1124.24	1007.50	-11.59	11995.94	11638.75	5250.47	5593.76	-3.07	6.14
2	13	Upwind tendon	kN	19424.60	19420.79	1125.03	1019.23	-10.38	22799.68	22478.50	16049.52	16363.09	-1.43	1.92
2	13	RNA accel. (X)	m/s^2	0.05	0.00	0.14	0.14	-2.17	0.47	0.41	-0.37	-0.41	-14.48	-10.13

Figure 5.9 presents the power spectral densities of RAFT and OrcaFlex for a case with $Hs = 1$ [m], $Tp = 7.22$ [s], $Vw = 5$ [m/s]. The figure demonstrates that RAFT captures the first-order wave response accurately. However, the introduction of wind loading results in a narrower PSD with higher peaks in the RAFT model. This corresponds to a smaller area under the PSD curve, indicating reduced overall dynamic energy in both pitch and surge responses. This difference arises primarily from the linearisation of the turbine controller and wind loading in RAFT. In contrast, OrcaFlex employs a nonlinear controller and wind model, which introduces broader spectral energy distribution. As a result, more energy is present near the system's natural frequencies, leading to increased excitations.

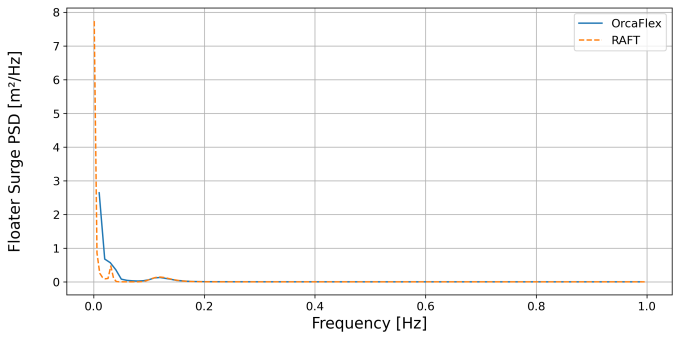

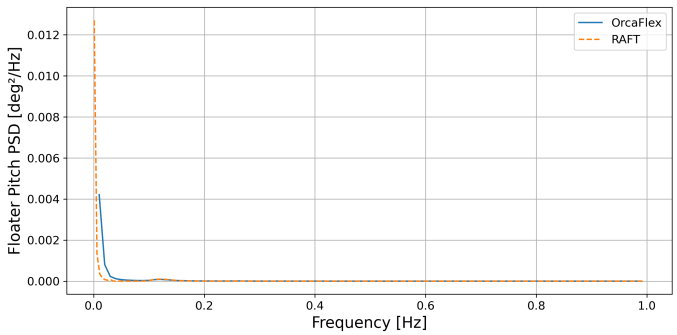

(a) Floater surge and pitch PSD.

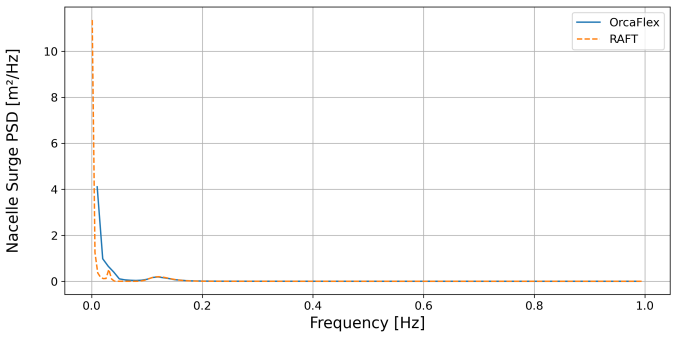

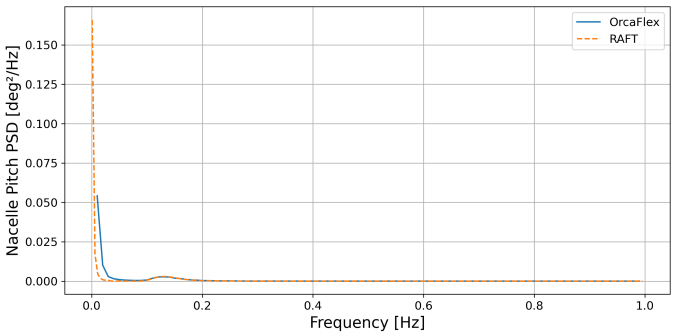

(b) Nacelle surge and pitch PSD.

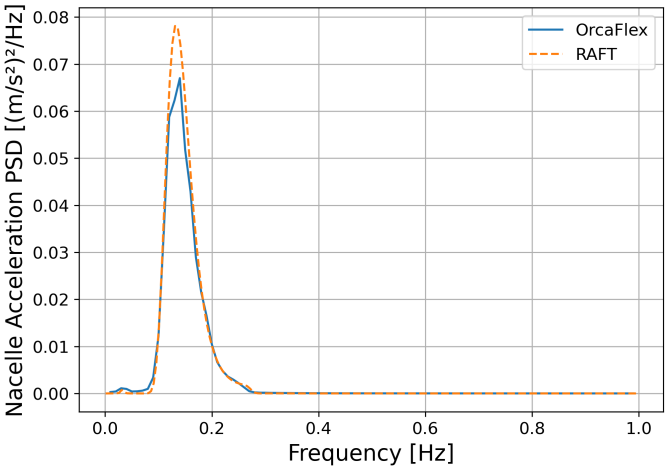

(c) Nacelle acceleration PSD.

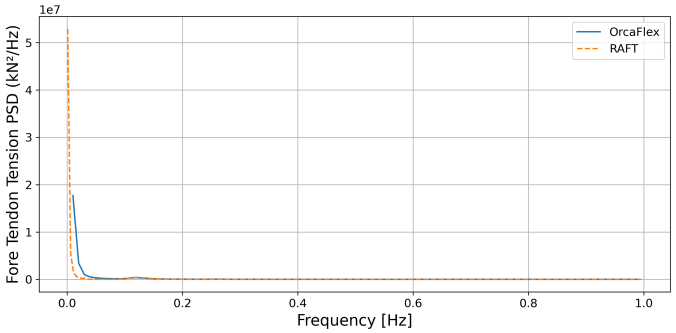

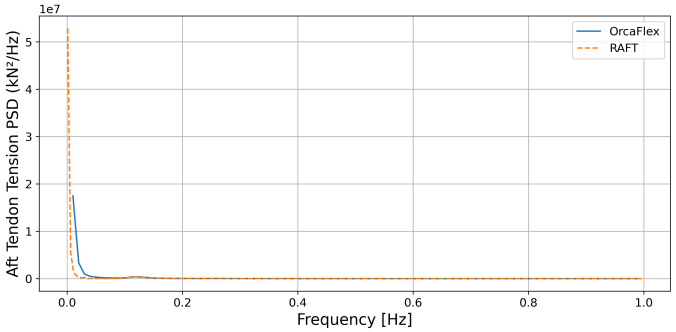

(d) Fore and aft tendon tension PSD.

Figure 5.9: Power spectral density comparisons at $H_s = 1$ [m], $T_p = 7.22$ [s], $V_w = 5$ [m/s] subjected to first-order waves and wind loading.

When looking at the PSD of the case with $Hs = 2$ [m], $Tp = 7.94$ [s], $Vw = 13$ [m/s] in Figure 5.10, it becomes clear that RAFT underestimates Orcaflex due to an underestimation of the low frequency response resonance at the surge natural frequency. This is most likely due the same reason as the previous load case of more spectral energy being absorbed at the systems surge natural frequency, leading to increased response. For this load case however, the pitch response gets overestimated. This is due to the large peak at a almost 0 frequency which gets amplified by the surge motion via the surge-pitch coupling.

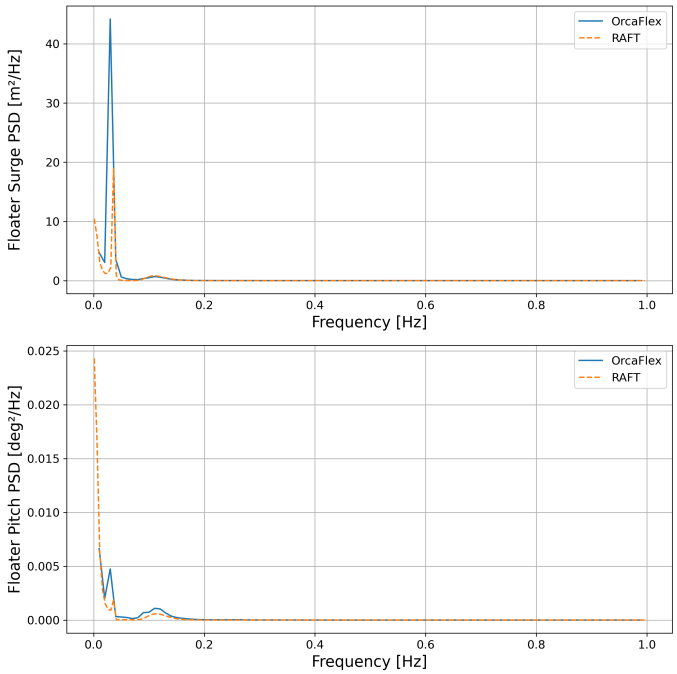

(a) Floater surge and pitch PSD.

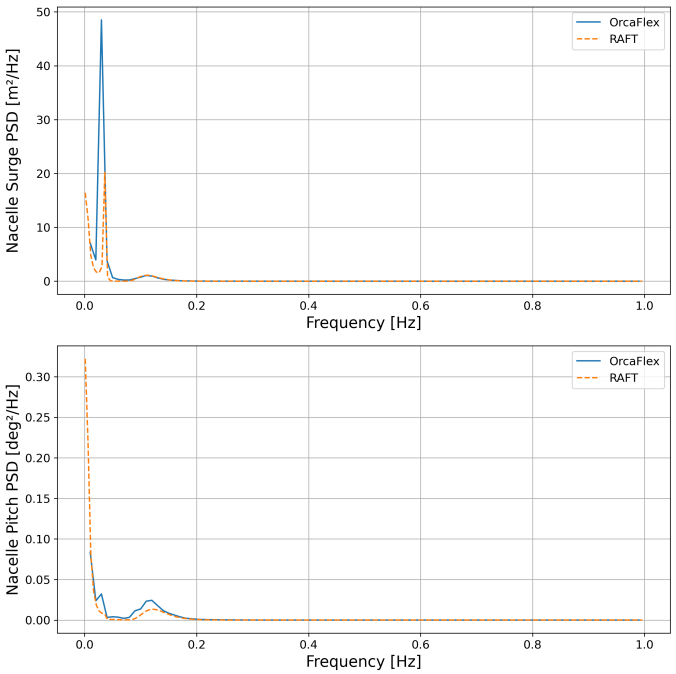

(b) Nacelle surge and pitch PSD.

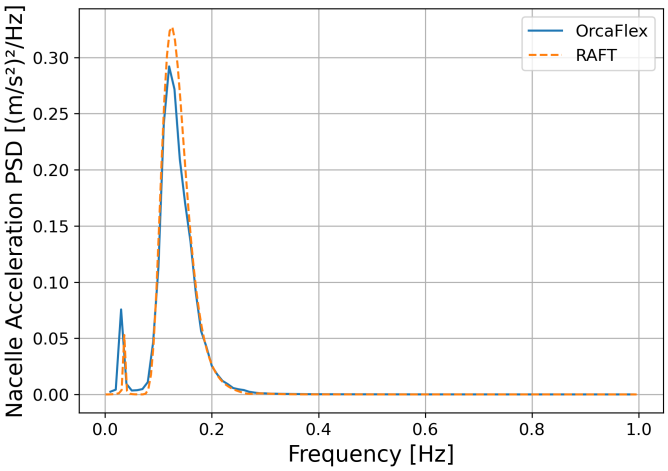

(c) Nacelle acceleration PSD.

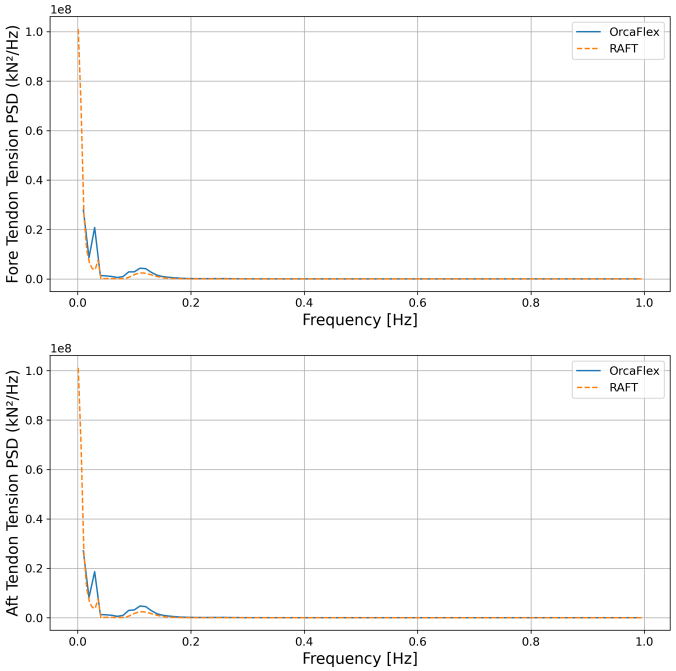

(d) Fore and aft tendon tension PSD.

Figure 5.10: Power spectral density comparisons at $H_s = 2$ [m], $T_p = 7.94$ [s], $V_w = 13$ [m/s] subjected to first-order waves and wind loading.

5.4.2. Comparison with First- & Second-order Waves and Wind

Table 5.5 presents the statistical comparison between RAFT and OrcaFlex for cases where first-order and second-order wave forces, as well as wind loading are included. These load cases follow similar trends as previously observed. Specifically, the second-order wave forces have minimal influence in the smaller sea states, which is expected given that second-order effects are typically much smaller in magnitude under such conditions. However, for higher wind speeds and more extreme sea states, several discrepancies emerge. As highlighted in the table, the surge motion, which had consistently been under predicted by RAFT in earlier cases, becomes over predicted at a severe sea state with high wind speeds. Additionally, a notable difference in the mean pitch offset appears. Where OrcaFlex has a negative static pitch angle, RAFT has a positive static pitch angle. This suggests a difference in the treatment of static equilibrium or aerodynamic loading between the two models.

Table 5.5: Statistical comparison of RAFT and OrcaFlex simulations under first- and second-order wave and wind loading with $H_s = 1$ [m], $T_p = 7.22$ [s], $V_w = 5$ [m/s], $H_s = 2$ [m], $T_p = 7.94$ [s], $V_w = 13$ [m/s] and $H_s = 5$ [m], $T_p = 10.34$ [s], $V_w = 25$ [m/s].

Hs	Vw	Variable	Unit	Mean_RAFT	Mean_OrcaFlex	Std_RAFT	Std_OrcaFlex	STD [%]	Max_RAFT	Max_OrcaFlex	Min_RAFT	Min_OrcaFlex	△Max [%]	△Min [%]
1	5	Surge (platform)	m	0.82	0.82	0.25	0.30	16.42	1.57	1.71	0.08	-0.07	8.43	-210.44
1	5	Pitch (platform)	deg	0.03	0.03	0.01	0.01	19.50	0.06	0.07	0.01	0.00	9.69	-715.01
1	5	Surge (hub)	m	1.06	1.03	0.29	0.36	19.01	1.94	2.12	0.18	-0.06	8.34	-399.31
1	5	Pitch (hub)	deg	0.12	0.12	0.03	0.04	18.21	0.22	0.24	0.01	-0.01	9.87	-291.23
1	5	Downwind tendon	kN	11914.40	11810.66	574.37	712.49	19.39	13637.52	13948.14	10191.29	9673.19	2.23	-5.36
1	5	Upwind tendon	kN	16093.00	16187.42	574.27	716.15	19.81	17815.82	18335.86	14370.18	14038.98	2.84	-2.36
1	5	RNA accel. (X)	m/s^2	0.02	0.00	0.07	0.07	-3.38	0.23	0.20	-0.19	-0.20	-13.16	-6.40
2	13	Surge (platform)	m	2.12	2.03	0.60	0.72	16.66	3.92	4.18	0.33	-0.12	6.30	-363.56
2	13	Pitch (platform)	deg	0.08	0.07	0.02	0.02	-14.51	0.14	0.12	0.03	0.03	-14.73	-15.52
2	13	Surge (hub)	m	2.74	2.55	0.67	0.79	14.31	4.76	4.91	0.71	0.19	3.04	-281.99
2	13	Pitch (hub)	deg	0.30	0.26	0.07	0.06	-12.24	0.50	0.44	0.10	0.09	-12.46	-13.35
2	13	Downwind tendon	kN	8599.63	8599.91	1147.41	997.04	-15.08	12041.85	11591.05	5157.41	5608.78	-3.89	8.05
2	13	Upwind tendon	kN	19447.44	19437.50	1148.06	1007.71	-13.93	22891.61	22460.63	16003.27	16414.38	-1.92	2.50
2	13	RNA accel. (X)	m/s^2	0.05	0.00	0.14	0.14	-4.14	0.48	0.41	-0.38	-0.41	-16.48	-8.19
5	25	Surge (platform)	m	0.20	0.16	1.17	1.03	-13.80	3.71	3.24	-3.30	-2.92	-14.61	12.90
5	25	Pitch (platform)	deg	0.01	-0.04	0.02	0.02	-11.81	0.06	0.01	-0.05	-0.09	-370.48	-43.99
5	25	Surge (hub)	m	0.23	0.18	1.25	1.13	-10.87	3.98	3.56	-3.52	-3.21	-11.88	9.75
5	25	Pitch (hub)	deg	0.01	-0.13	0.07	0.08	5.81	0.24	0.11	-0.21	-0.36	-116.37	-42.21
5	25	Downwind tendon	kN	13522.49	13778.50	1197.76	1086.55	-10.24	17115.77	17038.14	9929.20	10518.85	-0.46	5.61
5	25	Upwind tendon	kN	14478.01	14221.45	1197.69	1067.25	-12.22	18071.07	17423.21	10884.96	11019.70	-3.72	1.22
5	25	RNA accel. (X)	m/s^2	0.00	0.00	0.37	0.37	-1.01	1.13	1.11	-1.12	-1.11	-1.22	0.79

The difference in static pitch offset between RAFT and OrcaFlex primarily originates from discrepancies in the turbine controller implementation. In OrcaFlex, when the wind speed slightly exceeds the cut-out threshold, the blades feather and the turbine system pitches backward due to the tendons pulling it toward equilibrium. In contrast, RAFT employs a simplified controller with a constant thrust above the cut-out wind speed, ignoring the feathering behaviour. This results in an overestimation of the mean pitch offset in RAFT under high wind conditions.

Regarding the dynamic response, Figure 5.11 shows large peaks at the surge natural frequency. These peaks can be attributed to the lack of a nacelle fore–aft speed damping gain in RAFT. This damping term, which is intended to suppress low-frequency surge–pitch resonance by means of the turbine controller, does not function correctly in the current RAFT software. The absence of this control mechanism leads to resonance amplification at the surge natural frequency, causing noticeable discrepancies and overestimations in both surge and pitch responses, especially at higher wind speeds.

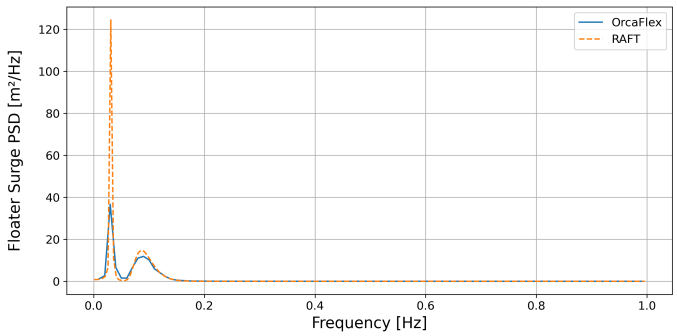

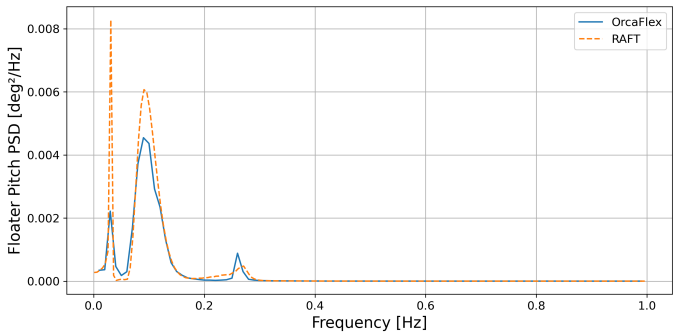

(a) Floater surge and pitch PSD.

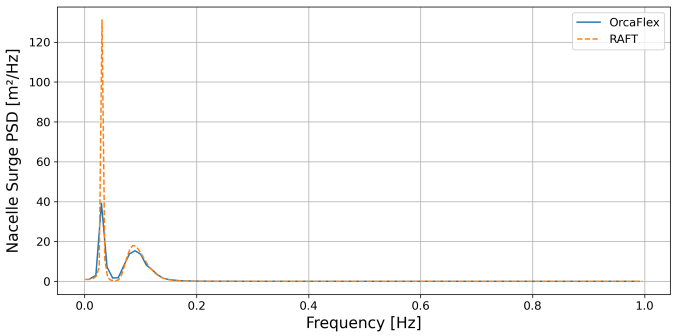

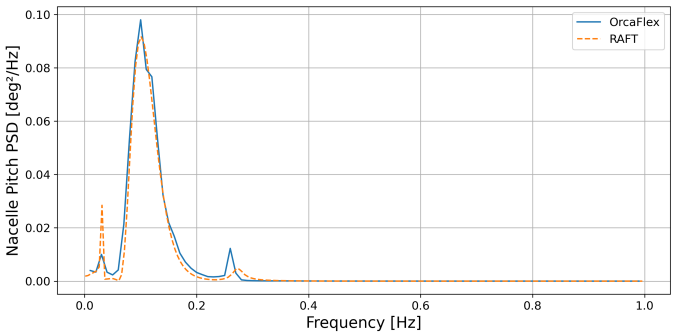

(b) Nacelle surge and pitch PSD.

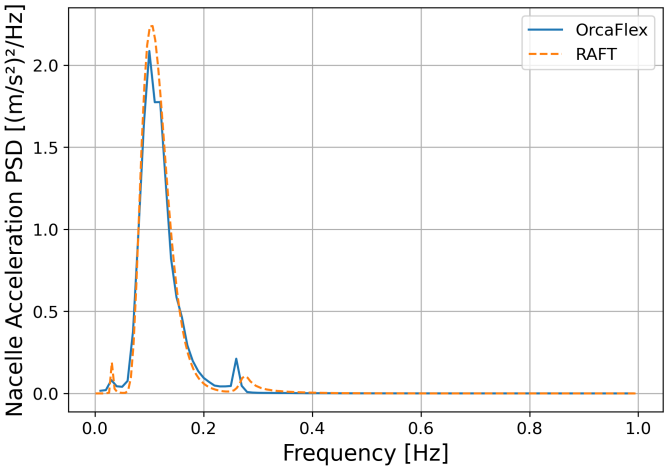

(c) Nacelle acceleration PSD.

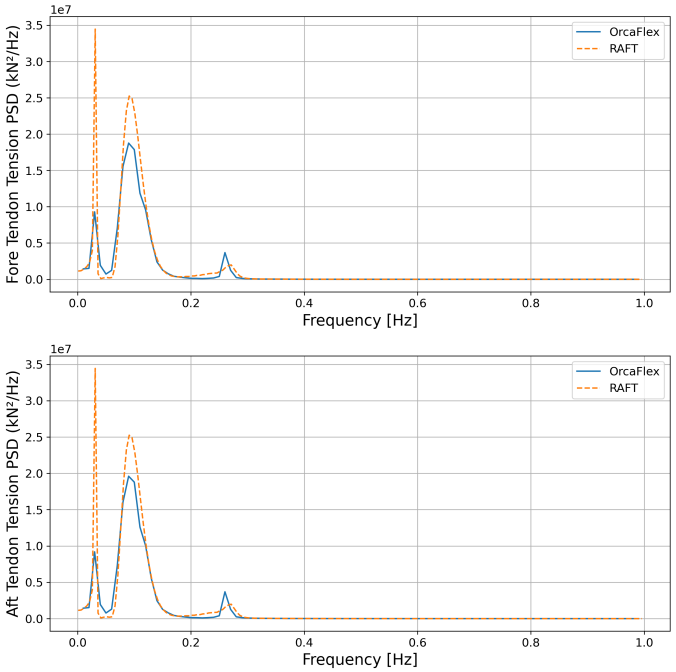

(d) Fore and aft tendon tension PSD.

Figure 5.11: Power spectral density comparisons at $H_s = 5$ [m], $T_p = 10.34$ [s], $V_w = 25$ [m/s] subjected to first- and second-order waves and wind loading.

5.5. Added Mass and Damping Comparison

This framework assumes linearised constant added mass coefficients and linearised constant viscous damping as this significantly reduces computational time compared to a full diffraction analysis. For the base case considered, an OrcaWave simulation was performed to obtain frequency-dependent added mass and radiation damping through diffraction analysis. Table 5.6 presents the results of using frequency-dependent hydrodynamic coefficients instead of linearised constant coefficients for load

cases. The first one is a first-order wave case in a sea state with $H_s = 2$ [m] and $T_p = 7.94$ [s]. The second one is a load case combining first- and second-order wave loading in the same sea state as the first load case with additionally a wind speed of 13 [m/s].

As highlighted in the table, several significant differences are observed. Most notably, the pitch response is underestimated in the linearised case compared to the frequency-dependent case. This discrepancy is primarily driven by an increased peak at the first-order wave frequency in pitch, as shown in Figure 5.12. The origin of this is the overestimation of added mass in RAFT at this frequency range relative to OrcaFlex, resulting in a reduced dynamic response prediction. RAFT calculates a constant pitch added mass which is approximately 30% larger.

This trend continues in the combined load case including wind and second-order waves, where RAFT again underestimates the pitch response when using frequency-dependent coefficients. However, the relative reduction in pitch response is approximately the same as in the first-order-only case. This consistency is as expected, assuming that the added mass predominantly causes the discrepancies near the first-order wave frequency and is the only hydrodynamic term varied in these comparisons.

In the more severe load case, the surge response is also increasingly underestimated when frequency-dependent added mass and damping are used. This is evident in Figure 5.13, where the surge peak in the difference-frequency region is significantly underestimated. This underestimation can again be attributed to a difference in added mass in this frequency range. Additionally, differences in surge damping between RAFT and OrcaFlex may contribute to this discrepancy.

This comparison shows that RAFT has a underestimates the pitch behaviour in the absence of wind loading and at lower sea states. However, for increasing wind speeds and sea states this difference becomes within smaller acceptable margins. This means that the eventual optimisation designs will underestimate the pitch behaviour of the system. This might become an issue, but taking in consideration that pitch motions are small for TLPs an often not limiting it is currently acceptable for the goal of this framework.

Table 5.6: Comparison between constant and frequency-dependent added mass and damping for RAFT and OrcaFlex simulations at $H_s = 2$ [m], $T_p = 7.94$ [s], $V_w = 0$ [m/s] subjected to only first-order wave loads and $H_s = 2$ [m], $T_p = 7.94$ [s], $V_w = 13$ [m/s] subjected to first- and second-order waves and wind loading.

Added mass and damping	Hs	Vw	Variable	Unit	Mean_RAFT	Mean_OrcaFlex	Std_RAFT	Std_OrcaFlex	STD [%]	Max_RAFT	Max_OrcaFlex	Min_RAFT	Min_OrcaFlex	△Max [%]	△Min [%]
constant	2	0	Surge (platform)	m	0.00	0.00	0.19	0.18	-5.07	0.56	0.53	-0.56	-0.53	-5.08	5.05
constant	2	0	Pitch (platform)	deg	0.00	0.00	0.00	0.00	0.77	0.01	0.01	-0.01	-0.01	0.79	-0.75
constant	2	0	Surge (hub)	m	0.00	0.00	0.22	0.22	-2.71	0.66	0.65	-0.66	-0.65	-2.71	2.70
constant	2	0	Pitch (hub)	deg	0.00	0.00	0.03	0.03	5.50	0.08	0.09	-0.08	-0.09	5.53	-5.48
constant	2	0	Downwind tendon	kN	14000.00	13995.21	306.64	312.43	1.85	14919.93	14932.51	13080.07	13057.91	0.08	-0.17
constant	2	0	Upwind tendon	kN	14000.00	13995.58	306.63	307.09	0.15	14919.90	14916.84	13080.10	13074.32	-0.02	-0.04
constant	2	0	RNA accel. (X)	m/s^2	0.00	0.00	0.14	0.14	-0.29	0.42	0.42	-0.42	-0.42	-0.32	0.26
Frequency dependent	2	0	Surge (platform)	m	0.00	0.00	0.19	0.19	0.40	0.56	0.56	-0.56	-0.56	0.49	-0.31
Frequency dependent	2	0	Pitch (platform)	deg	0.00	0.00	0.00	0.01	29.18	0.01	0.02	-0.01	-0.02	29.34	-29.03
Frequency dependent	2	0	Surge (hub)	m	0.00	0.00	0.22	0.23	5.51	0.66	0.70	-0.66	-0.70	5.64	-5.39
Frequency dependent	2	0	Pitch (hub)	deg	0.00	0.00	0.03	0.03	21.92	0.08	0.10	-0.08	-0.10	22.23	-21.61
Frequency dependent	2	0	Downwind tendon	kN	14000.00	13992.61	306.64	435.02	29.51	14919.93	15297.67	13080.07	12687.54	2.47	-3.09
Frequency dependent	2	0	Upwind tendon	kN	14000.00	13998.25	306.63	432.66	29.13	14919.90	15296.24	13080.10	12700.26	2.46	-2.99
Frequency dependent	2	0	RNA accel. (X)	m/s^2	0.00	0.00	0.14	0.16	13.50	0.42	0.48	-0.42	-0.49	13.36	-13.64
constant	2	13	Surge (platform)	m	2.12	2.03	0.60	0.72	16.66	3.92	4.18	0.33	-0.12	6.30	-363.56
constant	2	13	Pitch (platform)	deg	0.08	0.07	0.02	0.02	-14.51	0.14	0.12	0.03	0.03	-14.73	-15.52
constant	2	13	Surge (hub)	m	2.74	2.55	0.67	0.79	14.31	4.76	4.91	0.71	0.19	3.04	-281.99
constant	2	13	Pitch (hub)	deg	0.30	0.26	0.07	0.06	-12.24	0.50	0.44	0.10	0.09	-12.46	-13.35
constant	2	13	Downwind tendon	kN	8599.63	8599.91	1147.41	997.04	-15.08	12041.85	11591.05	5157.41	5608.78	-3.89	8.05
constant	2	13	Upwind tendon	kN	19447.44	19437.50	1148.06	1007.71	-13.93	22891.61	22460.63	16003.27	16414.38	-1.92	2.50
constant	2	13	RNA accel. (X)	m/s^2	0.05	0.00	0.14	0.14	-4.14	0.48	0.41	-0.38	-0.41	-16.48	-8.19
Frequency dependent	2	13	Surge (platform)	m	2.12	2.05	0.60	0.87	31.33	3.92	4.67	0.33	-0.56	15.97	-158.46
Frequency dependent	2	13	Pitch (platform)	deg	0.08	0.07	0.02	0.02	13.65	0.14	0.14	0.03	0.01	-0.66	-137.30
Frequency dependent	2	13	Surge (hub)	m	2.74	2.58	0.67	0.97	30.14	4.76	5.48	0.71	-0.32	13.07	-325.23
Frequency dependent	2	13	Pitch (hub)	deg	0.30	0.27	0.07	0.08	12.57	0.50	0.50	0.10	0.04	0.21	-130.20
Frequency dependent	2	13	Downwind tendon	kN	8599.63	8501.95	1147.41	1319.33	13.03	12041.85	12459.95	5157.41	4543.94	3.36	-13.50
Frequency dependent	2	13	Upwind tendon	kN	19447.44	19538.92	1148.06	1338.89	14.25	22891.61	23555.58	16003.27	15522.27	2.82	-3.10
Frequency dependent	2	13	RNA accel. (X)	m/s^2	0.05	0.00	0.14	0.16	8.26	0.48	0.47	-0.38	-0.47	-2.57	-19.09

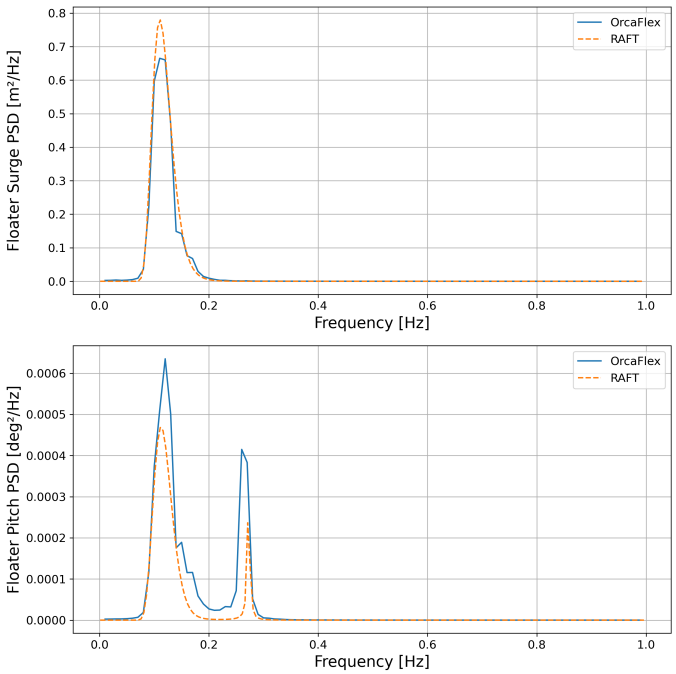

(a) Floater surge and pitch PSD.

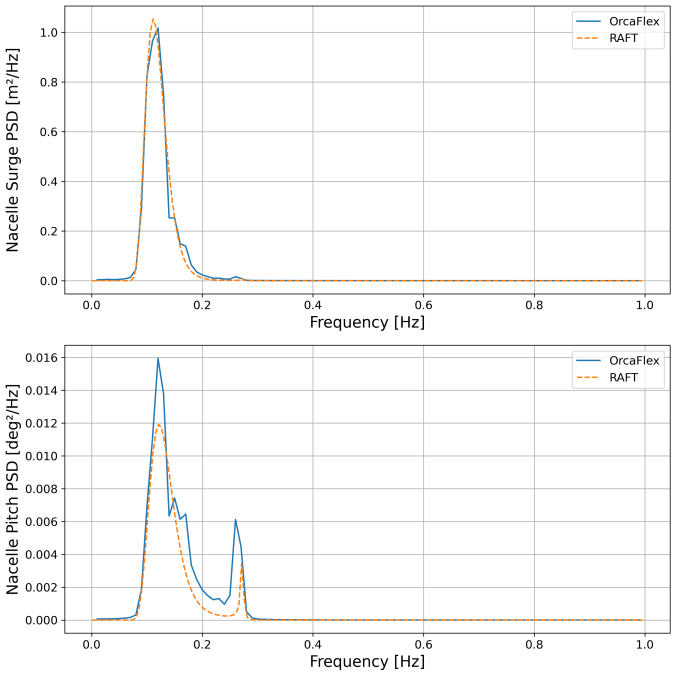

(b) Nacelle surge and pitch PSD.

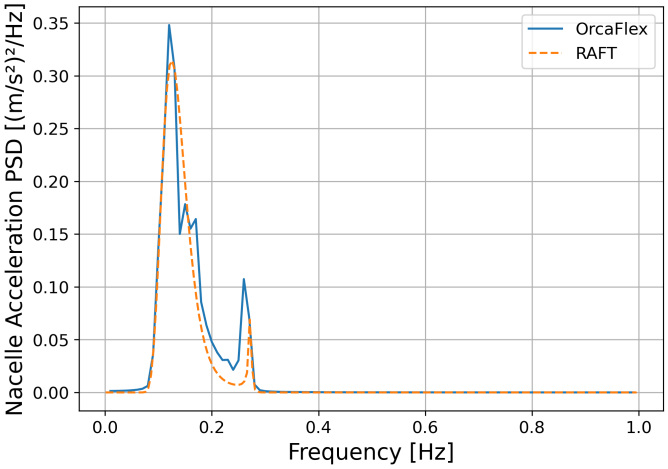

(c) Nacelle acceleration PSD.

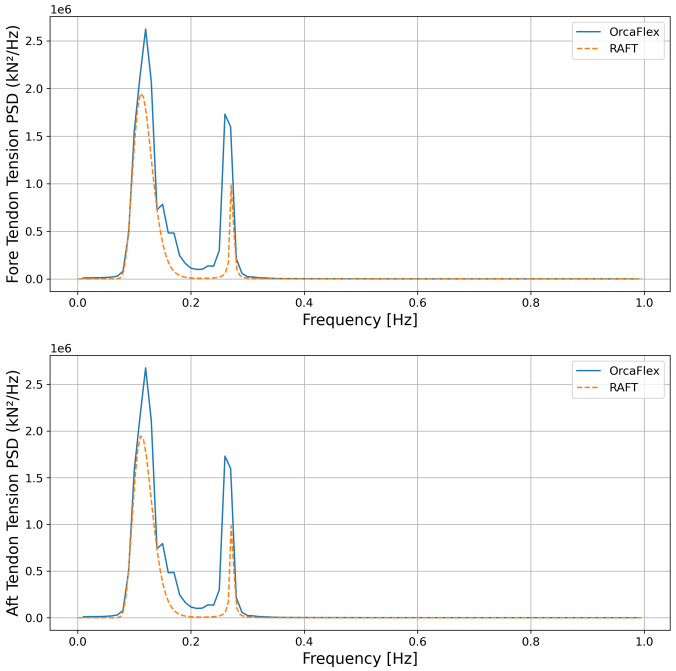

(d) Fore and aft tendon tension PSD.

Figure 5.12: Power spectral density comparisons for the impact of linearised and frequency dependent added mass at $H_s = 2$ [m], $T_p = 7.94$ [s], $V_w = 0$ [m/s] subjected to first-order waves.

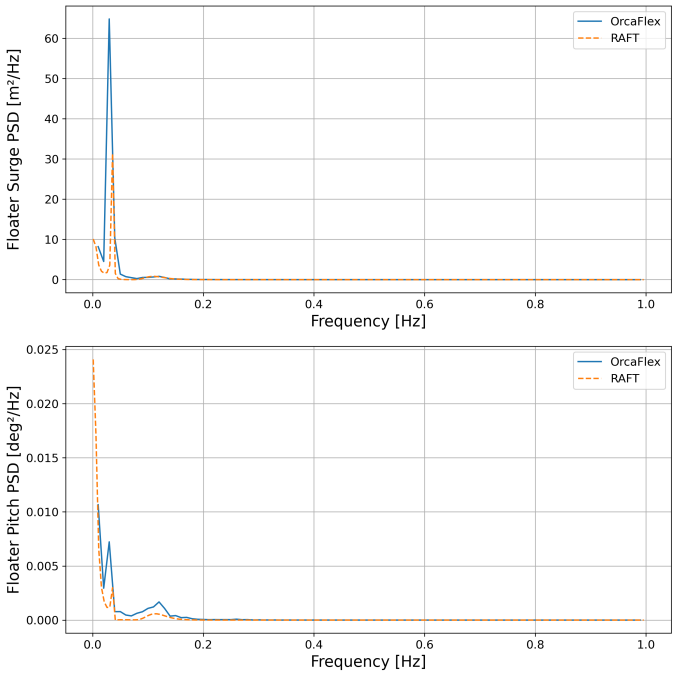

(a) Floater surge and pitch PSD.

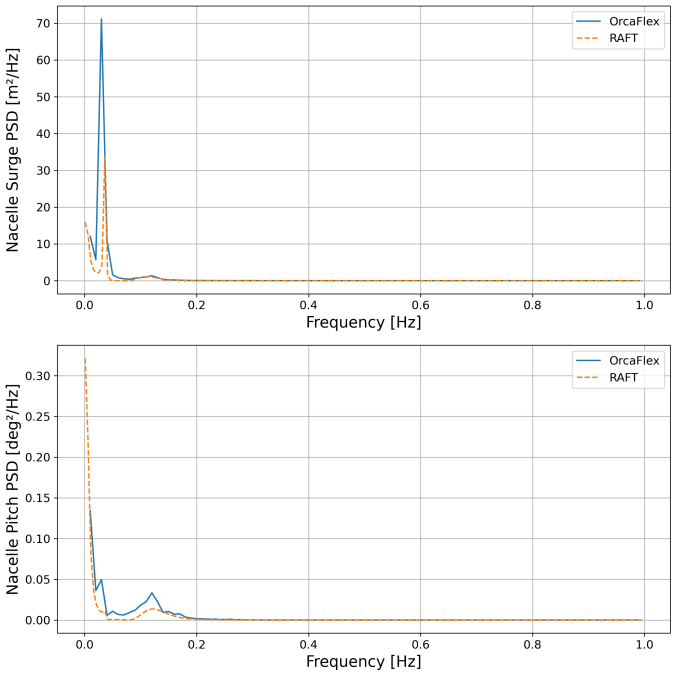

(b) Nacelle surge and pitch PSD.

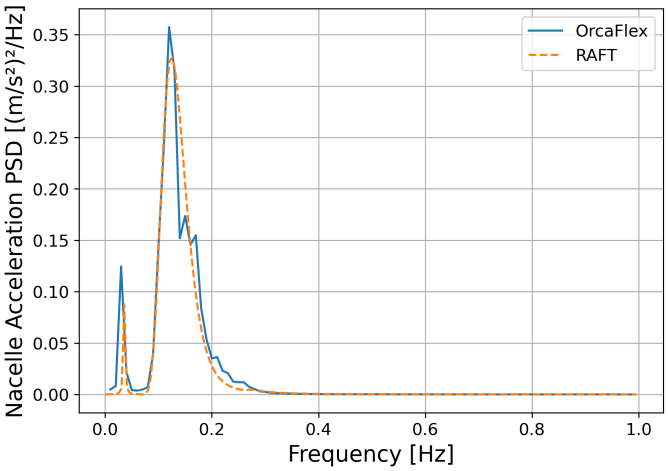

(c) Nacelle acceleration PSD.

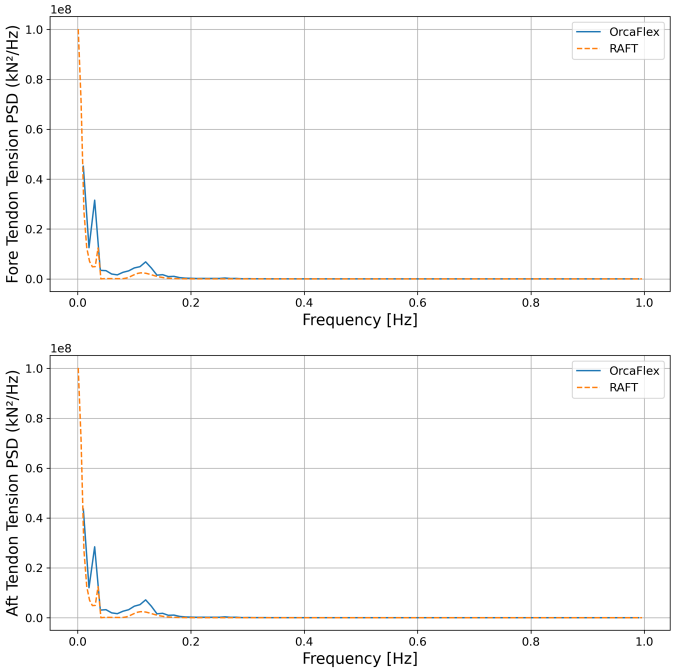

(d) Fore and aft tendon tension PSD.

Figure 5.13: Power spectral density comparisons for the impact of linearised and frequency dependent added mass at $H_s = 2$ [m], $T_p = 7.94$ [s], $V_w = 13$ [m/s] subjected to first- and second-order waves and wind loading.

Relevance of Radiation Damping

Next to the assumption of constant added mass and viscous damping, this research assumes that radiation damping is of minor relevance due to the slender-body approximation. To assess the validity of this assumption in the RAFT simulations, Table 5.7 presents system response statistics under various damping configurations. These results were obtained by performing Orcaflex simulations with no damping, diffraction generated radiation damping, RAFT generated viscous damping and a combination of both types of damping.

The results show that radiation damping does influence the response, but the effect is significantly smaller compared to that of viscous damping. Moreover, the responses obtained using only viscous damping closely match those from simulations that include both viscous and radiation damping. This confirms the validity of the current assumption to neglect radiation damping in the RAFT simulations. However, this simplification may lead to slightly conservative results but the deviation is minor.

Table 5.7: Platform and mooring responses under different damping models at $H_s = 2$ [m], $T_p = 7.94$ [s], $V_w = 13$ [m/s].

Hs [m]	Tp [s]	Vw [m/s]	Variable	Unit	No Damping	Radiation Damping	Viscous Damping	Viscous + Radiation Damping
2	7.94	13	Surge (platform)	m	9.59	7.02	4.99	4.67
2	7.94	13	Pitch (platform)	deg	0.17	0.15	0.14	0.14
2	7.94	13	Surge (hub)	kN	10.54	7.85	5.82	5.48
2	7.94	13	Pitch (hub)	kN	0.56	0.51	0.51	0.50
2	7.94	13	Mooring line 1	m/s^2	2628.85	3861.91	4373.33	4543.94
2	7.94	13	Mooring line 2	m	25695.43	24332.42	23724.40	23555.58
2	7.94	13	RNA accel. (X)	deg	0.63	0.51	0.52	0.47

5.6. Tendon Angle Comparison

The framework under development in this research aims to simulate a wide range of TLP configurations, including variations in tendon angle. To assess the models validity for inclined tendons, a comparison is made using the base case with tendons inclined at $80°$. The results of this comparison are shown in Figure 5.14. The figures illustrate significant discrepancies between RAFT and OrcaFlex simulations.

RAFT is a linear model, currently based on an analytical description of the mooring matrix for quick calculations. With the current implementation it is not able to accurately capture all different couplings and coupled modes. As the tendon angle decreases, coupling between surge, heave and pitch becomes more pronounced. These coupled modes are not well captured, leading to substantial overestimation of system response. The RAFT model has higher surge natural frequency with decreasing tendon angle that falls within the wave excitation region, as indicated by the red vertical line in Figure 5.14a. This leads to large overestimation of responses in surge that also amplify nacelle accelerations and tendon tensions, as presented in Figure 5.14b and Figure 5.14c.

This analysis highlights a limitation of the current RAFT model as it provides accurate results for (near) vertical tendons but fails to reliably predict system behaviour when tendon angles are more inclined, as it largely over predicts the responses. To compare, the coupled surge–pitch natural frequency, which is captured by OrcaFlex, indicated with a green vertical line in Figure 5.14a, remains lower and stays outside the first order wave excitation range, preventing extreme resonance to occur.

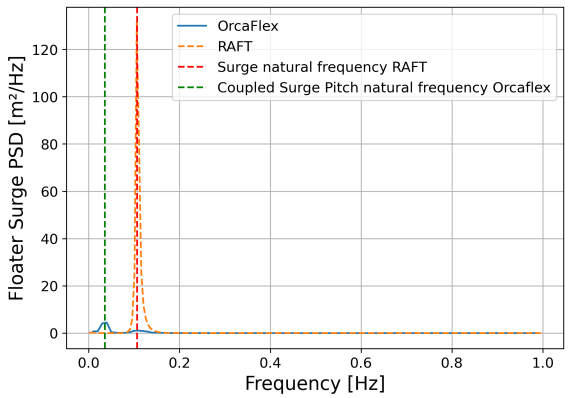

(a) Surge PSD for a TLP with tendons under an angle.

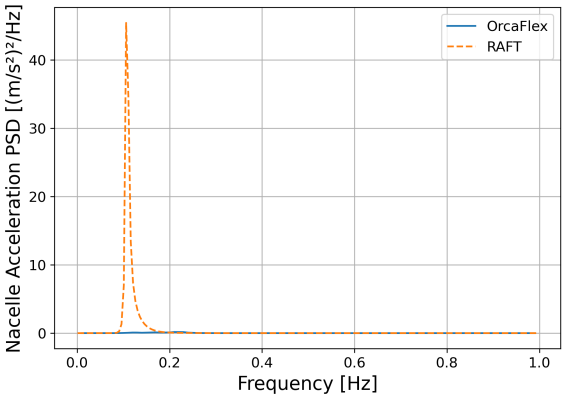

(b) Nacelle acceleration PSD for a TLP with tendons under an angle.

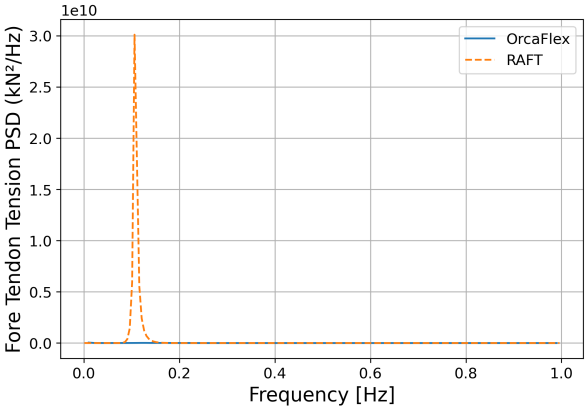

(c) Tendon tension PSD for a TLP with tendons under an angle.

Figure 5.14: PSD comparison for a TLP with tendons under an $80°$ angle.

5.7. Modelling Effects, Consequences & Limitations

Over the course of this comparison study, it can be concluded that RAFT is capable of simulating first- and second-order hydrodynamic forces within an error margin of approximately $\pm 10\%$ compared to time-domain simulations for TLPs with (near) vertical tendons. When wind loading is introduced, these error margins increase due to larger platform offsets and increasing mismatches caused by the linearisation of the mooring system and controller behaviour. Nonetheless, the RAFT software maintains an overall error margin within $\pm 16\%$ compared to time-domain simulations for the base case. The resulting maximal over- and under predictions are summarized in Table 5.8.

Table 5.8: Indication of trends throughout the comparison and associated correction factors

Variable	RAFT under(+)/over(-) prediction [%]
Maximum Platform surge	10%
Maximum hub pitch	-16%
Minimum tendon tension	-4%
Maxmimum tendon tension	-2%
Maximum nacelle acceleration	-4%

The key sources of discrepancy and the consequences of linearising the behaviour of tension leg platform floating wind turbines in the current RAFT model are the following.

- Linearised mooring stiffness, which does not capture the non-linear restoring behaviour at large offsets, leads to over and under estimations of the system response. Due to the strong coupling

in TLPs, even small deviations in surge offset can significantly affect pitch behaviour, highlighting the sensitivity of TLP dynamics to such interactions. It was indicated that the linear mooring representation may introduce up to $\pm$ 10% error in response compared to non-linear time domain simulations for the current base case.

- For TLPs with inclined tendons, the previously mentioned couplings become increasingly important for the system's dynamic behaviour. Since the current linear RAFT model with an analytical mooring matrix does not accurately capture these coupling effects, it significantly overestimates the system response as the tendon angle decreases. This imposes a limitation on the model, restricting the accurate use to configurations with (near) vertical tendons.
- Underestimation of added mass at first-order wave frequencies leads to under-prediction pitch dynamic response. This highlights the need for further comparison and validation studies that incorporate frequency-dependent hydrodynamic effects and assessing the impact on final design results.
- Absence of fore–aft aerodynamic damping terms in the controller, particularly at high wind speeds, affects low-frequency surge and pitch responses. This highlights the need for a more realistic linear controller that remains effective across the full range of operational conditions.

While these discrepancies currently prevent full validation of RAFT against OrcaFlex, the adjusted RAFT model remains a valuable tool within the optimisation framework due to the significant computational advantages. The primary objective of this study is to quickly converge toward a subset of promising design spaces which can be analysed in greater detail using high-fidelity tools. RAFT provides the necessary modelling fidelity to guide the design process and explore the design space for TLPs with (near) vertical tendons. Table 5.9 presents a comparison of simulation runtimes between RAFT and OrcaFlex. RAFT requires approximately 1.5% of the computational time needed by OrcaFlex, while maintaining a maximum error margin of $\pm 16\%$ for the response variables.

Table 5.9: Indication of computational time per load case using RAFT or orcaflex.

Software	Type of analysis	Calculation time per load case (including full QTF calculation)
RAFT	FD	$\pm$ 90 seconds
Orcaflex	TD	$\pm$ 1.5 hours

6

TLP Design Characteristics

The optimisation studies produced a wide range of designs, offering insight into the design space and the influence of design variables on system performance. First, an analysis is performed to assess the design characteristics related to system response. Next, the relationship between design variables and the resulting LCOE is analysed. The goal of this analysis is to identify the design driving parameters, which may reduce the design space during further optimisation studies by taking into account less design variables.

6.1. Design Characteristics for System Response

Figure 6.1 shows the mutual information between each design variable and the response results. This metric captures both linear and non-linear relationships and shows how strongly two variables are related. It does not show how much one variable affects another, but how much knowing one variable reduces the uncertainty in the other. An interpretation guide is given in Table 6.1.

Only feasible designs that satisfy all constraints, except the 1P/3P natural frequency constraint which will be discussed in subsection 6.1.3, are included in this analysis. This avoids correlations being influenced by infeasible or non-physical designs. More figures showing correlations between design variables and system response results can be found in Appendix D.

Table 6.1: How the read the mutual information heat map

MI index	Meaning
0	No mutual information, variables are independent.
0 - 0.6	low mutual information, minimal dependence.
0.6 - 1.2	Moderate mutual information, noticeable dependence.
1.2 -	High mutual information, strong dependence.

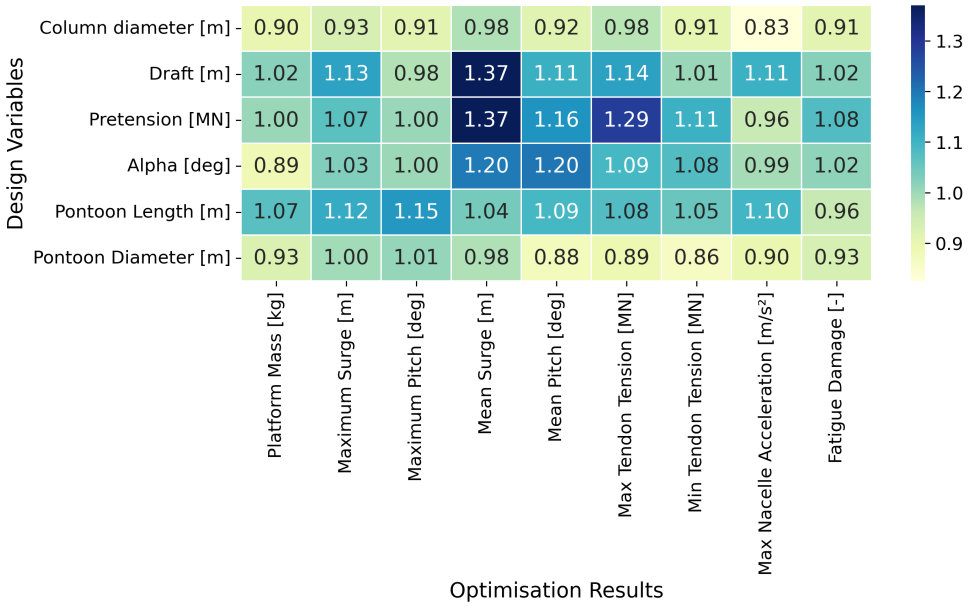

Figure 6.1: Mutual information relation between design variables and optimisation results.

When looking at Figure 6.1, it should first be noted that all design variables have at least moderate mutual information with the response results, indicating that they all depend on each other. However, some design variables show a stronger relationship with the system response. Table 6.2 lists the variables with the strongest relationships, which will be discussed in this section.

Table 6.2: An overview of the significant correlations between design variable and respone results.

Design variable	Significant correlations
Draft	Surge, Tendon Tension, Pitch, Nacelle acceleration,
Pretension	Surge, Tendon Tensions
Tendon angle	Pitch, Surge
Pontoon length	Pitch, Nacelle acceleration

6.1.1. The Influence of Design Variables

This section presents the most significant relations between different design variables and the dynamic system response. It should be noted that the mean response refers to the maximum mean response across all load cases, while the maximum response corresponds to the maximum response observed across all load cases

The Influence of Draft

Figure 6.2 shows how the draft of different concepts relates to the response variables it most strongly affects. It becomes clear that increasing the draft leads to a reduction in surge motion and nacelle acceleration. Furthermore, an increasing draft increases the maximum experienced tendon tension and mean pitch angle. Several interrelated factors explain this trend.

- **Higher tendon stiffness:** A larger draft results in shorter tendons. Since tendon stiffness scales with T_{pre}/L and EA/L, shorter tendons provide more restoring force and reduce motions in surge, pitch and nacelle accelerations. This effect of a stiffer system is also reflected in the increase of the system surge natural frequencies with increasing draft, as shown in Figure 6.3. Furthermore, as surge offsets and tendon lengths decrease, the system has no negative mean pitch behaviour at deeper drafts.
- **Increased pretension:** A deeper draft often comes with more buoyancy increasing the pretension, this trend can also be seen in Figure 6.4. This increase in pretension will also induce experienced maximum tendon tensions, as both the mean tension and the axial stiffness increase.

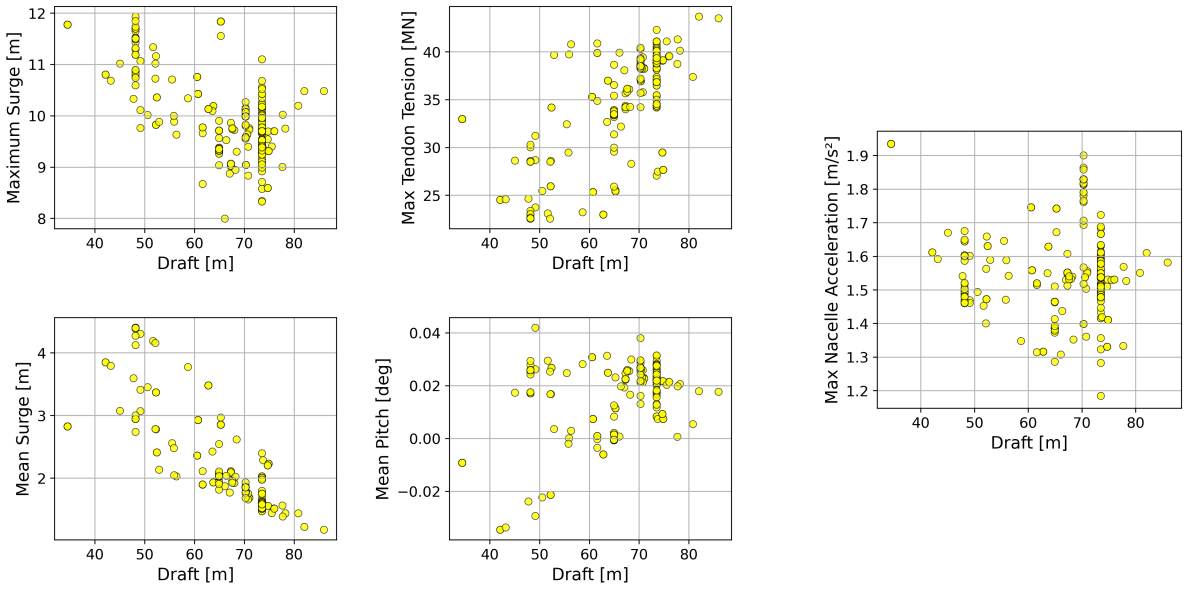

Figure 6.2: Draft specific relations with response results.

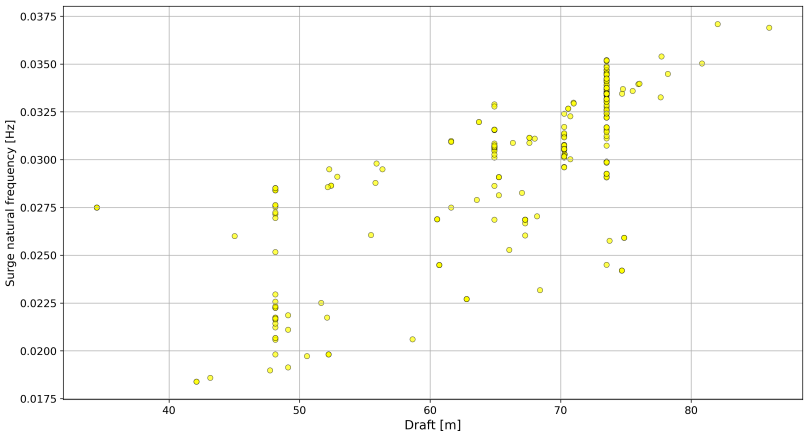

Figure 6.3: Draft relation with the surge natural frequency.

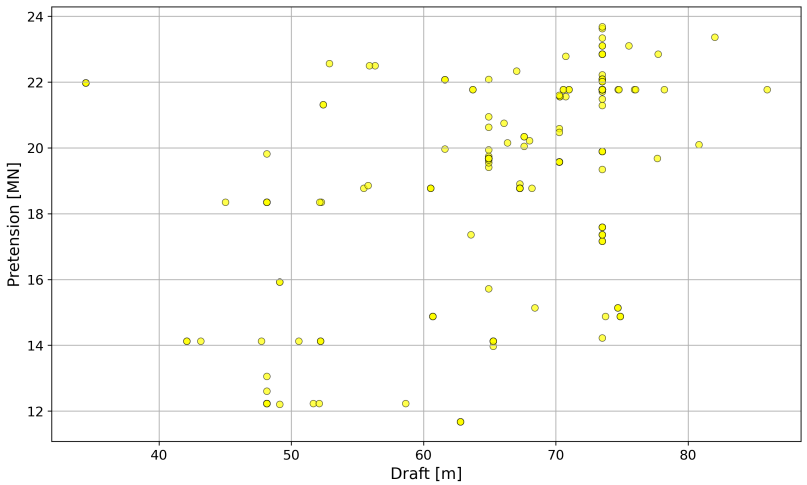

Figure 6.4: Draft relation with pretension.

The Influence of Pretension

Figure 6.5 presents the relationship between tendon pretension and the response variables it significantly influences. The figure shows that increasing the pretension reduces surge motion. This is because surge stiffness is mainly governed by the term T_{pre}/L, where a higher pretension increases the restoring force. In addition, since the minimum and maximum tendon tensions are defined as the mean pretension plus or minus the dynamic variation, higher pretension results in larger absolute values for both maximum and minimum tensions.

The results also show that no design has a pretension below 11 MN. This can be explained by two effects. First, a lower pretension increases the risk of slack events, since the minimum tendon tension is given by the mean pretension minus the dynamic tension variation. With lower pretension, this minimum more easily drops below zero. Second, lower pretension reduces the system's surge stiffness, which increases the surge offset causing it to exceed the surge constraint.

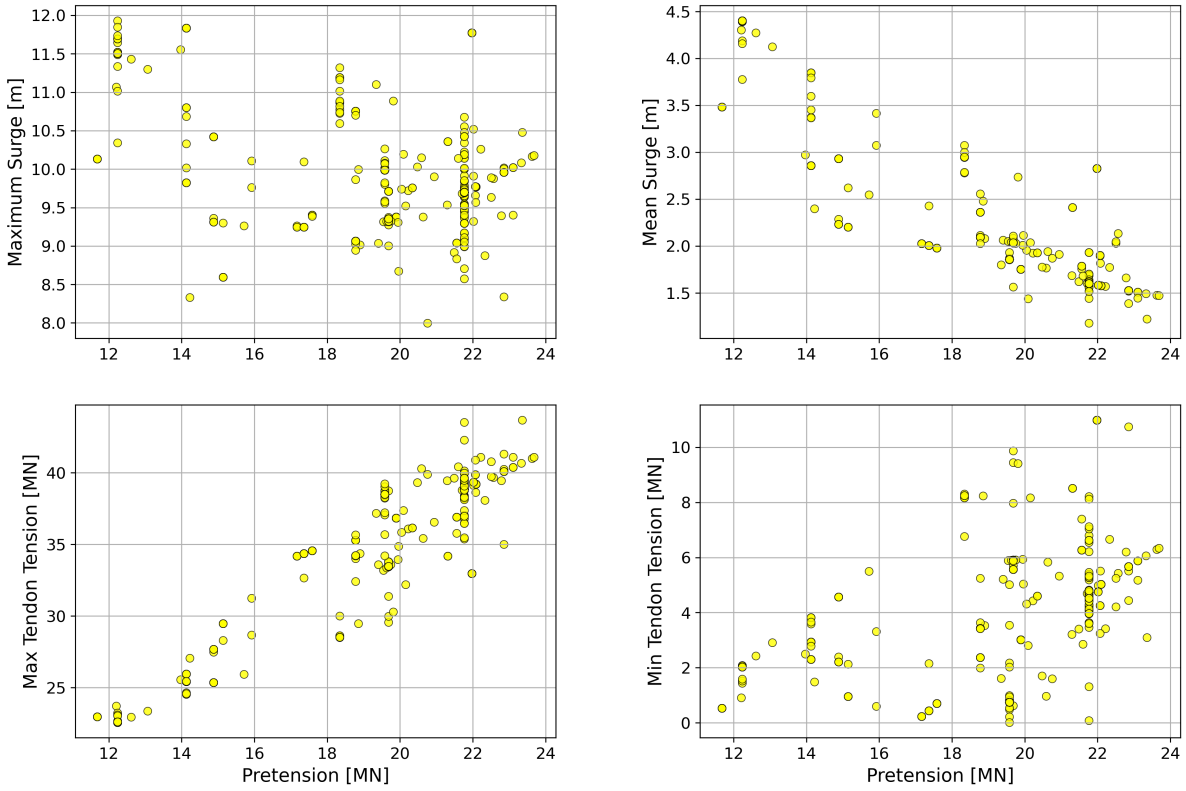

Figure 6.5: Pretension specific relations with response results.

The Influence of Tendon Angles

Figure 6.6 shows the relationship between the tendon angle and the mean pitch and surge. When the tendon angle decreases, the mean pitch angle reduces. This occurs because at lower tendon angles the asymmetry in the system increases, leading to significantly larger tensions in the fore tendon compared to the aft tendon. This leads to an increase in vertical restoring force at the fore tendon, causing a moment which results in a negative mean pitch at surge offsets. A visual representation of this behaviour is shown in Figure 6.7.

Furthermore, as the tendon angle decreases the mean surge offset increases, this is counter-intuitive as a decreasing tendon angle would usually lead to larger surge stiffness. However, when looking at Figure 6.8. It can be seen that decreasing tendon angle is closely related to the draft and pretension. As these design variable decrease relatively more with decreasing tendon angle, the mean surge offset increases overall. This shows that the draft, tendon angle and pretension are highly dependent on each other throughout the design space.

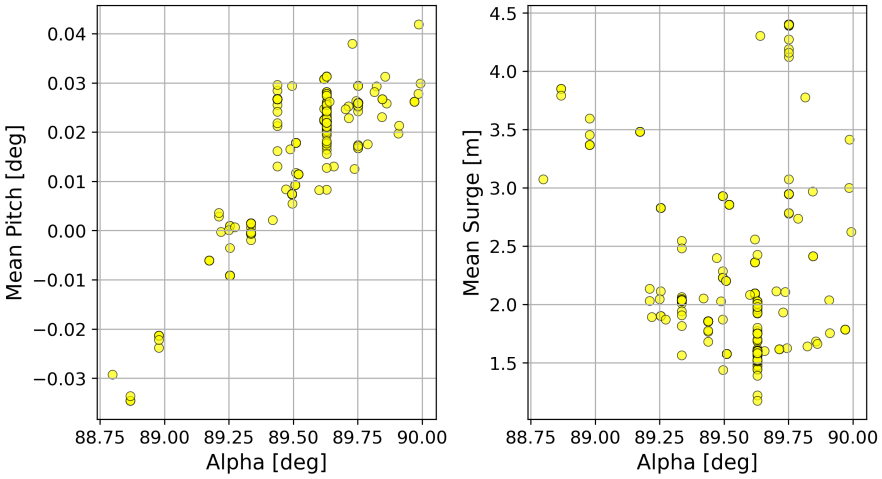

Figure 6.6: Tendon angle specific relations with response results.

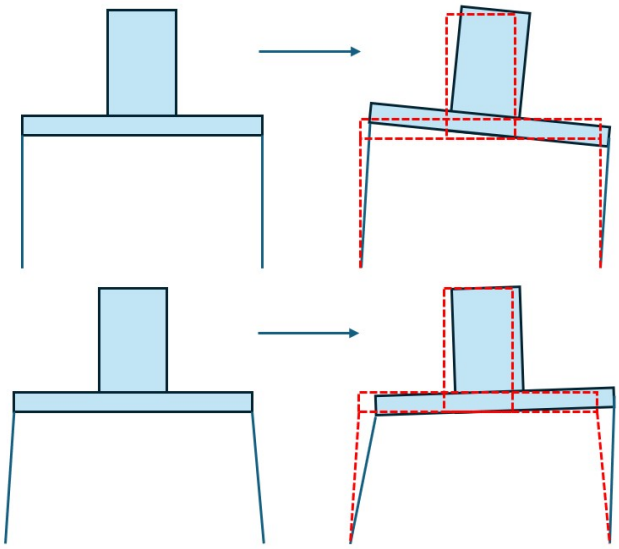

Figure 6.7: The mean pitch for decreasing tendon angle.

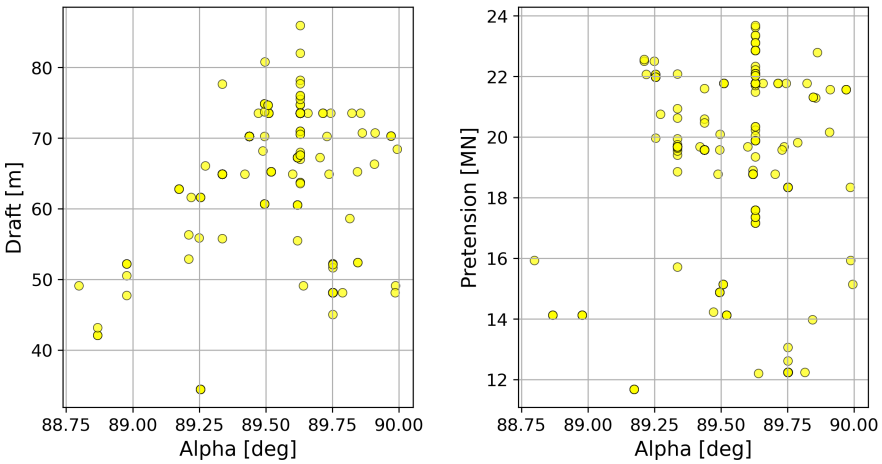

Figure 6.8: Tendon angle relations with draft and pretension.

Next to this, designs with lower tendon angles show increased responses, which results in lower minimum tendon tensions which can be seen in Figure 6.9. This indicates greater tension variation in these configurations and this is also the reason why configurations with decreasing tendon angles ($\alpha \leq 88.8°$) are identified as infeasible designs. This is in line with observations in Chapter 5 which showed that the model overpredicts dynamic responses at lower tendon angles, causing these designs to violate the constraints set in this study.

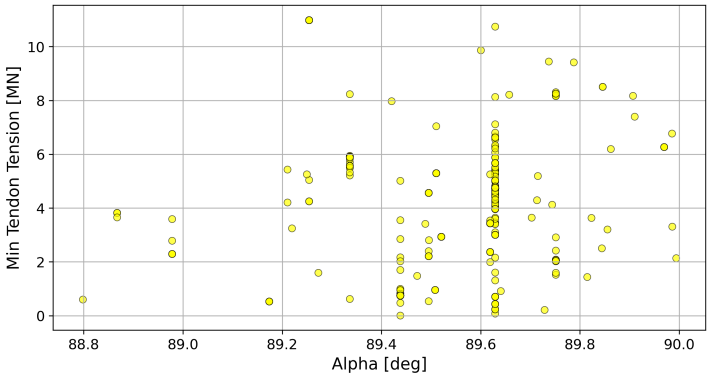

Figure 6.9: Tendon angle relations with dynamic response for surge and minimum tendon tension.

The Influence of Pontoon Length

Figure 6.10 shows how the pontoon length influences the maximum pitch angle and nacelle acceleration. As the pontoon length increases, both response variables decrease. This makes sense as a large pontoon length means a longer arm for the tendons which results in more pitch stability, reducing the pitch motion and nacelle acceleration.

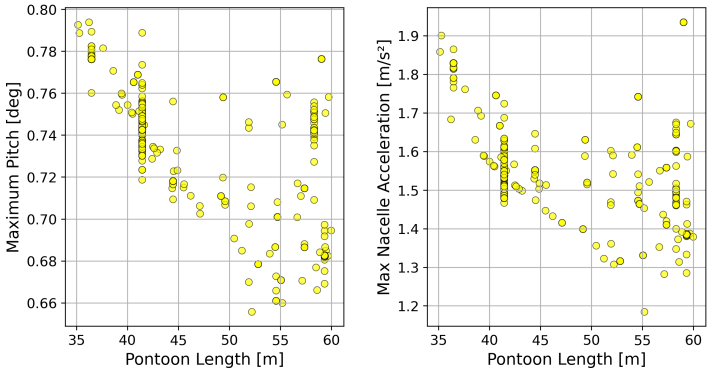

Figure 6.10: Pontoon length relations with maximum pitch and nacelle acceleration.

6.1.2. System Dynamic Performance Driving Parameters.

From this analysis, it is clear that the draft, pretension, tendon angle and pontoon length have the most pronounced influence on the design variables for determining the dynamic performance of tension leg platforms. While other variables also influence system behaviour, their impact was less clear. At this particular site, draft is closely related to the mooring system, as increasing the draft has a relatively large effect on tendon length. Pretension has a double relation where pretension directly influences system response, but also determines the extensional stiffness of the tendons, affecting system response and tendon tensions. Next to this, it could be seen throughout the figures that no viable designs exist with tendon angles below approximately 88.6°. This is in line with the findings in Section 5.6 stating that RAFT overestimates the response below these angles making the designs infeasible.

Although more influential design variables were identified, the TLP is a highly coupled system where a slight variation in geometry alters mass, buoyancy and pretension for example. This emphasizes the

need to take all design variables into account. This is also indicated by Figure 6.1 presented at the beginning of this section showing that all design variables have moderate to significant relation with the system response.

6.1.3. 3P Design Limit

During the evaluation of the design concepts, a limitation was identified for this specific TLP configuration and reference turbine. Due to the inherently stiff behaviour of the TLP system and the properties of the reference tower, all feasible designs converged to solutions with the first pitch-bending natural frequency falling within the 3P excitation frequency range of the turbine. This trend is illustrated in Figure 6.11.

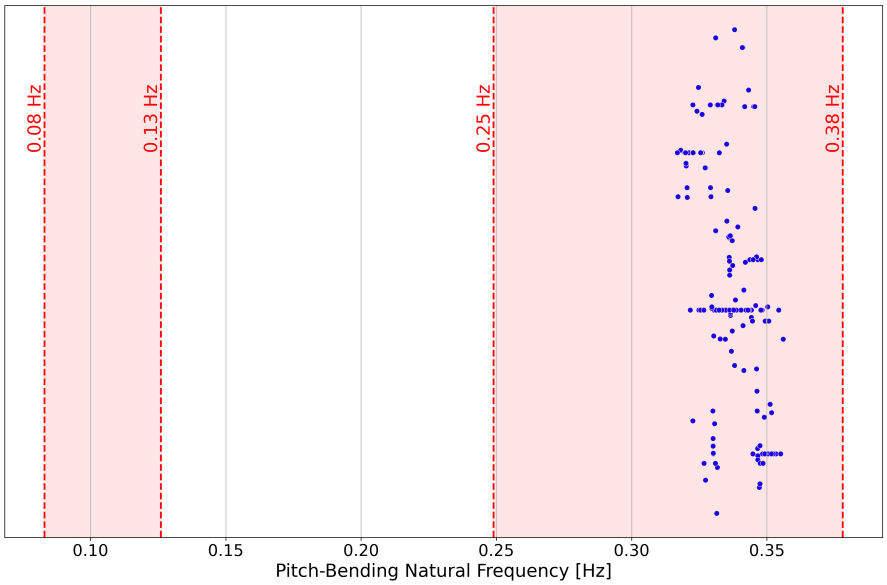

Figure 6.11: An indication the location of the first pitch bending frequencies of the different concepts.

When the system's natural frequencies fall within the 3P excitation range, significant resonance effects may occur due to tower shadowing and wind shear. These effects can trigger structural resonance and result in large power pulsations, which are undesirable for both performance and reliability [67]. To avoid or mitigate resonance within the 3P region, several strategies can be considered:

- **Controller tuning:** Adjust the turbine controller to actively dampen 3P excitation, or configure the pitch control to quickly pass through the resonance zone during transient conditions [67].
- **Tower design modification:** Modify the tower geometry or material properties to shift the pitch-bending mode away from the 3P frequency band.
- **Tendon stiffness adjustment:** Use stiffer or more flexible tendons to alter the pitch-bending natural frequency, thereby avoiding the 3P resonance zone. This is also influenced by tendon length and therefore the water depth as pitch stiffness is governed by EA/L.

For the remainder of this research, the constraint on the pitch-bending natural frequency was relaxed to avoid over-constraining the design space. While adjusting tendon stiffness could offer a potential solution within the framework, the current reference tendon specifications do not allow for practical modification. Nevertheless, this presents an interesting opportunity for further research.

6.2. Design Characteristics for System Cost

As the objective of this study is to reduce the levelised cost of energy, an assessment was made to determine which design variables and system responses most significantly influence this objective. A mutual information plot is generated for this purpose, which can be seen in Figure 6.12. The most significant relations observed in this figure are summarised in Table 6.3.

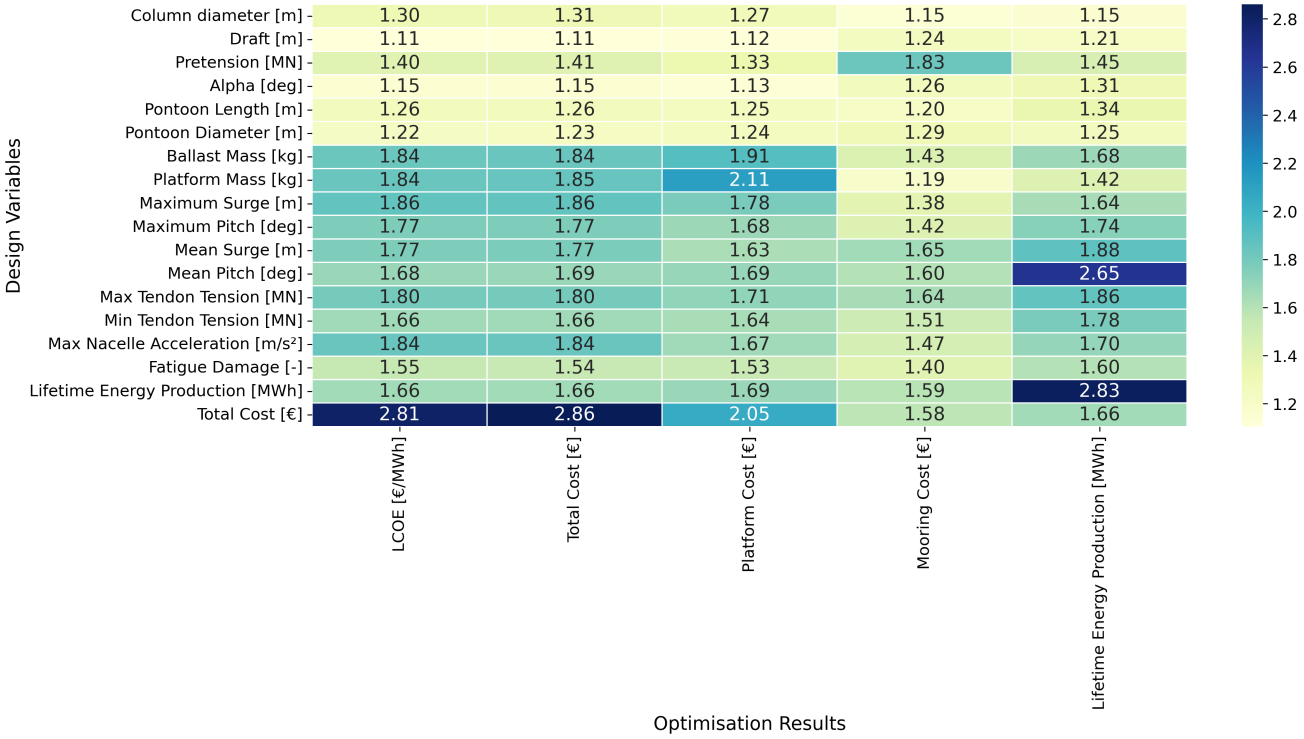

Figure 6.12: Mutual information between design variables and system responses with cost related optimisation results.

Table 6.3: Significant mutual information relations of desing variables or responses with cost related results.

Variable	Significant correlation with outcome
Pretension	Mooring cost
Ballast mass	LCOE, total cost, platform cost, LEP
Platform mass	LCOE, total cost, platform cost, LEP
Surge	Platform cost, mooring cost
Mean pitch	LCOE, total cost, platform cost, LEP
Maximum tendon tension	LCOE, total cost, platform cost
Minimum tendon tension	LCOE, total cost
Nacelle acceleration	Platform cost

Two general observations can be made. First, the lifetime energy production has less influence on the LCOE than the cost components. This is because all feasible designs exhibit relatively small pitch motions, leading to similar energy production over their lifetime. In contrast, cost varies more significantly across designs, making it the dominant factor in LCOE variation.

Second, several system response parameters show a strong relation to cost. These indicate that designs with larger motions and higher tendon tension variations often use less material and have lower mooring pretension, resulting in lower cost. An elaboration of this can be seen in subsection 6.2.3.

6.2.1. The Influence of Design Variables

As shown in Figure 6.13, an increasing pretension leads to higher mooring cost. This is directly linked to the influence of pretension on the number and size of required anchors and tendons. It can also be seen that the most cost-efficient designs, in terms of LCOE, are associated with low pretensions and therefore low mooring costs.

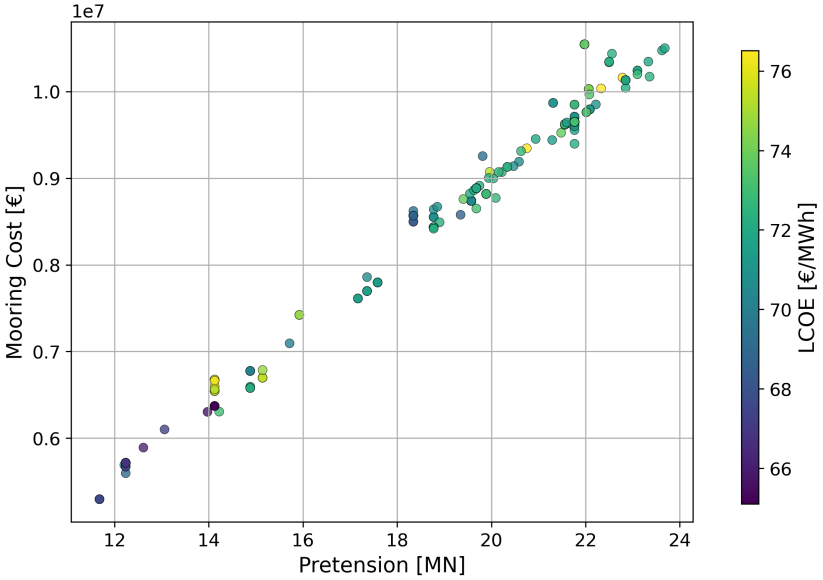

Figure 6.13: Pretension with relation to mooring cost.

6.2.2. The Influence of Platform Mass and Ballast Mass

From Figure 6.14 and Figure 6.15, it is clear that a decrease in mass leads to a reduction in cost. However, based on the steeper slope and stronger trend in Figure 6.15, platform mass has a greater influence on total system cost than ballast mass. This is consistent with expectations, as the platform mass is significantly larger and the cost price per ton of platform mass is approximately four times that of the ballast mass.

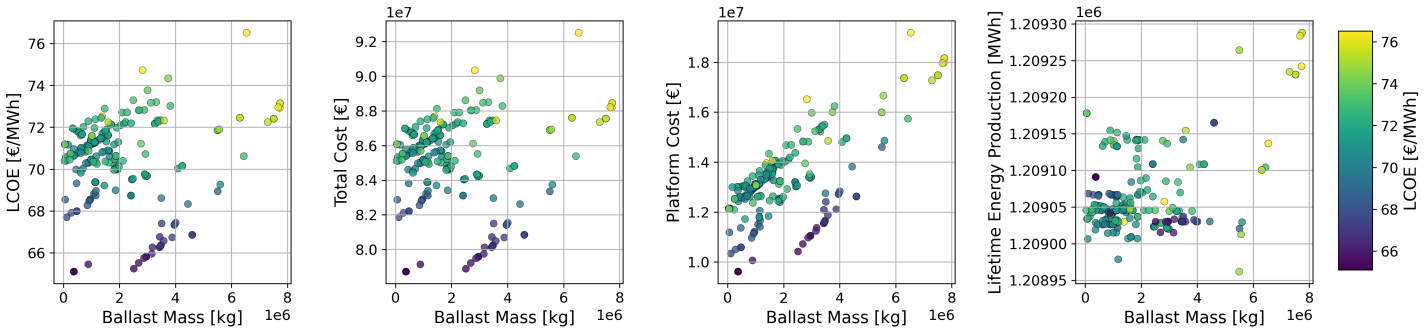

Figure 6.14: Ballast mass with relation to cost related results.

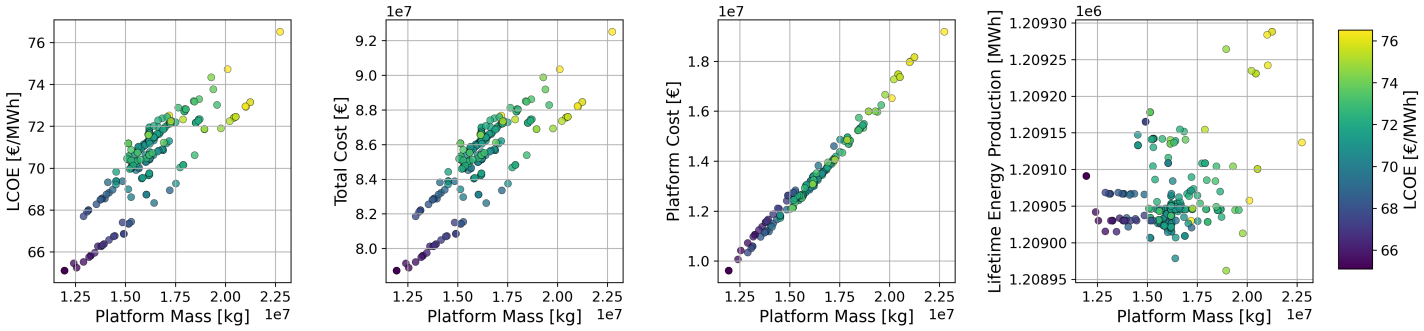

Figure 6.15: Platform mass with relation to cost related results.

In order to understand which parameters has the largest influence on the platform cost, Figure 6.16 shows the influence of the different design variables on the platform cost. The most significant trends in these graphs are the decreasing cost with decreasing column and pontoon diameter. Indicating that these have the largest influence on the eventual platform cost.

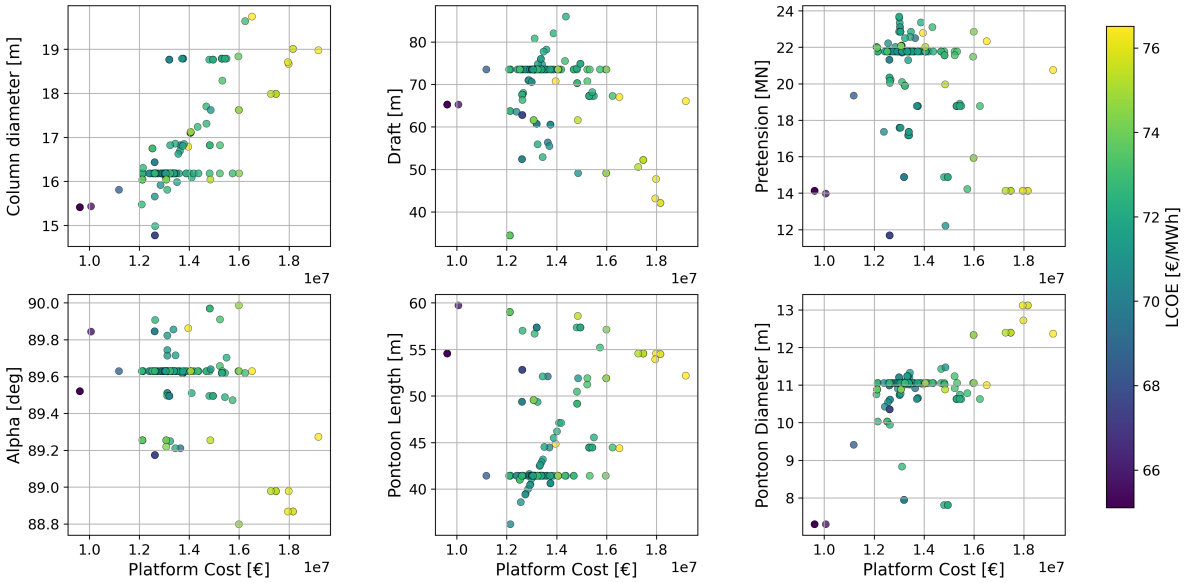

Figure 6.16: The influence of design variables on platform cost.

6.2.3. The Influence of Response

Although multiple response results show a strong correlation with cost, they generally follow the same trends as elaborated upon before. Therefore, only a few response–cost relations are discussed in this subsection. Figure 6.17 shows that configurations that decrease in platform cost, increase in surge offset. An increase in surge offset is associated with a decrease in surge stiffness. This means that the configuration has either longer tendons, thereby reducing the draft which reduces the platform cost, or the system has lower pretension, thereby reducing the buoyancy force which results in more slender column diameters and therefore a reduced platform cost. At the same time, the effect of decreasing pretension, which increases the surge offset, can be noticed in the mooring cost which can be seen in Figure 6.18. A similar trend is seen in Figure 6.19, where higher nacelle accelerations are associated with lower platform cost. Generally, designs with less structural mass and mooring requirements result in larger motions but lower costs.

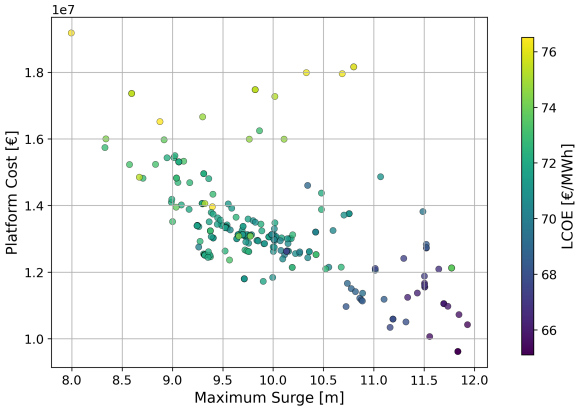

Figure 6.17: Maximum surge response with relation to structural cost

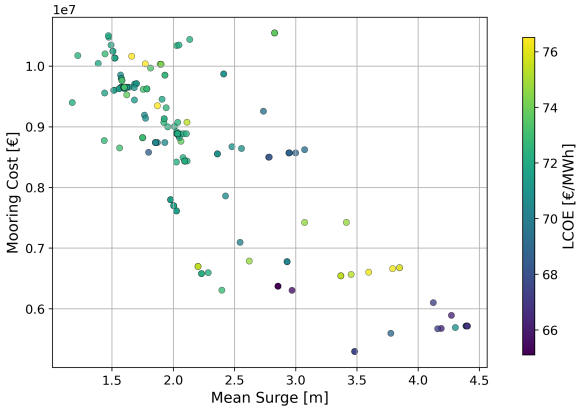

Figure 6.18: Mean surge response with relation to mooring cost

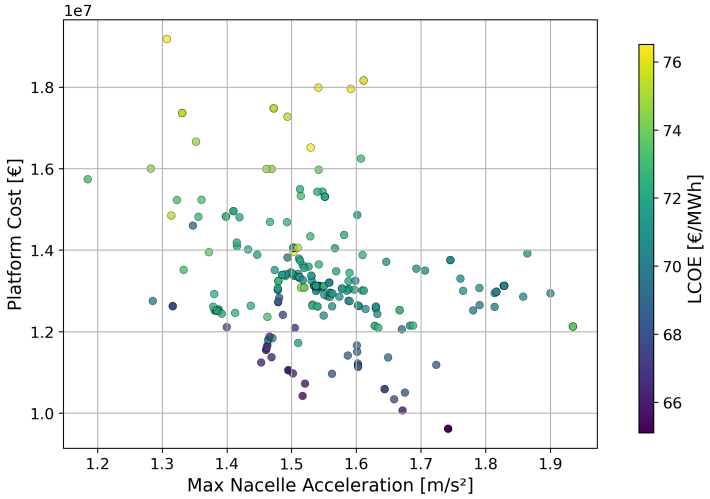

Figure 6.19: Maximum Nacelle Acceleration with relation to Platform cost

Figure 6.20 reveals two main trends. First, when the mean pitch angle increases, the system cost generally decreases. This is expected, since a reduction in structural mass and mooring stiffness will induce larger pitch motion, leading to lower costs. Second, a clear relationship is observed between the mean pitch angle and the lifetime energy production. A decrease in mean pitch angle, increases the LEP. This is attributed to the pitch-back motion of the platform, discussed in Figure 6.1.1, which keeps the turbine in a more upright position during most operational conditions, thereby improving the energy generation over the system's lifetime.

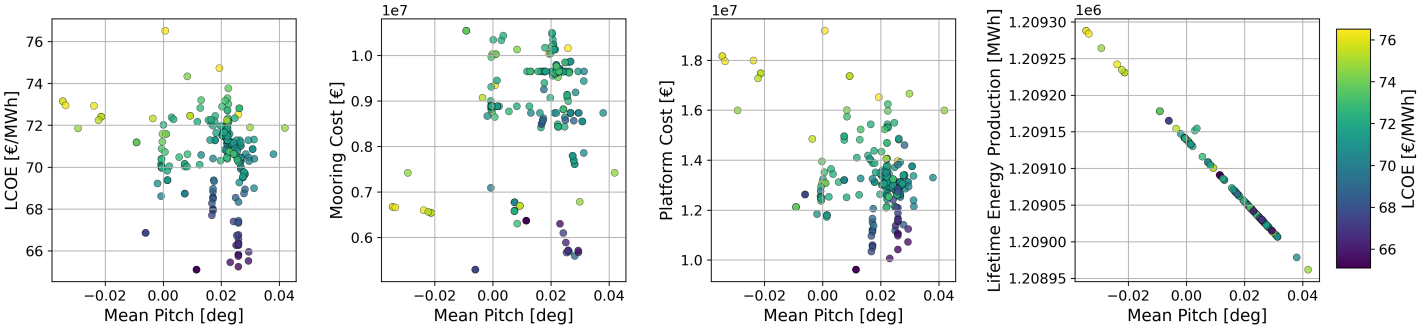

Figure 6.20: Mean pitch vs Cost related results.

6.2.4. System Cost Driving Parameters

From this analysis, it becomes clear that the key drivers of LCOE in this study are the platform mass and tendon pretension. These two parameters have the most significant impact on system cost and therefore on the resulting LCOE. For the platform mass, the main column diameter and pontoon diameter showed to have the most significant influence. However, it was also showed that the platform mass is dependent on all design variables in terms of geometry which again emphasizes the need to take all design variables into account for system optimisation. Furthermore, the lifetime energy production is relatively similar across all feasible designs, making the influence on the LCOE less significant.

7

Optimisation Study Results

This chapter presents the results of an optimisation study using the developed optimisation framework. The outcomes are evaluated in terms of their performance, quality and relevance within the broader context of the frameworks intended application.

7.1. Optimisation Study Results Analysis

This section presents how the optimisation algorithm converges, what design spaces were identified and the most cost-efficient design which resulted from the optimisation study. For this analysis, all the feasible design concepts of multiple optimisation runs are merged to give a complete overview. Furthermore, in the figures presented in this section, vague colours indicate regions of the design space with fewer evaluated concepts, while more pronounced colours represent areas with a higher concentration of evaluated designs.

7.1.1. Convergence

Figure 7.1 shows how the LCOE progresses per generation with relation to the dynamic constraints. It can be seen that throughout the generations the LCOE decreases, which indicates that the algorithm successfully converges to more cost-efficient designs.

The LCOE decreases where the maximum surge increases towards the constraint and minimum tension decreases towards the constraint. For the other dynamic response the similar trends can be seen where an increase or decrease in response leads to decreasing LCOE. However, these all stay well within the given constraints. Especially fatigue remains small which might be an indication of over designed structures due to the possibly conservative diameter over thickness ratio in this research.

Figure 7.1 effectively shows that the limiting constraints for feasible designs are the maximum surge and minimum tendon tension. As these limits are approached throughout the generations, the LCOE reduces. This does not mean that all designs evaluated by the algorithm that meet these governing constraints also satisfy the other constraints, as these plots only show the feasible designs. Infeasible designs could occur when remaining within the surge constraints but overshooting the fatigue constraint for example.

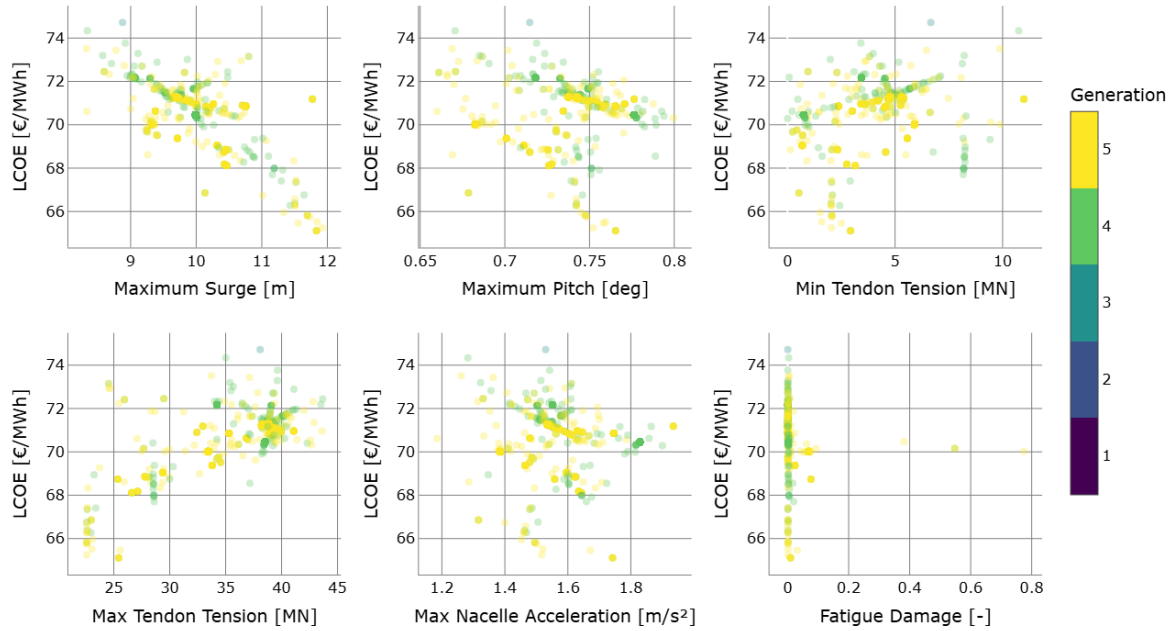

Figure 7.1: Convergence of the optimisation with respect to dynamic constraints, including only feasible design concepts.

7.1.2. Design Space

As the genetic algorithm explores the design space, different design spaces were identified which can be recognised by clustering of concepts in Figure 7.2. While there are multiple different combinations possible between the design variables, three main design spaces were identified. In the accompanying figures, a red star indicates the design variables of a representative concept from each cluster.

- **Design space #1:**
  Small column diameter, moderate draft, low pretension, long pontoons and large pontoon diameter (Figure 7.2).
- **Design space #2:**
  Moderate column diameter, large draft, large pretension, short pontoons, and large pontoon diameter (Figure 7.3).
- **Design space #3:**
  Large column diameter, large draft, moderate pretension, long pontoons, and small pontoon diameter (Figure 7.4).

Despite the identification of different design spaces, all feasible configurations have LCOE values which are close to each other (65–76 [€/MWh]). This demonstrates that multiple TLP designs can achieve similar economic performance through different combinations of design variables. As a result, the final selection of a concept within this framework allows for site-specific factors such as water depth and logistical constraints.

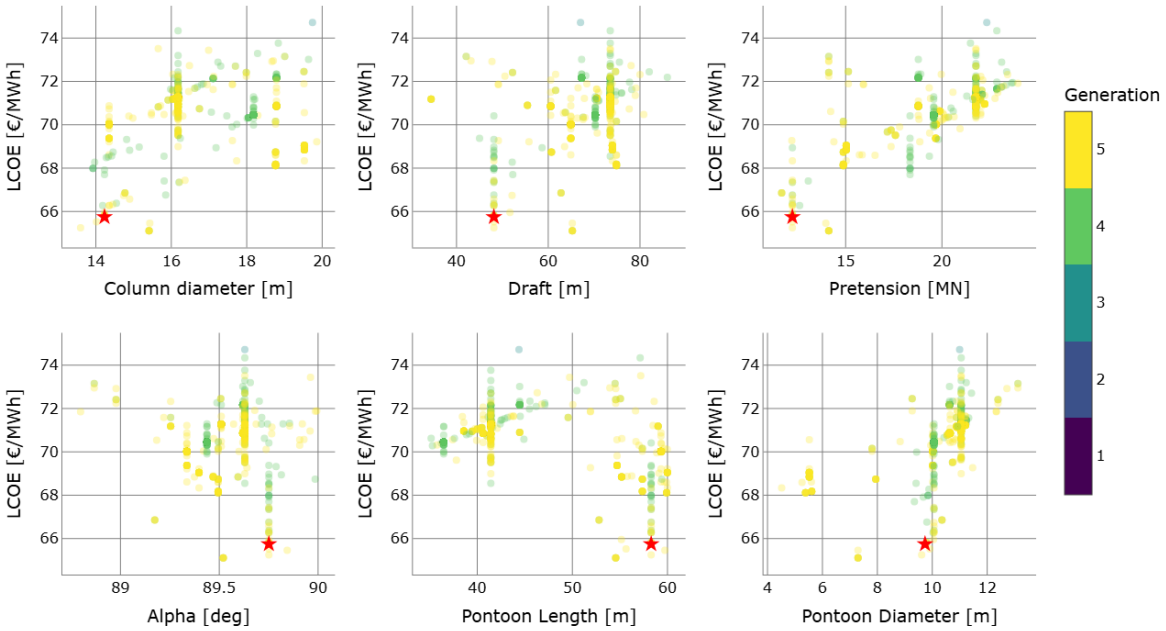

Figure 7.2: Design space #1 where the red star indicates a single design throughout the variables.

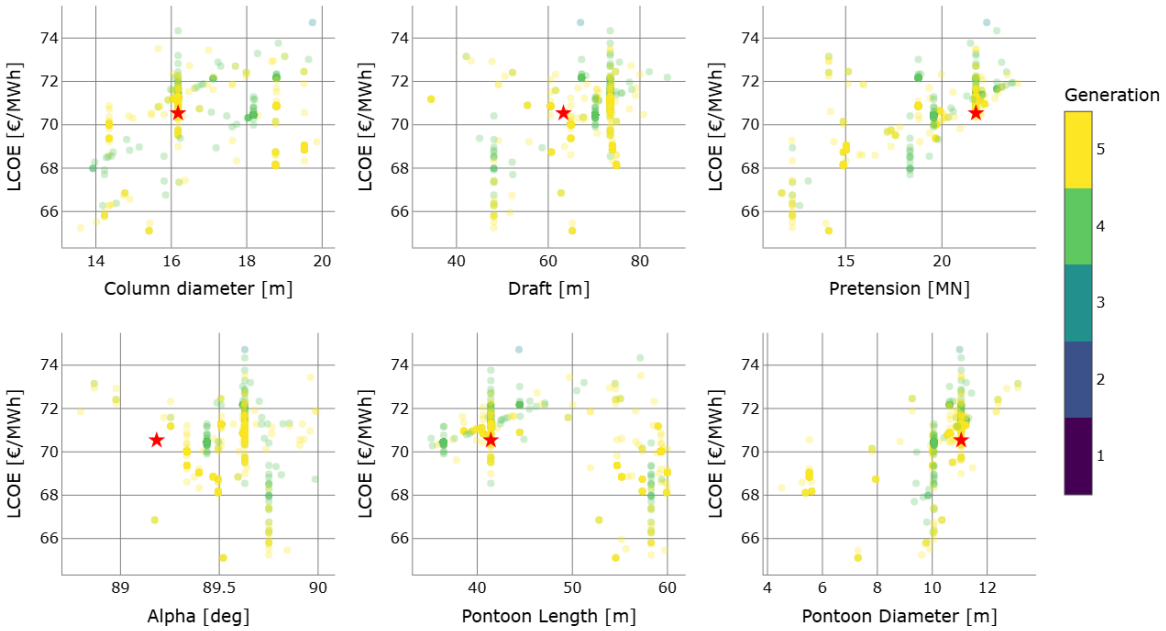

Figure 7.3: Design space #2 where the red star indicates a single design throughout the variables.

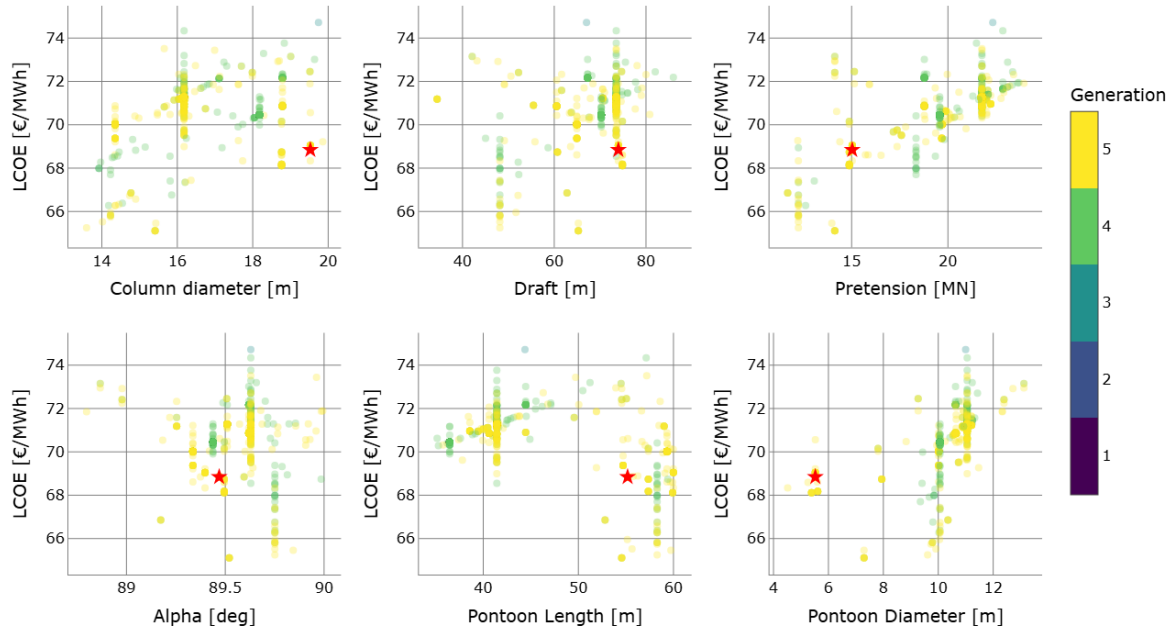

Figure 7.4: Design space #3 where the red star indicates a single design throughout the variables.

7.1.3. Design Concepts Resulting from the Optimisation Study

From the different design spaces three concepts were selected to analyse the optimisation results in more depth. The designs are visually presented in Figure 7.5, with their properties listed in Table 7.1. Result #1 was the most cost-efficient design which resulted from this optimisation study.

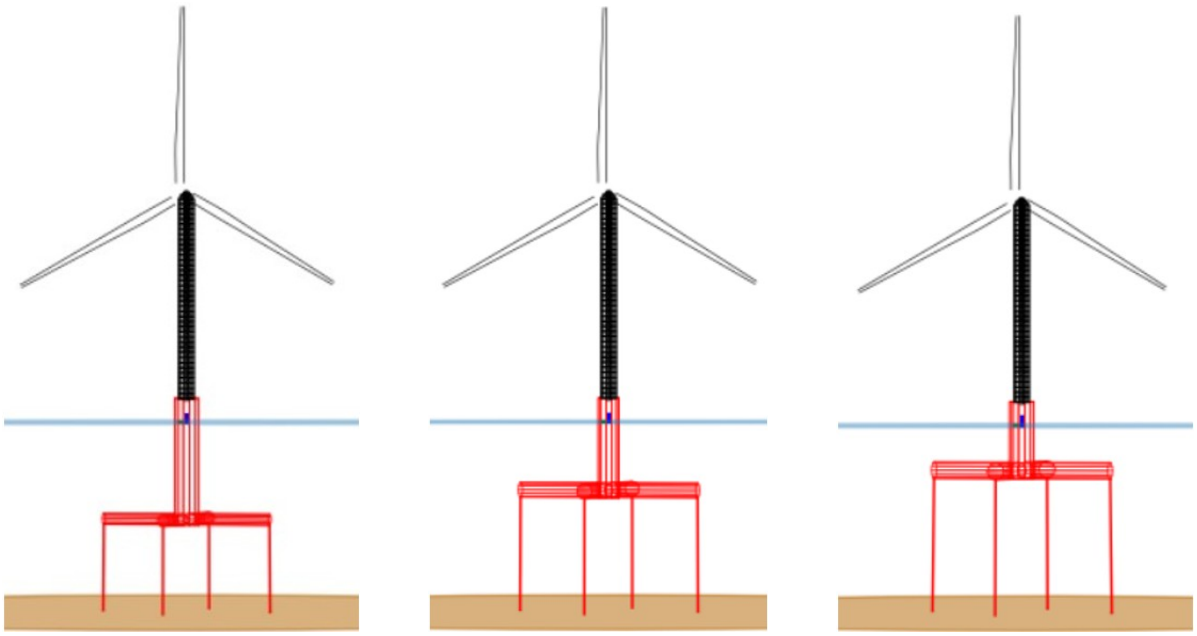

(a) Result #1 **(b)** Result #2 **(c)** Result #3

Figure 7.5: Optimal results in terms of LCOE from several runs.

Table 7.1: Basic Properties of the optimisation outcome results.

Property	#1	#2	#3	Unit
Main column diameter	15.41	13.59	16.04	[m]
Main column draft	65.26	48.15	34.47	[m]
Pontoon diameter	7.30	9.61	10.88	[m]
Pontoon length	54.56	58.29	59.01	[m]
Pretension	14.12	12.23	21.98	[MN]
Tendon Angle	89.52	89.75	89.25	[deg]
Platform cost	9.61	10.98	12.12	[M€]
Mooring cost	6.37	5.63	10.54	[M€]
Constant costs (O&M, installation, etc.)	61.2	61.2	61.2	[M€]
LEP	1.21	1.21	1.21	[TWh]
LCOE	65.11	65.25	71.18	[€/MWh]

The most cost-efficient design, result #1, is a design with slender columns and a deeper draft. The reason for this is that these columns with small diameters significantly reduce the platform cost, which was also identified in Chapter 6. Furthermore, as the tendons are relatively short and the pretension is moderate, the mooring cost is also limited.

Result #2 shows to have more platform costs compared to Result #1. This is mainly due to the larger pontoon diameter and pontoon length, which show to have a larger impact than the reduced main column diameter and main column length. However, this design performed better compared to the other designs in terms of mooring cost. This is due to the low pretension. This also further emphasizes the relation found in Chapter 6 which indicated that the mooring cost significantly reduces as the pretension reduces.

Lastly, result #3 is a concept with a shallow draft. As can be seen in Table 7.1, this concept has high mooring cost compared to the other results due to the large pretension. It might seem counter intuitive that a more shallow structure has a larger pretension, as you would assume the buoyancy force of such a design is low. However, due the increment in tendon length, the pretension also needs to increase to remain within the surge constraint as explained in Chapter 6, increasing the mooring cost. Furthermore, to keep the vertical forces in balance, an increase in buoyancy is created by increasing pontoon and main column diameter, increasing the platform cost compared to the other results.

To conclude, since column and pontoon diameter strongly influence platform mass, the most cost-efficient designs have slender columns while still satisfying all constraints. Additionally, because pretension drives mooring cost, the optimisation favours designs with lower pretension. These designs often have a larger draft to maintain sufficient surge stiffness and remain within the surge constraint.

7.1.4. Interpretation of the Optimisation Study Results

To assess the potential for further design improvements, it is essential to first understand the limitations that prevent additional cost reductions, as well as the current constraints related to platform dimensioning and the associated logistical and manufacturing aspects. This section evaluates the most critical constraints of the current most cost-efficient design and explores how they are affected by the governing design variables in terms of cost. Additionally, it discusses the real-world feasibility of the design in terms of construction yard capacity and transport requirements.

As discussed in subsection 7.1.3, the optimal design consists of slender cylinders combined with moderate pretension. When evaluating this design in terms of system response, the minimum tendon tension and maximum surge were identified as the most critical constraints. The response of the most cost-efficient design with respect to the constraints can be seen in Table 7.2.

Table 7.2: System response of the most cost-efficient design compared to the design constraints.

Response	Maximum/Minimum Value	Constraint Limit	Unit
Maximum Surge	11.83	12	[m]
Maximum Pitch	0.76	10	[deg]
Minimum Tendon Tension	2.93	0	[MN]
Maximum Tendon Tension	25.44	80	[MN]
Maximum Nacelle Acceleration	1.74	2.8	[m/s^2]
Fatigue Damage	0.01	1	[-]

These constraints effectively limit further cost reductions. To be more specific, the most influential variables on cost, identified in Chapter 6, have the following effect on the constraints.

- **Reducing pretension**, directly lowers mooring cost and indirectly lowers platform costs due to decreased buoyancy requirements. However, it leads to larger surge excursions that exceed the surge constraint and reduces the mean tendon tension, resulting in violations of the the minimum tendon tension limit.
- **Reducing platform diameters** decreases platform mass and cost but also reduces buoyancy and therefore pretension, increasing the likelihood of exceeding surge and minimum tendon tension constraints.

Furthermore, the current optimal design features a large draft of approximately 65 m and a pontoon span of about 110 m from end to end. These large dimensions present practical constraints for both manufacturing and installation. Assuming a conservative scenario in which each structure requires a dedicated assembly area without overlap, the total area occupied per platform is approximately 1 hectare. This means that constructing all platforms of a large wind farm at the same time would require exceptional yard capacity. Table 7.3 presents a selection of the largest offshore wind development ports worldwide. The table shows that only a few of these ports currently have sufficient space to accommodate more than 25 units at once.

In addition, common heavy-lift barges used for float-over operations and offshore installation typically offer deck spaces around 150 m by 40 m [45]. For this reason, only one TLP can be transported per barge at a time. This restriction increases logistical complexity and increases installation time, which significantly adds to the eventual costs.

Table 7.3: Yard areas at selected major offshore wind construction ports.

Port	Terminal Area [ha]	Source
Port of Esbjerg - (Denmark)	450	[44]
Port of Paulsboro - (USA)	81	[100]
Rotterdam Maasvlakte - (Netherlands)	70	[99]
Eemshaven - (Netherlands)	25	[109]

7.1.5. General Design Insights and Recommendations

Because the surge response constraint and the tendon tension constraints were identified as the primary limiting factors in this study, further improving the cost-efficiency of the structure should focus on reducing both surge motions and tendon tension variations. Reduced surge and tendon tension responses would allow for lower pretensions and reduced main column or pontoon dimensions, which in turn could decrease both platform and mooring costs. Additionally, reducing overall system dimensions would simplify construction and installation logistics, leading to further cost savings.

Based on the trends identified in this research and the configuration of the current model, the following general design recommendations can be formulated for the most cost-efficient concept. These recommendations also include the sensitivity of such design adjustments and their effects on the final results. The recommendations are also expected to be beneficial across all design concepts evaluated in this study.

Increasing Added Mass and Damping

In the equation of motion solved for response, two important terms are the hydrodynamic added mass and the viscous damping. Increasing these terms can reduce platform motions. Table 7.4 and Table 7.5 show the impact of varying added mass and damping on system response and the potential effects on system cost and dimensions. In these tables Added mass $= 1$ represents the original added mass of the most cost-efficient design, Added mass $= 0.8$ represents a 20% reduction of added mass compared to this original value.

First of all, added mass has a more significant effect on the platform response compared to viscous damping. Under the most extreme load cases, the response is driven by the energy of the first-order wave forcing rather than by the sharp resonance peaks at the natural frequencies. Resonant peaks are narrow, so they contribute little to overall response levels as they have a low impact on standard deviation. In contrast, the wide spectral peak of first-order waves dominates the motion, resulting in damping having a small effect.

As shown in Table 7.4, a 20% increase in added mass reduces system motions significantly. The surge motion for example is reduced by $\pm$ 9%. Conservatively, a 9% reduction in surge response can be linearly linked to a 9% reduction in the required pretension. Lower pretension decreases the mooring costs and platform costs, as less buoyancy is needed to balance the mooring loads. This reduction in buoyancy allows for shorter pontoons, reducing the overall platform footprint, which is beneficial for manufacturing and installation purposes. It may also allow for lower drafts in the case the main column length poses issues. It should be noted that for the tables in this section, a reduction in platform footprint and a reduction in draft are presented as separate cases. These results have the goal of giving insight into how the currently large and limiting sizing parameters of the current most cost-efficient design may be influenced by design modifications.

Table 7.4: Percentage decrease of response and cost metrics for different added mass values for $H_s = 10.50$ m, $T_p = 14.30$ s, $V_w = 10.59$ m/s.

Variable	**Reduction of Response [%]**				
Added Mass	**0.80**	**0.90**	**1.00**	**1.10**	**1.20**
Maximum Floater Surge	-12.54	-5.45	0.00	4.57	9.09
Maximum Hub Pitch	-4.92	-2.21	0.00	1.85	3.40
Maximum Fore Tendon Tension	-1.94	-0.76	0.00	0.51	1.11
Maximum Aft Tendon Tension	13.27	5.19	0.00	-3.52	-7.57
Maximum Nacelle Acceleration	-15.92	-7.30	0.00	6.28	11.79
	Reduction of Cost/Platform Dimensions [%]				
Mooring Cost	-12.54	-5.45	0.00	4.57	9.09
Platform Cost	-7.40	-3.22	0.00	2.70	5.36
Total Cost Decrease	-9.45	-4.11	0.00	3.44	6.85
Platform Footprint Reduction	-41.39	-17.13	0.00	13.30	25.54
Draft Reduction	-14.19	-6.17	0.00	5.17	10.29

Table 7.5: Percentage decrease of response and cost metrics for different viscous damping values for $H_s = 10.50$ m, $T_p = 14.30$ s, $V_w = 10.59$ m/s.

Variable	Reduction of Response [%]				
Viscous Damping	**0.80**	**0.90**	**1.00**	**1.10**	**1.20**
Maximum Floater Surge	-1.22	-0.55	0.00	0.46	0.86
Maximum Hub Pitch	1.17	0.62	0.00	-0.69	-1.44
Maximum Fore Tendon Tension	-0.33	-0.14	0.00	0.10	0.16
Maximum Aft Tendon Tension	2.25	0.95	0.00	-0.67	-1.11
Maximum Nacelle Acceleration	-0.25	-0.12	0.00	0.11	0.23
	Reduction of Cost/Platform Dimensions [%]				
Mooring Cost	-1.22	-0.55	0.00	0.46	0.86
Platform Cost	-0.72	-0.32	0.00	0.27	0.51
Total Cost Decrease	-0.92	-0.41	0.00	0.35	0.65
Platform Footprint Reduction	-3.70	-1.65	0.00	1.38	2.57
Draft Reduction	-1.38	-0.62	0.00	0.52	0.97

In order to increase the added mass and damping to get to these reductions in cost and footprint, an efficient design recommendation is proposed by adding (holed) fins to the structure. This increases damping and added mass as described in literature [71]. However, it should be noted that these design additions may increase drag and inertial forces which should then be accounted for in the system analysis to assess the overall impact of such design modifications.

Damp Tendon Tensions

Tendon tension was identified as a limiting factor in the current study. Introducing tendon damping in the axial direction can reduce dynamic tendon tensions. An example of a damper is shown in Figure 7.6, where a spring-damper element is marked by the red rectangle. Literature shows that incorporating this type of damper in mooring lines reduces dynamic tendon tensions by 11–25% [16]. Lower dynamic tendon tensions directly reduce system costs by allowing the pretension to be lowered without risking slack events caused by insufficient mean tension. Although the most cost-efficient design identified here did not experience violation of fatigue-related constraints, this reduction in dynamic loads may also decrease fatigue at the connection between the pontoon and the main column. This may enable more efficient structural design and help reduce platform costs. It should be noted that incorporating such damping systems introduces additional complexity and cost to the overall design, which requires further evaluation. Moreover, to the knowledge of the author, tendon dampers suitable for offshore applications and capable of handling the tension magnitudes in this TLP concept are not yet commercially available.

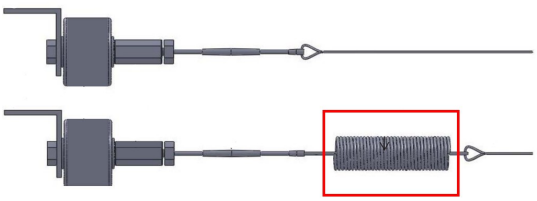

Figure 7.6: An example comparison of a tendon with and without a spring damper [16].

Improving Structural Design

In this research, a constant diameter over thickness ratio (D/t) is assumed for the main column and pontoon design. This parameter strongly affects the amount of steel required and thus the structural cost. A conservative D/t leads to heavier and more expensive structures, which can result in over designed structures. For example, the most cost-efficient design identified in this study has a lifetime fatigue damage of only 0.01, indicating over designed structural capacity. Allowing more thin-walled designs (higher D/t) may also shift the optimisation outcome potentially leading to platform diameter becoming less dominant in driving cost, while other variables such as draft and pontoon length could become more influential.

Table 7.6 shows the impact of different D/t values on fatigue and platform cost. Fatigue damage increases with D/t and must be carefully managed, but cost reductions are significant. In this analysis, steel mass is reduced for higher D/t, while total mass is kept constant by substituting less expensive ballast mass.

Table 7.6: Indicative influence of column slenderness (D/t) on fatigue, platform cost and total cost.

D/t	Fatigue Damage [-]	Reduction of Platform Cost [%]
60	0.01	0.00
100	0.54	31.38
140	3.16	44.96

To reduce system cost while maintaining structural fatigue life, more efficient structural designs are required. Examples of improving the structural design are including braces and stringers, as illustrated in Figure 7.7. These design elements improve the structure's ability to handle stress while potentially significantly reducing mass. Braces take up part of the experienced loads, reducing the loads at the connection between the pontoon and main column. Stringers efficiently increase the structural moment of inertia, thereby reducing bending stresses with just a relatively small increase in mass.

By placing the stringers on the outside of the pontoon, two potential design improvements can be combined. First, when placing the stringers on the pontoon exterior, the stringer areas are further away from the centreline compared to design with stringers on the pontoon insides. This increases the cross section moment of inertia, reducing the experienced bending stress. Next to this, stringers on the pontoon exterior increase the added mass and viscous damping which has beneficial effects, as mentioned before in subsection 7.1.5.

In practice, these solutions should be welded onto the structure at the construction site, which may introduce additional manufacturing costs. This is particularly relevant for components like stringers, where welding long structural elements can be time-consuming and labour-intensive. However, despite the additional costs, these design adjustments may still lead to more cost-efficient structures due to significant reductions in steel consumption.

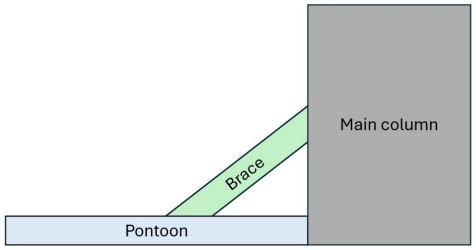

(a) Example of a brace to improve the current design.

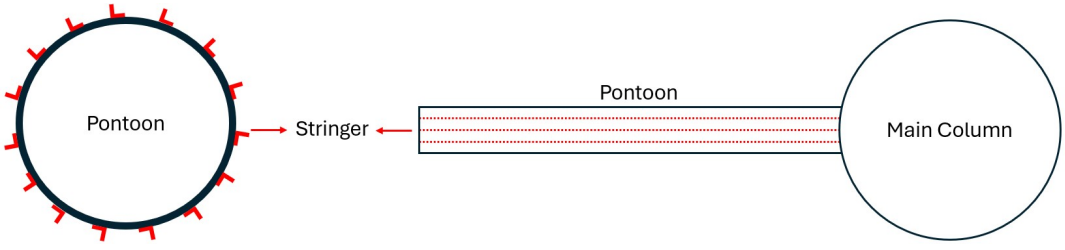

(b) Example of an implementation of stringers to improve the current design.

Figure 7.7: An example of a brace and an example with stringers on the pontoon exterior surface to improve system structural design.

Tendon Material Selection

As tendon material properties and tendon area influence system response and mooring cost, the impact of different tendon axial stiffnesses was analysed. Table 7.7 shows the relative influence for different tendon axial stiffnesses with a load case of $H_s = 1.71$ m, $T_p = 7.72$ s, $V_w = 10.59$ m/s. In this table, $EA = 1$ represents the original value of the most cost-efficient design, $EA = 0.6$ represents 60% of the original axial stiffness. It can be seen that generally, with increasing tendon axial stiffness the system response decreases.

Table 7.7: Percentage reduction of response metrics for different tendon stiffnesses (EA).

Variable	Reduction of Response [%]								
EA	**0.6**	**0.7**	**0.8**	**0.9**	**1.0**	**1.1**	**1.2**	**1.3**	**1.4**
Maximum Floater Surge	-2.36	-1.64	-2.60	-2.93	0.00	3.69	6.27	7.73	8.27
Maximum Hub Pitch	-5.36	-3.41	-1.95	-0.85	0.00	0.71	1.31	1.83	2.28
Maximum Fore Tendon Tension	-0.66	-0.41	-0.35	-0.31	0.00	0.35	0.56	0.62	0.50
Maximum Aft Tendon Tension	1.73	1.11	0.92	0.76	0.00	-0.91	-1.49	-1.66	-1.34
Maximum Nacelle Acceleration	-1.39	-0.39	-0.45	-0.65	0.00	0.70	0.96	0.85	0.44

However, Table 7.7 shows that some response metrics do not vary consistently with varying tendon axial stiffness. This occurs because varying EA shifts the platform's natural frequencies and therefore alters the interaction with the aero-hydrodynamic excitation and frequency dependent aerodynamic added mass and damping. Figure 7.8 shows the normalised surge spectrum, including the terms in the equation of motion for different frequencies and the natural frequencies for each EA value.

In this figure, all frequency-independent components, such as hydrodynamic added mass, viscous damping and system stiffness, are normalised to one. The aero-hydrodynamic excitation, aerodynamic added mass and aerodynamic damping are frequency-dependent. At different frequencies, the combinations of the terms in the equation of motion influence the eventual maximum system response. This effect is most significant for surge, where the surge natural frequencies for different EA values are indicated by the vertical lines at low frequencies with a value of approximately 0.2 [rad/s]. In this range, the forcing and aerodynamic terms exhibit more significant variation with frequency than at the higher-frequency pitch bending modes (the vertical lines indicated at approximately 2 [rad/s]) , where these terms remain relatively constant.

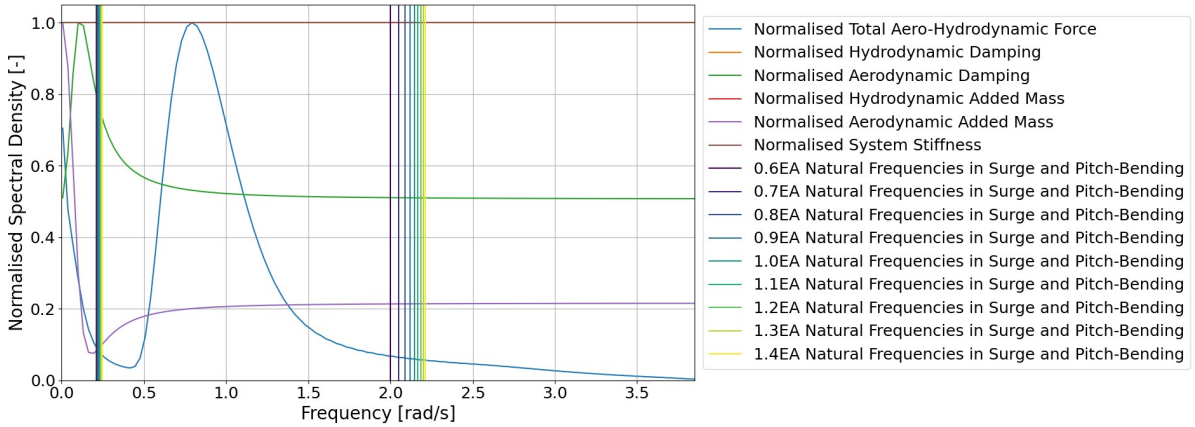

Figure 7.8: Indication of different terms of the equation of motion with varying frequency and the natural frequencies for different axial stiffness values with $H_s = 1.71$ [m], $T_p = 7.72$ [s], $V_w = 10.59$ [m/s].

Consequently, the maximum surge response is sensitive to the platform's natural frequency placement and therefore to tendon axial stiffness. This surge response also directly influences the nacelle acceleration. A clear overview of how these responses vary with different tendon properties can be seen in Figure 7.9.

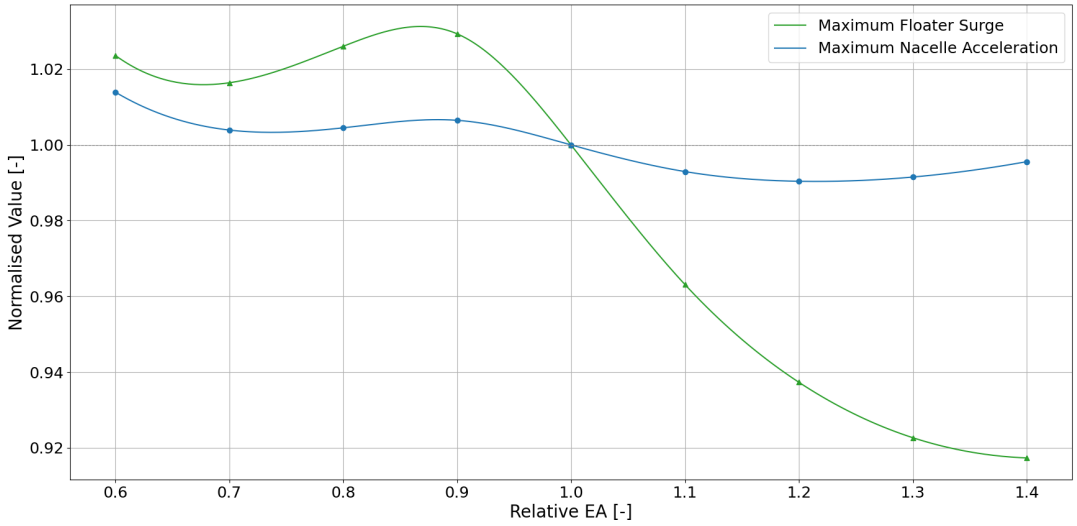

Figure 7.9: Normalised variation of responses with respect to varying axial stiffness (EA) with $H_s = 1.71$ [m], $T_p = 7.72$ [s], $V_w = 10.59$ [m/s].

Overall, this sensitivity study shows that changing the tendon axial stiffness offers two options to decrease the mooring cost. The first option is to use more flexible, often less expensive tendons, at the cost of increased responses. The second option is to use stiffer, more expensive tendons to reduce the responses, which in turn may reduce system cost by a reduction of pretension for example. Furthermore, it was shown that a lower EA does not always result in an increased response. Since EA also shifts the system natural frequencies, the maximum response may decrease if the new natural frequencies align with a higher damping and added mass or lower excitation.

Material and Equipment Selection
In this study the total variable platform cost, based on the platform material and equipment selection, used the following cost estimates.

- A steel shell structure with a cost of 800 €/ton.
- A Magna Dense ballast with a cost of 150 €/ton.
- Anchoring costs of 100 €/kN of pretension
- Steel wire tendon costs of 70 €/m/MN (MBL).

Table 7.8 shows the sensitivity of these cost parameters for the most cost-efficient design of this optimisation study. This table shows how a range of component cost factors influences the total variable system cost. For example, it can be seen that by reducing the platform steel cost with 50% the total variable platform cost reduces by 29.90%. This table also shows that the ballast cost and mooring line cost are of smaller influence compared to the platform steel cost and anchor cost.

Table 7.8: Sensitivity of component costs to total variable system cost where the most cost-efficient design with current cost paramters has component cost factor of 1.

Component cost factor	0.50	0.75	1.00	1.25	1.50
Platform steel cost effect on total variable platform cost [%]	29.90	14.95	0.00	-14.95	-29.90
Ballast cost effect on total variable platform cost [%]	0.18	0.09	0.00	-0.09	-0.18
Anchor cost effect on total variable platform cost [%]	17.67	8.84	0.00	-8.84	-17.67
Mooring line cost effect on total variable platform cost [%]	2.26	1.13	0.00	-1.13	-2.26

In order to further reduce platform cost, a practical solution is to use more cost-efficient materials such as concrete [34]. The implementation of a concrete structure should however be evaluated in more detail to assess the structural integrity of such a structure while reducing the system costs. Another

potentially large cost reduction would be to use more cost-efficient anchors. Currently, the study is based on suction pile anchors. However, vertical load anchors or torpedo pile anchors might offer a more cost-efficient solution for the current problem, reducing the anchor cost in certain cases up to 30% according to literature [21] [90].

Subsystem (Re)Design for Constraint Management
Currently, the maximum surge constraint is imposed to prevent damage to the turbine power cable [46]. Overall, it may be more efficient to redesign the power cable to be compatible with larger surge offsets. Allowing the cable to tolerate greater excursions could relax the surge constraint. This may lead to reductions in pretension and platform dimensions, lowering total system costs.

However, it should be noted that with increasing site water depth, surge offset becomes less of a constraint for the power cable. In shallow to intermediate water depths, dynamic power cables, typically installed in a lazy-wave configuration, have limited vertical space to accommodate platform motions while still meeting design constraints on the curvature and clearances of the power cable. This results in increased cable tension and fatigue directly related to the the platform motions, as platform motions influence a greater proportion of the cable length in shallow waters compared to deeper sites [73].

In deeper waters, the available water column allows for larger cable deformations preventing excessive tensions and fatigue. This reduces sensitivity to surge excursions, suggesting that the currently applied surge constraint may be overly conservative for deep-water TLP applications. As water depth increases, the focus in power cable design can shift from dynamic response limitations toward optimising the cable's spatial footprint and installation practicality within the overall system layout [1]. For this reason, in deep waters, the redesign of the power cable may become unnecessary.

Another subsystem proposed in literature to reduce the surge offset, is the inclusion of thrusters. While dynamic positioning (DP) thrusters limit surge motions during extreme environmental conditions [89], their application in floating wind is generally considered impractical. DP systems are associated with high capital costs and increased power consumption. As such, they are unlikely to present a viable solution for floating offshore wind turbines.

7.2. Optimisation Quality

This section assesses the quality of the optimisation results, focusing on whether the results are physically realistic and whether the genetic algorithm adequately explored the design space, minimising the likelihood of missing potential cost-efficient design spaces.

7.2.1. Physical Quality of the Results

To verify the physical validity of the optimisation outcome, a comparison is made between RAFT and Orcaflex results for design #2 in Table 7.1 which resulted from the optimisation study. This is done for the full wind and wave load cases, including both first- and second-order wave effects. The comparison focuses on the most limiting response, namely surge and the tendon tensions. Table 7.9 presents the over(-)/under(+) prediction of RAFT compared to Orcaflex simulations for the base case design and a design resulting from the optimisation study. The discrepancies of RAFT compared to the non-linear time domain simulations are consistent across the different designs. This confirms the physical validity of the optimisation study results and demonstrates that RAFT can consistently and reliably simulate various TLP configurations with (near) vertical tendons. One main difference between the two design concepts is the tendon tension at high wind speeds. This difference originates from the pitch back behaviour of the optimisation study concept at this wind speed, effectively reducing the tendon tension variations.

Table 7.9: Over(-)/under(+) prediction of RAFT compared to OrcaFlex simulations for the base case design and a design resulting of the optimisation study.

Hs	Vw	Variable	Over(-)/Under(+) prediction base case [%]	Over(-)/Under(+) prediction Optimisation results [%]
1	5	Surge (platform)	8.43%	8.43%
1	5	Minimum aft tendon tension	-5.36%	-5.38%
1	5	Maximum fore tendon tension	2.84%	2.85%
2	13	Surge (platform)	6.30%	9.83%
2	13	Minimum aft tendon tension	8.05%	-0.34%
2	13	Maximum fore tendon tension	-1.92%	-0.33%
5	25	Surge (platform)	-14.61%	-14.94%
5	25	Minimum aft tendon tension	5.61%	8.92%
5	25	Maximum fore tendon tension	-3.72%	-5.72%

7.2.2. Convergence Quality

Genetic algorithms are designed to explore the entire design space in search of a global optimum. However, this process depends on the assumption that the initial population provides sufficient coverage of the full design space. Given the highly non-linear, six-dimensional design space used in this research, it is important to verify whether existing design spaces remain unexplored. To reduce this risk, the optimisation is ran multiple times. Table 7.10 lists the top three LCOE results for five optimisation runs, providing insight into the consistency and coverage of the results.

It can be observed from Table 7.10 that the optimisation results vary between different runs. Next to this, within the different runs the optimisation often converges to a top three of designs in the same design space. These trends highlight the influence of the initial population on the search process and indicates that the algorithm initially converges to local optimum. This behaviour particularly occurs in high-dimensional and non-linear design spaces, where the initial population may restrict the algorithm's ability to fully explore the entire design space. A visual representation is given in Figure 7.10. From this figure it can also be seen how the initial population influences the eventual number of feasible candidates per optimisation run. Run one and two find feasible design solutions from the third generation onwards, resulting in a reduced amount of feasible design outcomes compared to run three, four and five for example.

Table 7.10: Top 3 designs per optimisation routine (ranked by LCOE).

Run	Concept	$LCOE$ [€/MWh]	D_{column} [m]	**Draft** [m]	$D_{pontoon}$ [m]	$L_{pontoon}$ [m]	T_{pre} [MN]	α [deg]
1	1	69.26	17.62	49.12	11.47	51.90	12.21	89.64
	2	71.85	17.62	49.12	12.33	51.90	15.92	88.80
	3	71.87	17.62	49.12	12.33	51.90	15.92	89.99
2	1	65.11	15.41	65.26	7.30	54.56	14.12	89.52
	2	65.46	15.43	65.26	7.30	59.73	13.97	89.84
	3	70.31	14.98	66.34	9.94	57.01	20.15	89.91
3	1	68.54	15.81	73.52	9.41	41.43	19.35	89.63
	2	68.74	18.76	60.70	7.94	57.36	14.88	89.49
	3	68.99	16.18	63.57	11.05	41.43	17.36	89.63
4	1	68.61	14.35	64.92	10.02	59.32	15.72	89.34
	2	69.22	14.35	55.80	10.02	59.32	18.85	89.34
	3	69.38	14.35	64.92	10.02	54.70	19.68	89.34
5	1	65.25	13.59	48.15	9.61	58.29	12.24	89.75
	2	65.52	14.02	48.15	9.91	55.64	12.24	89.75
	3	65.75	14.23	48.15	9.74	58.29	12.24	89.75

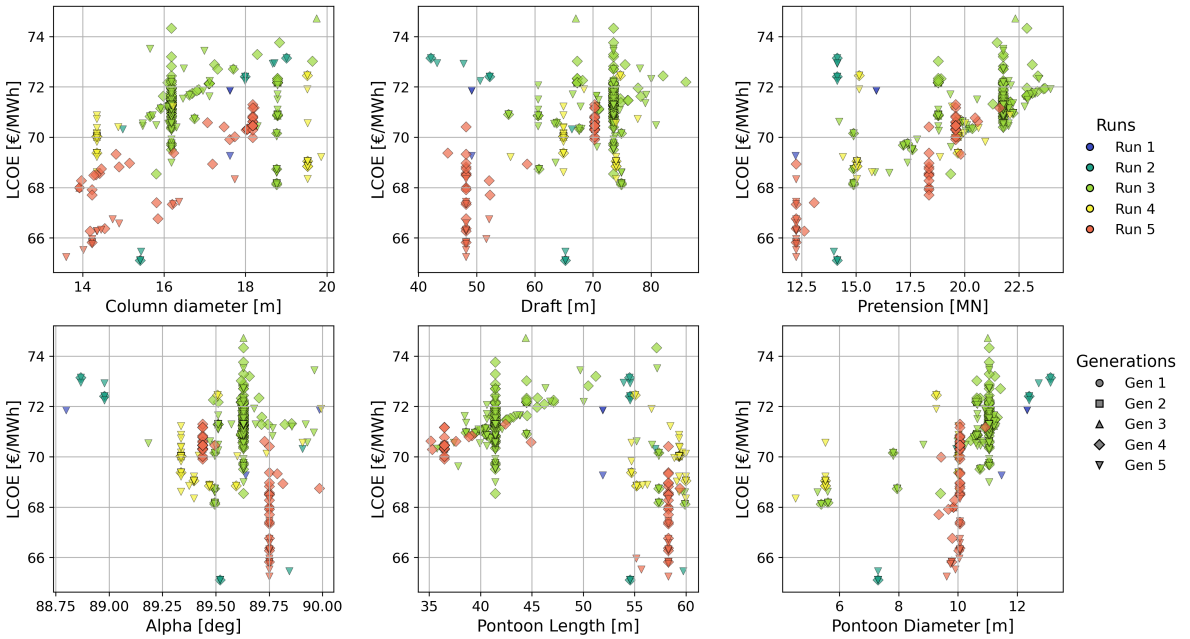

Figure 7.10: The exploration per optimisation run.

However, when looking at Figure 7.10 it can be noted that from the fourth and fifth generation onward, the optimisation runs start to become more diverse again. This can be seen by the shapes of the markers. Clear examples are run three and run five exploring in column diameter, pretension, pontoon length and pontoon diameter. This shows that the optimisation framework has the ability to escape local minima and search for a global optimum.

Overall, the optimisation framework shows to effectively converge across the design space. Multiple runs revealed that the algorithm initially converges to local optima, influenced by the starting population. However, with increasing generations, the diversity increases again. This shows that the current approach is capable of escaping local minima and progressing toward more optimal designs even after the initial local convergence. While increasing population size and the number of generations could enhance the optimisation results per run, the complexity and non-linearity of the design space make it more efficient, within current computational constraints, to perform multiple smaller runs rather than a single large run which still may have the risk of premature convergence.

7.3. Relevance of the Optimisation Framework

With this development of a dedicated optimisation framework for tension leg platforms with (near) vertical tendons, it is important to reflect on the broader relevance. This section discusses how the framework and the results align with current industry and how it contributes to the advancement of floating wind platform design.

7.3.1. Computational Efficiency & Adaptability

As mentioned before, this optimisation framework provides a major computational advantage over traditional time-domain model based optimisation. The framework can efficiently explore a wide range of TLP design concepts and converge to optimal configurations which remain within operational and practical constraints. In each optimisation run, 2,500 different TLP concepts were evaluated. Because the computational time was reduced by 98.5% compared to conventional time-domain models, the optimisation allows for inclusion of six design variables where the performance of every concept was tested against 14 different load cases. This ability to take into account an extensive set of load cases also shows how the developed optimisation framework may contribute to a preliminary general performance assessment during the front-end engineering design phase, enabling the current framework to provide early-stage insights that support certification preparation while reducing the required engineering time from weeks to days.

Additionally, the framework remains adaptable. The configuration input can be adjusted via the `YAML` input file which makes the framework useable for different TLP concepts, geometries and site-specific load cases. This versatility makes the developed framework a foundation for optimisation in floating wind development.

7.3.2. Comparison with Existing Studies

Table 7.11 compares the LCOE of the most cost-efficient TLP design identified in this study with LCOE values of other floating wind concepts. All concepts are evaluated with similar site conditions, including water depth and distance to shore. The TLP concepts are evaluated with the same cost model used in this study while for the semi-submersible and spar platforms, slight modifications to the cost model were made based on adjustments reported in literature [26].

It is important to acknowledge the presence of uncertainties across the different concepts, particularly with respect to their estimated lifetime energy production. For concepts that are already in use, such as the WindFloat Kincardine semi-submersible and the Hywind Tampen spar, the lifetime energy production values are based on operational data obtained from literature. For the remaining concepts, energy production estimates rely on theoretical estimations performed in literature corresponding to their respective turbine sizes.

The most cost-efficient TLP concept yields an LCOE of 65.11 €/MWh, which is comparable to LCOE values for alternative floating substructures. While the TLP is slightly less cost-effective than some of the other concepts, this is primarily attributed to the higher platform costs in the current design. However, comparison with the Kincardine and Hywind platforms reveals that an increase in turbine size significantly improves lifetime energy production. These energy gains are larger than the increase in system costs, resulting in a reduced overall LCOE.

This analysis demonstrates that the developed framework enables consistent comparison not only between different TLP configurations but also with other substructure types reported in literature. This supports the applicability of the framework for early-stage concept evaluation in offshore wind development. Nonetheless, due to sensitivities in the cost models and the assumptions involved in platform designs across studies, the LCOE comparison should be interpreted with caution. A more comprehensive cost comparison across multiple studies is recommended to reduce uncertainties and strengthen the robustness of the conclusions.

Table 7.11: LCOE of several floating wind concepts.

Concept	Turbine Rating [MW]	Total Cost [M€]	LEP [TWh]	LCOE [€/MWh]	Development Stage	Source
CENTEC - TLP	10	64.80	1.02	63.5	Theoretical Concept	[26, 77]
KRISO - TLP	15	70.94	1.21	58.63	Theoretical Concept	[11]
Pelastar - TLP	10	64.17	1.02	62.88	Theoretical Concept	[48, 77]
Windfloat Kincardine - semi-sub	9.5	52.99	0.75	70.65	In Operation	[58, 88]
Highwind Tampen - spar	8.6	48.17	0.72	67.07	In Operation	[30, 96]
RAFT study TLP	15	78.78	1.21	65.11	Theoretical Concept	

8

Discussion

This chapter presents a discussion on the developed optimisation framework and obtained results. First, the constructed RAFT model will be discussed, which will be followed by a discussion on the identified TLP design characteristics and the results of the optimisation study.

8.1. RAFT Model

As discussed in Chapter 5, the RAFT model developed for this optimisation framework shows accurate dynamic representation for TLPs with (near) vertical tendons. Furthermore, it showed to significantly reduce computational resources. Some discrepancies were identified when RAFT was compared to the reference model. These discrepancies primarily arise from simplifications to improve computational speed. Most discrepancies are within acceptable margins, while a few others posed limitations on the current model.

First, the use of a linearised mooring stiffness in combination with a quasi-static solver, accounting for the mean offset, shows to work effectively. However, RAFT does not capture the non-linear restoring behaviour of tendons at large offsets in dynamic analysis. This simplification can lead to an overestimation of dynamic response leading to more conservative designs. For TLPs, surge is coupled to pitch and heave. These couplings amplify the dynamic response for those degrees of freedom. As a result, small inaccuracies in surge prediction can significantly affect pitch motion, heave motion and tendon tensions for example, especially under more extreme load cases.

Second, the model is limited in the ability to capture the coupled dynamics of TLPs with inclined tendons. As the tendon angle deviates from vertical, the couplings between surge, pitch and heave become more pronounced. The current analytical, linearised implementation does not account for these interactions, leading to significant overestimation of platform motions and tendon loads in such configurations. This restricts the reliable use of the RAFT model to concepts with (near) vertical tendon layouts.

Third, the sum-frequency force approximation showed relatively accurate results, but remains limited to highly slender designs for reliable results. For the purposes of this study, the simplified sum-frequency force calculation provides reasonable estimates to take into account the significance for TLP design. However, a more detailed investigation into sum-frequency forces across a broader range of designs and conditions would strengthen the framework by showing when these forces become more critical.

Finally, as linearising the hydrodynamic coefficients shows to have a relatively large influence, the RAFT model would benefit from a more comprehensive computationally efficient hydrodynamic analysis. This is especially relevant for accurately modelling the frequency-dependent added mass, which significantly impacts system response. In contrast, the frequency dependent radiation damping was found to have only a minor effect, in line with the slender-body assumption applied in this study. As such, a more detailed hydrodynamic analysis for the radiation damping is likely to give little additional benefit. Incorporating surrogate models based on diffraction analyses would, for example, enhance the accuracy of the RAFT model while remaining within computational margins [56]. Furthermore, RAFT

would benefit of the implementation of a nacelle velocity feedback gain or similar damping mechanisms, to prevent over prediction of the low frequency motions at high wind speeds.

Overall, the RAFT model provides a fast and accurate tool for early-stage optimisation of TLPs with (near) vertical tendons. While simplifications such as linearised mooring and hydrodynamic coefficients contribute to computational efficiency, they limit the model's applicability to configurations with strong non-linear coupling. Enhancing RAFT with more detailed hydrodynamic representations and compatibility for inclined tendons would improve the versatility and enable exploration of a broader design space.

8.2. TLP Design Characteristics

The trends in design characteristics show that draft, pretension, tendon angle and pontoon length have the most significant influence on TLP dynamic performance. Draft significantly affects tendon length and therefore mooring stiffness. Pretension has a double influence as it directly impacts system response and affects the axial stiffness of the tendons, which was shown to affect platform response and tendon tension variations. This optimisation would benefit from a more detailed research into the axial stiffness of tendons.

Furthermore, no feasible designs were identified with a tendon angle below approximately 88.6° from horizontal, aligning with earlier findings in Section 5.6 that RAFT overestimates system response at lower tendon angles. This highlights the strong influence of tendon angle on system response and how future enhancements of the framework would benefit of incorporating these coupled effects.

Another finding of this study was that all feasible designs have a first pitch-bending natural frequency within the 3P excitation range of the rotor, due to the platform and turbine tower configuration. This overlap poses a risk of resonance caused by wind shear and tower shadowing effects, potentially increasing fatigue damage and power fluctuations. While not addressed in the current framework, this issue could be mitigated through controller tuning to add damping near the 3P band or by adjusting tower and tendon properties to shift natural frequencies. These strategies offer interesting extensions of the framework for improving the dynamic performance of future TLP designs.

In terms of LCOE, the results indicate that platform mass and tendon pretension are the primary cost drivers that affect the levelised cost of energy. The platform mass was most significantly influenced by the main column and pontoon diameters. This is mainly due to the fixed diameter-to-thickness ratio assumed in this research. Varying this parameter has shown to significantly impact the platform cost.

Overall, although there are design variables which have a more pronounced influence on the dynamic behaviour or system cost, the TLP behaves as a highly coupled system, where small geometric changes impact mass, buoyancy and pretension, emphasizing the need to take all the design variables into consideration as they are all related and underlining the added value of an integrated optimisation framework such as presented in this research.

8.3. Optimisation Results

The optimisation study shows that the developed framework successfully converges toward increasingly cost-effective designs as the generations progress. Several distinct and promising regions in the design space were explored, each yielding competitive LCOE results. This indicates that multiple feasible TLP configurations exist, offering design flexibility depending on site-specific and logistical constraints.

Based on the interpretation of the optimisation study results, several practical design solutions were identified that could further reduce platform cost and logistical and manufacturing complexity. Some of these solutions show promising potential. However, it should be noted that more detailed research is required to assess their impact on overall system performance and cost to make more robust conclusions on their impact.

Regarding the convergence of the genetic algorithm, the convergence behaviour varied across optimisation runs, indicating the framework's sensitivity to the initial population. This sensitivity led to initial convergence toward local minima. Nevertheless, as more generations were completed, the de-

sign space diversified again, suggesting the framework's capability to escape local minima. Increasing the population and number of generations per run can further mitigate local convergence, this will be at the cost of additional computational resources however. Within the current computational limits it was deemed more efficient to run multiple smaller optimisation runs for this complex non-linear design space to uncover design spaces and cost-efficient designs. However, it is important to note that the main goal of this study was not necessarily to find the best design, but to show that the optimisation framework works well and can be applied to TLPWT design problems. For future use in larger or real-world projects, it is recommended to use a larger population and more generations to improve the results of the framework.

When compared to results from other floating wind concepts, the optimised TLP designs achieved a competitive LCOE. These results support the potential of tension leg platforms as a viable solution for future large-scale offshore wind development. Still, a more extensive comparison of cost models used in different studies would improve the validation of the optimisation results and strengthen confidence in cross-study conclusions.

9

Conclusion & Recommendations

The scope of this research was to develop an automated optimisation framework for 15 MW tension leg platforms. The motivation was to improve the cost-efficiency of floating offshore wind turbines, enabling better access to deep-water wind resources. Throughout this research, several sub-questions were addressed to guide the development and validation of the framework. These sub-questions and their respective conclusions are summarised in Section 9.1, followed by the main conclusion which answers the main research question. After this, recommendations are presented for further research in Section 9.2.

9.1. Conclusion

Before answering the research questions, there are a couple of findings throughout this research which are worth noting next to the formulated research questions.

- At large mean thrust forces, several design concepts exhibited a negative mean pitch offset as a result of the thrust induced surge offset. This not only influenced the experienced tendon tensions, but also contributed to an increase in lifetime energy production. A negative mean pitch for large thrust forces implies that the turbine remains more upright at smaller thrust forces, improving energy generation. However, because all evaluated TLP concepts had relatively small pitch motions, the resulting variation in lifetime energy production remained limited.
- Throughout the optimisation study, surge motion consistently appeared as the most critical design constraint, followed by tendon tension limits. This highlights the importance of implementing surge reduction systems or redesigning subsystems, such as the power cable, to relax the surge offset constraint and broaden the feasible design space.
- Various design concepts demonstrated similar performance in terms of dynamic response and Levelised Cost of Energy (LCOE), despite differing significantly in layout. This indicates that the optimisation framework can identify multiple viable design configurations, allowing flexibility based on logistical constraints or offshore floating wind park developer specific preferences.
- Adjustments to system properties, such as diameter-over-thickness ratio and tendon axial stiffness, or the incorporation of practical design solutions, such as fins and braces, can reduce system cost as well as logistical and manufacturing complexity. Such design additions may contribute to the commercial viability of TLPWT, while remaining relatively straightforward to implement.

How can TLP-specific dynamic effects be represented in a frequency-domain based optimisation framework?

Sum-frequency forces can have significant impact on TLP response and fatigue, especially when idling. In order to include these effects, a slender body approach was used which estimates the sum-frequency forces using Rainey approximation. Although this method shows to approximate the sum-frequency forces with some overprediction at higher frequencies. It is suitable for the current application to take into account the effects of sum-frequency forces in TLP design.

As tension leg platform mooring stiffness varies non-linearly with horizontal excursion, a quasi-static approach is used that considers mooring linearisation around mean offset to minimise the effects of the linearisation. The quasi-static analysis shows to have great resemblance with the non-linear reference model. However, non-linear couplings at the offset position are not accounted for and therefore pose limitations on the linearisation of tension leg platform moorings.

Furthermore, in order to take into account the critical TLP pitch-bending modes, tower flexibility was incorporated in the RAFT software in order to make the TLP response more realistic.

What is the validity of linearising TLPWT with respect to system response?

The linearisation of tension leg platform wind turbine response is valid within a 16% error margin compared to non-linear time domain simulations for configurations with (near) vertical tendons. In these cases, the system coupling between the different degrees of freedom is limited, allowing the linear model to provide accurate results. Furthermore, it was discovered that the linearisation of TLPs leads to over predicted motions and larger tendon tensions for increasing excursions due the inability to take into account the non-linear varying mooring stiffnesses. These effects may cause op to 10% errors in the linear model compared to non-linear time domain simulations.

For increasing tendon angles, coupling effects between surge, heave and pitch become more pronounced. These effects are not fully captured in the current analytical linear model, leading to natural frequencies that shift into significant excitation zones and therefore overestimation of platform response.

In conclusion, linearisation of the model in this research is suitable for stiff TLP systems with (near) vertical tendons, but it becomes less reliable when strongly coupled modes dominate the dynamic behaviour.

Which design variables most significantly contribute to tension leg platform performance?

The most influential design variables for TLP dynamic behaviour were found to be the draft, pretension, tendon angle and pontoon length. While other variables also affected system behaviour, their impact was less pronounced. Increasing the draft consistently reduced surge, pitch and nacelle acceleration. Lowering the pretension led to reduced maximum and minimum tendon tensions. With decreasing tendon angle the systems dynamic behaviour is significantly influenced, moving the natural frequencies into excitation zones causing large excursions and tendon tensions. Larger pontoon lengths caused reductions in system pitch response and nacelle accelerations.

In terms of LCOE, the dominant cost drivers were platform mass and tendon pretension. The pretension directly influenced the cost of anchors and tendons, while the platform cost scaled with platform mass where main column and pontoon diameter had the most significant influence. LEP remained relatively constant across feasible designs due to limited pitch variation, although a slight improvement was observed in configurations that exhibited the behaviour of a negative mean pitch angle. These configurations remain more vertical in operational conditions increasing the lifetime energy production.

While there are design variables which have more significant relations with the optimisation results, all design variables show to have considerable impact on system dynamic response and/or cost. Therefore, all identified design variables should be taken into account in such an optimisation study. The main reason for this is the highly interrelated couplings for TLPs for varying mass, buoyancy and mooring properties.

What key elements should a cost model include to account for the cost of a tension leg platform, enabling comparison with other design studies?

In this research, a cost model was constructed to allow for concept comparison within the optimisation study, but also keeping the results of the framework comparable to other studies. Where most cost studies have a general cost function per type of platform which only depends on the turbine rating, the cost function in this research incorporates a more specific approach making the platform and mooring cost a function of platform steel mass, ballast mass, anchor vertical load requirements and cable cost. These varying costs make all the designs within the framework comparable to each other. To also make cross-study comparison possible, a more elaborate set of constant costs for every concept is included which include turbine cost, installation cost, transmission cost, operational and maintenance costs and

decommissioning costs. Together with the lifetime energy production the LCOE could be determined per concept which shows to be competitive and comparable with existing studies.

How can an optimisation problem be structured to allow for efficient exploration of the design space in the context of TLPWT optimisation?

An effective optimisation run for floating wind systems should combine computational efficiency with sufficient coverage of the design space. This can be achieved through a multistep approach. First, concepts that violate hard physical constraints, such as negative ballast mass are directly heavily penalized. This prevents the algorithm from wasting computational resources on physically infeasible designs. Second, a quasi-static feasibility check can be used to filter out designs that violate soft constraints, such as maximum allowable surge and tendon tension limits, at their mean offset. Only the remaining feasible individuals proceed to full dynamic simulation, where constraint violations are appropriately penalised in the fitness evaluation.

To further improve exploration and reduce the risk of drawing conclusions from potentially prematurely converged optimisation runs, the optimisation process was multi-started using smaller initial populations. This enables efficient identification of the different design spaces and gives an overall confidence in the exploration of the design space. Overall, this strategy ensures that the optimisation remains both efficient and robust, identifying optimal designs without excessive computational requirements.

"How can a frequency-domain-based optimisation framework be developed for 15 MW tension leg platform wind turbines to enable efficient, accurate and cost-effective design iterations, considering tension leg platform specific dynamics?"

To answer this question, a frequency-domain-based optimisation framework was developed, combining a quasi-static equilibrium solver with linear frequency-domain analysis at the offset position including TLP specific dynamics. This approach enables efficient evaluation of dynamic responses while maintaining sufficient accuracy for early-stage design. Validation against non-linear OrcaFlex simulations showed that the linear model achieved accuracy within $16\,\%$ for configurations with (near) vertical tendons. By reducing computational time with 98.5%, the framework enables evaluation of an extensive set of load cases. This extensive set of load cases not only allows for thorough concept performance evaluation, but may also contribute to a preliminary general performance assessment during the front-end engineering design phase. This enables the current framework to provide early-stage insights that may support certification preparation while reducing the required engineering time from weeks to days.

The framework integrates a full set of physical and operational constraints and applies a genetic algorithm to explore the six-dimensional design space. The optimisation framework successfully identified and converged to cost-efficient and dynamically feasible TLPWT designs, with a levelised costs of energy comparable to those in other floating wind studies. These results confirm the framework's value as a practical tool for early-phase concept development. This provides a robust basis for tension leg platform specific optimisation, making tension leg platforms more economically viable for future offshore wind developments in deeper waters.

9.2. Recommendations

While the optimisation framework developed in this research has demonstrated the ability to converge to cost-effective designs for TLPs with (near) vertical tendon configurations, several opportunities exist to further improve the accuracy, flexibility, applicability and eventual cost-efficiency.

- **Extend RAFT to include all coupled modes:**
  Investigating the coupled dynamic modes of tension leg platforms with inclined tendons and incorporating these into the linearised analytical mooring module in the RAFT model would significantly enhance the fidelity of the framework. This would enable exploration of a broader design space, increasing the potential to discover more cost-effective design concepts.
- **Expand RAFT validation studies:**
  While significant validation has been performed, as presented in Chapter 5. Additional confidence in the model may be gained by further validation studies across a wider range of mooring systems, water depths and environmental conditions, which would increase confidence in the models

accuracy. Ultimately, the goal would be to validate the tool across a comprehensive set of site conditions and material configurations.

- **Incorporate six degrees of freedom:**
  Extending the framework to a six degree of freedom analysis (including sway, roll and yaw) would allow a more realistic representation of TLP dynamics, particularly due the strong coupling between all degrees of freedom. For example, rotor torque-induced yaw is a known challenge in floating offshore wind which could be captured in this more elaborate analysis.
- **Include tower design in the optimisation study:**
  Integrating tower design as part of the optimisation would allow for a full system evaluation, particularly to avoid structural resonance issues by 3P excitations. While complete tower optimisation would be computationally expensive, an approach using a standard set of tower designs with different stiffness properties, would give a practical compromise between accuracy and efficiency.
- **Explore optimisation formulations:**
  Exploring alternative sets of constraints could further improve the insights gained on design driving parameters and how the optimisation converges to cost-efficient designs. Furthermore, including design variables like axial stiffness and column diameter-tot-thickness ratios could also yield valuable results.
- **Add practical design improvements to improve cost-efficiency and reduce installation and manufacturing complexity:** Future research could include the analysis of more practical solutions to reduce the platform cost or influence the limits identified in this research. As mentioned in subsection 7.1.5, these solutions include:
  - Increase added mass and damping by including (holed) fins on the structure to reduce surge responses.
  - Including tendon damping to reduce the dynamic tendon tensions.
  - Improve structural design to reduce platform material usage and therefore platform cost.
  - Select different mooring line materials and properties to directly reduce mooring line cost or indirectly reduce cost by reducing response and therefore required pretension for example.
  - Use different types of platform materials and anchors to reduce overall costs.
  - Redesign or implement subsystems that influence the current design constraints. For example, the allowable surge offset is currently limited by assumptions for the power cable design. By exploring alternative cable configurations or connection strategies, this constraint could potentially be relaxed, enabling a broader and more cost-effective design space.
- **Turbine scaling:**
  As the framework is adjustable for different turbines, a study into the effects of turbine scaling on optimisation results could reveal how developments in turbine size affect the platform design.

In summary, future research should focus on expanding the model's capabilities, improving model validation for different system properties and site conditions and extending the optimisation with different sets of constraints and practical cost limiting solutions. Applying the framework to case studies involving larger offshore wind turbines will help to indicate TLP development for the future of floating offshore wind. These steps will enhance the framework's robustness and versatility, enabling optimisation across a wider range of configurations and conditions, while also providing insights into the role of TLPs as a cost-effective foundation for floating offshore wind.

References

[1] 2H Offshore Engineering. *Dynamic Power Cable Layout Solutions for Floating Offshore Wind*. Tech. rep. Accessed: 2025-07-15. Quest Floating Wind Energy, 2021. URL: https://questfwe.com/wp-content/uploads/2021/07/2H-Offshore-Dynamic-Power-Cable-Layout-Solutions.pdf.

[2] N. J. Abbas et al. "A reference open-source controller for fixed and floating offshore wind turbines". In: *Wind Energy Science* 7.1 (2022), pp. 53–73. DOI: 10.5194/wes-7-53-2022. URL: https://wes.copernicus.org/articles/7/53/2022/.

[3] Mohammed Khair Al-Solihat and Meyer Nahon. "Stiffness of slack and taut moorings". In: *Ships and Offshore Structures* (2015). Published online: 6 Oct 2015. ISSN: 1744-5302. DOI: 10.1080/17445302.2015.1089052. URL: https://doi.org/10.1080/17445302.2015.1089052.

[4] Erin E. Bachynski and Torgeir Moan. "Design considerations for tension leg platform wind turbines". In: *Marine Structures* 29 (1 Dec. 2012), pp. 89–114. ISSN: 09518339. DOI: 10.1016/j.marstruc.2012.09.001.

[5] Erin Elizabeth Bachynski and Forfatter Forfattersen. "Design and Dynamic Analysis of Tension Leg Platform Wind Turbines (electronic version)". In: 2014. ISBN: 978-82-326-0096-0.

[6] Y. H. Bae and M. H. Kim. "Rotor-floater-tether coupled dynamics including second-order sum-frequency wave loads for a mono-column-TLP-type FOWT (floating offshore wind turbine)". In: *Ocean Engineering* 61 (2013), pp. 109–122. ISSN: 00298018. DOI: 10.1016/j.oceaneng.2013.01.010.

[7] D. Benasciutti and R. Tovo. "Comparison of spectral methods for fatigue analysis of broad-band Gaussian random processes". In: *Probabilistic Engineering Mechanics* 21.4 (2006), pp. 287–299. ISSN: 0266-8920. DOI: https://doi.org/10.1016/j.probengmech.2005.10.003. URL: https://www.sciencedirect.com/science/article/pii/S0266892005000718.

[8] Travis Benn. *Offshore vs. Onshore Wind Turbines: Which Is Best?* 2024. URL: https://lumifyenergy.com/blog/offshore-vs-onshore-wind-turbines/#:~:text=The%20average%20capacity%20of%20an,of%20up%20to%20260%20metres..

[9] Rphael Berthier. *Discrete, continuous and continuized accelerations*. 2022. URL: https://francisbach.com/continuized-acceleration/.

[10] Bluewater Energy Services B.V. *METCentre and Bluewater sign agreement to install a floating wind system offshore Norway*. Accessed: 2025-06-09. 2023. URL: https://www.bluewater.com/metcentre-bluewater-sign-agreement-to-install-a-floating-wind-system-offshore-norway/.

[11] Sung Youn Boo et al. "Concept Design of a 15 MW TLP-Type Floating Wind Platform for Korean Offshore Installation". In: *Journal of Marine Science and Engineering* 12.5 (2024), p. 796. DOI: 10.3390/jmse12050796. URL: https://doi.org/10.3390/jmse12050796.

[12] T. Burton et al. *Wind Energy Handbook*. Wiley, 2011. ISBN: 9781119993926. URL: https://books.google.nl/books?id=dip2LwCRCscC.

[13] Lucas Carmo and Matthew Hall. "Slender-body approach for computing second-order wave loads in the frequency domain". In: *Ocean Engineering* 322 (Apr. 2025). ISSN: 00298018. DOI: 10.1016/j.oceaneng.2025.120558.

[14] Peng Chen et al. "A frequency domain method for fully coupled modelling and dynamic analysis of floating wind turbines". In: *Marine Structures* 99 (Jan. 2025), p. 103715. ISSN: 09518339. DOI: 10.1016/j.marstruc.2024.103715. URL: https://linkinghub.elsevier.com/retrieve/pii/S0951833924001436.

[15] Hemayet Chowdhury et al. *A Continuous Space Neural Language Model for Bengali Language*. Jan. 2020. DOI: 10.48550/arXiv.2001.05315.

[16] Hao Dai et al. "Model test study on the damping performance of a novel tendon tension damper for TLP". In: *Journal of Physics: Conference Series*. Vol. 628. 1. IOP Publishing, 2015, p. 012056. DOI: 10.1088/1742-6596/628/1/012056. URL: https://iopscience.iop.org/article/10.1088/1742-6596/628/1/012056.

[17] José Manuel Vázquez D'andrea et al. *Study of the Motions and Nacelle Accelerations of the Windcrete Floating Offshore Wind Turbine According to the IEC 64100-3 Procedure*. 2020.

[18] Dassault Systèmes SolidWorks Corp. *Mean Stress Correction Methods (Goodman, Gerber, Soderberg)*. Accessed via SolidWorks Help: Goodman method is recommended for positive mean stress cycles. Solid-

Works. 2018. URL: https://help.solidworks.com/2018/english/solidworks/cworks/c_Mean_Stress_Correction.htm.

[19] Kalyanmoy Deb. *Multi-Objective Optimization Using Evolutionary Algorithms*. John Wiley & Sons, 2001.

[20] Kalyanmoy Deb and Ram Bhusan Agrawal. "Simulated Binary Crossover for Continuous Search Space". In: *Complex Systems* 9.2 (1995), pp. 115–148.

[21] Delmar Systems. *Stevmanta® Anchors*. Accessed: 2025-07-14. 2024. URL: https://delmarsystems.com/products/anchors/stevmanta/.

[22] Det Norske Veritas. *DNV-RP-C302: Buckling of Offshore Structures*. Recommended Practice. DNV. 2010. URL: https://rules.dnv.com/docs/pdf/DNV/codes/docs/2010-10/RP-C302.pdf.

[23] L. Dong et al. "On turbulence models and lidar measurements for wind turbine control". In: *Wind Energy Science* 6.6 (2021), pp. 1491–1500. DOI: 10.5194/wes-6-1491-2021. URL: https://wes.copernicus.org/articles/6/1491/2021/.

[24] Suguang Dou et al. "Optimization of floating wind turbine support structures using frequency-domain analysis and analytical gradients". In: *Journal of Physics: Conference Series*. Vol. 1618. IOP Publishing Ltd, Sept. 2020. DOI: 10.1088/1742-6596/1618/4/042028.

[25] Dr. M.B. Zaayer. *AE4W02TU Introduction to Wind Turbines: Physics and Technology*. Delft University of Technology, Faculty of Aerospace Engineering. Course material. 2023-2024.

[26] H. Díaz and C. Guedes Soares. "Cost and financial evaluation model for the design of floating offshore wind farms". In: *Ocean Engineering* 287 (Nov. 2023). ISSN: 00298018. DOI: 10.1016/j.oceaneng.2023.115841.

[27] H. Díaz et al. "Micro sitting of floating wind turbines in a wind farm using a multi-criteria framework". In: *Renewable Energy* 204 (2023), pp. 449–474. ISSN: 0960-1481. DOI: https://doi.org/10.1016/j.renene.2023.01.016. URL: https://www.sciencedirect.com/science/article/pii/S0960148123000162.

[28] Equinor. *Hywind Scotland*. 2025. URL: https://www.equinor.com/energy/hywind-scotland.

[29] Equinor. *Hywind Tampen*. 2025. URL: https://www.equinor.com/energy/hywind-tampen.

[30] Equinor ASA. *Annual Report 2024*. Annual Report. Combines financial and sustainability reporting. Equinor ASA, 2025. URL: https://cdn.equinor.com/files/h61q9gi9/global/16ccbc5a098c3b971979118420c4f83ddee18fb4.pdf.

[31] European Marine Observation and Data Network (EMODnet). *EMODnet Map Viewer*. https://emodnet.ec.europa.eu/geoviewer/. Funded by the European Commission Directorate-General for Maritime Affairs and Fisheries (DG MARE) and the European Maritime Fisheries and Aquaculture Fund (EMFAF). Licensed under CC BY 4.0. 2025. (Visited on 06/03/2025).

[32] O Faltinsen. "O.-Faltinsen-Sea-Loads-on-Ships-and-Offshore-Structures-Cambridge-Ocean-Technology-Series-Cambridge-University-Press-1993". In: (1993).

[33] O. M. Faltinsen et al. "Nonlinear wave loads on a slender vertical cylinder". In: *Journal of Fluid Mechanics* 289 (1995). DOI: 10.1017/S0022112095001297.

[34] Juliana Ferreira Fernandes et al. "A Review of the Application of Concrete to Offshore Structures". In: *Journal / Conference Proceedings (unconfirmed)* (2008). Review covers 35 years of offshore concrete structures, 350 platforms worldwide; metadata from ResearchGate :contentReference[oaicite:0]index=0.

[35] Evan Gaertner et al. *Definition of the IEA Wind 15-Megawatt Offshore Reference Wind Turbine Technical Report*. 2020. URL: www.nrel.gov/publications..

[36] Alberto Ghigo et al. "Platform optimization and cost analysis in a floating offshore wind farm". In: *Journal of Marine Science and Engineering* 8 (11 Nov. 2020), pp. 1–26. ISSN: 20771312. DOI: 10.3390/jmse8110835.

[37] Glosten. *The PelaStar Tension Leg Platform (TLP)*. https://pelastar.com/the-pelastar-tlp/. Accessed: 2025-06-03. 2025.

[38] Sébastien Gueydon and Jason Jonkman. *Update on the Comparison of Second-Order Loads on a Tension Leg Platform for Wind Turbines: Preprint*. 2016. URL: www.nrel.gov/publications..

[39] Kurtis Gurley and Ahsan Kareem. "Simulation of Ringing in Offshore Systems under Viscous Loads". In: *Journal of Engineering Mechanics-asce - J ENG MECH-ASCE* 124 (May 1998). DOI: 10.1061/(ASCE)0733-9399(1998)124:5(582).

[40] Matthew Hall. "Generalized Quasi-Static Mooring System Modeling with Analytic Jacobians". In: *Energies* 17 (13 July 2024). ISSN: 19961073. DOI: 10.3390/en17133155.

[41] Matthew Hall et al. "An Open-Source Frequency-Domain Model for Floating Wind Turbine Design Optimization". In: *Journal of Physics: Conference Series*. Vol. 2265. Institute of Physics, June 2022. DOI: 10.1088/1742-6596/2265/4/042020.

[42] Matthew Hall et al. “Hydrodynamics-based floating wind turbine support platform optimization: A basis function approach”. In: *Renewable Energy* 66 (June 2014), pp. 559–569. ISSN: 09601481. DOI: 10.1016/j.renene.2013.12.035.

[43] M.O.L. Hansen. “Aerodynamics of wind turbines: Third edition”. In: *Aerodynamics of Wind Turbines: Third Edition* (May 2015), pp. 1–173. DOI: 10.4324/9781315769981.

[44] Harbours Review. *Port of Esbjerg*. Accessed: 2025-07-06. 2024. URL: https://harboursreview.com/port-esbjerg.html.

[45] Heerema Marine Contractors. *Barge Fleet*. https://www.heerema.com/heerema-marine-contractors/fleet/barges. Accessed: 2025-07-06. 2024.

[46] John Marius Hegseth et al. “Integrated design optimization of spar floating wind turbines”. In: *Marine Structures* 72 (July 2020). ISSN: 09518339. DOI: 10.1016/j.marstruc.2020.102771.

[47] Jeroen Hoving and Pim van der Male. *OE44097 Offshore Support Structures*. 2024.

[48] William L. Jr. Hurley and Charles J. Nordstrom. *PelaStar Cost of Energy: A Cost Study of the PelaStar Floating Foundation System in United Kingdom Waters*. Technical Report WIN_WI1016_2. Energy Technologies Institute (ETI) and UK Energy Research Centre (UKERC), 2015. DOI: 10.5286/UKERC.EDC.000613. URL: https://ukerc.rl.ac.uk/publications/technical_report/WIN_WI1016_2.pdf.

[49] *Hywind Buchan Deep Metocean Design Basis*. Tech. rep. RE2014-002. Available upon request from project developer. Norway: Statoil ASA, May 2014.

[50] Victor Igwemezie et al. “Current trend in offshore wind energy sector and material requirements for fatigue resistance improvement in large wind turbine support structures – A review”. In: *Renewable and Sustainable Energy Reviews* 101 (2019), pp. 181–196. ISSN: 1364-0321. DOI: https://doi.org/10.1016/j.rser.2018.11.002. URL: https://www.sciencedirect.com/science/article/pii/S1364032118307342.

[51] International Electrotechnical Commission. *IEC 61400-3:2009 - Wind Turbines – Part 3: Design Requirements for Offshore Wind Turbines*. https://webstore.iec.ch/publication/2225. Standard, IEC. 2009.

[52] J M Jonkman and D Matha. “Dynamics of offshore floating wind turbines—analysis of three concepts”. In: *Wind Energy* 14 (4 2011), pp. 557–569. DOI: https://doi.org/10.1002/we.442. URL: https://onlinelibrary.wiley.com/doi/abs/10.1002/we.442.

[53] Jason Jonkman et al. *OpenFast*. 2023. URL: https://openfast.readthedocs.io/en/dev/index.html.

[54] J M J Journée et al. *OFFSHORE HYDROMECHANICS Third Edition (2015)*. 2015.

[55] J. C. Kaimal et al. “Spectral characteristics of surface□layer turbulence”. In: *Quarterly Journal of the Royal Meteorological Society* 98.417 (July 1972), pp. 563–589. DOI: 10.1002/qj.49709841707. URL: https://doi.org/10.1002/qj.49709841707.

[56] Theodoros Kalimeris and Erin Bachynski-Polić. *Floating wind turbine optimization via surrogate modelling Hovedoppgave i European Wind Energy Master (MS Wind) Veileder: Norges teknisk-naturvitenskapelige universitet Institutt for marin teknikk*. 2023.

[57] Meysam Karimi et al. “A multi-objective design optimization approach for floating offshore wind turbine support structures”. In: *Journal of Ocean Engineering and Marine Energy* 3 (1 Feb. 2017), pp. 69–87. ISSN: 21986452. DOI: 10.1007/s40722-016-0072-4.

[58] Kincardine Offshore Windfarm Limited. *Annual Report and Financial Statements for the year ended 31 March 2024*. Annual report. Companies House UK / Buds Offshore Energy, 2024. URL: https://budsoffshoreenergy.com/wp-content/uploads/2024/10/companies_house_document.pdf.

[59] Bart Jan Klootwijk. *Optimisation of Floating Offshore Wind Substructures: A Higher-Fidelity Approach*. 2023. URL: http://repository.tudelft.nl/..

[60] Kevin Leenders. “Mooring Analysis for a TLP Supporting a 15 MW Wind Turbine: Identifying Critical Design Parameters That Influence the Design Life of a Mooring System Regarding Higher-Order Loads”. Supervisors: Dr. O.C. Géné, Dr. Ing. S. Schreier, Dr. Ir. M.R. Karimi, Dr. Ir. D. Van der Heul. Master’s Thesis. Delft, The Netherlands: TU Delft, Apr. 2023.

[61] Mareike Leimeister et al. “A fully integrated optimization framework for designing a complex geometry offshore wind turbine spar-type floating support structure”. In: *Wind Energy Science Discussions* (2020). Preprint. URL: https://wes.copernicus.org/preprints/wes-2020-93/.

[62] Mareike Leimeister et al. “Development of a Framework for Wind Turbine Design and Optimization”. In: *Modelling* 2 (1 Mar. 2021), pp. 105–128. ISSN: 26733951. DOI: 10.3390/modelling2010006.

[63] Frank Lemmer. *Low-Order Modeling, Controller Design and Optimization of Floating Oshore Wind Turbines*. 2018.

[64] Frank Lemmer. *Qualification of innovative floating substructures for 10MW wind turbines and water depths greater than 50m Duration 40 months Deliverable D4.3 Optimization framework and methodology for optimized floater design*. 2016.

[65] Qian Li et al. “Influence of Initialization on the Performance of Metaheuristic Optimizers”. In: *Applied Soft Computing* 91 (2020), p. 106193.

[66] Wei Li et al. “Global design methodology for semi-submersible hulls of floating wind turbines”. In: *Renewable Energy* 225 (2024), p. 120291. ISSN: 0960-1481. DOI: https://doi.org/10.1016/j.renene.2024.120291. URL: https://www.sciencedirect.com/science/article/pii/S0960148124003562.

[67] Jijian Lian et al. “A Theoretical Approach for Resonance Analysis of Wind Turbines under 1P/3P Loads”. In: *Energies* 15.16 (2022). Open access under CC BY 4.0 license, p. 5787. DOI: 10.3390/en15165787. URL: https://www.mdpi.com/1996-1073/15/16/5787.

[68] LKAB. *LKAB - Ballast for offshore wind turbines*. 2025. URL: https://www.lkabminerals.com/product-application/offshore-wind-structures/.

[69] Kai-Tung Ma. *Floating Offshore Wind Turbines - Comparing Floater Types and Designing Mooring Systems*. 2021. URL: https://sut-us.org/event/Floating-Offshore-Wind-Turbines-Comparing-Floater-Types-and-Designing-Mooring-Systems/637614244128108779.

[70] Kai-Tung Ma et al. *Mooring System Engineering for Offshore Structures*. Elsevier, 2019. ISBN: 9780128185513. DOI: 10.1016/C2018-0-02217-3.

[71] Ed Mackay et al. “Experimental study of hydrodynamic loads induced by the motion of a vertical circular cylinder with a porous outer skirt”. In: *Ocean Engineering* 242 (2024), p. 110118. DOI: 10.1016/j.oceaneng.2024.110118. URL: https://www.sciencedirect.com/science/article/pii/S002980182402050X.

[72] Jijo Malayil. *World’s largest monopile factory to advance wind energy projects*. Accessed: 2025-05-29. 2024. URL: https://interestingengineering.com/energy/worlds-largest-monopile-factory-wind-energy.

[73] Hayden Marcollo and Louise Efthimiou. *Floating Offshore Wind Dynamic Cables: Overview of Design and Risks*. Technical Report. Accessed: 2025-07-15. World Forum Offshore Wind e.V., 2024. URL: https://wfo-global.org/wp-content/uploads/2024/02/WFO-Cables-and-FOSS-White-Paper.pdf.

[74] Joaquim R. R. A.. Martins and S. Andrew. Ning. *Engineering design optimization*. Cambridge University Press, 2022, p. 637. ISBN: 9781108833417.

[75] Denis Matha et al. *Subcontract Report Model Development and Loads Analysis of an Offshore Wind Turbine on a Tension Leg Platform, with a Comparison to Other Floating Turbine Concepts Thesis Supervisors*. 2010. URL: http://www.osti.gov/bridge.

[76] Brad L. Miller and David E. Goldberg. “Genetic Algorithms, Tournament Selection, and the Effects of Noise”. In: *Complex Systems* (1995). Study shows how tournament size directly controls selection pressure and impacts convergence.

[77] Walter Musial et al. *Cost of Floating Offshore Wind Energy Using New England Aqua Ventus Concrete Semisubmersible Technology*. Technical Report NREL/TP-5000-75618. National Renewable Energy Laboratory, 2020. DOI: 10.2172/1768672. URL: https://www.nrel.gov/docs/fy20osti/75618.pdf.

[78] Vicente Negro et al. “Uncertainties in the design of support structures and foundations for offshore wind turbines”. In: *Renewable Energy* 63 (Mar. 2014), pp. 125–132. DOI: 10.1016/j.rene.2013.08.041.

[79] Andrew Ning. “Using blade element momentum methods with gradient-based design optimization”. In: *Structural and Multidisciplinary Optimization* 64 (2 Aug. 2021), pp. 991–1014. ISSN: 16151488. DOI: 10.1007/s00158-021-02883-6.

[80] OCAS et al. *Concept Design of a 15 MW TLP-Type Floating Wind Platform for Offshore Wind Turbines*. Tech. rep. Accessed: 2025-06-05. GICON Group, 2021. URL: https://diving-rov-specialists.com/index_htm_files/os-240-concept-design-of-a-15-mw-tlp-type-floating-wind-platform.pdf.

[81] Gabriela Ochoa. “Setting the Mutation Rate: Scope and Limitations of the 1/L Heuristic”. In: *Proceedings of PPSN VI*. Vol. 1917. Lecture Notes in Computer Science. Springer, 2002, pp. 89–98.

[82] Orcina. *OrcaFlex, Version 11.2*. Commercial software for dynamic analysis of offshore systems. Orcina Ltd. Ulverston, UK, 2023. URL: https://www.orcina.com.

[83] S. Papadopoulou et al. “Mooring line materials for mini-TLP platforms”. In: *Journal of Physics: Conference Series*. Vol. 2875. Institute of Physics, 2024. DOI: 10.1088/1742-6596/2875/1/012031.

[84] Francesco Papi et al. “Going beyond BEM with BEM: an insight into dynamic inflow effects on floating wind turbines”. In: *Wind Energy Science* 9 (5 May 2024), pp. 1069–1088. ISSN: 23667451. DOI: 10.5194/wes-9-1069-2024.

[85] Katarzyna Patryniak et al. *Multidisciplinary design analysis and optimisation frameworks for floating offshore wind turbines: State of the art*. May 2022. DOI: 10.1016/j.oceaneng.2022.111002.

[86] Mario Paz and Young Hoon Kim. *Structural Dynamics: Theory and Computation*. Jan. 2019. ISBN: 978-3-319-94742-6. DOI: 10.1007/978-3-319-94743-3.

[87] Nicolò Pollini et al. "Design optimization of a TetraSpar-type floater and tower for the IEA Wind 15 MW reference wind turbine". In: *Marine Structures* 90 (July 2023). ISSN: 09518339. DOI: 10.1016/j.marstruc.2023.103437.

[88] Principle Power. *Designing and operating the world's largest floating offshore Wind Farm*. 2021. URL: https://www.principlepower.com/projects/kincardine-offshore-wind-farm.

[89] Dongsheng Qiao et al. "Evaluation of the positioning capability of a novel concept design of dynamic positioning-assisted mooring systems for floating offshore wind turbines". In: *Ocean Engineering* 299 (2024), p. 117286. DOI: 10.1016/j.oceaneng.2024.117286. URL: https://www.sciencedirect.com/science/article/pii/S0029801824006231.

[90] Pedro Rabelo. *Delp Mooring: Efficient Mooring Design for Floating Wind*. Presented at Floating Wind Solutions Conference. Accessed: 2025-07-14. 2024. URL: https://floatingwindsolutions.com/wp-content/uploads/2024/02/Delp-Mooring-Pedro-Rabelo.pdf.

[91] Md. Hafizur Rahman and Chhavi Gupta. "Computation of Rayleigh damping coefficient of a rectangular submerged floating tunnel (SFT)". In: *SN Applied Sciences* 2.5 (2020), p. 936. DOI: 10.1007/s42452-020-2629-z. URL: https://link.springer.com/article/10.1007/s42452-020-2629-z.

[92] R. C. T. Rainey. "Slender-body approximations for second-order forces on offshore structures". In: *Proceedings of the Royal Society of London. Series A: Mathematical and Physical Sciences* 436.1896 (1992), pp. 185–203. DOI: 10.1098/rspa.1992.0002. URL: https://doi.org/10.1098/rspa.1992.0002.

[93] Peter J Rohrer et al. *omae2023-101930 gradient-based design optimization of fully-flexible floating wind turbines using modal analysis*. 2023.

[94] Élie Rongé et al. "Evaluation of second and third-order numerical wave-loading models for floating offshore wind TLPs". In: *Ocean Engineering* 288 (2023), p. 116064. ISSN: 0029-8018. DOI: https://doi.org/10.1016/j.oceaneng.2023.116064. URL: https://www.sciencedirect.com/science/article/pii/S0029801823024484.

[95] Salamander. *The Salamander Project*. 2025. URL: https://salamanderfloatingwind.com/.

[96] Linda Sandvik. "Equinor's Hywind Tampen underperformed in first year". In: *EnergyWatch* (2025). Accessed: 2025-07-17. URL: https://energywatch.com/EnergyNews/Renewables/article17785306.ece.

[97] Bart de Schutter. *SC42056 Optimisation for Systems and Control*. 2024.

[98] I. Senjanović et al. "Investigation of nonlinear restoring stiffness in dynamic analysis of tension leg platforms". In: *Engineering Structures* 56 (2013), pp. 117–125. DOI: 10.1016/j.engstruct.2013.04.020.

[99] Sif Group. *Marshalling and Logistics*. https://sif-group.com/en/marshalling-and-logistics/. Accessed: 2025-07-06. 2024.

[100] South Jersey Port Corporation. *Paulsboro Marine Terminal*. https://www.southjerseyport.com/facilities/paulsboro-marine-terminal/. 200 acres (80.94 ha), 40 ft MLW draft at berths; accessed 6 July 2025. 2025.

[101] Carlos Eduardo S Souza et al. "Frequency-Dependent Aerodynamic Damping and Inertia in Linearized Dynamic Analysis of Floating Wind Turbines". In: *Journal of Physics: Conference Series*. Vol. 1452. Institute of Physics Publishing, Mar. 2020. DOI: 10.1088/1742-6596/1452/1/012040.

[102] Victoria Sykes et al. *A review and analysis of optimisation techniques applied to floating offshore wind platforms*. Oct. 2023. DOI: 10.1016/j.oceaneng.2023.115247.

[103] The MathWorks, Inc. *Genetic Algorithm Options – MATLAB & Simulink*. https://www.mathworks.com/help/gads/genetic-algorithm-options.html. Accessed 2025-06-09.

[104] Christopher Tracy. *Parametric Design of Floating Wind Turbines*. 2007.

[105] Axelle Vire and Delphine Tavernier. *AE4W31 Floating Offshore Wind Energy Lecture Slides*. 2024.

[106] Dana Vrajitoru. "Large Population or Many Generations for Genetic Algorithms? Implications in Information Retrieval". In: *Genetic Algorithms in Engineering Applications*. Springer, 2000, pp. 14–23.

[107] Junrong Wang et al. "Investigation of second-order low-frequency wave forces approximations for moored floating structures". In: *Ocean Engineering* 282 (Aug. 2023). ISSN: 00298018. DOI: 10.1016/j.oceaneng.2023.114987.

[108] Tom Wilson. *Floating wind farms overcome storms to deliver record power output*. Accessed: 2025-06-05. 2021. URL: https://www.ft.com/content/6097e183-d3b4-45dd-8de8-9a91556cd3b1.

[109] WindEurope. *Eemshaven — base port for world's largest offshore wind farm*. https://windeurope.org/policy/topics/offshore-wind-ports/eemshaven-base-port-for-worlds-largest-offshore-wind-farm/. Accessed: 2025-07-06. 2021.

[110] Wire Rope Exchange. *New Guinness World Record for Teufelberger-Redaelli's Flexpack Rope*. Accessed: 2025-05-29. 2024. URL: https://wireropeexchange.com/world-record-teufelberger-redaelli-flexpack/.

[111] Wei Yu et al. "Control co-design optimization of floating offshore wind turbines with tuned liquid multi-column dampers". In: *Wind Energy Science* 9 (4 Apr. 2024), pp. 1053–1068. ISSN: 23667451. DOI: 10.5194/wes-9-1053-2024.

[112] Yang Yu et al. "Investigation of TLP's hydrodynamic response with different tendon connection angles". In: *Theoretical and Applied Mechanics Letters* 8.4 (2018), pp. 291–297. ISSN: 2095-0349. DOI: https://doi.org/10.1016/j.taml.2018.04.009. URL: https://www.sciencedirect.com/science/article/pii/S2095034918301934.

[113] F ; Zahle et al. "Definition of the IEA Wind 22-Megawatt Offshore Reference Wind Turbine". In: *Citation* (2024). DOI: 10.11581/DTU.00000317. URL: https://doi.org/10.11581/DTU.00000317.

[114] Hongjian Zhang et al. "Novel method for designing and optimising the floating platforms of offshore wind turbines". In: *Ocean Engineering* 266 (Dec. 2022). ISSN: 00298018. DOI: 10.1016/j.oceaneng.2022.112781.

[115] Xinshu Zhang et al. "Multi-objective optimization of Tension Leg Platform using evolutionary algorithm based on surrogate model". In: *Ocean Engineering* 148 (Jan. 2018). ., pp. 612–631. ISSN: 00298018. DOI: 10.1016/j.oceaneng.2017.11.038.

[116] Shengtao Zhou et al. "Global sensitivity study on the semisubmersible substructure of a floating wind turbine: Manufacturing cost, structural properties and hydrodynamics". In: *Ocean Engineering* 221 (Feb. 2021). Study on the sensitivity analysis of a semisub. ISSN: 00298018. DOI: 10.1016/j.oceaneng.2021.108585.

A

Simplified Scaling of a TLP

Originally the MIT/NREL TLP supports a 5MW turbine. To make it compatible for a 15MW turbine, a scaled base case was made to form the basis of the construction of this framework. This was done with the following scaling rules in a simple spreadsheet based on the MIT/NREL platform 1 used in the research by Erin Bachynski [5].

1. **Surge and sway natural periods**
   To avoid first-order wave excitation, the surge and sway natural periods should exceed 25 seconds. The undamped, decoupled surge natural period $T_{n,1}$ is estimated using Equation A.1, where M_{11} is the surge mass, A_{11} is the added mass, and K_{11} is the restoring stiffness in surge.

$$T_{n,1} = 2\pi\sqrt{\frac{M_{11} + A_{11}}{K_{11}}} \tag{A.1}$$

2. **Heave, roll, and pitch natural periods**
   These periods should be shorter than 3.5 seconds to remain outside the wave energy band for first-order excitation. The rigid-body pitch or heave natural period $T_{n,3}$ can be approximated by Equation A.2, where C_{33} is the hydrostatic stiffness and K_{33} is the mooring/tendon stiffness in heave or pitch.

$$T_{n,3} = 2\pi\sqrt{\frac{M_{33} + A_{33}}{C_{33} + K_{33}}} \tag{A.2}$$

3. **Mean offset limitation**
   To control the tendon angle and avoid slack events, the mean platform offset must not exceed 10% of the water depth. The mean surge force $\bar{F}_1$ due to waves is estimated using Equation A.3 based on regular wave theory for a significant wave height of 4 m and period of 10 s, where ζ_a is the wave amplitude, D_1 is the column diameter, ω is the wave frequency, and $C_D = 1$ is the drag coefficient.

$$\bar{F}_1 = \frac{1}{2}\rho g \zeta_a^2 \frac{D_1}{2} + \frac{3\pi}{2}\rho C_D D_1 \omega^2 \zeta_a^3 \tag{A.3}$$

4. **Tendon yield strength constraint**
   The tendon cross-sectional area A_t must be large enough to ensure the stress under maximum loading ($T_{pretension}$ is about 30% of the MBL [80]) does not exceed the yield strength σ_y.

$$\frac{T_{pretension}}{0.3A_t} \leq \sigma_y \tag{A.4}$$

5. **Minimum displacement**
   The platform displacement volume Δ must satisfy Equation A.5. This constraint is based on preliminary findings suggesting that sufficient displacement is necessary to survive extreme environmental conditions by providing adequate inertia and pretension stiffness.

$$\Delta \geq 2000 \text{ m}^3 \tag{A.5}$$

B

Structural Details

B.1. Tower Mass and Stiffness Matrices

The complete tower element mass and stiffness matrices used based on literature [86].

$$K_e = \begin{bmatrix} \frac{EA}{L} & 0 & 0 & 0 & 0 & 0 & -\frac{EA}{L} & 0 & 0 & 0 & 0 & 0 \\ 0 & \frac{12EI_y}{L^3} & 0 & 0 & 0 & \frac{6EI_y}{L^2} & 0 & -\frac{12EI_y}{L^3} & 0 & 0 & 0 & \frac{6EI_y}{L^2} \\ 0 & 0 & \frac{12EI_z}{L^3} & 0 & -\frac{6EI_z}{L^2} & 0 & 0 & 0 & -\frac{12EI_z}{L^3} & 0 & -\frac{6EI_z}{L^2} & 0 \\ 0 & 0 & 0 & \frac{GI}{L} & 0 & 0 & 0 & 0 & 0 & -\frac{GI}{L} & 0 & 0 \\ 0 & 0 & -\frac{6EI_z}{L^2} & 0 & \frac{4EI_z}{L} & 0 & 0 & 0 & \frac{6EI_z}{L^2} & 0 & \frac{2EI_z}{L} & 0 \\ 0 & \frac{6EI_y}{L^2} & 0 & 0 & 0 & \frac{4EI_y}{L} & 0 & -\frac{6EI_y}{L^2} & 0 & 0 & 0 & \frac{2EI_y}{L} \\ -\frac{EA}{L} & 0 & 0 & 0 & 0 & 0 & \frac{EA}{L} & 0 & 0 & 0 & 0 & 0 \\ 0 & -\frac{12EI_y}{L^3} & 0 & 0 & 0 & -\frac{6EI_y}{L^2} & 0 & \frac{12EI_y}{L^3} & 0 & 0 & 0 & -\frac{6EI_y}{L^2} \\ 0 & 0 & -\frac{12EI_z}{L^3} & 0 & \frac{6EI_z}{L^2} & 0 & 0 & 0 & \frac{12EI_z}{L^3} & 0 & \frac{6EI_z}{L^2} & 0 \\ 0 & 0 & 0 & -\frac{GI}{L} & 0 & 0 & 0 & 0 & 0 & \frac{GI}{L} & 0 & 0 \\ 0 & 0 & -\frac{6EI_z}{L^2} & 0 & \frac{2EI_z}{L} & 0 & 0 & 0 & \frac{6EI_z}{L^2} & 0 & \frac{4EI_z}{L} & 0 \\ 0 & \frac{6EI_y}{L^2} & 0 & 0 & 0 & \frac{2EI_y}{L} & 0 & -\frac{6EI_y}{L^2} & 0 & 0 & 0 & \frac{4EI_y}{L} \end{bmatrix} \begin{bmatrix} \delta_1 \\ \delta_2 \\ \delta_3 \\ \delta_4 \\ \delta_5 \\ \delta_6 \\ \delta_7 \\ \delta_8 \\ \delta_9 \\ \delta_{10} \\ \delta_{11} \\ \delta_{12} \end{bmatrix}$$

$$M_e = \frac{\bar{m}L}{420} \begin{bmatrix} 140 & 0 & 0 & 0 & 0 & 0 & 0 & 70 & 0 & 0 & 0 & 0 \\ 0 & 156 & 0 & 0 & -22L & 0 & 0 & 0 & 54 & 0 & 13L & 0 \\ 0 & 0 & 156 & 0 & 0 & 22L & 0 & 0 & 54 & 0 & -13L & 0 \\ 0 & 0 & 0 & \frac{140I_e}{A} & 0 & 0 & 0 & 0 & 0 & \frac{70I_e}{A} & 0 & 0 \\ 0 & -22L & 0 & 0 & 4L^2 & 0 & 0 & 0 & -13L & 0 & -3L^2 & 0 \\ 0 & 0 & 22L & 0 & 0 & 4L^2 & 0 & 0 & 0 & -3L^2 & 0 & -22L \\ 0 & 0 & 0 & 0 & 0 & 0 & 140 & 0 & 0 & 0 & 0 & 0 \\ 70 & 0 & 0 & 0 & 0 & 0 & 0 & 156 & 0 & 0 & -22L & 0 \\ 0 & 54 & 0 & 0 & -13L & 0 & 0 & 0 & 156 & 0 & 0 & 22L \\ 0 & 0 & 54 & \frac{70I_e}{A} & 0 & -3L^2 & 0 & 0 & 0 & \frac{140I_e}{A} & 0 & 0 \\ 0 & 13L & -13L & 0 & -3L^2 & 0 & 0 & -22L & 0 & 0 & 4L^2 & 0 \\ 0 & 0 & 0 & 0 & 0 & -22L & 0 & 0 & 22L & 0 & 0 & 4L^2 \end{bmatrix} \begin{bmatrix} \delta_1 \\ \delta_2 \\ \delta_3 \\ \delta_4 \\ \delta_5 \\ \delta_6 \\ \delta_7 \\ \delta_8 \\ \delta_9 \\ \delta_{10} \\ \delta_{11} \\ \delta_{12} \end{bmatrix}$$

B.2. Tower Properties

Table B.1: Tower Material Properties.

Parameter	Symbol	Value	Unit
Young's modulus, steel	E	200	GPa
Shear modulus, steel	G	79.3	GPa
Density, steel	ρ	7850	kg/m^3

Table B.2: Tower Element Properties.

Location	Height [m]	Outer Diameter [m]	Thickness [mm]	Mass Density [kg/m]	Fore-aft inertia [kg.m]	Side-side inertia [kg.m]
Tower Base	15.00	10	88.528	23006.32	282532.26	282532.26
	18.25	10	88.528	23006.32	282532.26	282532.26
	21.50	10	88.528	23006.32	282532.26	282532.26
	24.75	10	88.528	23006.32	282532.26	282532.26
	28.00	10	88.528	23006.32	282532.26	282532.26
	31.25	10	88.528	23006.32	282532.26	282532.26
	34.50	10	88.528	23006.32	282532.26	282532.26
	37.75	10	88.528	23006.32	282532.26	282532.26
	41.00	10	78.377	20389.17	250900.87	250900.87
	44.25	10	78.377	20389.17	250900.87	250900.87
	47.50	10	78.377	20389.17	250900.87	250900.87
	50.75	10	78.377	20389.17	250900.87	250900.87
	54.00	10	68.146	17745.94	218821.54	218821.54
	57.25	10	68.146	17745.94	218821.54	218821.54
	60.50	10	68.146	17745.94	218821.54	218821.54
	63.75	10	68.146	17745.94	218821.54	218821.54
	67.00	10	57.782	15062.74	186120.99	186120.99
	70.25	10	57.782	15062.74	186120.99	186120.99
	73.50	10	57.782	15062.74	186120.99	186120.99
	76.75	10	57.782	15062.74	186120.99	186120.99
	80.00	10	47.297	12342.49	152828.66	152828.66
	83.25	10	47.297	12342.49	152828.66	152828.66
	86.50	10	47.297	12342.49	152828.66	152828.66
	89.75	10	47.297	12342.49	152828.66	152828.66
	93.00	10	36.876	9633.13	119529.37	119529.37
	96.25	10	36.876	9633.13	119529.37	119529.37
	99.50	10	36.876	9633.13	119529.37	119529.37
	102.75	10	36.876	9633.13	119529.37	119529.37
	106.00	10	26.873	7027.09	87367.84	87367.84
	109.25	10	26.873	7027.09	87367.84	87367.84
	112.50	10	26.873	7027.09	87367.84	87367.84
	115.75	10	26.873	7027.09	87367.84	87367.84
	119.00	10	17.749	4645.48	57862.74	57862.74
	122.25	10	17.749	4645.48	57862.74	57862.74
	125.50	10	17.749	4645.48	57862.74	57862.74
	128.75	10	17.749	4645.48	57862.74	57862.74
	132.00	10	9.911	2596.06	32386.52	32386.52
	134.60	10	9.911	2596.06	32386.52	32386.52
	137.20	10	9.911	2596.06	32386.52	32386.52
	139.80	10	9.911	2596.06	32386.52	32386.52
Tower top	144.386	6.5	7.936	1350.87	7116.87	7116.87

Table B.3: Tower Element Properties Continued.

Location	Height [m]	Fore-aft stiffness [N.m^2]	Side-side stiffness [N.m^2]	Torsional stiffness [N.m^2]	Axial stiffness [N]
Tower base	15.00	6.77E+12	6.77E+12	5.37E+12	5.51E+11
	18.25	6.77E+12	6.77E+12	5.37E+12	5.51E+11
	21.50	6.77E+12	6.77E+12	5.37E+12	5.51E+11
	24.75	6.77E+12	6.77E+12	5.37E+12	5.51E+11
	28.00	6.77E+12	6.77E+12	5.37E+12	5.51E+11
	31.25	6.77E+12	6.77E+12	5.37E+12	5.51E+11
	34.50	6.77E+12	6.77E+12	5.37E+12	5.51E+11
	37.75	6.77E+12	6.77E+12	5.37E+12	5.51E+11
	41.00	6.01E+12	6.01E+12	4.77E+12	4.89E+11
	44.25	6.01E+12	6.01E+12	4.77E+12	4.89E+11
	47.50	6.01E+12	6.01E+12	4.77E+12	4.89E+11
	50.75	6.01E+12	6.01E+12	4.77E+12	4.89E+11
	54.00	5.24E+12	5.24E+12	4.16E+12	4.25E+11
	57.25	5.24E+12	5.24E+12	4.16E+12	4.25E+11
	60.50	5.24E+12	5.24E+12	4.16E+12	4.25E+11
	63.75	5.24E+12	5.24E+12	4.16E+12	4.25E+11
	67.00	4.46E+12	4.46E+12	3.54E+12	3.61E+11
	70.25	4.46E+12	4.46E+12	3.54E+12	3.61E+11
	73.50	4.46E+12	4.46E+12	3.54E+12	3.61E+11
	76.75	4.46E+12	4.46E+12	3.54E+12	3.61E+11
	80.00	3.66E+12	3.66E+12	2.90E+12	2.96E+11
	83.25	3.66E+12	3.66E+12	2.90E+12	2.96E+11
	86.50	3.66E+12	3.66E+12	2.90E+12	2.96E+11
	89.75	3.66E+12	3.66E+12	2.90E+12	2.96E+11
	93.00	2.86E+12	2.86E+12	2.27E+12	2.31E+11
	96.25	2.86E+12	2.86E+12	2.27E+12	2.31E+11
	99.50	2.86E+12	2.86E+12	2.27E+12	2.31E+11
	102.75	2.86E+12	2.86E+12	2.27E+12	2.31E+11
	106.00	2.09E+12	2.09E+12	1.66E+12	1.68E+11
	109.25	2.09E+12	2.09E+12	1.66E+12	1.68E+11
	112.50	2.09E+12	2.09E+12	1.66E+12	1.68E+11
	115.75	2.09E+12	2.09E+12	1.66E+12	1.68E+11
	119.00	1.39E+12	1.39E+12	1.10E+12	1.11E+11
	122.25	1.39E+12	1.39E+12	1.10E+12	1.11E+11
	125.50	1.39E+12	1.39E+12	1.10E+12	1.11E+11
	128.75	1.39E+12	1.39E+12	1.10E+12	1.11E+11
	132.00	7.76E+11	7.76E+11	6.15E+11	6.22E+10
	134.60	7.76E+11	7.76E+11	6.15E+11	6.22E+10
	137.20	7.76E+11	7.76E+11	6.15E+11	6.22E+10
	139.80	7.76E+11	7.76E+11	6.15E+11	6.22E+10
Tower top	144.386	1.71E+11	1.71E+11	1.35E+11	3.24E+10

B.3. Stress Concentration Factors

For the fatigue calculation, stress concentration factors for this particular joint were determined according to DNV-C302 [22]. The pontoon main column joint was identified as an F joint. The stress concentration factors for in plane bending and axial loads could then be determined by Equation B.1 and Equation B.2. The input variables for these equations are depicted in Figure B.1.

$$SCF_{axial} = \gamma^{0.2}\tau\left(2.65 + 5(\beta - 0.65)^2\right) + \tau\beta\left(\mathrm{C}_2\alpha - 3\right)\sin\theta \tag{B.1}$$

$$SCF_{bending} = 1.45\beta\tau^{0.85}\gamma^{(1-0.68\beta)}(\sin\theta)^{0.7} \tag{B.2}$$

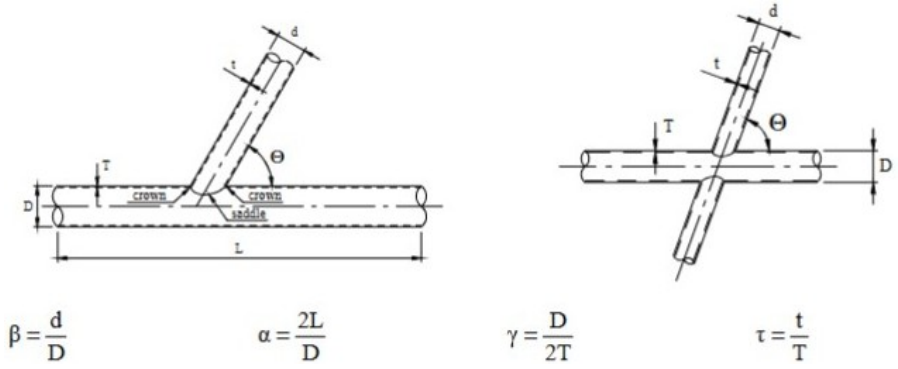

$$\beta = \frac{d}{D} \qquad \alpha = \frac{2L}{D} \qquad \gamma = \frac{D}{2T} \qquad \tau = \frac{t}{T}$$

Figure B.1: Coefficients to determine the stress concentration factor at the intersection of the pontoon and main column.

C

Additional RAFT Validation Results

C.1. First-order Waves

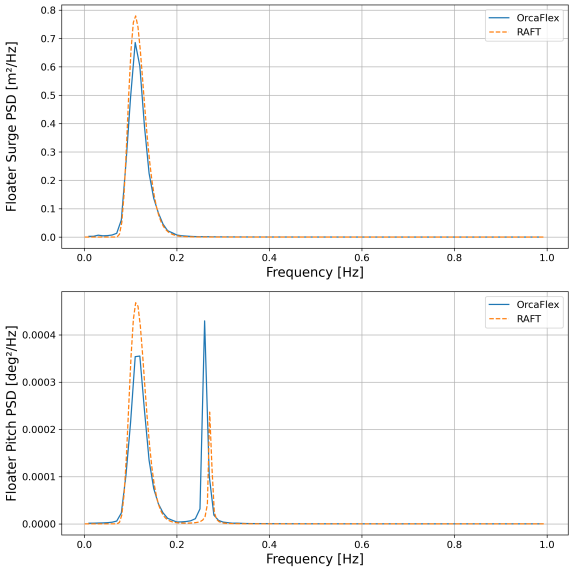

(a) Floater surge and pitch PSD.

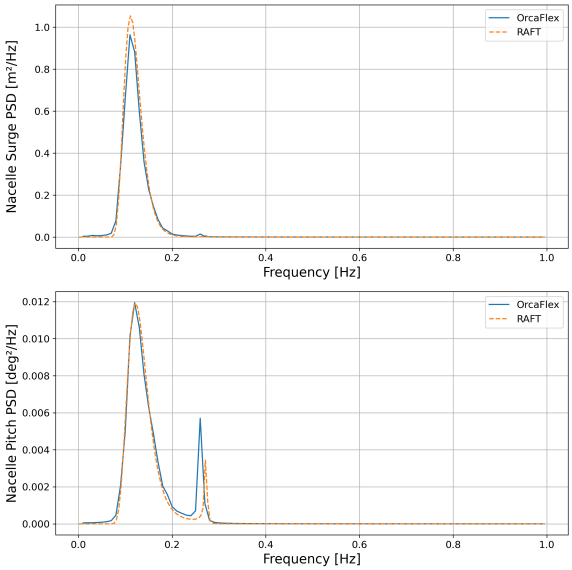

(b) Nacelle surge and pitch PSD.

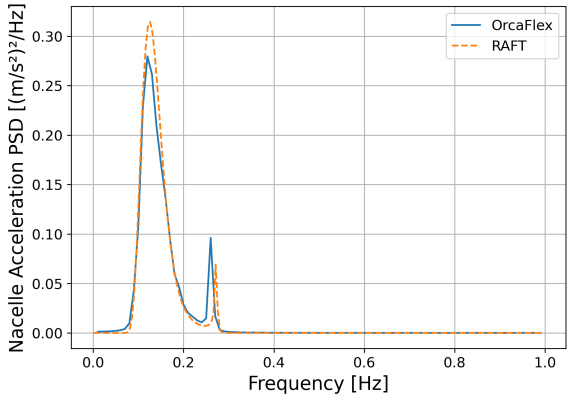

(c) Nacelle acceleration PSD.

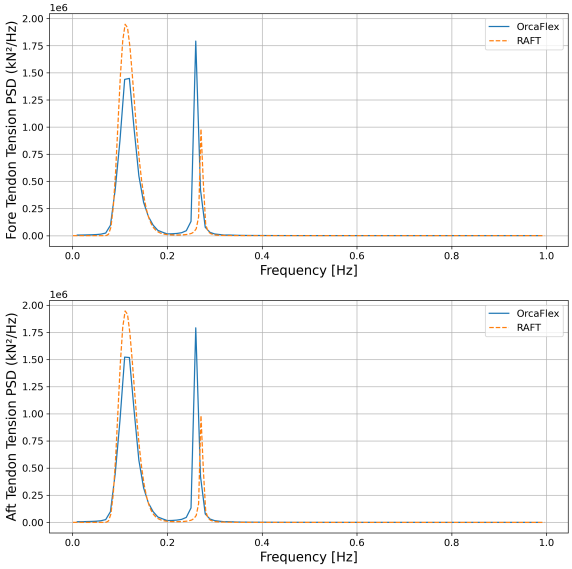

(d) Fore and aft tendon tension PSD.

Figure C.1: Power spectral density comparisons at $H_s = 2$ [m], $T_p = 7.94$ [s], $V_W = 0$ [m/s] subjected to first order waves.

C.2. First- and second-order Waves with Wind

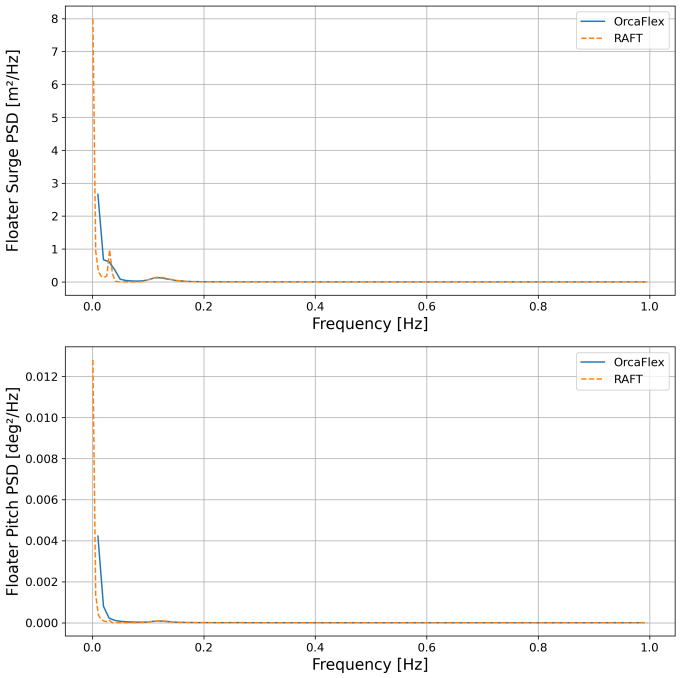

(a) Floater surge and pitch PSD.

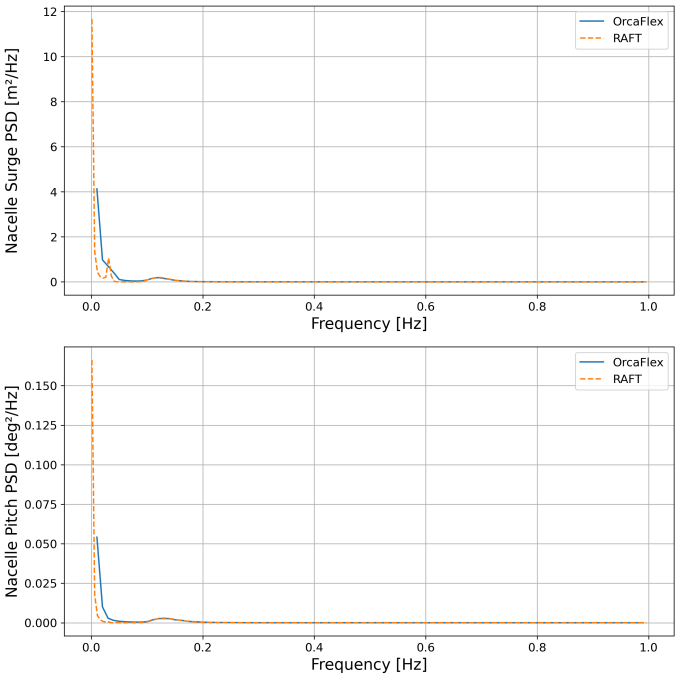

(b) Nacelle surge and pitch PSD.

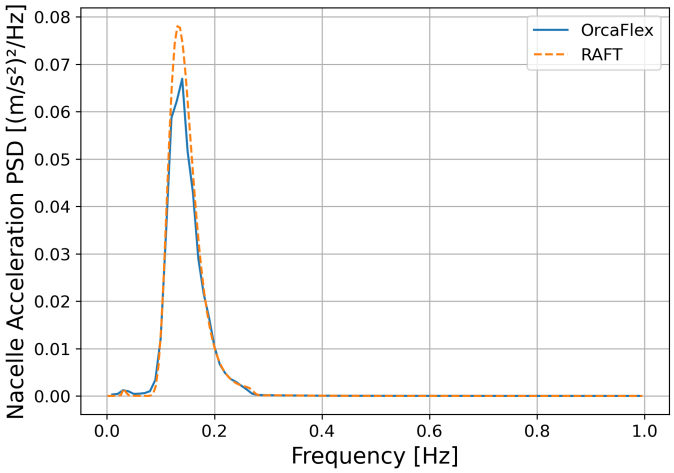

(c) Nacelle acceleration PSD.

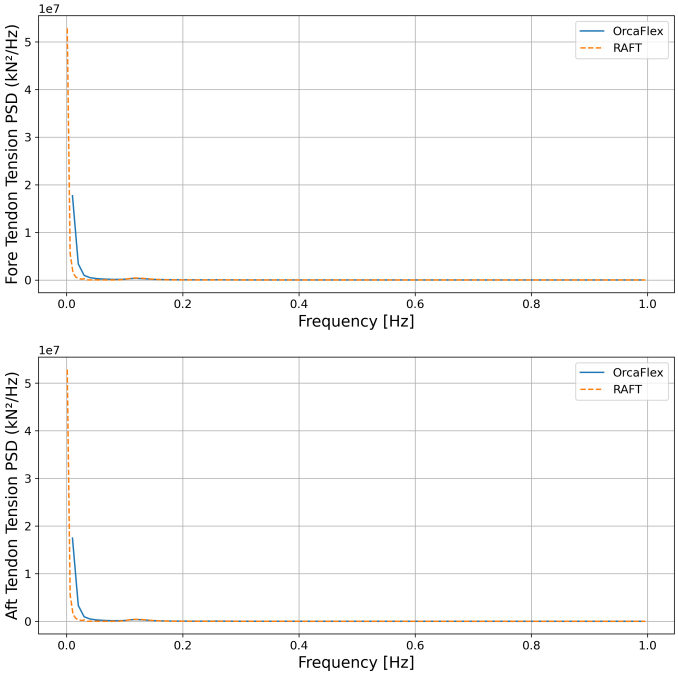

(d) Fore and aft tendon tension PSD.

Figure C.2: Power spectral density comparisons at $H_s = 1$ [m], $T_p = 7.22$ [s], $V_W = 5$ [m/s] subjected to first and second order waves.

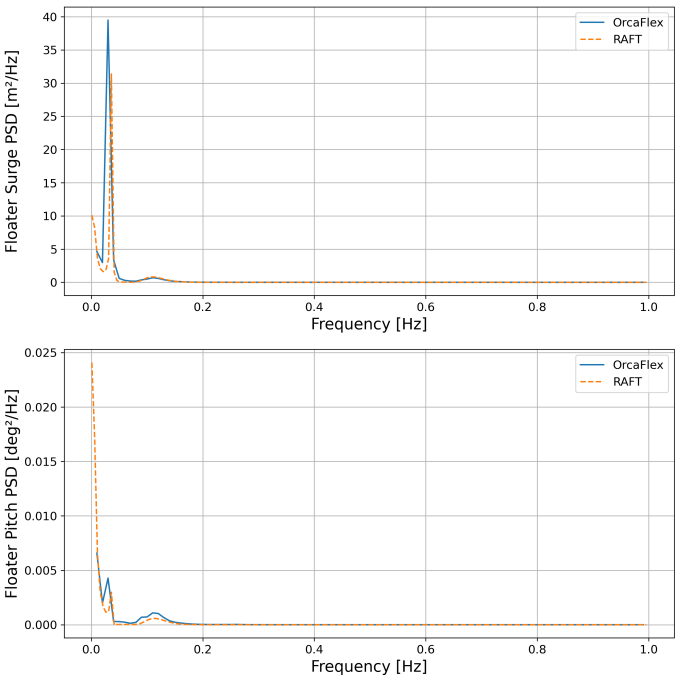

(a) Floater surge and pitch PSD.

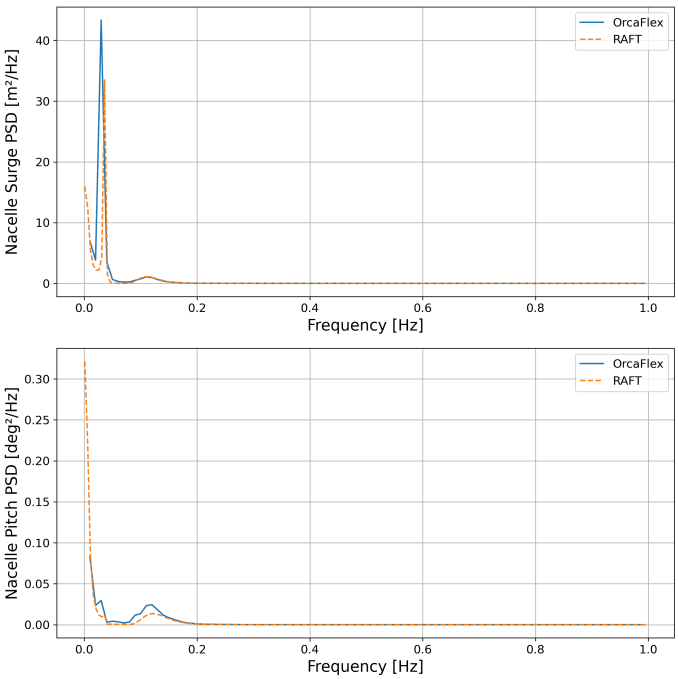

(b) Nacelle surge and pitch PSD.

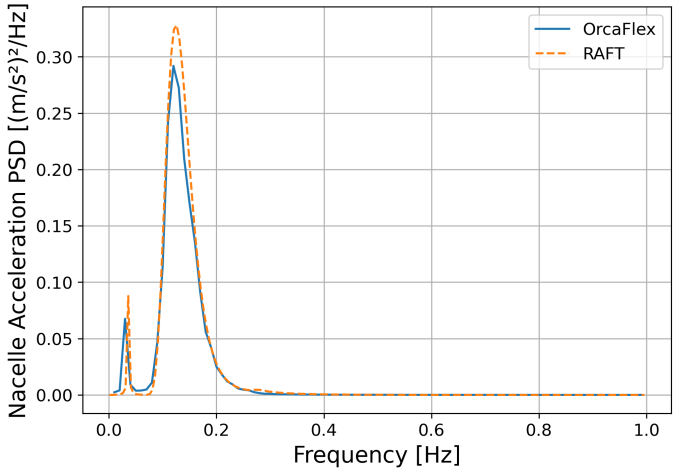

(c) Nacelle acceleration PSD.

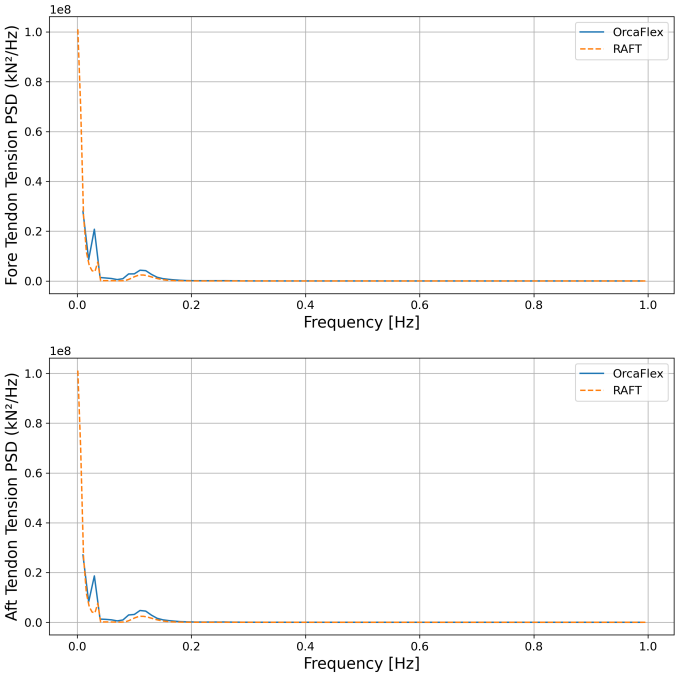

(d) Fore and aft tendon tension PSD.

Figure C.3: Power spectral density comparisons at $H_s = 2$ [m], $T_p = 7.94$ [s], $V_W = 13$ [m/s] subjected to first and second order waves.

D

Additional TLP Design Characteristics Results

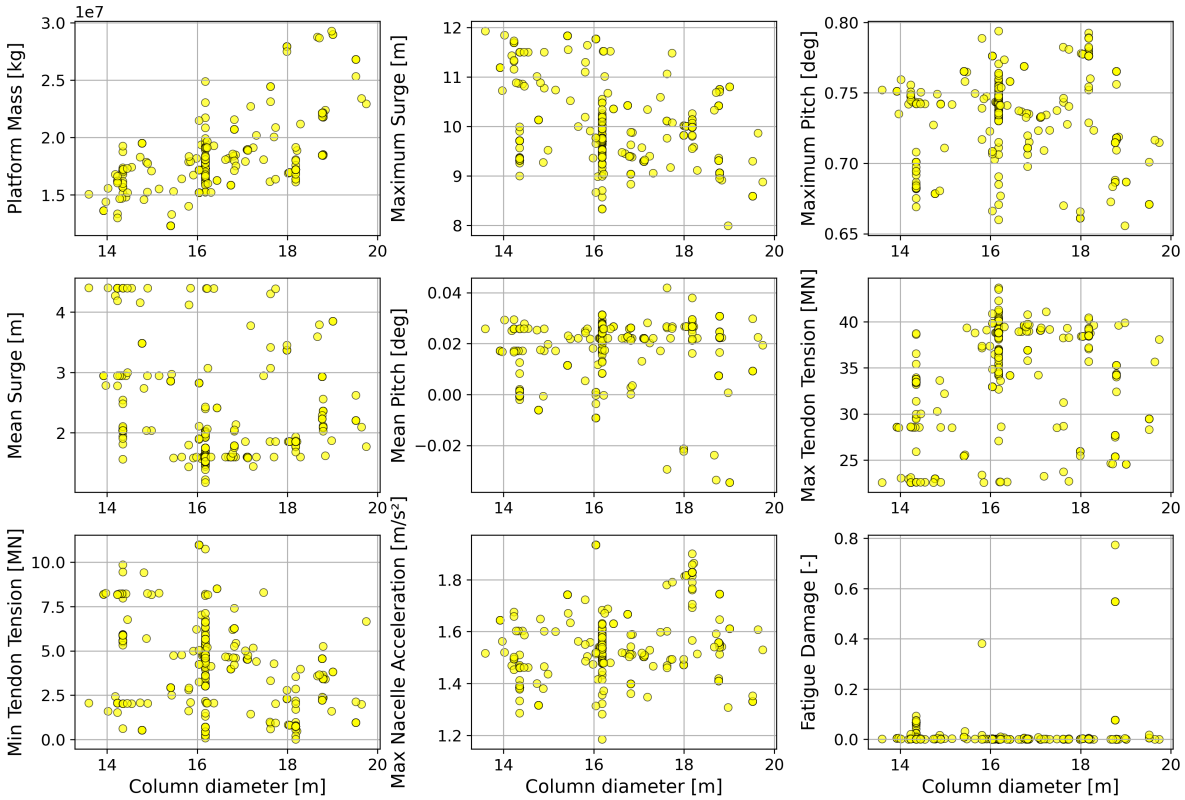

Figure D.1: Column diameter vs outputs

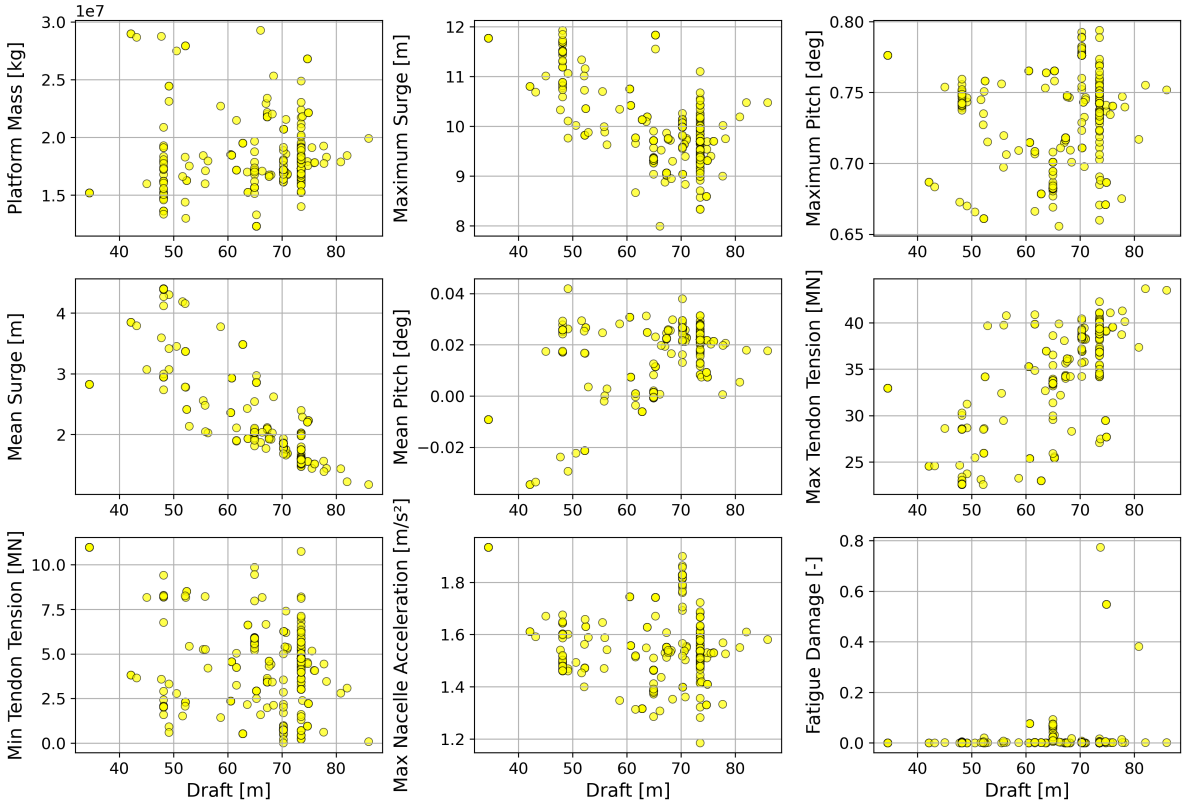

Figure D.2: Main column draft with relation to response results.

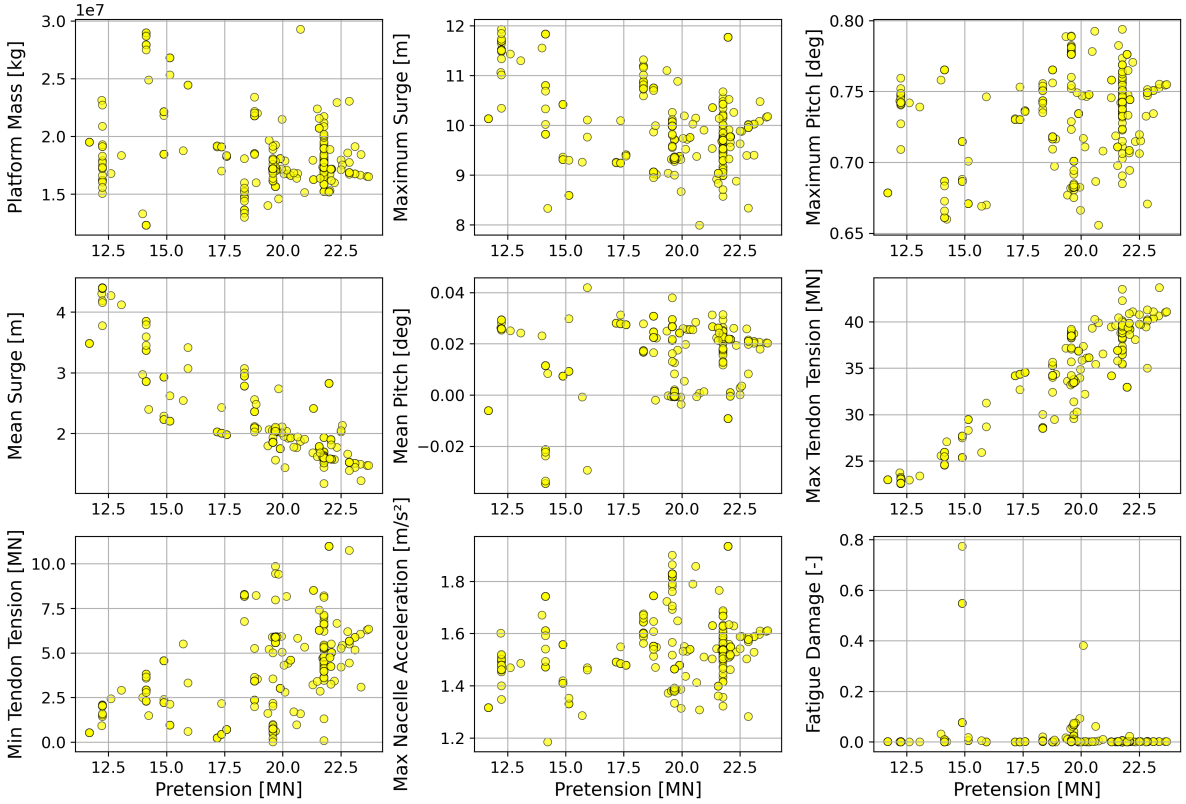

Figure D.3: Pretension with relation to response results.

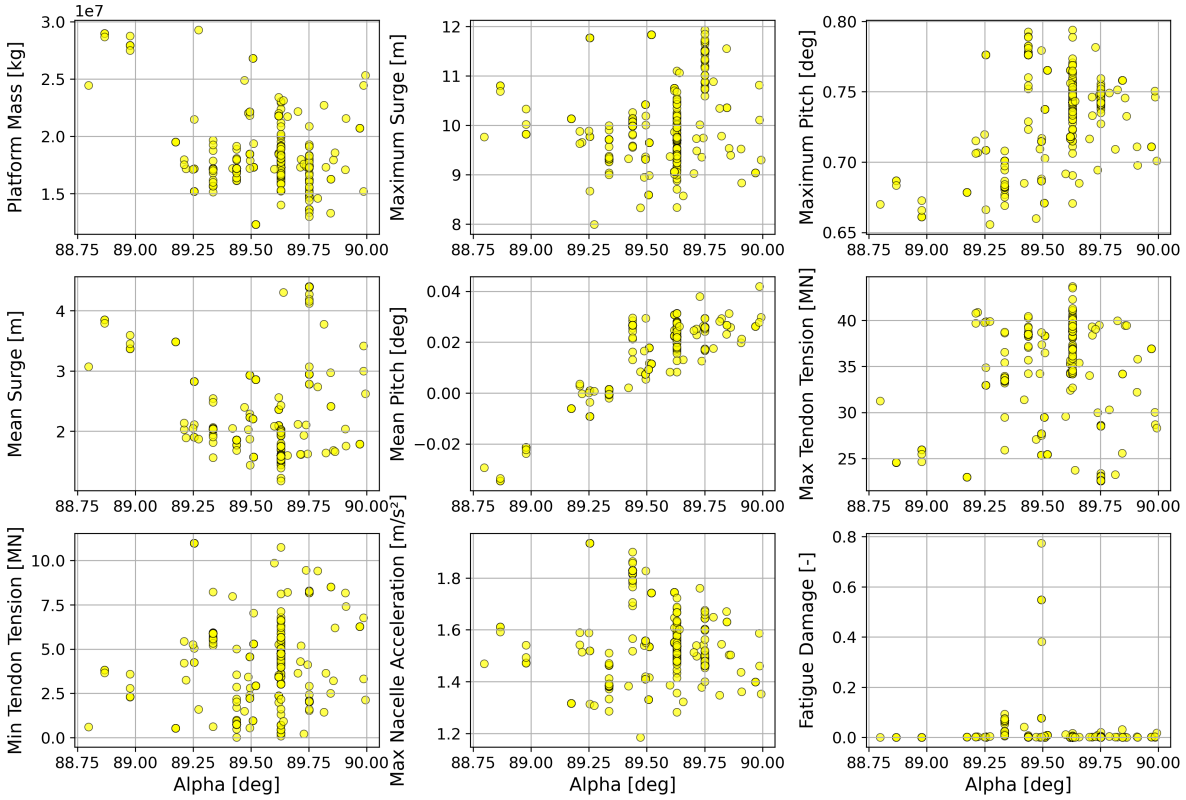

Figure D.4: Tendon angle with relation to response results.

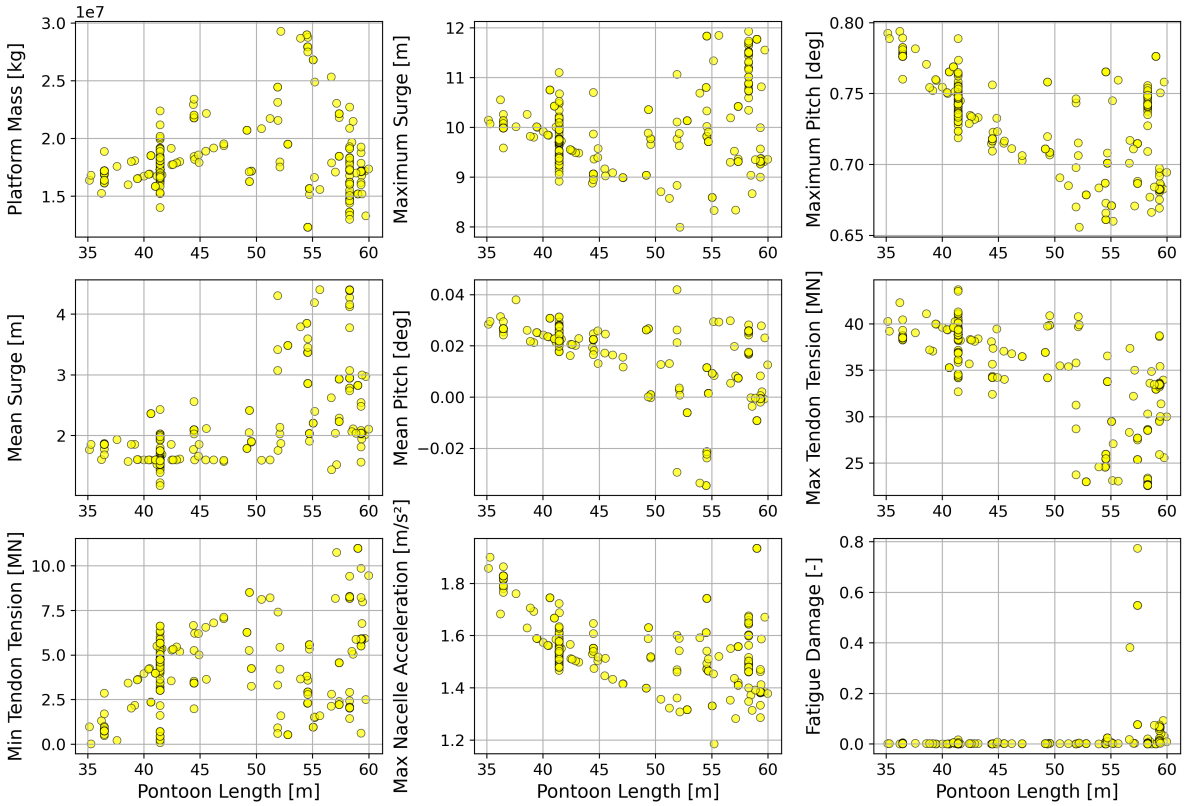

Figure D.5: Pontoon length with relation to response results.

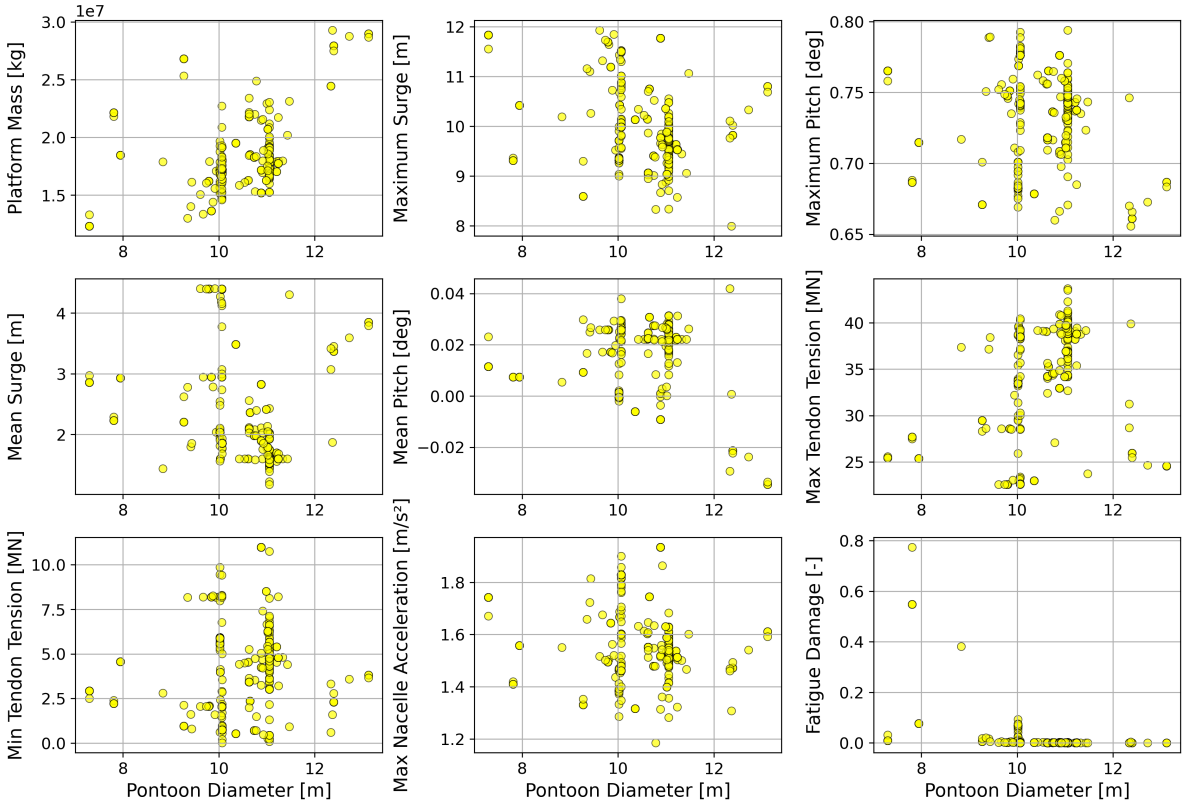

Figure D.6: Pontoon diameter with relation to response results.